Mechanical and Physical Properties of Edmonton Stiff Clay Treated with Cement and Fly Ash

by

Adriana E. Luis Goncalves

A thesis submitted in partial fulfillment of the requirements for the degree of

Master of Science

in
GEOTECHNICAL ENGINEERING

Department of Civil and Environmental Engineering
University of Alberta

Abstract

Cementitious binders have been widely used to improve the mechanical, hydraulic, and physical properties of soft soils by deep soil mixing and jet grouting in the past 50 years. However, the majority of previous investigations are limited to the stabilization of very soft clays in marine environments or sandy soils, which are often mixed with cement contents lower than 15%. This research considers a context where the soil-cement mix (soilcrete) would be produced with stiff clays as a deep foundation to support heavy loads that require cement contents higher than 20% to meet the design requirements for strength. The objective of the present research is to determine the mechanical properties of Edmonton stiff clay mixed with binders composed by cementitious additives. Two binders were used for the investigation, which contained 100% Portland cement and a mix of 90% Portland cement and 10% fly ash.

In the first phase of this research, unconfined compressive strength tests were carried out at different curing ages on soilcrete specimens produced with different cement contents. The results demonstrate that soilcrete with cement contents near 22% continue developing strength at a faster rate after 28 days, when compared to soilcrete with greater cement content. Soilcrete behaves similar to an overconsolidated clay, and reaches peak strength at strains lower than 1% at mature age (>56 days). Scanning electron microscope images show the main differences in the microstructure of soilcrete between the binders.

In the second phase of this research, mechanical properties of specimens produced in the laboratory were investigated through isotropically consolidated–undrained triaxial tests, confined to a pressure ranging from 100 kPa to 3 MPa. Effects of consolidation and shear failure on the soilcrete permeability were quantified. The microstructures of soilcrete failure surface and outer surface were inspected with scanning electron microscope. Computed tomography (CT) scanned

images of the soilcrete were analyzed and a method was proposed to estimate the porosity of the specimen and porosity distribution. The results show strain softening behaviour on all the specimens, and suggest the breakage of cement bonds with confining pressure over 1 MPa. The peak friction angle is the same for both soilcrete, with greater cohesion in specimens with cement only. Significant cohesion remained at the fully-softened state. The new method of analyzing CT scanned images predicted the soilcrete porosities that match the lab-estimated porosity very well.

Key words: soilcrete, cemented clay, unconfined compression, triaxial test, mechanical properties, porosity, SEM, CT scan.

Acknowledgments

Almost two years ago, I started my postgraduate studies in the University of Alberta and it has been an incredible and rewarding journey. I wish to dedicate the following lines to express my sincere gratitude to everyone that contributed to this journey, and especially this project.

In the first place, I want to express my appreciation to my supervisor Dr. Lijun Deng, who has been always helpful, patient and understanding from the beginning, and to Dr. Rick Chalaturnyk, who believed in me and accepted me into the program. Thanks to you both for your helpful insight, and for granting me this opportunity.

I would like to express my gratitude to the Natural Sciences and Engineering Research Council of Canada (NSERC) who funded this research project under the Collaborative R&D program (CRDPJ 493088). My gratitude is extended to Keller Canada Ltd (Edmonton), who provided financial and technical support for the project. I would like to thank especially Claude Berard from Keller, Dr. Lisheng Shao and Dr. Allen Sehn from Hayward Baker Inc. for designing the lab tests, and Dr. Andy Li from the University of Alberta for his thoughtful advice since the beginning of this research project. I also acknowledge Gilbert Wong and Keivan Khalegui from the GeoRef lab at the University of Alberta for providing support for triaxial testing, and Chunhui Liu, Wanying Pang and Allen Gao, graduate students at the University of Alberta, for assisting in preparing the laboratory specimens.

To my friends Ed, JJ and Mau. We have sticked together since day 1, and I am truly grateful for all the laughter, the coffee breaks, our poutine dinners, and most specially for your friendship and support through these months. Now I have three brothers in Canada that will always remind me of my roots and my beloved Venezuela. *Los quiero mucho mis poutines*.

Last but not least, I want to thank my Parents and my brother Carlos for their constant support since I came to Canada, and their valuable words of advice on difficult times. Mom, Dad, you always believed in me and taught me I could dream big and work hard to get where I wanted. I am here today because of you.

Table of Contents

List of Figures

List of Tables

1. Introduction

This chapter includes the background on the use of the deep soil mixing technique for ground improvement of cohesive soils, the objectives of the present research, a brief description of research scope, and the thesis organization**.**

1.1. Background

The development of infrastructure in areas with problematic soils is a common challenge for the current civil engineering practice. The need of extending populated centers and industrial developments to areas with non-suitable soils leads to the use of mechanical or chemical techniques to improve the mechanical and physical properties of the native soil. One of these techniques, known as the deep soil mixing (DSM), has been developed to improve the mechanical properties of soils through the inclusion and in-situ mixing of solidifying/stabilizing additives.

The use of DSM has been investigated for cohesive soils in marine environments with inclusions of cement and lime (Porbaha et al. 1998, Ahnberg et al. 2007). For onshore developments, the use of DSM is more focused on the improvement of sandy soils for embankments that usually require cement contents less than 15% by weight. However, the current need of developing areas inland for the construction of heavy oil tanks requires the inclusion of greater cement contents (>20%) to achieve the design strength requirements with the use of DSM.

The use of Portland cement as the stabilizing additive (i.e., binder) for DSM in cohesive soils has been well investigated in the literature for the production of cement-stabilized materials, termed as "*soilcrete*". Recent publications (e.g., Horpibulsuk et al 2005, Bushra and Robbinson 2013) investigated the effect of the inclusion of alternative cementing products, such as fly ash, on the strength of soilcrete. Their findings suggest that the strength developed by these mixtures with time is similar to the strength achieved when using cement only, but the addition of fly ash modifies the physical properties of the soilcrete in a way that may affect the mechanical performance under the action of stresses.

Research on soilcrete specimens produced with cement-only binders have shown that the development of strength with axial strain changes with increasing confining stress. These changes occur because of the breakage of the cementing bonds after yielding and have been investigated at microscopic scale (Horpibulsuk et al. 2004). Even though there is publication on the development of strength on soilcrete produced with combined binders under unconfined conditions, the microstructure produced in soilcrete with fly ash inclusions may affect the strength development when soilcrete is subject to confining stress.

A literature review reveals a lack of knowledge on the mechanical behavior of soilcrete with fly ash inclusion, and the effect of the microstructural changes cause by fly ash on the mechanical behaviour under the action of confining stresses is not very clear. Most of the related research has been focused on the use of DSM for improving the mechanical properties of soft marine clays. The soils considered for the present investigation are Edmonton stiff clay, more representative of onshore sites, where cohesive soils are naturally stiff but still require ground improvement for the support of heavy loads. Furthermore, the previous research on soilcrete with cohesive soils is usually limited to confining pressures less than 1 MPa; Horpibulsuk et al. (2004) show that a greater confining stress is required in order to exceed the yielding strength of the soilcrete specimens and observe changes in the mechanical behaviour due to breakage of the cementation.

1.2. Objectives

Due to the lack of knowledge on the use of DSM on stiff clays with high cement contents and the effects of inclusion of alternative cementing agents on the performance of the soilcrete under confining stress, the present research project was conducted.

The objectives of this research are the following:

- Design a laboratory mixing plan to produce soilcrete specimens with Edmonton stiff clay and high cement content, using ordinary Portland cement and fly ash.
- Investigate the development of the mechanical properties with curing age of soilcrete specimens subject to unconfined compression.
- Investigate the mechanical and physical properties of mature soilcrete specimens subject to undrained triaxial compression.

- Investigate the microstructure of the failure surface and outer surface of soilcrete specimens.
- Develop a methodology to estimate the porosity of soilcrete specimens using images taken with a computed tomography scanner.

1.3. Test program

To fulfil the research objectives, a series of tests on laboratory produced soilcrete specimens were carried out as follows.

The first phase of the research designed five types of soilcrete. The specimens were produced with an ordinary Portland cement binder and a compound binder of 90% Portland cement and 10% fly ash by weight. Unconfined compression strength tests were carried out on the specimens at curing ages between 3 to 56 days. Scanning electron microscope images of the shear failure surface were inspected. The mechanical properties of each soilcrete type were processed and compared.

The second phase of the research produced specimens of soilcrete with two binder types. The specimens were subjected to a confining stress ranging from 100 to 3000 kPa, and sheared with axial loading under undrained conditions. Consolidated undrained triaxial tests were combined with permeability measurement, scanning electron microscope images, and computed tomography scanner image analysis. The mechanical and physical properties of the soilcrete were calculated and compared to investigate the effect of the microstructural differences of the soilcrete specimens on the strength development with confining pressure, at mature age (>56 days).

1.4. Thesis organization

This thesis consists of five chapters. Chapter 1 is an introduction to the present research. Chapter 2 constitutes a literature review on the history of deep soil mixing technique, the main chemical reactions occurring on the deep soil mixing procedure, and the research development on the use of this technique for improving cohesive soil with cement and other alternative cementing products. Chapter 3 investigates the development of the mechanical properties with curing age of Edmonton stiff clay treated with cement and fly ash using unconfined compression tests. Chapter 4 investigates the development of the mechanical and physical properties with confining stress of

Edmonton stiff clay treated with cement and fly ash. Chapter 5 summarizes the conclusions of this research.

Chapters 3 and 4 have been submitted to the journal Construction and Building Materials for possible publication. Although the papers have multiple authors, the thesis author carried out most of the work, and therefore these papers are included as chapters of this thesis.

Appendix A contains the soil characterization, the soilcrete mix design, and the raw data of unconfined compression strength tests. Appendix B contains the raw data of isotropically-consolidation undrained triaxial tests. Appendix C compiles the images taken with the scanning electron microscope on soilcrete samples. Appendix D compiles the images for the CT scan analysis and a report of mercury intrusion porosimetry tests. The mixing procedure for laboratory production of soilcrete and the standard test procedure for triaxial testing on soilcrete specimens are attached in Appendix E and F, respectively.

2. Literature Review

2.1. Ground improvement and use in engineering practice

As cities and populated areas continue to expand, land with favorable geotechnical properties for development of roads and civil structures tend to become scarce leading to the use of less suitable areas with problematic soils. This challenge is common nowadays, and is an important part of the current civil and geotechnical engineering practice. Usually, one or several ground improvement techniques need to be applied in order to improve the mechanical properties and other geotechnical conditions of the local soils.

Ground improvement techniques are designed to improve deficiencies in local soils, which may require remediation due to conditions that are induced naturally or by human activity. Naturally induced conditions may be due to the local geology, hydrology, temperature, and seismicity, which are proper of each location. Human induced conditions are related to the human activities that had taken place previously at the site or nearby locations, such as the presence of fill or dredged material not suitable for construction, or the existence of solid waste that might require remediation for future development of the land.

Ground improvement techniques are classified depending on their basic work principles, which can be replacement, densification, consolidation or dewatering, grouting, admixture stabilization, thermal stabilization, reinforcement, and miscellaneous (Kitazume and Terashi 2012). Most of these techniques are limited because of the environmental restrictions for civil engineering activities that require excavation and replacement of soil, or activities that produce noise and vibration.

2.2. Deep soil mixing technique

The deep soil mixing (DSM) is part of the admixture stabilization techniques used to improve the mechanical, hydraulic, and physical properties of soils. This is possible by adding a chemical additive (i.e. binder) into the natural soil and forming stabilized soil columns with diverse radius and disposition, by using an auger. Although DSM might be perceived as a costly ground improvement technique, there are several advantages when compared with other traditional methods, since the strength of the stabilized material can be improved greatly, with reduction of

settlement and hydraulic conductivity. Principally, DSM provides a low construction related noise and vibration while improving large extensions of land not suitable for infrastructure.

The use of DSM as a ground improvement technique was first developed in 1954 in the United States (Bruce et al. 2013). However, most of the research after the invention of the method took place mainly in Japan and Scandinavia between 1960 and early 1970's, due to the need of developing infrastructure on soft cohesive soils and marine or port environments. The use of lime, cement, and other additives became popular in Southeast Asia and Scandinavia, with most of the research published in their own languages. In 1996, an international conference on grouting and deep mixing was hosted in Tokyo, Japan; this conference allowed a widespread divulgation of the advances in this technique. Since then, many studies have been conducted on the use of the DSM technique with different additives and in the applications of the technique for development of infrastructure in other locations around the world.

2.2.1. Use of dry method versus wet method

The basic principle of the DSM technique is to combine the soil *in situ* with a stabilizing additive or a combination of additives (i.e., binder), in order to enhance the mechanical, hydraulic, and physical properties of the native soil by producing a stabilized mix, termed as "*soilcrete*". During this process, the goal is to achieve a uniform distribution of the binder in the volume being treated, usually by employing a cutting tool that rotates in a vertical and/or horizontal direction along the cutting arm. The addition of the binder into the soil can occur through the dry or wet method.

The dry method in DSM adds the binder into the soil as a dry powder. To use this method, the soil needs to be soft to allow the tools to penetrate, cut, and properly mix all the elements, meaning that the soil should be saturated or nearly saturated. A mixing tool with blades cuts the soil to reach the specified depth, where the binder is delivered with compressed air and injected into the soil upon retrieval of the mixing tool (Kirsch and Bell 2012).

When the wet method is applied, the binder is added by mixing the dry binder powder with water to form a slurry. In this case, the soil does not need to be saturated prior to the addition of the slurry, since additional moisture is added to the soil through the slurry during the mixing process. The equipment used for this method may have maximum eight rotary hollow shafts,

similar to an auger, with cutting tools and mixing blades above the nozzle that injects the slurry (Han 2015). Several configurations exist for these machines, which depend mainly on the depth to achieve during improvement and the configuration of the final improved section, as individual columns or cut-off walls.

2.2.2. Application of DSM

The DSM is mostly used to improve strength and reduce the compressibility of cohesive soils. In granular soils, it can be used for applications such as liquefaction mitigation and seepage cut-off. The extension of DSM could go as deep as 70 m for marine sites, or 30 m for inland operations (Han 2015). Favorable soil conditions for the use of DSM are usually: water content less than 200% (for dry method) and less than 60% (for wet method), loss on ignition less than 10%, and pH greater than 5. The use of DSM might be limited or restricted in locations with abundance of boulders into the soil and in locations with limited access for large equipment.

The application of DSM on inland sites has been largely used in the pavement industry for embankment improvement and stability on cohesive soils. For instance, Horpibulsuk et al. (2006, 2009, 2010) conducted research on soft clays improved with cement and fly ash, and studied the effects of binder dosage on the mechanical properties and microstructure of the soilcrete. Lo and Wardani (2002) investigated the mechanical properties of compacted silts stabilized with cement and fly ash. Jamshidi and Lake (2014) investigated the reduction of seepage and the strength development with curing time for sandy soils stabilized with cement. These investigations conducted for applications on the pavement industry are usually limited to the use of maximum 10% cement content by weight. However, when using DSM to enhance the bearing capacity of cohesive soils under large superstructures (such as oil storage tanks) greater cement contents are required to meet the design strength.

The application of DSM for foundation of heavy structures has been investigated outside Canada. Investigations conducted by Rampello and Callisto (2003) on stiff silty clays in Italy found that the addition on the site of several DSM columns with cement content in a range of 18 to 21% allowed reductions of a maximum of 30% on the settlement below the center of the tank. Pakbaz and Alipour (2012) and Eskisar (2015) conducted research on soft lean clays from Iran and Turkey in order to assess the strength improvement of the soil and investigate the changes in

the mechanical properties with cement stabilization. Their results show important improvement of strength on the native soils, but were limited to a cement content of 10%. The published resources related to cement stabilization through the DSM when using more than 20% cement content to improve the strength have been mostly conducted on soft cohesive soils (e.g., Uddin et al. 1997, Miura et al. 2001, Sassanian and Newson 2014), which are representative of marine environments. The research on stiff cohesive soils has shown to be very limited in the literature.

2.3. Hardening reactions on soilcrete

The hardening process of a cementing binder occurs in four phases: hydration of the binder, ion exchange, formation of cement hydration products, and formation of pozzolanic reaction products. These reactions allow for hardening to occur in the short term, and to develop for long term when the proper curing conditions are provided, as shown in Figure 2-1 (Kitazume and Terashi 2012).

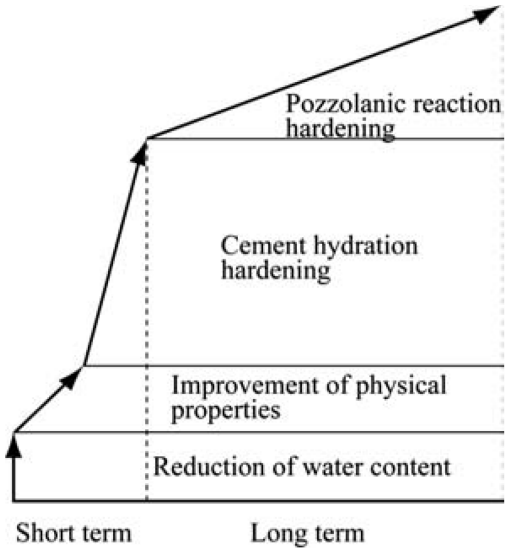

Figure 2- 1. Mechanism of cement stabilization (Kitazume and Terashi 2012).

In the first two phases, the reaction occurs when the binder enters in contact with water. The water content in the mix is decreased due to the hydroxide ion (OH^-) exchange between water and the cement components. Hydration occurs shortly after the first 3 hours in which this reaction takes place, producing the following cementitious products (Lorenzo and Bergado 2006):

Hydrated calcium silicates (C_2SH_x, $C_3S_2H_x$)

Hydrated calcium aluminates (C_3AH_x, C_4AH_x)

Hydrated lime or calcium hydroxide $Ca(OH)_2$

where: C, S, A, and H are symbols for calcium oxide (CaO), silicate (SiO_2), aluminate (Al_2O_3), and water (H_2O), respectively.

In the third phase, cement clusters of gels start forming and hardening the mix, causing a loss in the workability. If the conditions of humidity and temperature are maintained, the cement silica or alumina gels (CSH or CAH) expand and stretch out filling the voids and attaching to the aggregate or soil particles. After the first month of curing, the hydration reactions tend to be complete. As a result, the cement clusters are bonded with the aggregates and the pH of the mix has increased due to the ion exchange and the production of calcium hydroxides ($Ca(OH)_2$).

In the fourth phase, the increased alkalinity of the soil after hydration and continuum curing conditions allow for pozzolanic reactions to take place and generate stronger bonds due to the crystallization of the gels, which continue developing with time (Kosmatka et al. 2002). The reactions in this phase are mainly the production of silica and alumina gels as follows (Das and Sivakugan 2016):

$Ca(OH)_2 + SiO_2 \rightarrow CSH$

$Ca(OH)_2 + Al_2O_3 \rightarrow CAH$

2.3.1. Influence of stabilizing binders on the mechanical properties of soilcrete

The most commonly used additives in DSM are lime, ordinary Portland cement, and other cementitious additives such fly ash, gypsum, and slag.

2.3.1.1. Lime

Lime based stabilization is common in soils with very high water content and it has been shown to provide stabilization in soft cohesive soils (Ahnberg et al. 2003). The pore water chemical composition is especially important in this case, since the addition of lime to the soil generates

pozzolanic hardening and not hydration products. Therefore, the reaction of lime with water is what causes the increase in soil alkalinity to trigger the pozzolanic reactions.

2.3.1.2. Ordinary Portland cement

Ordinary Portland cement is being increasingly used as a stabilizing material for ground improvement. Cement based stabilization can be used for granular or cohesive soils alike, being more effective in granular soils and low plasticity clays (Das and Sivakugan 2016). Similar as in lime stabilization, cement decreases the workability of the stabilized soil due to hardening reactions. However, the strength improvement in cement stabilization tends to be greater than in lime-stabilized soils, mainly because the calcium hydroxides produced during hydration of cement are more reactive than the free lime present in lime binders (Sassanian and Newson 2014).

2.3.1.3. Fly ash

Fly ash is a by-product of the pulverized coal combustion process in electrical power plants, and is mainly composed by silica, alumina and various oxides (Kosmatka et al. 2002), causing fly ash to be pozzolanic in nature. Therefore, fly ash reacts with calcium hydroxides to generate cementitious products. It is often used as a supplementary cementitious material (SCM) due to the technical benefits that it can add to the hardening in lime or cement stabilization, such as resistance to alkali-aggregate reactivity.

There are two main classes of fly ash. Class C fly ash contains free lime in its composition, allowing the fly ash itself to be a cementing product without being combined with lime or cement. Class F fly ash on the other hand, contains no calcium hydroxides by itself, and need to be combined with lime or cement to allow for the pH in the mix to increase and trigger the pozzolanic reactions for hardening to occur.

Fly ash can be used as a partial replacement of ordinary Portland cement, since the reactivity is similar to cement and the cost is significantly less (Das and Sivakugan 2016). However, laboratory investigations are usually recommended to select the proper dosage of the components into the stabilizing binder to achieve the design purpose (e.g., increase bearing capacity, reduce settlement, decrease hydraulic conductivity, etc.).

2.3.1.4. Combination of additives

In DSM the additive used for stabilization, known as the "*binder*", can be composed by one or more additives. Binders that include the combination of several cementitious additives such as ordinary Portland cement, gypsum, and fly ash are commonly used in practice to maintain a balance between the economy and mechanical or physical properties of the soilcrete.

Horpibulsuk et al. (2009) conducted research on cohesive soils stabilized with different dosages of cement and fly ash. Their results show that fly ash generates dispersion of the cement cluster present in the soilcrete allowing for more surface of the cement particles to take part in the hardening reactions. The dispersion effects of fly ash on the soilcrete were inspected by using scanning electron microscope (SEM) images on samples with different contents of fly ash.

Horpibulsuk et al. (2011) and Bushra and Robinson (2013) conducted research on similar soils to gather more information on the effects of dosages of fly ash on the improvement of strength in soilcrete. Their investigations found that by replacing 10 to 20% of the Portland cement in the binder with fly ash, the strength of soilcrete is nearly the same as that of cement-only soilcrete. Therefore, additions of fly ash in a range of 10 to 20% per binder weight reduces the cement use in the binder, and in consequence reduces the costs.

Horpibulsuk et al. (2011) and Ma et al. (2014) showed that the dispersion effect of fly ash in a soilcrete mixture can be accounted as a cement content, since it enhances the strength of the soilcrete mix. The total cement content C_T is calculated with Equation [1] (Horpibulsuk et al. 2011):

$$C_T = C_c(1 + 0.75C_f) \qquad [1]$$

where C_c and C_f are the mass of cement and mass of fly ash by mass of soil solids, respectively.

2.3.2. Influence of pore water on the mechanical properties of soilcrete.

The chemistry of the pore water might influence as well the improvement of strength in soilcrete materials. Ahnberg et al. (2003) suggested that in cement base soilcrete the pore water alkalinity is more important for the hardening reactions than the alkalinity of the soil, since the cement reacts mainly with the pore water. The pH of the pore water increases during hydration reactions

and continues developing hardening reactions as long as the water content present in the mix is adequate. Therefore, the water content with respect to the cement content by weight in a binder is crucial for the improvement of strength.

Miura (2001), Lorenzo and Bergado (2004), and Horpibulsuk et al. (2005) defined the clay water content in the soil (w_c) as the total water mass per mass of soil solids in the soilcrete. w_c is defined in Equation [2]:

$$w_c = \frac{m_w + m_{ws}}{m_s} \cdot (100\%) \qquad [2]$$

where: m_w is the mass of water in the clay, m_{ws} is the mass of water in the water/binder slurry, and m_s the mass of soil solids. Their research showed that the hardening of soilcrete relies on the water content available with respect to the cement content, following the principle of Abraham's law for hardening of concrete (Miura et al. 2001, Horpibulsuk et al. 2003). This relationship is better known as the clay water to cement ratio w_c/C_T.

Lee et al. (2005), Bruce et al. (2013) and Ma et al. (2014) compared the w_c/C_T ratio to the achieved strength; they found that the strength improvement is greater as the w_c/C_T ratio decreases, and the greater strength development is achieved in a range of w_c/C_T from 2.5 to 1.5 (Figure 2-2).

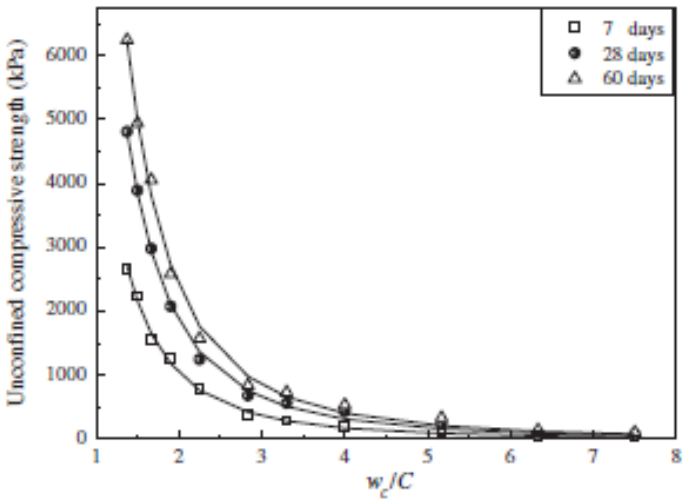

Figure 2- 2. Improvement of unconfined strength in cement improved clays with respect to w_c/C_T (Ma et al. 2014).

2.3.3. Effect of soil properties on mechanical properties of soilcrete.

The soil type can also influence the strength development of a soilcrete material. Previous research suggests that granular soils are more suitable for strength development than cohesive soils, such as clays. The principal reason for this behaviour is that sandy soils possess lesser specific surface than clayey soils, and the later would require greater amounts of stabilizing binder to bond the particles together.

Several factors may affect the suitability of a clayey soil for cement stabilization, mainly the texture and mineralogy composition. Clay minerals tend to consume the calcium hydroxides (lime) produced during hydration of cementitious products. The affinity of montmorillonite clay minerals (expansive clays) to lime reduces the pH of the pore water in a greater extent than less active clay minerals, such as kaolinite or illite. Therefore, in presence of active clay minerals, the requirement of lime to promote hardening through pozzolanic reactions is not fulfilled unless greater amounts of cement are added, and the developed strength is usually lower than in soilcrete with less active clays (Bell 1993).

Due to the size of the clay minerals, their identification cannot be done with optical mineralogical techniques, but with the application of X-ray diffraction (XRD) tests. Clay minerals have crystalline structures, conformed by colloidal silica or alumina crystal sheets arranged in groups (Holtz et al. 2011). In the analysis of the clay mineral, it is possible to compare the intensity of the peaks given in the diffraction spectrum of a specific soil and the spectrum of known minerals, to define the type of clay minerals. Microscopic analysis and chemical analysis can be used to define the constituents of the non-clay fraction and the organic content, respectively (Mitchell and Soga 2005).

Some clay minerals are easily recognizable through the XRD spectrums on the crystals, or by inspection of images taken with SEM. However, many soils might be composed by combinations of several clay minerals. In such case, a detailed qualitative analysis may not be assessed. In order to approximate to the clay mineral in a specific soil, Holtz et al. (2011) developed a guide to identify the clay minerals (Figure 2-3) based on Casagrande's plasticity chart and clay mineralogy data from Mitchell and Soga (2005).

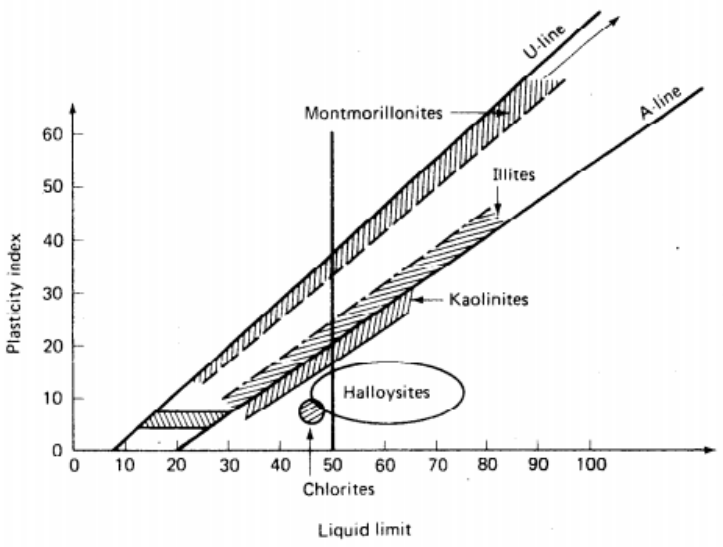

Figure 2- 3. Identification of clay minerals with index properties on Casagrande's plasticity chart (Holtz et al. 2011).

Illite clay minerals are very common in clayey soils, especially in glacio-lacustrine clay deposits in central and North America. According to the chart (Figure 2-3), glacial lake clays from the great lakes in U.S. and Canada would most probably plot above the A-line, due to their illitic nature (Holtz 2011).

2.4. Previous research in DSM in cohesive soils

Previous research in DSM has focused on the application of the technique for improvement of the mechanical properties of soft cohesive soils in marine sites, for improvement of embankments, or for pavement. Table 2-1 summarizes the recent research in this area, describes the characteristics of the soil and stabilizing binders used, and explained the type of testing.

Most of these investigations (Table 2-1) were conducted in soft marine clays stabilized with cement contents in the order of 2 to 18%. The research conducted on soilcrete produced with high cement contents (>20%) is usually limited to applications in soft cohesive soils (Miura et al. 2001, Kamruzzaman et al. 2009). Therefore, there is a knowledge gap in the use of cement contents greater than 20% by weight on stiff cohesive soils for applications of the DSM on inland sites that require great strength improvement.

Table 2- 1. Summary of research conducted for DSM on Cohesive soils

Reference	Type of soil	Type of binder	Cement content by weight	Tests conducted
Ahnberg (2007)	Soft clay	Cement, slag, lime and fly ash	5 to 20%	CU and CD
Banks (2001)	Kaolin clay	Cement	2 to 10%	UC, CU and CD
Bushra and Robinson (2013)	Marine clay	Cement and fly ash	10 to 20% cement and 10 to 30% Fly ash	UC and oedometer
Chew et al. (2004)	Marine clay	Cement	5 to 50%	UC and SEM
Eskisar (2015)	Lean clay	Cement	5 to 10%	UC and oedometer
Horpibulsuk et al. (2003)	Soft clay	Cement	5 to 20%	UC
Horpibulsuk et al. (2004)	Soft clay	Cement	6 to 18%	CU
Horpibulsuk et al. (2005)	Soft clay	Cement	8 to 33%	UC and CD
Horpibulsuk et al. (2009)	Silty clay	Cement and fly ash	10% cement with 10 to 40% fly ash replacement per binder weight	UC and SEM
Horpibulsuk et al. (2010)	Silty clay	Cement	0 to 10%	UC and SEM
Horpibulsuk et al. (2011)	Soft clay	Cement and ash	0 to 30% cement content with 0 to 60% ash replacement per binder weight	UC
Jamshidi and Lake (2014)	Silty sand	Cement	10%	UC and permeability
Kamruzzaman et al. (2009)	Marine clay	Cement	10 to 60%	UC, SEM, oedometer and CU
Kasama et al. (2006)	Soft clay	Cement	5 to 10%	CU
Lee et al. (2005)	Marine clay	Cement	soil/cement ratio 1 to 4	UC
Lo and Wardani (2002)	Sandy silt	Cement and fly ash	2% cement and 4% fly ash	UC, CU and CD
Lorenzo and Bergado (2006)	Soft clay	Cement	5 to 20%	UC and CU
Ma et al. (2014)	Soft clay	Cement, sodium silicate and sodium hydroxide	10 to 80% cement and 10% cement with 2 to 6% other additives	UC and SEM
Miura et al. (2001)	Soft clay	Cement	8 to 33%	UC and CD
Pakbaz and Alipour (2012)	Lean clay	Cement	4 to 10%	UC and oedometer
Uddin et al. (1997)	Soft clay	Cement	5 to 40%	UC, oedometer and CU

UC: unconfined compression test.
CU: consolidated undrained triaxial test.
CD: consolidated drained triaxial test.

Laboratory investigations are usually implemented for research on cement-stabilized soils. The soilcrete specimens are mixed in the laboratory and later subject to different types of tests. The test results are used to compare the effectivity of several dosages of binder, and to assess the mechanical properties of the stabilized material to determine if the improvement of these properties is suitable for the design purpose.

The unconfined compressive strength (UCS) of soilcrete specimens produced in the laboratory has been used in investigations on soilcrete due to its simplicity and rapid reproduction in the laboratory. Although the UCS can be an indicator of the actual strength achieved in the field (Han 2015), other investigations subject the soilcrete specimens to confining pressure and controlled drainage conditions through triaxial tests. These advanced tests account for the presence of surrounding stresses and estimate an approximation to the actual strength developed in the field.

The effect of confining stress on soilcrete specimens has been investigated in several studies listed in Table 2-1. The use of consolidated drained (CD) or undrained tests (CU) is intended for assessing the strength development and deformability of soilcrete specimens under confining stress, which may resemble better the field conditions of deep soilcrete columns.

Porbaha et al. (2000), Banks (2001), Lo and Wardani (2002), and Ahnberg (2007) show that specimens of soilcrete tested under short-term undrained condition allow very little deformation to occur before reaching the peak strength, when compared to specimens under drained conditions. The tendency of soilcrete to reach peak strength and later fail with low axial strain under undrained tests makes the undrained condition more critical. The comparison of drained and undrained tests by Porbaha (2000) is shown in Figure 2-4.

Uddin et al. (1997), Banks (2001), Chew et al. (2004), Horpibulsuk et al. (2004), and Kasama et al. (2006) conducted isotropically consolidated-undrained (ICU) triaxial tests of soilcrete specimens produced with very soft clays or sand-clay mixed with cement contents between 2 and 18% by mass of soil solids. The results show that the soilcrete behaved overconsolidated when subject to confining pressure ranging from 50 kPa to 1 MPa.

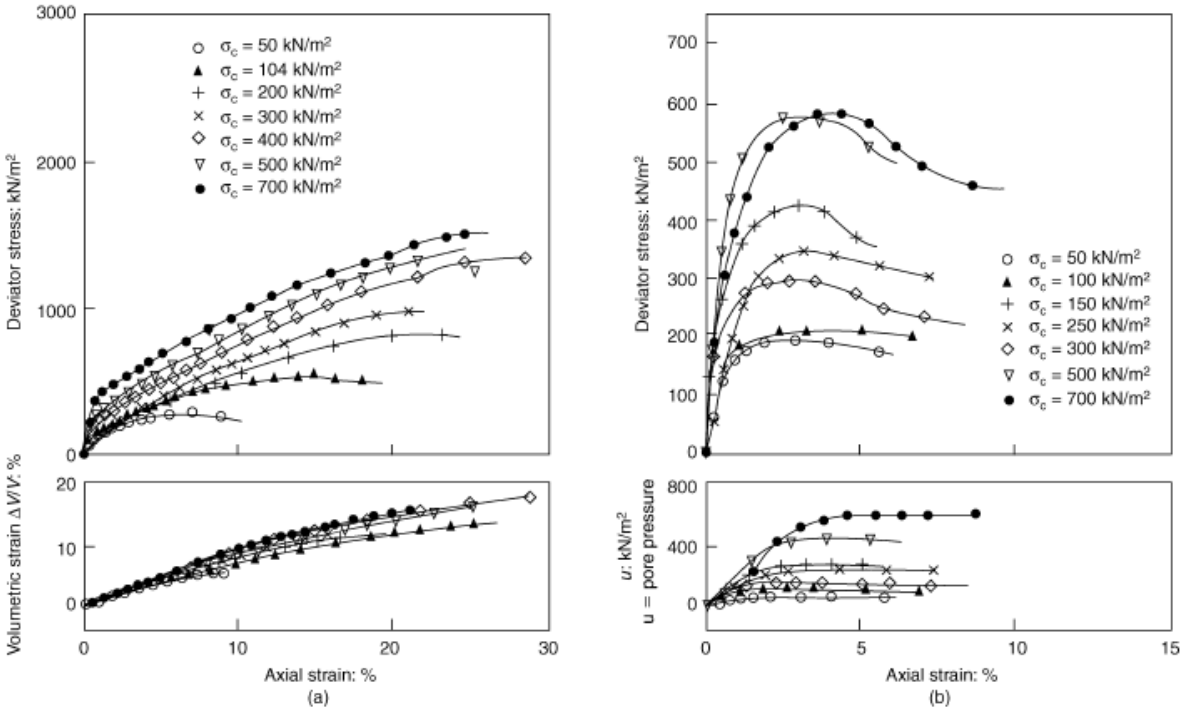

Figure 2- 4. Consolidated triaxial test results for laboratory soilcrete specimens by Porbaha et al. (2000): (a) drained test and (b) undrained test.

Horpibulsuk et al. (2004) conducted research on soilcrete produced with cement subjected to confining stress in a range of 50 kPa to 3 MPa. Their results show that the soilcrete tends to allow for greater volumetric deformation when reaching the yield strength P_y'. When the soilcrete is subject to a broad range of confining stress it tends to develop a strain softening behaviour similar to an overconsolidated (OC) soil before reaching P_y' and transition to normally consolidated (NC) behaviour with confining stress beyond P_y'. The transition from OC to NC behavior occurs between 1 and 2 MPa for soilcrete with cement inclusion of 18%, and the peak strength shows to increase greatly with confining stresses beyond P_y'.

These results suggest a change in fabric of the soilcrete due to the breakage of cement bonds when confining pressure increases beyond P_y'. When producing soilcrete specimens with greater cement content the confining stresses should be selected accordingly to be able to assess results in both the OC and NC range. The results presented in the literature are typical for soilcrete produced with cement-only binders, but there is a lack of knowledge on the behaviour developed by soilcrete specimens produced with inclusion of fly ash in the binder. Since previous research

acknowledge changes in the microstructure of the soilcrete with inclusion of fly ash, and the changes in physical properties, such as porosity (e.g, Horpibulsuk et al. 2009, and Kamruzzaman et al. 2009), the mechanical properties might change as well. Therefore, further investigation in this topic is recommended.

2.5. Use of images on analysis of physical properties in soilcrete

2.5.1. Scanning electron microscopy (SEM)

The use of SEM images on investigations with clayey materials is usually focused on determining the clay mineral type of the soil. The SEM method has been recently used for soilcrete specimens. For example, Tomac et al. (2005) studied in detail the binder and soil interaction, and the changes on microstructure of the material, which in consequence affects the mechanical behaviour.

Kamruzzaman et al. (2009) used SEM images to investigate the effect of confining stress on the destructuration of the cementing bonds on a soilcrete produced with marine clays and variable cement contents subject to UCS and ICU triaxial tests. The results show a destructuration of the bonding mainly in the failure surface, and little to no effect of the stresses on other sections of the specimen.

Horpibulsuk et al. (2009) made a similar analysis on compacted soilcrete samples produced with combinations of cement and fly ash, to investigate the effects of fly ash on the mechanical properties and porosity of soilcrete. Their findings show a dispersive effect of the fly ash on cement clusters, which results in an enhancement of the strength and a decrease in the porosity of the specimen, with respect to soilcrete produced with cement only.

2.5.2. Computed tomography scan

Non-destructive tests such as SEM and computed tomography (CT) scanned images have become popular to determine physical characteristics of rock, minerals and soils, in combination with destructive tests like UCS. For instance, Peyton et al. (1992) used CT scanned images to estimate porosity and pore size distribution on rock samples, by inspecting the macropores (diameter > 0.5 mm).

Further investigations on clays and rocks focused on the use of the grayscale colors given through the CT scan to determine indirectly the porosity of the specimen. Research conducted by Saadat et al. (2011) on bentonite samples and by Mao et al. (2012) on coal inspected the specimens with CT scanned images, to analyze the color given by saturated and dry specimens. The shades in the CT scanned images were used to determine the density of the samples through a CT number, which is determined when comparing the shade of the material with the shade of water or air.

Investigations on concrete-like geomaterials, such as Waller (2011), estimated the porosity variation on the specimen with a qualitative approach. For specimens in Waller (2011), the porosity is determined in sections that develop a specific color in the CT scanned images, and the results are used to establish the upper and lower bound for the porosity of the specimen. This approach could be used in soilcrete specimens. However, the determination of the porosity is subjective and might lead to errors and high variability among interpretation of the reader. Therefore, a different approach might be used with the high resolution of CT scanned images available nowadays.

3. Development of Mechanical Properties of Edmonton Stiff Clay Treated with Cement and Fly Ash[1]

Abstract

Cohesive soils are often mixed in situ with cementitious binders to serve as a deep foundation. However, there is limited research on cemented stiff clay in applications where high soil strength is required. The present research is aimed to determine the mechanical properties of soilcrete produced with Edmonton stiff clay. The equivalent cement content is high, between 18 and 30%. Two cementitious binders were used: 100% ordinary Portland cement and a mix of 90% cement and 10% fly ash. Unconfined compressive strength tests were carried out at different curing ages. Scanning electron microscopy images were taken to inspect soilcrete texture and examine the effects of fly ash. Results showed that soilcrete behaves similar to an overconsolidated clay; the specimens reach peak strength at strain lower than 1% at mature age (>56 days). The peak strength decreases with increasing water to cement ratio. The measured moduli range widely from 30 to 270 MPa; the initial and secant moduli have a linear relation. The residual strength is nearly linearly related to the peak strength. SEM images show that addition of 10% fly ash helps disperse the cement and reduce cement clusters; the damage on soilcrete occurs along the failure plane due to crushing of cement clusters.

Key words: soilcrete, stiff clay, unconfined compression, strength, Young's modulus, SEM

3.1. Introduction

Ground improvement techniques such as the deep soil mixing (DSM) have been used broadly for stabilization of large areas required for pavement embankments, marine structures, contaminant remediation, and so on (Bruce et al. 2013, Han 2015) by producing cement-treated soils, termed as *"soilcrete"*. In such applications, the techniques are commonly used to modify the hydraulic properties of soils, decrease the compressibility, or enhance the bearing capacity of cohesive soils depending on the type of application. Ground improvement techniques using a mixture of cement, lime, and other additives have been exercised in practice and investigated extensively

[1] A version of this chapter has been submitted as Luis and Deng (2017) to the journal Construction and Building Materials for possible publication

(e.g. Porbaha et al. 2000, Ahnberg et al. 2003, Lorenzo and Bergado 2004). Notably, many preceding studies were focused on characterizing the physical and mechanical properties of very soft soils in the coastal areas, where the soils have been admixed with solidifying/stabilizing binders (e.g., Portland cement, lime, fly ash) to study the influence of binder content, water content, curing conditions, temperature, and other parameters on the hardening of soft soils. In addition, the mechanical and hydraulic behaviour of soils with cement-based solidification/stabilization was investigated for the pavement subgrade (e.g., Horpibulsuk et al. 2006, 2010) or conducted on granular soils (Lo and Wardani, 2002, Jamshidi and Lake 2014).

The DSM technique may also be used to increase the bearing capacity and reduce the settlement of heavy structures such as oil storage tanks built upon cohesive soils. In such a context, Rampello and Callisto (2003) investigated the settlement of stiff silty clays in Italy treated with cement content in a range of 18 to 21% of the dry soil mass. Pakbaz and Alipour (2012) and Eskisar (2015) studied the soft lean clays from Iran and Turkey and showed an improvement of strength by adding a maximum of 10% cement content by weight. It is noted that much of the published literature in soilcrete research was directed towards very soft cohesive soils with about 20% or less cement content in coastal areas (e.g., Uddin et al. 1997, Miura et al. 2001, Sasanian and Newson 2014); it appears that research toward stiff clay treated with very high cement content for onshore heavy foundation support is very limited.

The growing demand for construction of large, heavy structures increases the use of DSM technique that is desired to greatly improve the soil strength when the in-situ stiff soils are incompetent in supporting the structures. A literature review suggests that there is a lack of research in the mechanical properties of stiff cohesive soils stabilized with cement content near or greater than 20%, where the cemented stiff soil is required as a foundation support.

The additive (also known as the "*binder*") used in the DSM technique can be composed of one or more materials. Binders that include the combination of several cementitious additives such as ordinary Portland cement, gypsum, and fly ash are commonly used in practice to maintain a balance between the economy and properties of the soilcrete. For instance, Horpibulsuk et al. (2009) found that fly ash generates dispersion in the soilcrete by separating the cement clusters and allow for more surface of cement particles to generate hardening. Horpibulsuk et al. (2011) and Bushra and Robinson (2013) found that by replacing 10% to 20%

of the Portland cement with fly ash, the strength of soilcrete is nearly the same as that of cement-only soilcrete. Therefore, Horpibulsuk et al. (2011) proposed to consider a fraction of the fly ash content in the binder as a cement content when designing soilcrete mixes.

The strength development in soilcrete has been shown to be dependent not on the total cement content of the binder, but on the ratio of the water content to the cement content (Miura et al. 2001, Ma et al. 2014). For the selection of the water content to use in the soilcrete previous investigations have acknowledged that the natural characteristics of clay play a fundamental role, especially the liquid limit of the clay (Horpibulsuk et al. 2005, Liu et al. 2013). The proper characterization of the native soil allows to design the soilcrete with an effective water content, which will provide workability to the mix. Since the natural conditions of the soil vary in each location, a laboratory investigation is recommended to be conducted on the native soil, and later the binder performance can be tested by using two or more binders with additives that work the best for the intended application.

The present research investigates the development of mechanical properties of soilcrete at various curing days. The soilcrete was produced with Edmonton stiff clay of glaciolacustrial origin and a high cement content in a range of 20 to 30% to achieve a great strength enhancement. Two binders were considered: ordinary Portland cement (OPC) and a mix of 90% OPC and 10% fly ash by weight. The mineralogy and oxide composition of the soil was characterized using X-Ray diffraction (XRD) and X-Ray fluorescence (XRF) techniques. The axial stress-strain behavior of soilcrete and post-peak behavior at various curing ages were investigated through unconfined compression strength (UCS) tests. The mechanical parameters such as the peak strength q_{peak}, strain at peak ε_{peak}, Young's modulus E_0, secant modulus E_{50}, and residual strength q_r were obtained from the UCS test results and analyzed in detail. The surface texture of soilcrete specimens at the failure and outer surfaces was inspected via scanning electron microscope (SEM) images; effects of fly ash on the texture were qualitatively examined.

3.2. Materials and methodology

3.2.1. Soil samples

Natural soil samples in disturbed and undisturbed states were collected from a site located in eastern Edmonton, where the DSM is to be performed to support oil storage tanks. Soils at this

site were formed as the glaciolacustrine deposit of Great Edmonton Lake that existed after the last glacial period in the Holocene (Godfrey 1993). Edmonton stiff clay is usually an interbedded combination of cohesive soils with sand or silt.

Undisturbed soils were recovered from Shelby tubes at a depth of 5 m or greater below ground surface (BGS) to determine the mechanical and physical properties of the natural soil. The undrained shear strength s_u of intact soil samples ranges from 63 to 72 kPa, which was determined from laboratory vane shear tests, meaning that the soil is considered as a "stiff" soil in term of consistency (Holtz et al. 2011). Disturbed soil samples were recovered with an auger from depths ranging from 5 to 9.5 m BGS and would be used as the base material to produce the soilcrete specimens.

Physical properties of soils were characterized in the laboratory, as listed in Table 3-1. The particle size distribution, shown in Figure 3-1, shows that the soil contains 24% clay size, 43% silt size, and 33% sand size particles by weight. Based on the Atterberg limit tests, the natural soil was classified as low plasticity clay with sand (i.e., sandy CL) according to Unified Soil Classification System (USCS, Holtz et al. 2011). The organic content of soil was 3.6% obtained from the loss-on-ignition tests at 440 °C in an oven. Natural water content of the soil was 21.8% and the liquidity index was 32.7% prone to the dry side, making the wet mixing method more appropriate for this soil type.

Figure 3-2 shows the X-Ray diffraction (XRD) spectrum of Edmonton clay sample. The soil contains minerals such as quartz, dolomite, albite, muscovite, calcite, and pyrite. The XRD profile suggests the presence of muscovite (or illite) in the soil, which is a mica-like mineral. The major oxide compounds by weight in the soil are listed in Table 3-2, as obtained with an X-Ray fluorescence (XRF) spectrometer. The XRF test shows that the amount of potassium oxide K_2O is 3.71% of the oxide composition of the entire soil sample (including sand); this infers that illite is the major mineral constituent of this soil, as only illite contains less than 10% potassium oxides in the mica-like clay group (Mitchell and Soga 2005). As noted in Holtz et al. (2011), illites are particularly common in the glaciolacustrine clay deposits in the central North America. Figure 3-3 shows the clay minerals of the natural soil inspected with SEM; the clay particles show to be similar to the illite clay particles exhibited in Holtz et al. (2011).

3.2.2. Binder materials

Two types of binders were adopted for present investigation. The first binder contains 100% ordinary Portland cement (OPC) and the second contains a mix of 90% OPC and 10% fly ash by weight. The binder types are named C and CF, respectively, throughout the study. The chemical composition of binder type C and CF was provided by the manufacturers and are listed in Table 3-2. The cement is known to be mainly composed of calcium silicates, whereas the fly ash is a by-product of the combustion of coal and contains primarily silicate glass composed of silica, alumina, iron, calcium, and other minor constituents like sodium and potassium. Due to the addition of fly ash, a small amount of sodium oxide Na_2O and potassium oxide K_2O are present in the CF binder, as shown in Table 3-2.

Since the natural clay is stiff and the natural water content is low, additional tap water was introduced to the clay through a water/binder slurry to generate a manageable material for mixing. Each binder was first mixed with the required amount of water to form a slurry and then mixed into the soil. This technique resembles the in-situ wet mixing method for which the slurry of tap water and binder is mixed with naturally moist soils in order to achieve proper mixing conditions (Kirsch and Bell 2012).

3.2.3. Soilcrete mix plan

The soil should be in moist conditions for the production of soilcrete according to studies by Lee et al. (2005), and the optimal water content of soilcrete should be around 1 to 3 times the liquid limit to ensure enough water for the hydration of cement to occur (Horpibulsuk et al. 2005, Liu et al. 2013). In the present research, the amount of water in the slurry (a mix of water and binder) was designed to achieve a water content (w_c) in the soilcrete of 1.25 to 1.35 times the liquid limit of the natural soil. Miura et al. (2001), Lorenzo and Bergado (2004), and Horpibulsuk et al. (2005) introduced the water content of a soilcrete mixture as in Equation [1]:

$$w_c = \frac{m_w + m_{ws}}{m_s} \cdot (100\%) \qquad [1]$$

where m_w is the mass of water in the natural clay, m_{ws} is the mass of water in the water/binder slurry, and m_s is the mass of soil solids.

The cement content (C_c) and fly ash content (C_f) are defined in Equations [2] and [3]:

$$C_c = \frac{m_c}{m_s} \cdot (100\%) \quad [2]$$

$$C_f = \frac{m_f}{m_s} \cdot (100\%) \quad [3]$$

where m_c and m_f are the mass of cement and fly ash, respectively.

The total cement content C_T is calculated using Equation [4] (Horpibulsuk et al. 2011):

$$C_T = C_c(1 + 0.75C_f) \quad [4]$$

where the coefficient 0.75 considers the dispersion caused by fly ash on the cement clusters. The fly ash content C_f is introduced into Equation [4] in a decimal form.

The in-place binder content used for this investigation ranges from 190 to 300 kg/m^3, where the binder content is defined as the ratio of binder mass to the volume of soilcrete (composed of moist soil and slurry) as mentioned in Filz et al. (2005). Five binder contents were used for this investigation as shown in Table 3-3 and each binder content is assigned with a unique binder ID. The selected binder contents covered the range typically used in the DSM practice.

Miura et al. (2001) and Ma et al. (2014) showed that the w_c/C_T ratio dominates the strength development in soilcrete produced with cohesive soils and the best strength improvement is achieved with w_c/C_T between 1.5 and 3. The as-built component quantities used in each binder ID are listed in Table 3-3. The amount of each component in the mix was selected in order to achieve a w_c/C_T range between 1.8 and 3.1 for the specimens tested during this investigation.

3.2.4. Soilcrete preparation

The binder and tap water were mixed with an electrical blender (model: Waring Commercial WSB60) to obtain a uniform slurry and immediately incorporated to the natural soil required for the soilcrete. The soil and slurry were mixed in an automatic dough mixer (model: Hobart Legacy HL200 18.9 L volume) with a dough blender hook for 2 min. The soilcrete paste was introduced into greased plastic cylinders with 75 mm diameter and 150 mm height by introducing the soilcrete paste in layers. The plastic cylinder was tapped at the bottom end

against a hard surface to extract air bubbles from the mix, until the surface was even. The cylinders were covered with plastic film and plastic lids to avoid loss of moisture during curing time. Finally, the specimens were stored at room temperature and left to cure for the duration required for each test, which ranges from 3 days to 56 days.

These procedures are similar to the methodology proposed by Bruce et al. (2013) for applications in the USA, which ensures that the soilcrete is not over-mixed in the laboratory and may resemble the conditions of in-situ soil mixing.

3.2.5. Unconfined compression strength test procedure

The plastic molds were cut on one side to extract the soilcrete specimens. Before each test, the specimens were capped at both ends with a gypsum layer, as standardized in ASTM (2015). During this process, the bottom and top of the specimen were leveled to ensure the even distribution of the compressive pressure during the test. Figure 3-4 shows a soilcrete specimen prepared for UCS test.

The UCS tests were performed on duplicated samples with the same binder ID (see Table 3-3) and curing age at an axial loading rate of 0.5 mm/min. The load and displacement were recorded until 10% axial strain, although specimens may collapse before reaching the 10% axial strain due to the brittleness of the soilcrete material. After failure, the shear plane and failure mode were inspected and recorded.

3.3. Results, analysis and discussion

UCS tests were performed on duplicated soilcrete specimens produced with the 5 binders designed for this investigation. The specimens were tested after curing for a period of 3 to 56 days to determine the development of the mechanical behaviour of soilcrete.

3.3.1. Axial stress-strain behaviour

Figure 3-5 exhibits the typical deviator stress q versus axial strain ε behaviour of soilcrete produced with C-1 and CF-2 binders. The $q–\varepsilon$ behaviour of soilcrete specimens is compared with the behaviour of natural undisturbed soil sample recovered from a depth of 9.5 m BGS. The development of strength in the soilcrete is presented at different curing ages in a range from 3 to

56 days. Soilcrete specimens tend to be similar to a heavily overconsolidated clay with significant strain softening, while the natural stiff clay behaved as a normally-consolidated soil without any post-peak softening.

Figure 3-5 shows that the peak strength (q_{peak}) for soilcrete increases with curing age and the curves show a shifting of the axial strain at peak (ε_{peak}), because the material becomes more brittle with the curing age due to the hardening. The post-peak curves suggest that the residual strength (q_r) of all soilcrete specimens seemed independent of the curing age; all residual strengths approached a constant value that is near the residual strength of the stiff clay, which suggests that at the residual state the soilcrete behaviour is govern by the residual strength of soil since the cementation bonds are broken. After reaching the peak, the specimens tended to collapse at axial strains less than 4 to 5% due to their brittle nature, while the natural soil specimen continued to maintain the natural cohesion bonding even after being compressed beyond 10% axial strain.

3.3.2. Peak strength developed with curing age

Duplicated soilcrete specimens for 5 binder ID were tested at various curing ages. The results of peak strength (q_{peak}) were compiled. Figure 3-6 shows the development of q_{peak} versus w_c/C_T ratio of the soilcrete at curing ages of 14, 28, and 56 days. The results show that q_{peak} decreases with the increasing w_c/C_T ratio and increases with longer curing ages; this observation agrees with the findings for many other soilcrete types in the literature (e.g., Porbaha et al. 2000). The results also suggest that 50% of q_{peak} at mature age (>56 days) was developed within the first 14 days of curing, for all the specimens tested.

After the first 28 days of curing, the soilcrete with the lowest w_c/C_T ratio achieved the highest q_{peak}. However, the results in Figure 3-6 show that soilcrete with w_c/C_T between 2.4 and 2.6 improved more strength than the soilcrete mixes with more cement during the second month of curing.

Figure 3-7 shows the average peak strength development with curing ages for all binder ID's. It suggests that the soilcrete with w_c/C_T between 2.4 and 2.6 (C-1 and CF-2) develop strength continuously at a faster rate than other soilcrete, especially after 28 days. Specimens

with CF-3 and C-2 binders, which contain the lowest w_c/C_T ratios, show to develop most of the strength during the first 14 days due to higher cement contents in the binder. The results suggest that when w_c/C_T is between 2.4 and 2.6 (as in C-1 and CF-2) the conditions are ideal to allow for the hardening reactions to continue developing after 28 days, while other binders develop more likely pozzolanic reactions that occur at a slower rate.

Particularly, results of CF-3 soilcrete suggest a rapid occurrence of the main hardening reactions, due to the dispersion effect of fly ash in the mix. This may lead most of the hydration to occur in the first 14 days and causes q_{peak} at mature ages to be similar to the one achieved by specimens that contain less cement content. Therefore, CF-3 may not be an efficient binder for the strength development, since C-1 and CF-2 achieved similar or greater strength with less cement content.

All the specimens were photographed after failure. Figure 3-8 exhibits the typical failure mode of soilcrete specimens. The images were taken for C-1 specimens at curing ages of 7 and 28 days. The failure plane developed after shear failure has an angle of 70° to 80° relative to the horizontal plane in all specimens.

3.3.3. Young's modulus E_0 and secant modulus E_{50}

The Young's modulus E_0 and secant modulus E_{50} were calculated for the soilcrete specimens at all curing ages. In the present study, E_0 is defined as the slope of the initial linear region of the stress-strain (q versus ε) curve and E_{50} is defined in Equation [5].

$$E_{50} = \frac{q_{50}}{\varepsilon_{50}} \qquad [5]$$

where q_{50} is the deviator stress developed at 50% of q_{peak} and ε_{50} is the corresponding axial strain.

Figure 3-9 compares E_0 and E_{50} of all test specimens. The measured moduli have a wide range from 30 to 270 MPa. The trend line of E_{50} versus E_0 plot shows a good linear relation where E_{50} is 94% of E_0 on average; it suggests that in most cases 50% of q_{peak} develops within the linear region of the stress-strain curve under unconfined compression. This behaviour implies that 50% of the maximum strength can be achieved without mobilizing significant damages to

the cementation. Figure 3-9 also shows a shaded zone where the moduli of soilcrete at mature age (> 56 days) are located. It is observed that the largest moduli were achieved on the specimens tested at mature age, when the soilcrete became stiffer.

Figure 3-10 shows the development of E_0 and E_{50} with the w_c/C_T ratio at curing ages of 14, 28 and 56 days. The trend is similar to the one observed for q_{peak} in Figure 3-6; in general, the moduli decreased as the w_c/C_T ratio increased. The moduli in the first month of curing was greater with less w_c/C_T ratio. After the mature age is reached, the moduli values are very similar among the soilcrete specimens with different w_c/C_T. This occurs because there is less improvement of moduli in the second month of curing in specimens with low w_c/C_T, when compared to the results for specimens with higher with w_c/C_T.

3.3.4. Strain at peak strength

Figure 3-11 shows the q_{peak} versus ε_{peak} correlation. It is observed that q_{peak} at different curing ages is reached at a very low axial strain between 0.42 and 1.25%. The ε_{peak} decreased with increasing peak strength, implying a softer response as the strength decreases.

Figure 3-12 illustrates that when soilcrete specimens are subject to compression in the first 28 days of curing, the dispersion of the axial strain values obtained at peak strength is greater than the dispersion at mature age. This may happen because the development of strength in each type of soilcrete occurs at different rates in the first stages of curing, when hydration processes are triggered. Moreover, the changes in the microstructure of the soilcrete tend to be more stable when mature curing age is reached, because pozzolanic reactions occur very slowly and the microstructure is stiff, resulting in similar axial deformations for different soilcrete after 56 days of curing.

3.3.5. Residual strength

For the soilcrete specimens in this investigation, Figure 3-5 suggests a tendency of stabilization of the strength after 3.5% strain. Therefore, q_r in the present research was taken as the post-peak stress developed at the axial strain of 3.5%.

Figure 3-13 summarizes the results of q_r versus w_c/C_T ratio for all soilcrete specimens. It suggests that q_r is insensitive to the curing age due to the dispersion of the points. For instance, the mature specimens at 56 days developed q_r similar to early-aged specimens (<28 days). The loss of strength occurs rapidly in soilcrete specimens (Figure 3-5) and q_r tends to be near the soil residual deviator stress measured from UCS tests of undisturbed soils.

Figure 3-14 shows the correlation of q_{peak} versus q_r for soilcrete specimens at early curing ages (<28 days) and mature ages (>56 days). The results exhibit nearly-linear trend lines; the specimens that have been curing for less than 28 days achieved a q_{peak} 3.7 times q_r. In mature samples, the change was more noticeable and q_{peak} is 7.3 times q_r, meaning that soilcrete after 56 days curing would lose 86% of the peak strength on average when loaded to the residual state.

3.4. SEM image analysis

Figure 3-15 shows the texture of the mature soilcrete specimens produced with binders C-1 and CF-2. The soilcrete images were taken on samples from the surface of mature specimens, after being dried in an oven. The images of the soilcrete show tightly-bonded texture due to the action of the cementitious binder. The image of C-1 soilcrete (Figure 3-15a) shows a cement cluster that bonds the cement and soil particles together through fibers expanding in all directions. This bonded structure is the result of the hydration and pozzolanic reactions that took place during curing of the soilcrete (Horpibulsuk et al. 2009). The image of CF-2 soilcrete (Figure 3-15b) shows several spherical particles of fly ash embedded in the bonded structure of the soilcrete. The addition of fly ash into the binder helped disperse the cement clusters.

Figures 3-16a and 3-16b compare the bonded texture of specimens C-1 and CF-2 with less magnification, for a visualization of the effect of fly ash dispersion on the cement clusters. In Figures 3-16 to 3-19, the inset drawing shows the location of samples for SEM imaging. The presence of cement clusters in Figure 3-16a gives the surface a wavy (or coarse) appearance, which is diminished in Figure 3-16b due to the dispersive action of fly ash.

Figure 3-17 shows the bonded texture of samples obtained from the failure surface of each soilcrete specimen after UCS test. The texture of the failure surfaces in these SEM images does not show a significant difference. Therefore, the texture of the failure surface under unconfined

conditions is not significantly affected by the addition of fly ash, perhaps because the surfaces had been smoothed during shear failure.

Figure 3-18 shows the texture of one sample taken from the failure surface and another from the outer surface of a mature C-1 specimen. The sample taken from the failure surface (Figure 3-18a) seems to contain less accumulation of cement clusters and have a flatter texture than the image taken from the outer surface (Figure 3-18b), where the clusters give the image a bulky texture. This suggests that the cement clusters were crushed and minimized during the shear caused by axial compression on the specimen. In consequence, the bonding of the particles was minimized and the failure plane is generated where the bonding was most affected.

Figure 3-19 compares the images of a sample from the failure plane and a sample from the outer surface of a mature CF-2 specimen. The images for these samples show the presence of fly ash embedded in the soilcrete structure and the fibers generated through hydration processes. Many fibers in Figure 3-19a, taken from the failure surface, were shown to be broken due to the action of shearing. On the contrary, the cementing fibers in Figure 3-19b, which was taken on the outer section of the specimen, are still bonded to the particles around them.

3.5. Conclusions

Five types of soilcrete were produced in the laboratory with Edmonton stiff clays and binders containing OPC or a mix of 90% OPC and 10% fly ash. The specimens were subject to UCS tests at different curing ages and images were taken on the specimens with SEM. The following conclusion may be drawn:

1 The q–ε behaviour of soilcrete specimens suggests that soilcrete behaved similar to a heavily overconsolidated clay with significant strain softening, while the natural stiff clay was normally-consolidated without any post-peak softening.
2 The results show that q_{peak} decreases with the increasing w_c/C_T ratio and increases with longer curing ages. After 28-day curing, the soilcrete with the lowest w_c/C_T ratio achieved the highest q_{peak}. However, the results show that soilcrete with w_c/C_T between 2.4 and 2.6 improved more strength than the soilcrete mixes with more cement during the second month of curing.

3 The q_{peak} versus ε_{peak} correlation shows that q_{peak} at different curing ages is reached at a very low axial strain from 0.42 to 1.25%. The ε_{peak} decreases with increasing q_{peak}, implying a stiffer stress-strain response as q_{peak} increases.

4 The measured moduli have a wide range from 30 to 270 MPa. E_{50} versus E_0 plot shows a good linear relation where E_{50} is 94% of E_0 on average; it suggests that in most cases 50% of q_{peak} develops within the linear region of the stress-strain curve under unconfined compression. Therefore, 50% of the maximum strength can be achieved without mobilizing significant damages to the cementation.

5 The development of the moduli on the first 28 days of curing is greater in specimens with lower w_c/C_T ratio; however, after 56 days of curing the increase of moduli in specimens with lower w_c/C_T is less significant, and the moduli values are similar for the different soilcrete mixes. A similar trend was shown for q_{peak} versus w_c/C_T.

6 For all specimens, the residual strength q_r ranges from 100 and 200 kPa. The relation of q_r versus q_{peak} exhibits nearly-linear trend lines; the specimens that have been curing for less than 28 days achieved a q_{peak} 3.7 times q_r. For mature samples q_{peak} is 7.3 times q_r.

7 SEM images taken from soilcrete samples show that soilcrete have a bonded and compact text, due to the action of hydration and pozzolanic reactions that develop cementation bonds. The dispersive action of fly ash on the soilcrete generates a more uniform appearance, with less concentrated cement clusters.

8 Samples taken from the failure surface have less cement clusters and cement bonding than samples from the outer surface of the soilcrete specimens, suggesting that the damage in a specimen of soilcrete subject to UCS occurs mainly along the failure plane, due to crushing of the cement clusters. The texture in the rest of the specimen presents less disturbance induced by crushing.

Table 3- 1. Natural soil characteristics determined in the laboratory.

Property	Value
USCS classification	Sandy CL
Liquid Limit	40.9
Plastic Limit	12.5
Plasticity Index	28.4
Natural water content (%)	21.8
pH	8.1
s_u of undisturbed soil samples (kPa)	63-72 (Vane shear), 50 (UCS)
Specific gravity	2.54

Table 3- 2. Oxide composition of soil and binders.

	Composition (% by weight)		
Oxide	Soil	C [1]	CF [1]
SiO_2	65.66	20.80	19.87
Al_2O_3	10.56	4.20	4.75
Fe_2O_3	8.13	2.40	3.58
CaO	5.21	63.50	62.76
MgO	-	2.00	2.54
SO_3	1.96	3.50	2.67
Na_2O	-	-	0.24
TiO_2	1.18	-	0.44
K_2O	3.71	-	0.18
P_2O_5	-	-	0.04
SrO	-	-	0.08
Mn_2O_3	-	-	0.11
LOI[2]	3.6	2.37	2.32
Total	100	98.77	99.58

1. C: 100% ordinary Portland cement; CF: 90% ordinary Portland cement and 10% class F fly ash. 2. LOI: loss on ignition at 440°C for soil and 1000°C for binder C and CF.

Table 3- 3. Component quantities in each soilcrete.

Property	Binder ID				
	C-1	C-2	CF -1	CF-2	CF-3
w_c (%)	54.1	55.1	59.7	53.4	51.9
C_c (%)	22.5	30.0	18.0	20.2	24.8
C_f (%)	0	0	2.0	2.2	2.8
C_T (%)	22.5	30.0	18.2	20.6	25.3
w_c/C_T	2.4	1.8	3.3	2.6	2.1
Binder content (kg/m^3)	225	290	190	225	275

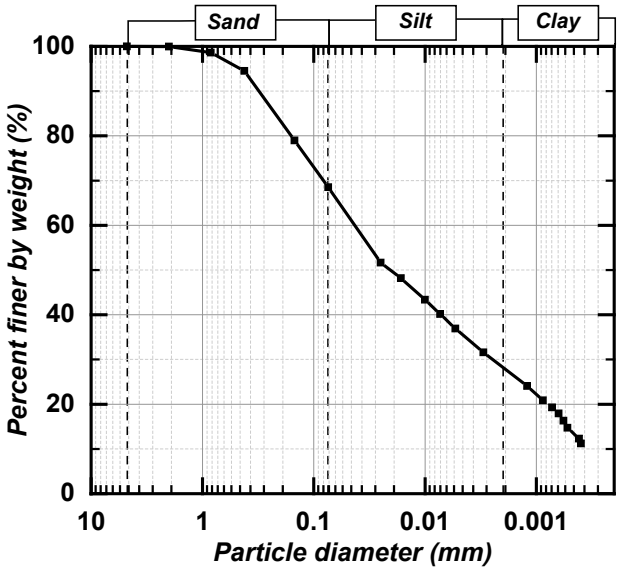

Figure 3- 1. Particle size distribution of the natural soil sample.

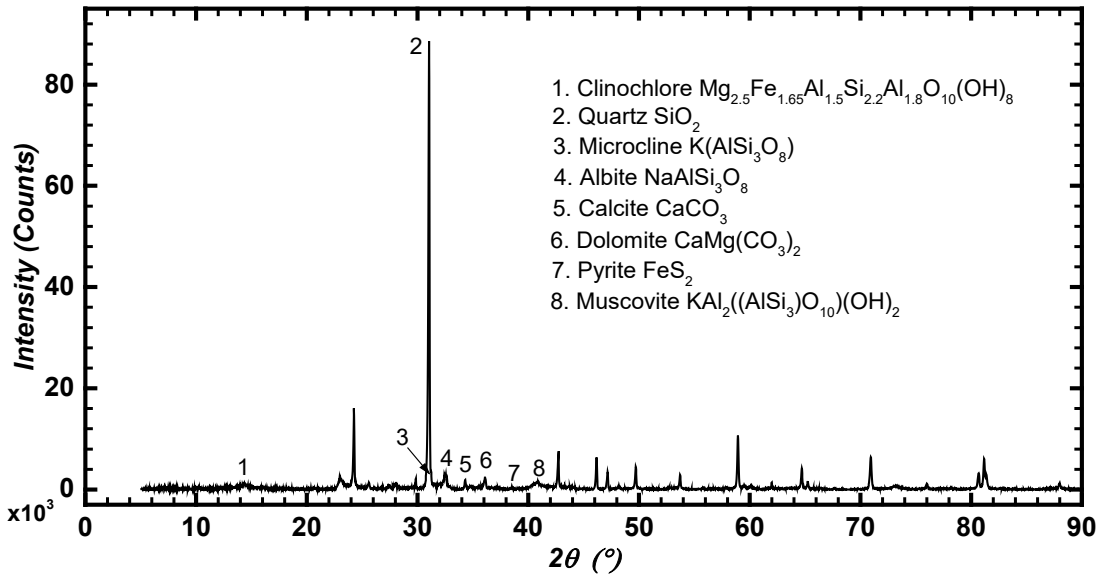

Figure 3- 2. X-Ray Diffraction (XRD) spectrum on soil sample minerals.

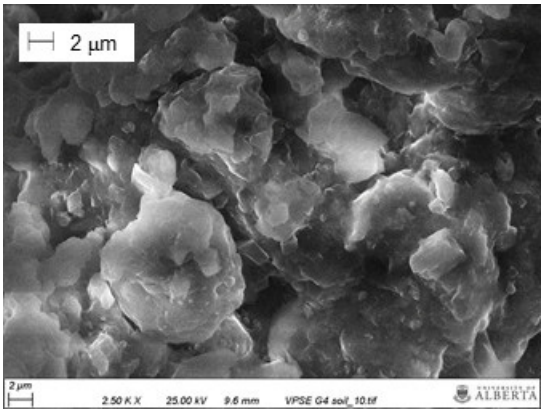

Figure 3- 3. SEM image of clay minerals of natural soil sample.

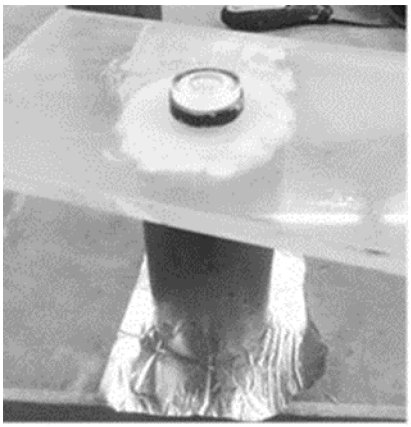

Figure 3- 4. Soilcrete before performing UCS test. Detail of gypsum cap on soilcrete being leveled.

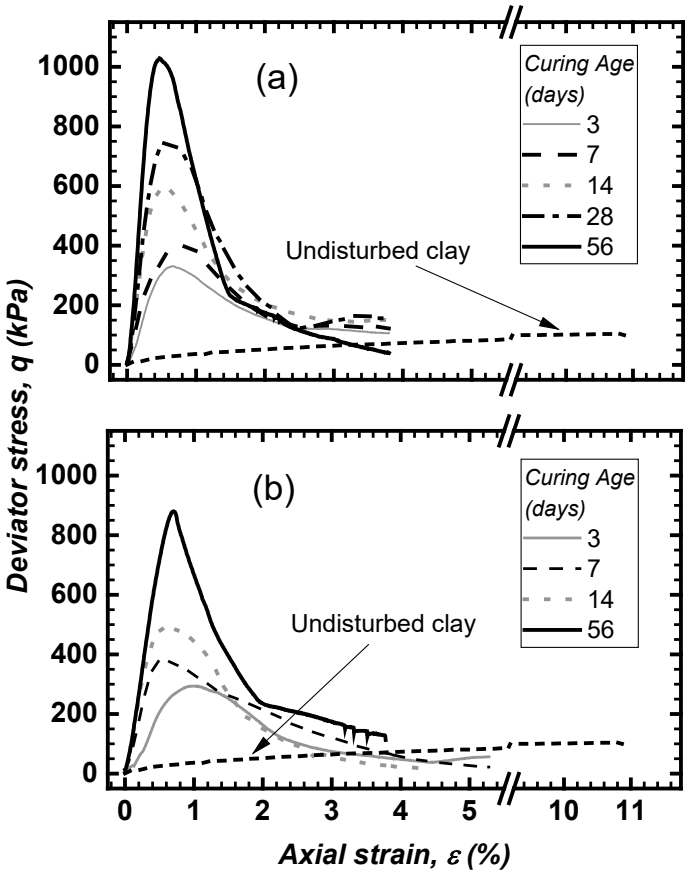

Figure 3- 5. Typical axial deviator stress versus axial strain curves for soilcrete at several curing ages compared to an undisturbed stiff clay sample: (a) C-1 soilcrete and (b) CF-2 soilcrete.

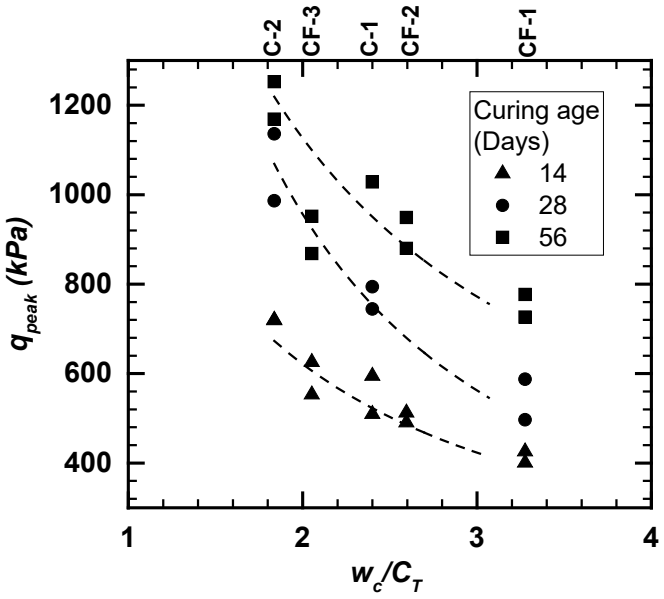

Figure 3- 6. Peak strength (q_{peak}) versus w_c/C_T ratio for curing ages between 14 and 56 days.

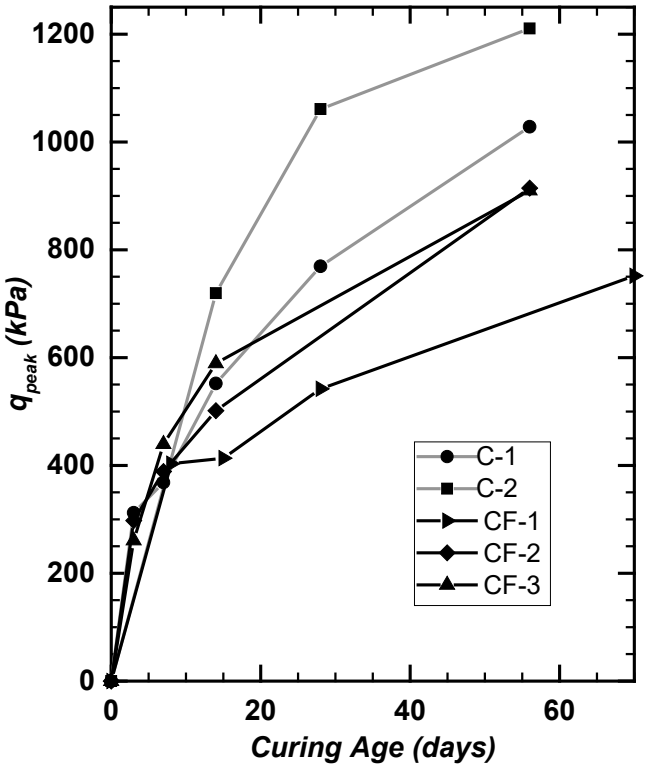

Figure 3- 7. Average peak strength (q_{peak}) development versus curing age for all tested binders.

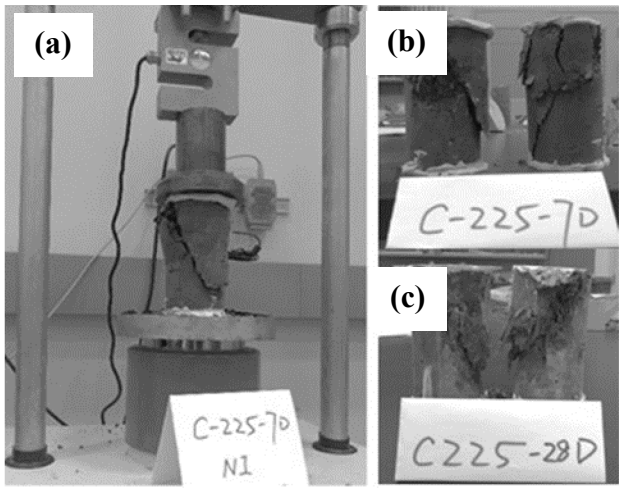

Figure 3- 8. Failure plane in C-1 soilcrete specimens with different curing ages: (a) specimen cured for 7 days failed on loading frame, (b) specimens failed at 7 days of curing and (c) specimens failed at 28 days of curing.

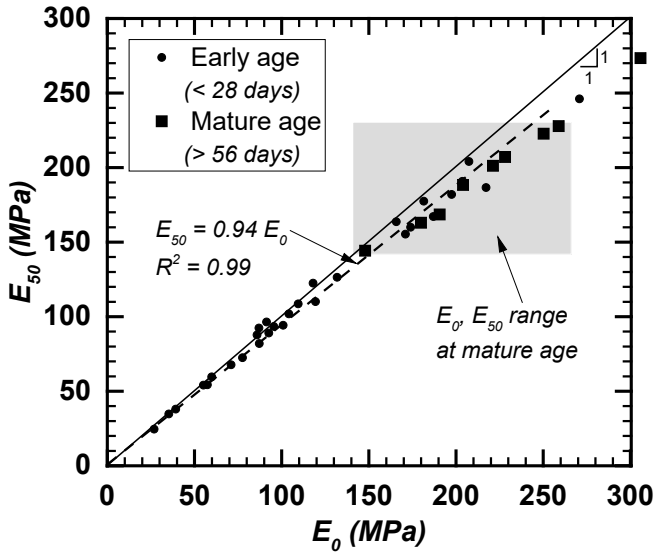

Figure 3- 9. Young's modulus E_0 versus secant modulus E_{50} for all soilcrete specimens. Shaded area shows the range of results at the mature age (>56 days). Dash line illustrates linear trend of results where $E_{50} = 0.94\ E_0$.

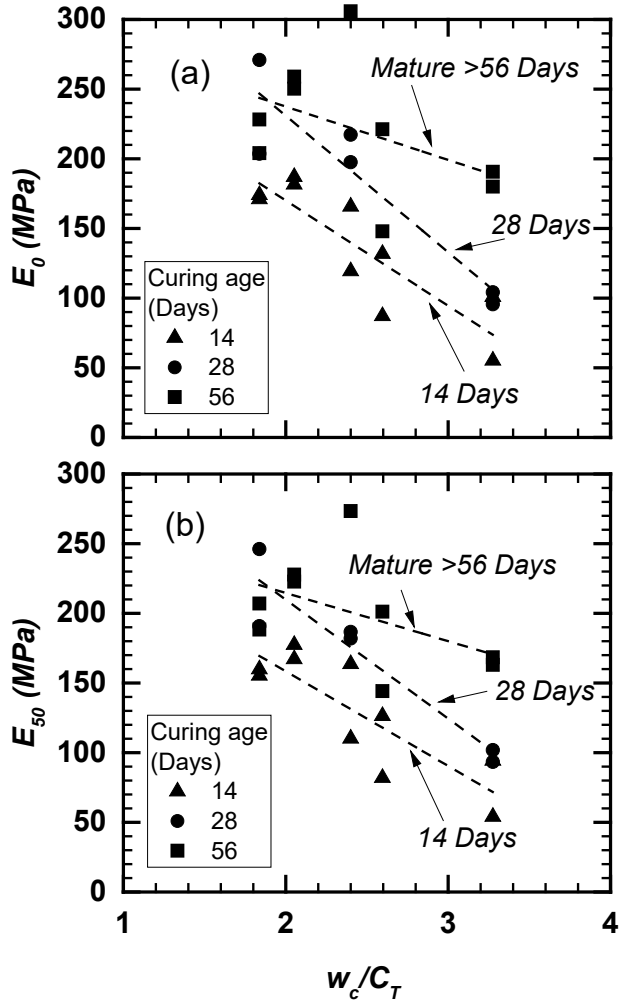

Figure 3- 10. Elastic modulus versus w_c/C_T ratio at several curing ages: (a) Young's modulus E_0 and (b) secant modulus E_{50}.

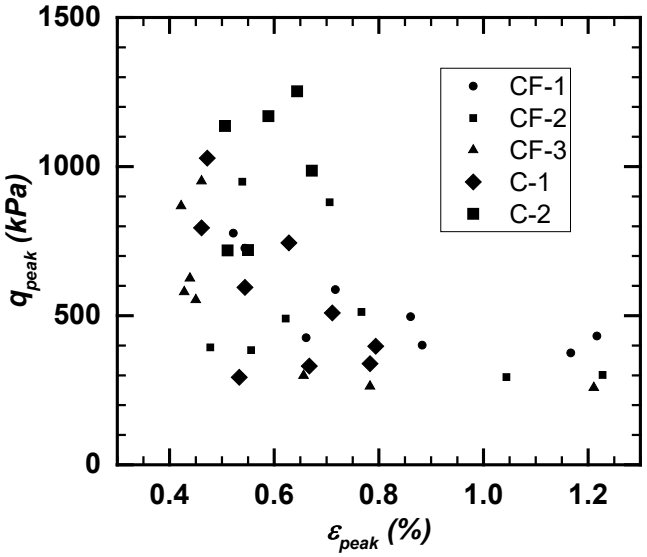

Figure 3- 11. Maximum deviator stress versus axial strain at peak for each binder mix.

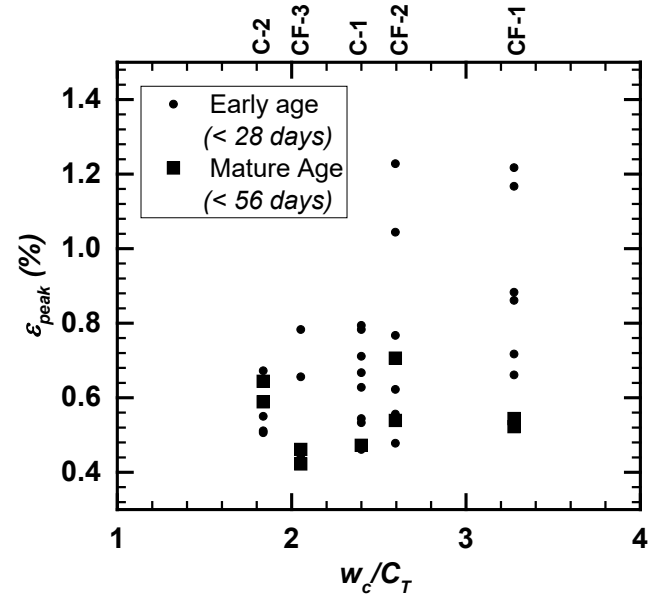

Figure 3- 12. Axial strain at peak strength (ε_{peak}) versus w_c/C_T ratio at early and mature curing ages.

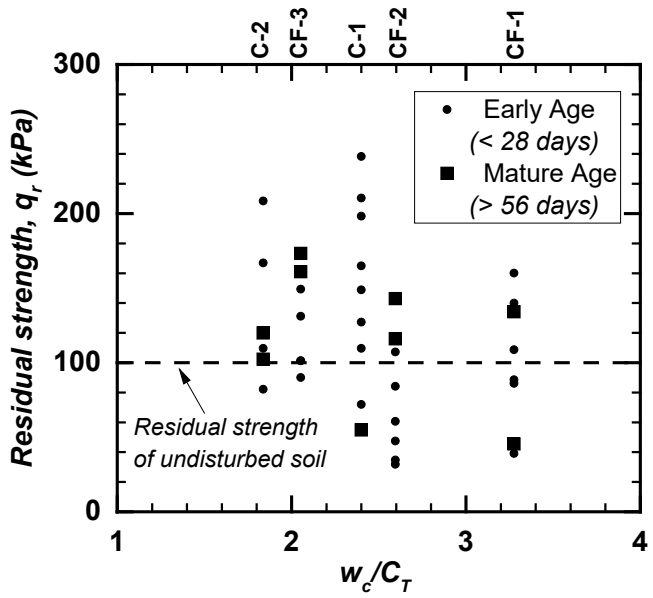

Figure 3- 13. Residual strength (q_r) versus w_c/C_T ratio compared to natural soil residual strength.

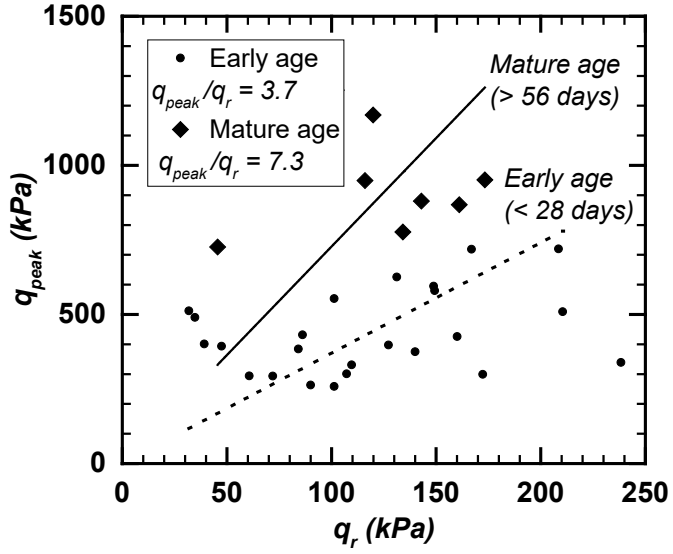

Figure 3- 14. q_{peak} versus q_r at early and mature age.

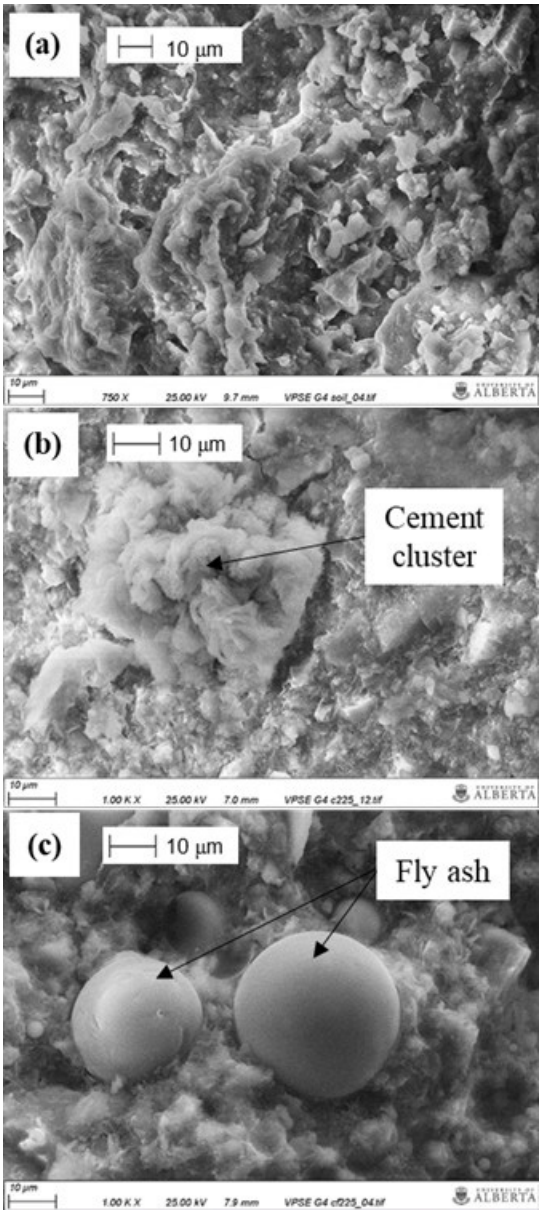

Figure 3- 15. SEM images for microstructural analysis: (a) dry remolded Edmonton stiff clay; (b) C-1 mature specimen (>56 days) and (c) CF-2 mature specimen (>56 days). Sample taken from the outer surface of the soilcrete specimen.

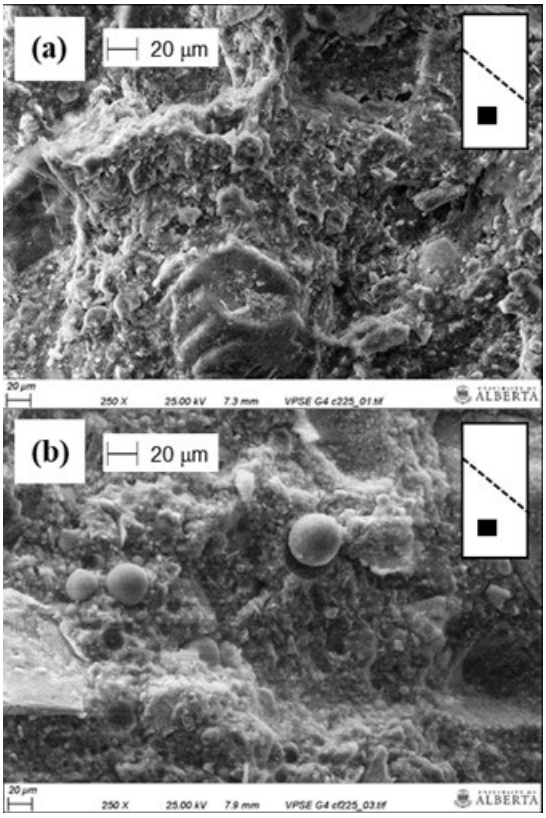

Figure 3- 16. SEM images for samples taken from the outer surface of the soilcrete specimen at mature age (>56 days): (a) C-1 specimen and (b) CF-2 specimen.

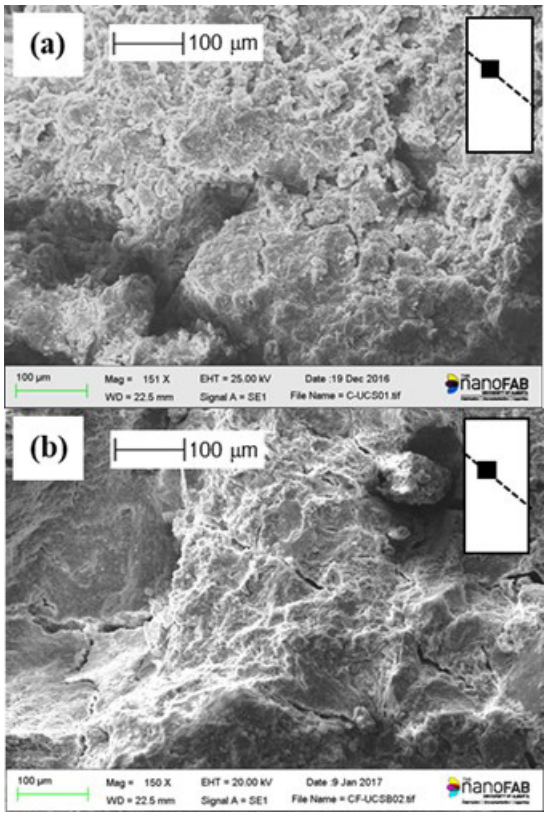

Figure 3- 17. SEM images of the failure surface for soilcrete mature specimens (>56 days) with different binder: (a) C-1 specimen; and (b) CF-2 specimen. Images were taken on the failure surface after a UCS test.

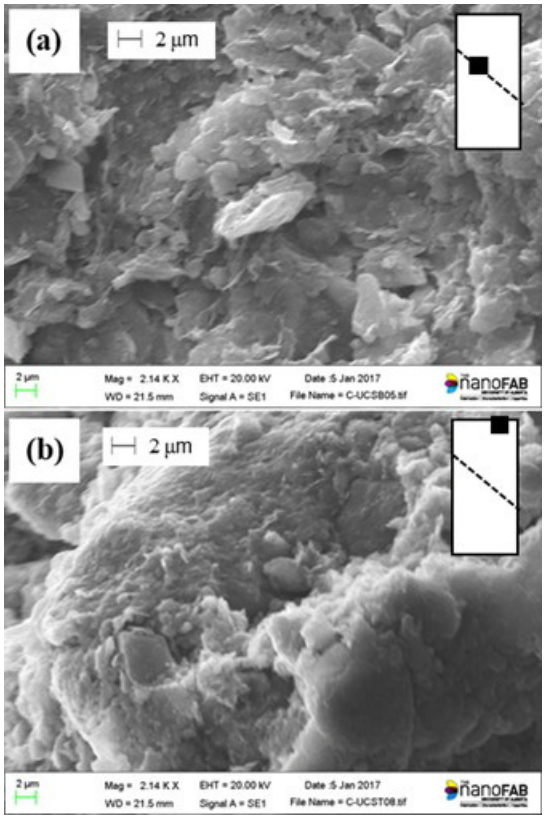

Figure 3- 18. SEM images for C-1 soilcrete mature specimens (>56 days): (a) image taken from the failure surface and (b) image from the external surface of the specimen.

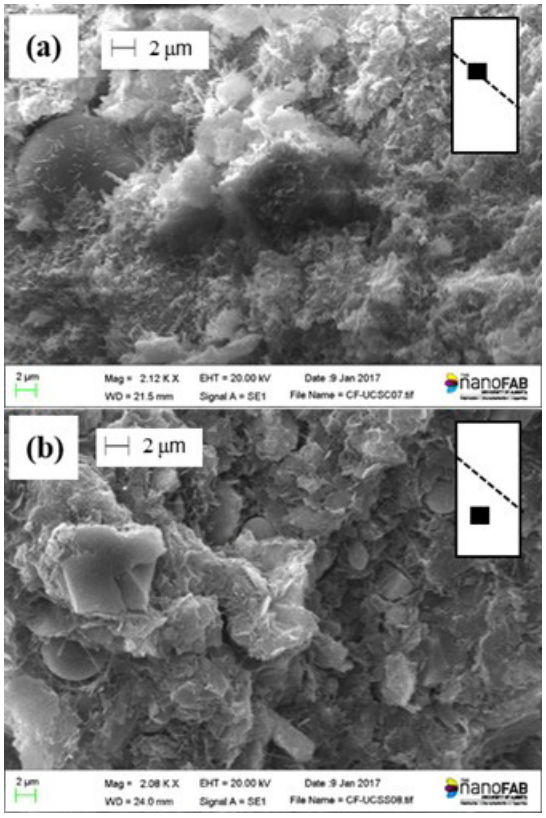

Figure 3- 19. SEM images for CF-2 soilcrete mature specimens (>56 days): (a) image taken from the failure surface and (b) image from the external surface of the specimen.

4. Mechanical and Physical Properties of Cement Treated Edmonton Stiff Clay Using Triaxial Tests and Image Analysis[2]

Abstract

Cementitious binders have been widely used to improve the strength of soft soils by deep soil mixing. Most of past research has been directed toward soft soils stabilized with a small cement content. This research investigates the mechanical and physical properties of Edmonton stiff clay treated with ordinary Portland cement and a compound binder of 90% cement and 10% fly ash by weight. The cement contents were greater than 20%. Laboratory-prepared soilcrete specimens were compressed in isotropically-consolidated undrained triaxial tests at a confining pressure ranging from 100 kPa to 3000 kPa. Effects of consolidation and shear failure on the permeability of soilcrete were quantified. The microstructure of soilcrete samples was inspected with scanning electron microscope. Several full-scale soilcrete specimens were scanned by computed tomographer and a new method of analyzing the images was developed to obtain the porosity and its distribution. This research determined the yield strength, peak and fully-softened strengths, moduli, and effective strength parameters of soilcrete. The results show that all specimens exhibited strain-softening behaviour. Specimens exhibited an effective peak friction angle of 38.3°, with an effective cohesion of 145.6 kPa and 107.9 kPa in C and CF soilcrete, respectively. Porosities estimated with the developed method matched the lab-estimated porosities very well.

Key words: soilcrete, stiff clay, triaxial test, mechanical properties, porosity, SEM, CT scan.

4.1. Introduction

The increasing use of ground improvement techniques such as deep soil mixing (DSM) and jet grouting arose with the need of installing urban and industrial developments in locations where *in situ* soils have an unsatisfactory bearing capacity and are susceptible to large settlement. A cementitious additive (i.e. a binder) or a combination of additives can be added to the soils as a

[2] A version of this chapter has been submitted as Luis et al. (2017) to the Canadian Geotechnical Journal for possible publication

powder or a slurry in order to enhance certain engineering properties of the soil. The resulting binder-soil mix is termed as "*soilcrete*".

A binder such as Portland cement is effective in improving the mechanical properties of soft soils through the DSM. Miura et al. (2001), Åhnberg et al. (2003), and Lorenzo and Bergado (2004) showed that the chemical reaction efficiency that hardens the soil through hydration and pozzolanic reactions depends principally on the amount of cement used and the water available for the reactions, following the concept of Abrams' law for hardening of concrete mixtures (Horpibulsuk et al. 2003). Factors such as the soil type, temperature, and curing conditions may also influence the properties of resulted materials (Porbaha et al. 2000, Liu and Starcher 2012). Therefore, laboratory strength tests of soilcrete are often recommended to guide the in situ DSM

The unconfined compressive strength (UCS) of soilcrete specimens produced in the laboratory may be an indicator of the actual strength achieved in the field (Porbaha et al. 2000, Han 2015). However, when large superstructures are supported by soilcrete columns, the soilcrete may be subjected to considerably high confining pressure, and the presence of groundwater and the drainage condition make the UCS unrepresentative of the actual in-situ behaviour. Porbaha et al. (2000), Banks (2001), and Lo and Wardani (2002) showed that specimens of soilcrete under undrained load condition developed very little deformation before reaching the peak strength when compared to drained test specimens, which makes the undrained condition more critical.

The growing need for the DSM to support large superstructures such as oil storage tanks in urban areas may lead to the use of cement mass greater than 20% of the mass of soil solids in order to meet the design specifications for strength. However, published literature related to applications of the DSM using high cement content has been very limited (Miura et al. 2001, Kamruzzaman et al. 2009). Further, there is a lack of research on the effects of confining stress on soilcrete made of stiff clays, because most of the previous research was conducted on cement-treated soft soils, typically in marine environment, pavement subgrade, or contaminant confinement (e.g., Uddin et al. 1997, Banks 2001, Chew et al. 2004, Horpibulsuk et al. 2004, and Kasama et al. 2006). The range of confining stress used in previous research was usually limited to 1 MPa. For an improved understanding of the effects of confinement on properties of soilcrete with high cement content, a greater confining stress should be used.

In addition to the use of destructive loading tests, researchers (e.g., Horpibulsuk et al. 2009, Kamruzzaman et al. 2009) used images taken with a scanning electron microscope (SEM) to investigate the soil–cement interaction and to quantify the effects of fly ash on the mechanical properties and porosity of soilcrete. Peyton et al. (1992), Waller (2011), and Mao et al. (2012) used computed tomography (CT) scanned images to estimate the porosity and pore size distribution of coal, rocks, and concrete. These studies qualitatively estimated the ranges of porosity through density measurement based on the grayscale color detected on the images.

Therefore, the present research investigated the effects of confining pressure on the mechanical and physical properties of mature soilcrete made of Edmonton stiff clay treated with cementitious binders, using triaxial tests and images analysis. Results of the present research may be used to support the binder design for DSM when the improvement of engineering properties of stiff clays is needed. This research adopted two types of binders: ordinary Portland cement and a mix of ordinary Portland cement and fly ash. A series of triaxial compression tests on laboratory-prepared soilcrete specimens were carried out for confining pressures ranging from 100 kPa to 3000 kPa. The mechanical and hydraulic properties of the soilcrete were assessed. The parameters analyzed in the present study include the peak strength q_{peak}, Young's modulus E_0, secant modulus E_{50}, fully-softened strength q_s, hydraulic conductivity k, porosity n, and effective strength parameters. SEM images were taken to investigate the effects of confining pressure and fly ash on the microstructure of soilcrete at the failure plane and outer surfaces. CT scan was performed on selected full-scale soilcrete specimens; a new method of post-processing the CT scanned images was developed to evaluate the porosity and its distribution along the specimens.

4.2. Materials and Methodology

4.2.1. Soils and cementitious binders

Natural disturbed soils were collected from a site in eastern Edmonton, where the DSM would be performed to support oil storage tanks that load the soils with overburden stresses between 50 to 250 kPa. The soil is a glaciolacustrine deposit formed in Glacial Lake Edmonton. Engineering properties of this soil type has been extensively investigated in the literature (e.g. Thomson 1970). The soil at the site is a low plasticity clay with a sand content of 33% and a natural water

content of 22%. The soil is classified as "sandy CL" according to Unified Soil Classification System (USCS). The soil characteristics are summarized in Table 4-1 and the particle size distribution is illustrated in Figure 4-1. With an undrained shear strength (s_u) of 63 to 72 kPa determined from laboratory vane shear tests, the soil is classified as a "stiff clay". However, the soil may be still incapable of providing sufficient bearing resistance to the tanks. The soil contains minerals such as quartz, illite (muscovite), dolomite, albite, calcite and pyrite, according to the X-Ray Diffraction (XRD) tests performed on a representative soil sample. The oxide composition of the soil was assessed with X-Ray fluorescence tests and the oxide distribution is listed in Table 4-2. From the gathered information, the primary clay mineral was from the mica group, particularly illite (muscovite), due to the presence of potassium ions (Holtz et al. 2011).

The binders used in the present study were composed of ordinary Portland cement or a mix of 90% ordinary Portland cement and 10% fly ash by weight. The binder types are named C and CF, respectively. The chemical composition of the binders is listed in Table 4-2, which shows about 63% calcium oxide (CaO) in both binders, typical for cement. The addition of small amount of sodium and potassium oxides in the CF binder is due to the presence of fly ash. The grains of each binder were inspected using SEM images, as shown in Figure 4-2. It is seen that the cement particles are flaky and the fly ash is mainly spherical.

4.2.2. Soilcrete preparation and properties

To prepare soilcrete specimens, the dry binder powder and tap water were mixed with an electrical blender (Warring Commercial model WSB60) to obtain a uniform slurry, and then combined with the natural soil by mixing the components for 2 min in an automatic dough mixer (Hobart model Legacy HL200 18.9 Litre). The final product was cast into plastic cylinders of 75 mm diameter and 150 mm length. The mixture was scooped to the cylinders in layers, and then the cylinder was tapped against a hard surface to extract air bubbles. The cylinders were capped with plastic lids and stored in a container at room temperature during curing time. The procedures are similar to the methodology proposed by Bruce et al. (2013) to resemble the conditions of the mixing performed in situ and to avoid over-mixing of the paste in the laboratory.

The as-built component quantities used in the mix of C and CF type soilcrete are summarized in Table 4-3. In the present study, the in-place binder content (B_c) used for all soilcrete was 225 kg/m^3, where B_c is defined in Equation [1] (e.g., Filz et al. 2005, Timoney et al. 2012):

$$B_c = \frac{m_c + m_f}{V_{soil} + V_{slurry}} \qquad [1]$$

where: m_c and m_f are the masses of cement and fly ash, respectively, and V_{soil} and V_{slurry} are the volumes of the natural soil and the slurry, respectively. The in-place binder content B_c is a critical parameter used in the design of soilcrete for DSM. A B_c of 225 kg/m^3 is commonly used in the practice and was kept constant for comparison purpose.

The water content (w_c) introduced by Miura et al. (2001), Lorenzo and Bergado (2004) and Horpibulsuk et al. (2005) is defined in Equation [2]:

$$w_c = \frac{m_w + m_{ws}}{m_s} \cdot (100\%) \qquad [2]$$

where*:* m_w is the mass of water in the clay, m_{ws} is the mass of water in the water/binder slurry, and m_s the mass of soil solids. In the present study, w_c was 1.20 times the liquid limit of the natural soil to ensure adequate mixing.

The cement content (C_c) and fly ash content (C_f) used in the binders are defined in Equations [3] and [4]:

$$C_c = \frac{m_c}{m_s} \cdot (100\%) \qquad [3]$$

$$C_f = \frac{m_f}{m_s} \cdot (100\%) \qquad [4]$$

The total cement content C_T is calculated with Equation [5] (Horpibulsuk et al. 2011):

$$C_T = C_c(1 + 0.75C_f) \qquad [5]$$

where the coefficient 0.75 considers the dispersion caused by the fly ash on the cement clusters. In Equation [5], C_f is in a decimal form.

The C_c and C_f for this study (Table 4-3) were selected in order to achieve C_T in a range of 20.6 to 22.5%. The water content w_c was selected in a range of 53.4 to 54.1% for CF and C soilcrete, respectively. Bruce et al. (2013) and Ma et al. (2014) show that the best strength development is achieved for w_c/C_T from 1.5 to 3.

4.2.3. Triaxial test procedure

The specimens were allowed to cure for at least 56 days in order to develop most of the strength expected at the mature age, since the UCS results presented by Luis and Deng (2017) show less development of strength after 28 days. The specimen was dissembled from the plastic cylinder and the weight and volume were measured for the initial void ratio estimation. The specimens were placed into a cylindrical confining cell with a maximum pressure capacity of 4 MPa. The pumps used to exert the confining and back pressures were purged prior to the test to ensure no air was entrapped in the system. The cell fluid was tap water and the pore fluid was deionized water. The specimen was placed in the confining cell following procedures listed in ASTM (2011).

A summary flowchart of the test procedure is shown in Figure 4-3. Based on the dry weight measured at end of consolidation tests, the degree of saturation of specimens after curing was estimated to be 0.8 to 0.98. To ensure full saturation during the triaxial test, the specimen was subject to 500 kPa back pressure, which was maintained constant through all stages of the test. The soilcrete was saturated for 24 to 36 hours by applying a confining pressure of 525 kPa. After the saturation period, the specimen was subjected to a B-test to confirm the level of saturation. The B parameter is defined in Equation [6]:

$$B = \frac{\Delta u}{\Delta \sigma_c'} \qquad [6]$$

where: Δu is the resultant pore pressure increment due to the confining pressure increment $\Delta\sigma_c'$ around the specimen. For geomaterials with a stiff skeleton, a B parameter of near 0.8 instead of 1.0 implies the saturation (Banks 2001, Quiroga et al. 2015). Specimens in present study had B values in a range of 0.7 to 0.9; therefore, they were considered fully saturated.

The soilcrete was isotropically consolidated in 3 or 4 stages until reaching the target effective confining pressure (σ_c') of 100, 200, 500, 800, 1000, 2000, and 3000 kPa, where each

stage took about 8 to 12 hours to complete. The σ_c' is the cell pressure minus the back pressure. Once the consolidation was finalized, the specimen was subject to a permeability test, by forcing upward flow within the soilcrete matrix. The differential pressure used in the permeability tests was about 10% of σ_c', which resulted in a hydraulic gradient in a range of 6 to 200. The permeability test was conducted according to the procedure of the constant head test with flexible wall permeameter (ASTM 2010). The results were used to assess the change in in hydraulic conductivity due to changes in the microstructure during the consolidation stage.

After consolidation, the specimen was subject to axial displacement under the undrained condition at a rate of 0.0125 mm / min (or 0.5% strain / hour). The specimen was subject to axial load until reaching approximately 15% axial strain. During the shearing, the pore pressure and deviator stress were recorded at every 120 sec.

The permeability test was conducted again after the shear failure was reached, before the specimen was dismounted for visual inspection. As shown in Figure 4-3, selected soilcrete specimens were also tested for the permeability after the saturation, consolidated, and then tested under the CT scan.

4.2.4. SEM and CT scan

For each binder type, three specimens that were sheared under σ_c' of 0, 500, and 3000 kPa, respectively, were selected for the SEM image analysis. The specimens were dismounted carefully after the triaxial test, and then dried in an oven for 24 hours. Three samples for each specimen were selected from the top, the bottom, and the failure plane, respectively. The samples were sputtered with a thin layer of gold (about 1.6×10^{-5} mm) before placing them into the SEM device. Several images were taken from each sample at various magnifications using the SEM device (ZEISS EVO MA10).

As shown in Figure 4-3, selected full-scale specimens were scanned in a computed tomographer, which provided transversal images of specimens at 0.3 mm interval with a resolution of 512 by 512 pixels. Two specimens for each binder type were consolidated at σ_c' of 500 and 3000 kPa and then subject to CT scanning. An intact specimen of each binder type

without consolidation was also scanned. The images from the scanner were later analyzed to determine the effects of confinement on the porosity of specimens.

4.3. Results of triaxial compression tests

Fourteen soilcrete specimens produced with C and CF binders were compressed in isotropically-consolidated undrained (ICU) condition after being subject to σ_c' ranging from 100 to 3000 kPa. All specimens for the ICU triaxial tests had been cured for 56 days or longer because the present study is aimed at studying the behaviour of mature soilcrete that is more critical to the DSM application.

4.3.1. Volumetric strain during consolidation and yield strength

Horpibulsuk et al. (2004) showed that the peak strength (q_{peak}) increased substantially after applying a σ_c' greater than the yield strength (P_y') due to the breakage of the bonding produced by hydration and pozzolanic reactions of cement. This makes P_y' an important parameter in addressing the change in mechanical behaviour of soilcrete.

Figure 4-4 shows the semi-log curves of the volumetric strain ($\Delta\varepsilon_v$) versus σ_c' of all specimens during the consolidation stage. The curves show that the slope increased as σ_c' passed through a certain point, similar to a consolidation curve of a natural soil. P_y' was estimated at the intersection of the tangents to the initial and final portions of the $\Delta\varepsilon_v$ versus σ_c' curves. It appears that P_y' were 1400 kPa for C specimens and 1200 kPa for CF specimens. These values are in accordance with previous findings by Miura et al. (2001) and Horpibulsuk et al. (2004) on soft clay with C_c between 16 and 33%, which developed a P_y' between 800 and 2500 kPa.

The different behaviour before and after yield (Figure 4-4) suggests two phases of straining in the soilcrete specimens. Prior to yield, the soilcrete experienced little strain due to the cementation bond, which enabled the soilcrete to show apparent overconsolidated behaviour. With σ_c' beyond the yield strength, the strain was much greater due to the partial loss of the cementation bond during yielding of the soilcrete (Horpibulsuk et al. 2004). In Figure 4-4, C soilcrete exhibited a greater $\Delta\varepsilon_v$ than CF soilcrete given the same σ_c', especially after yield.

4.3.2. Stress-strain behaviour in ICU triaxial tests

Figures 4-5a and 4-5b show the deviator stress (q) versus axial strain (ε) curves of C and CF soilcrete specimens. The results show that specimens at low σ_c' developed more strain before reaching the peak stress than those under high σ_c'. As anticipated, the peak deviator stress (q_{peak}) increased with increasing σ_c'. All specimens developed a strain-softening response, which was more pronounced at a low confining stress ($\sigma_c' < 1$ MPa); the specimens were more similar to a perfectly-plastic material once σ_c' was at the highest values (3 MPa).

Figures 4-5c and 4-5d show the pore pressure (u) versus axial strain curves, where u is the measured pore pressure subtracting the constant back pressure in the specimens. Specimens tested at σ_c' of 100 and 200 kPa developed positive u at small strain and then negative u after exceeding q_{peak} suggesting a high dilation potential, similar to heavily overconsolidated clays. When σ_c' was less than P_y', the maximum pore pressure (u_{max}) was reached at strains much less than the strains for q_{peak}. When σ_c' was greater than P_y', u_{max} was reached with a larger strain. Uddin et al. (1997) found similar behaviour in soilcrete produced with soft clays, and attributed the dilative response under low σ_c' to the heavily overconsolidated structure of the soilcrete. As σ_c' increased, the positive u_{max} increased; because the cementing bonds had been weakened by the effect of confinement, u was stabilized more rapidly at a large σ_c'. In this study, u was stabilized after axial strain around 10%, when the post-peak strength had been stabilized.

The fully-softened state (also known as critical state; see Fell et al. 2014) strength q_s is adopted as the stabilized deviator stress achieved after the peak stress. In the present research, the deviator stresses exhibited in Figures 4-5a and 4-5b seemed to stabilize at an axial strain of about 12%. q_s of all test specimens were obtained and compared with q_{peak} as shown in Figure 4-6. A linear relation between q_s and q_{peak} was observed; q_s in specimens of C and CF soilcrete were 90 and 87% of their respective q_{peak} on average. Therefore, there is a slightly greater loss of strength after peak in CF specimens. The peak deviator stress, initial void ratio, strain at the peak stress, and u_{peak} of all test specimens are summarized in Table 4-4.

Figure 4-7 shows the typical failure modes of specimens. All specimens developed an inclined shear failure plane (Figure 4-7a). In addition to the shear plane, a few specimens (e.g.

the one at σ_c' of 200 kPa shown in Figure 4-7b) exhibited deformation around the failure surface, which can be attributed to crushing or bulging deformation of the specimen (Figure 4-7b). Closer inspection revealed that the failure surface was rougher in specimens confined with σ_c' less than 1 MPa. For specimens confined at σ_c' of 2 and 3 MPa, the surface of the failure plane became much smoother. The difference suggests a change in the texture of the soilcrete in the failure surface due to the effect of σ_c'.

4.3.3. Axial strain at peak stress

The axial strain at peak strength (ε_{peak}) versus σ_c' is shown in Figure 4-8. For C specimens, ε_{peak} ranged from 1 to 8%. Specimens at σ_c' less than P_y' tended to develop the greatest ε_{peak}, and ε_{peak} decreased with increasing σ_c'. CF specimens also developed a decreasing ε_{peak} as σ_c' increased. Figure 4-8 shows that CF specimens generally exhibited greater ε_{peak} than C specimens at the same σ_c', implying that CF specimens had a softer initial response than C specimens.

4.3.4. Peak stress versus confining stress

Figure 4-9 shows the relation of q_{peak} and σ_c'. For C specimens (Figure 4-9a), q_{peak} appeared to remain almost constant when σ_c' was between 100 to 800 kPa. q_{peak} increased more significantly with σ_c' after P_y' was exceeded; the trend was in accordance with the findings of Horpibulsuk et al. (2004) for soilcrete produced with cement-only binders. The breakpoint where the transition from overconsolidated to normally consolidated behaviour occurred was near P_y'. This suggests that the increase in strength was derived from a change in the cementation bond of the soilcrete when the confining stress was greater than P_y'.

Specimens of CF soilcrete (Figure 4-9b) achieved q_{peak} usually less than C soilcrete due to a slight difference in the cement content. In CF specimens, q_{peak} increased progressively with increasing σ_c', in contrast to the results for C specimens, where q_{peak} remained constant with σ_c' less than P_y'. The presence of fly ash in CF specimen enabled the dispersion of the cement clusters during curing and hardening of the soilcrete. Therefore, the cementation was weaker in CF specimens, but the cementation bonds were spread more uniformly, leading to a more stable structure.

4.3.5. Young's modulus E_0 and secant modulus E_{50}

The initial Young's modulus E_0 and secant modulus E_{50} (defined at 50% of the peak strength) were obtained from the q versus ε curves for all specimens. The results are summarized in Table 4-5. Figure 4-10 shows the results of moduli versus σ_c'. It is observed that the moduli (E_0, E_{50}) generally increased with increasing σ_c' for both soilcrete types, except for several anomalies. The results also show that the C soilcrete had greater moduli than the CF soilcrete at the same σ_c'.

Figure 4-11 compares E_{50} to E_0. A linear regression shows that E_{50} was 0.91 and 0.93 times E_0 for C and CF soilcrete, respectively. This suggests that 50% of the strength was mobilized before the cementation bonds were damaged since E_{50} were very close to results of E_0, especially for CF soilcrete.

4.3.6. Effective strength parameters

Figure 4-12 shows the deviator stress (q) versus mean effective confining stress (p') curves during the ICU tests developed by the C and CF soilcrete. The results were used to estimate the effective strength parameters. The dash lines in Figure 4-12 represent the peak strength envelope with a slope M, whereas the solid straight lines represent the envelope of the fully-softened strength with a slope M_s.

The curves in Figure 4-12 are comparable to the typical stress path of clays during undrained triaxial tests. The p'-q stress path developed by the soilcrete specimens suggest heavily overconsolidated to lightly overconsolidated behaviour, which was dependent on σ_c'. For specimens at p' from 100 to 200 kPa, p' tended to decrease slightly and then grow, suggesting the dilative potential and the development of negative u. As σ_c' increased, the development of positive u decreased p', and the specimens exhibited normally consolidated behaviour with further increase of σ_c'. For C soilcrete, the transition from overconsolidated to normally consolidated behaviour appears to take place approximately when the initial p' exceeds P_y'. For CF soilcrete, the curve at σ_c' of 2000 kPa continued to show lightly overconsolidated behaviour.

The slope M of the peak strength envelope was determined for both binder types to estimate the effective strength parameters. The peak friction angle ϕ_{pk}' was estimated through a correlation with the parameter M as expressed in Equation [7] (Parry 2004):

$$M = \frac{6sin\phi_{pk}'}{3-sin\phi_{pk}'} \quad [7]$$

The effective cohesion (c') was determined using Equation [8] (Parry 2004):

$$c' = \frac{c}{M} \quad [8]$$

where c is the intercept with the q axis of the plot in Figure 4-12.

The parameters ϕ_s' and c_s' at the fully-softened state were calculated in a similar method, using the slope of the fully-softened envelop M_s and the intercept. The calculated effective strength parameters for C and CF soilcrete are listed in Table 4-6.

The strength envelopes shown in Figure 4-12 at the peak had the same slope, and the cohesion of C soilcrete was slightly greater than that of CF soilcrete (145.6 kPa and 107.9 kPa, respectively). This suggests that the two soilcrete types had the same peak friction angle (38.3°) but the C soilcrete had a stronger cohesion due to stronger cementation than CF soilcrete. The addition of binders into the soil substantially improved the effective strength parameters of the natural soil. Thomson (1970) showed that a glaciolascustrine soil from Glacial Lake Edmonton would typically have ϕ_{pk}' from 14° to 24° and c' from 20 to 55 kPa.

The ϕ_s' of C and CF soilcrete were 4.1° and 1.6° less than the respective ϕ_{pk}'. At the fully-softened state, a significant c_s' was still maintained. For CF specimens, c_s' is less than c' due to the breakage in cementation bonds. ϕ_s' ranged from 34.2 to 36.7° in this investigation, which is less than the results in previous research conducted on very soft soils treated with cement (e.g., Chen et al. 2015) where ϕ_s' ranged from 48 to 57° for cracked specimens subject to ICU tests. Moreover, the change in the strength parameters for CF specimens was less significant, suggesting that the structure of CF soilcrete was more stable under the effects of confining pressure, when compared to the C soilcrete.

4.3.7. Hydraulic conductivity versus confining stress

The hydraulic conductivity (k) was measured after saturation for two specimens of each binder type (Figure 4-3) that were later used for the CT scan test. The saturated samples were subject to upward permeability tests with two differential heads of 20 and 40 kPa resulting in a hydraulic gradient of 13.6 and 27.2; k was calculated for each test and the average was taken as the initial k (2×10^{-9} and 1×10^{-9} m/s for C and CF soilcrete, respectively).

For the specimens selected for the ICU test, k was measured at two stages: end of the consolidation and after shear (see Figure 4-3). Variations of k for both C and CF soilcrete are shown in Figure 4-13. Results show that k decreased after consolidation and were from 3 to 25% of the initial k. The decrease of k upon consolidation was associated with the volumetric strain due to the action of σ_c', which led to a decrease in pore volume. Specimens of CF soilcrete had an initial porosity in a range from 0.45 to 0.48, and specimens of C soilcrete had a slightly greater porosity from 0.48 to 0.51. After consolidation, the CF specimens developed k values 30 to 60% less than k of C soilcrete, due to a greater porosity of C soilcrete.

Figure 4-13 shows that k increased significantly after shear. In C specimens, the post-shear k were 3 to 400 times of the post-consolidation k. In CF specimens, the post-shear k were 30 to 700 times of the post-consolidation k. This confirms the presence of cracks and fractures in the soilcrete due to the effects of axial strain. The amplification in k between consolidation and shear stages is much larger in CF than that in C soilcrete. It is possibly because the CF soilcrete had rougher cracks and apertures and therefore was able to develop wider flow channels than C soilcrete at high confining pressure. The surface roughness will be further inspected using SEM images in the subsequent section. Figure 4-13 also shows that the amplification in k at high σ_c' was less pronounced than at low σ_c', due to the closure of the cracks at high σ_c'.

4.4. Image Analysis

SEM images were used to inspect the microstructure of soilcrete samples and to investigate the changes in the texture of specimens with confining stresses. CT scanned images were used to estimate the porosity and its distribution in the soilcrete specimens

4.4.1. Scanning electron microscopy

After ICU tests, samples located along the failure plane and other locations of specimens were inspected at several magnifications with SEM. Figure 4-14 compares the failure planes in samples of C and CF soilcrete confined at 0, 500, and 3000 kPa. It is shown that the roughness of the failure surface decreased with increasing σ_c', especially in samples taken from C soilcrete. This suggests that the reorientation of particles due to the action of high σ_c' leads to a smooth shear failure plane. By comparing images of C and CF soilcrete, it appears that a greater confining pressure was required to reach the same level of smoothness in CF soilcrete.

Figure 4-15 compares the images of a sample taken from the surface with a sample taken from the failure plane of the CF specimen at σ_c' of 3000 kPa. The sample taken from the failure plane (Figure 4-15b) was much smoother than the sample from the top surface (Figure 4-15a), perhaps because the action of axial load had smoothed the failure surface due to crushing. The results show resemblance with observations by Kamruzzaman et al. (2009) on cement-stabilized clay, where the sample taken from the outer section of the specimen showed little disturbance.

Figure 4-16 shows the images of a sample taken from the failure plane of CF soilcrete at σ_c' of 500 kPa. It is seen that the failure plane was still rough when confined at 500 kPa, in contrary to C specimens (Figure 4-14b) that had a smoother texture. Furthermore, Figure 4-16 shows that clearly a bonding net was generated by the hardening reactions in a CF specimen sample taken from the failure surface. These fibers were broken by the action of shearing.

4.4.2. CT scan image analysis

The image-processing software ImageJ (Rasband 1997) was used to analyze CT scan images of specimens, which were scanned on 480 transverse slices at an equal interval of 0.3 mm. The image of each slice is given in grayscale colored pixels, and the color of the pixel varies with the density of the physical element. A darker-colored pixel means less density, which implies a more porous element. The size of the element (0.35 mm squared) gives a reasonably good resolution to visualize the voids through the specimen, because it is much less than the specimen diameter (75 mm). Figures 4-17a and 4-17b show example images of a specimen of soilcrete CF confined to 500 kPa along a transverse and a longitudinal section plane, respectively. The color is

heterogeneous across the images. The 100% black patches in the images represent the least density (i.e., cavities) in the soilcrete, whereas the 100% white patches likely represent the zones with more concentrated cement clusters.

For a scanned specimen, the total number of pixels for each grayscale color was summed and displayed in a histogram, as shown in Figure 4-18. The modal color representing the most frequent color was then determined from the histogram. In this study, the modal color is adopted to separate the porous and filled fractions of the specimen (Figure 4-18). The pixels on the darker side (left of the modal color) are considered as the voids, which includes the pores, cracks, and the most porous materials. The porosity n is then calculated using the pixel color histogram:

$$n = \frac{V_v}{V_T} \qquad [9]$$

where: V_v is the voids volume calculated as the total number of pixels in the porous fraction, and V_T is the total volume of the specimen calculated as the total number of pixels in the 480-image sequence.

The porosity n could also be estimated from the laboratory-measured mass and volume of specimen using Equation [10]:

$$n = \frac{V_T - \frac{m_s}{G_{seq} \cdot \rho_w}}{V_T} \qquad [10]$$

where: V_T is the total volume of the specimen measured after curing and modified by the volumetric strain due to consolidation, G_{seq} is the equivalent specific gravity of the soilcrete, ρ_w is the density of water, and m_s is the mass of the soilcrete solids. G_{seq} was taken as 2.64 for the CF soilcrete and 2.65 for the C soilcrete, according to the specific gravity of clay (2.54), cement (3.15), and fly ash (2.40), and their relative mass contents.

Figure 4-19 shows the porosity of six soilcrete specimens after consolidation estimated using Equations [9] and [10]. Apparently, the porosity based on Equation [10] is very consistent with the porosity from the CT scan image analysis. The greatest difference in porosity was 0.04 for a C specimen at σ_c' of 3000 kPa. The simplicity of the proposed method and closeness of results with the laboratory values makes it useful in estimating the porosity, when compared to other qualitative methods (e.g., Waller 2011).

To estimate the porosity distribution, images of 25 equally-spaced slices in each specimen were extracted from the image sequence. The modal color was estimated from the color frequency histogram corresponding to the whole specimen, and the same modal color was used to define the porous fraction of each of the 25 slices. After defining the porous fraction and total pixel count of each slice, the porosity of each slice was estimated using Equation [9]. The results of all specimens are shown in Figure 4-20.

The porosity profiles in Figure 4-20 show that concentrations of greater porosity occur near one end of the mold. These results suggest that the mixture may be unevenly cast near mold ends, and the top of the specimen accumulated more voids than other locations. The specimen slice with lower porosity may be caused by the accumulation of denser materials such as cement clusters.

The profiles show that the CF soilcrete had more homogeneously distributed porosity than the C soilcrete. The standard deviation (s) of the porosity distribution shown in Figure 4-20 ranged from 0.083 to 0.155 for C specimens. In contrast, s of CF specimens ranged from 0.075 to 0.099, suggesting a more homogeneous distribution due to the dispersing effect of fly ash on the cement clusters.

4.5. Conclusions

Fourteen mature specimens of soilcrete produced with two binder types were subject to ICU triaxial compression at confining stresses from 100 to 3000 kPa; hydraulic conductivity was measured at various stages of ICU tests. The specimens were inspected with SEM and CT scanned images. The following conclusions may be drawn:

1. The $\Delta\varepsilon_v$ versus σ_c' curves shows that the slope increased significantly as σ_c' exceeded the yield strength P_y', similar to the consolidation curve of a clay. P_y' was 1400 kPa for C specimens and 1200 kPa for CF specimens, respectively.
2. Stress-strain relationships show slight strain-softening behaviour in all the specimens. When σ_c' was much less than P_y', the specimens were heavily overconsolidated; when σ_c' was greater than P_y', the specimens developed normally consolidated behaviour.

3. q_{peak} of CF specimens was less than that of C specimens due to the difference in the cement content. For C specimens, q_{peak} remained constant at σ_c' less than P_y'. For CF specimens, however, q_{peak} increased progressively with increasing σ_c'.
4. Soilcrete specimens exhibited the dilation potential at p' from 100 to 200 kPa. For C specimens, the transition from overconsolidated to normally consolidated behaviour occurred when the initial p' exceeded P_y'. The two types of soilcrete had the same peak friction angle (38.3°), but the C soilcrete had a stronger cohesion than CF soilcrete. At the fully-softened state, a significant c_s' was maintained and ϕ_s' ranged from 34.2 to 36.7°.
5. The post-consolidation k decreased with increasing σ_c'; k of CF specimens was less than k of C specimens due to a smaller porosity in CF specimens. After shear failure, k increased significantly from 3 to 700 times the post-consolidation k due to post-shear cracks; k amplification at high σ_c' was less pronounced because of crack closure.
6. SEM images showed rough failure surfaces when σ_c' was less than 1 MPa and smooth failure planes with greater σ_c'. CF specimens had rougher failure surfaces than C specimens at the same σ_c'.
7. For CT scanned images, the modal color was adopted to differentiate the voids from the solid volume and estimate the porosity. The porosity based on the developed method exhibited a good agreement with porosity estimated from laboratory data. Porosity was more homogenously distributed in CF specimens than in C specimens, and there were more voids near ends of specimens.

Table 4- 1. Natural soil characteristics determined in the laboratory

Property	Value
USCS classification	Sandy CL
Liquid Limit	40.9
Plastic Limit	12.5
Plasticity Index	28.4
Natural water content (%)	21.8
pH	8.1
Undisturbed soil s_u (kPa)	63-72
Specific gravity	2.54

Table 4- 2. Oxide composition of binders and soil

Oxide	Composition (% by weight)		
	Soil	C [1]	CF [1]
SiO_2	65.66	20.80	19.87
Al_2O_3	10.56	4.20	4.75
Fe_2O_3	8.13	2.40	3.58
CaO	5.21	63.50	62.76
MgO	0	2.00	2.54
SO_3	1.96	3.50	2.67
Na_2O	0	0	0.24
TiO_2	1.18	0	0.44
K_2O	3.71	0	0.18
P_2O_5	0	0	0.04
SrO	0	0	0.08
Mn_2O_3	0	0	0.11
LOI [2]	3.6	2.37	2.32
Total	100	98.77	99.58

1. C: 100% ordinary Portland cement; CF: 90% ordinary Portland cement and 10% class F fly ash. The specific gravity of cement and fly ash is 3.15 and 2.40, respectively.
2. LOI: loss on ignition at 440°C for soil and 1000°C for binder C and CF.

Table 4- 3. Binder characteristics

Property	Binder types	
	C	CF
B_c (kg/m^3)	225	225
w_c (%)	54.1	53.4
C_c (%)	22.5	20.2
C_f (%)	0	2.2
C_T (%)	22.5	20.6
w_c/C_T	2.4	2.6

Table 4- 4. Summary of results of ICU tests

Binder type: C					Binder type: CF				
σ_c' (kPa)	e_0 [1]	q_{peak} (kPa)	ε_{peak} (%)	u_{peak} (kPa)	σ_c' (kPa)	e_0 [1]	q_{peak} (kPa)	ε_{peak} (%)	u_{peak} (kPa)
100	1.02	1470.1	3.56	-153.4	100	0.85	1211.1	8.14	-221.6
200	0.94	1491.2	5.12	-120.8	200	0.88	1475.2	6.91	-124.8
500	0.94	1519.7	6.37	106.7	500	0.95	1339.4	3.18	55.3
800	0.97	1531.9	3.27	497.6	800	0.86	1453.4	5.46	460.8
1000	1.02	1749.8	4.26	622.4	1000	0.94	1919.3	6.86	529.9
2000	1.06	1845.4	2.17	1559.3	2000	0.86	1928.2	4.46	1458.2
3000	0.94	2742.6	1.26	2321.7	3000	0.88	2424.4	1.57	2323.8

Note: 1. e_0 = initial void ratio of specimens after curing.

Table 4- 5. Summary of estimated Young's modulus E_0 and secant modulus E_{50}

Binder type: C					Binder type: CF				
σ_c' (kPa)	E_0 (MPa)	E_{50} (MPa)	E_0/q_{peak}	E_{50}/q_{peak}	σ_c' (kPa)	E_0 (MPa)	E_{50} (MPa)	E_0/q_{peak}	E_{50}/q_{peak}
100	229.5	180.4	156	123	100	179.8	110.3	149	91
200	294.8	291.1	198	195	200	172.9	172.5	117	117
500	236.5	205.4	156	135	500	319.1	307.4	238	230
800	320.8	280.3	209	183	800	211.5	210.8	146	145
1000	385.0	383.4	220	219	1000	304.7	274.3	159	143
2000	371.9	342.9	202	186	2000	238.8	229.4	124	119
3000	495.7	446.5	181	163	3000	438.6	417.5	181	172

Table 4- 6. Summary of strength parameters for C and CF soilcrete specimens

Binder type	ϕ_{pk}' (°)	c' (kPa)	ϕ_s' (°)	c_s' (kPa)
C	38.3	145.6	34.2	187.5
CF	38.3	107.9	36.7	43.3

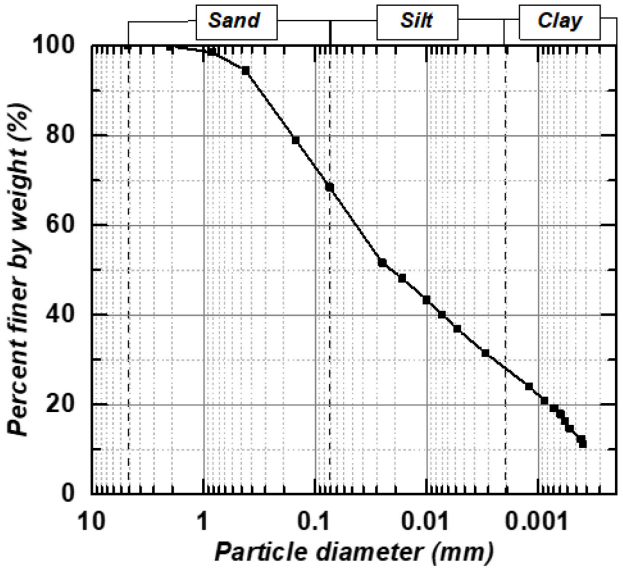

Figure 4- 1. Particle size distribution of natural soil sample.

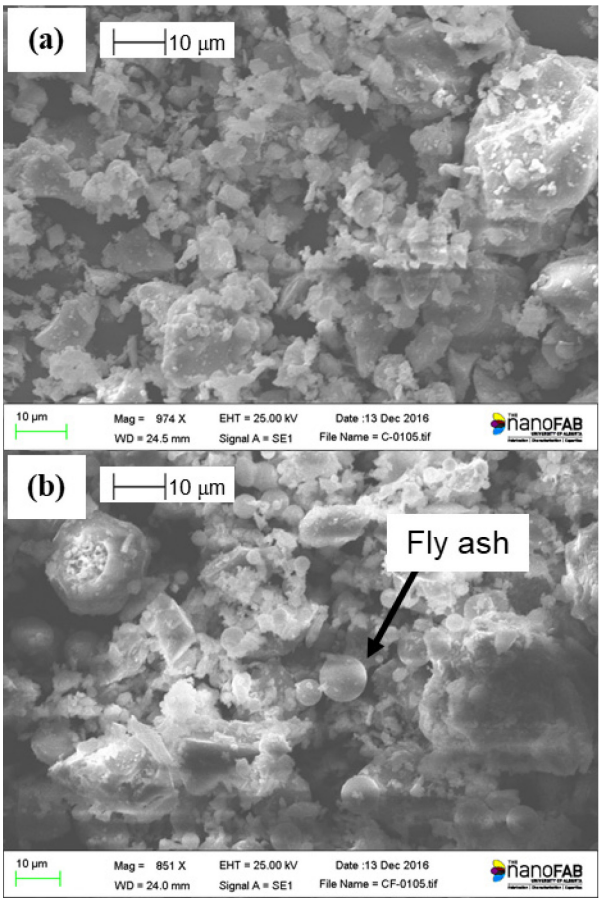

Figure 4- 2. SEM images of binders used for soilcrete production: (a) C binder: ordinary Portland cement and (b) CF binder: 90% ordinary Portland cement and 10% fly ash by weight.

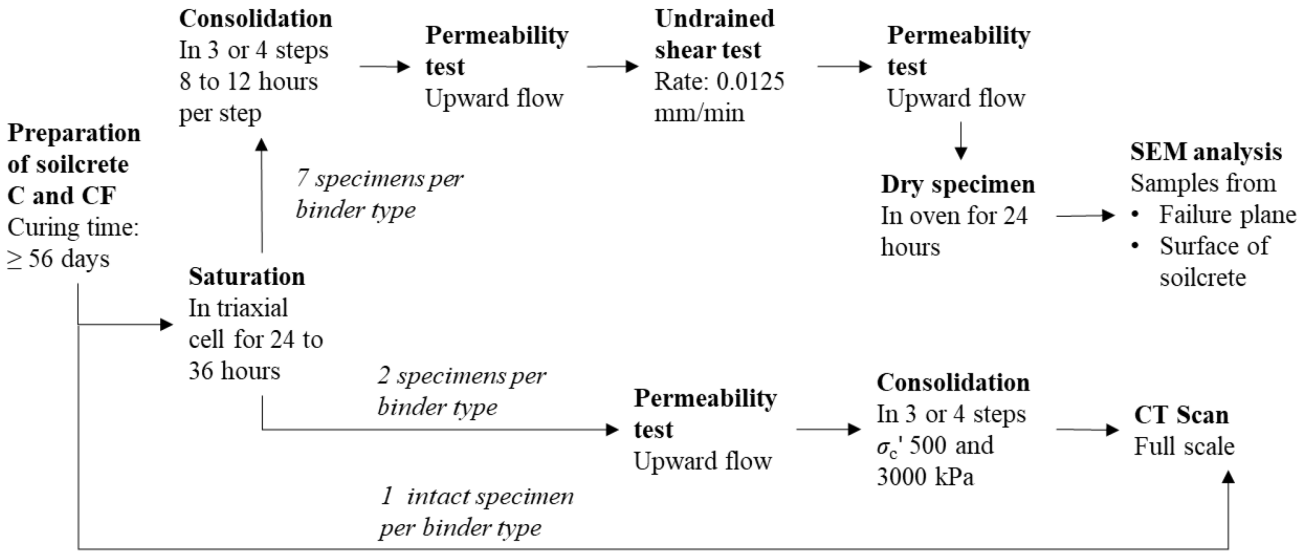

Figure 4- 3. Testing procedure flowchart.

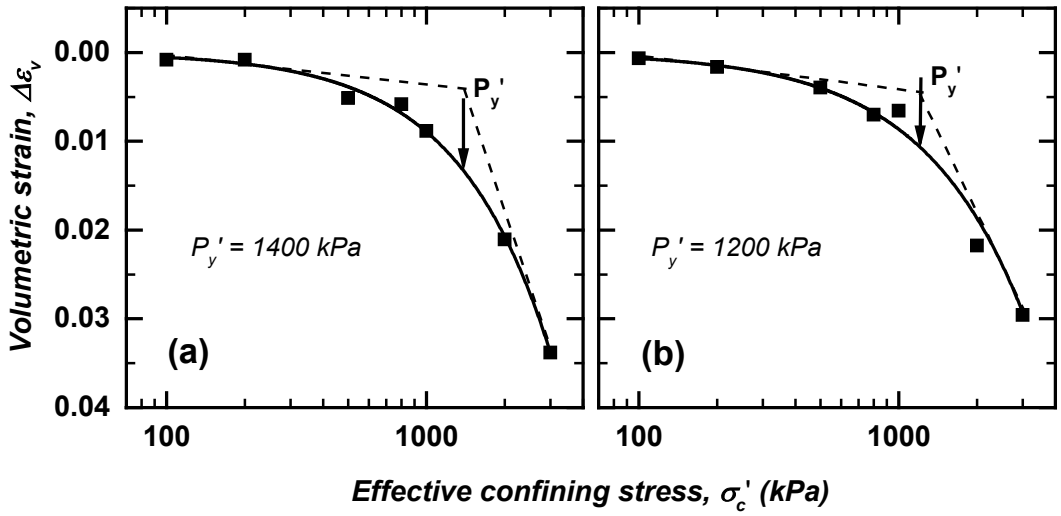

Figure 4- 4. Volumetric strain versus effective confining stress during the consolidation stage: a) C soilcrete and b) CF soilcrete.

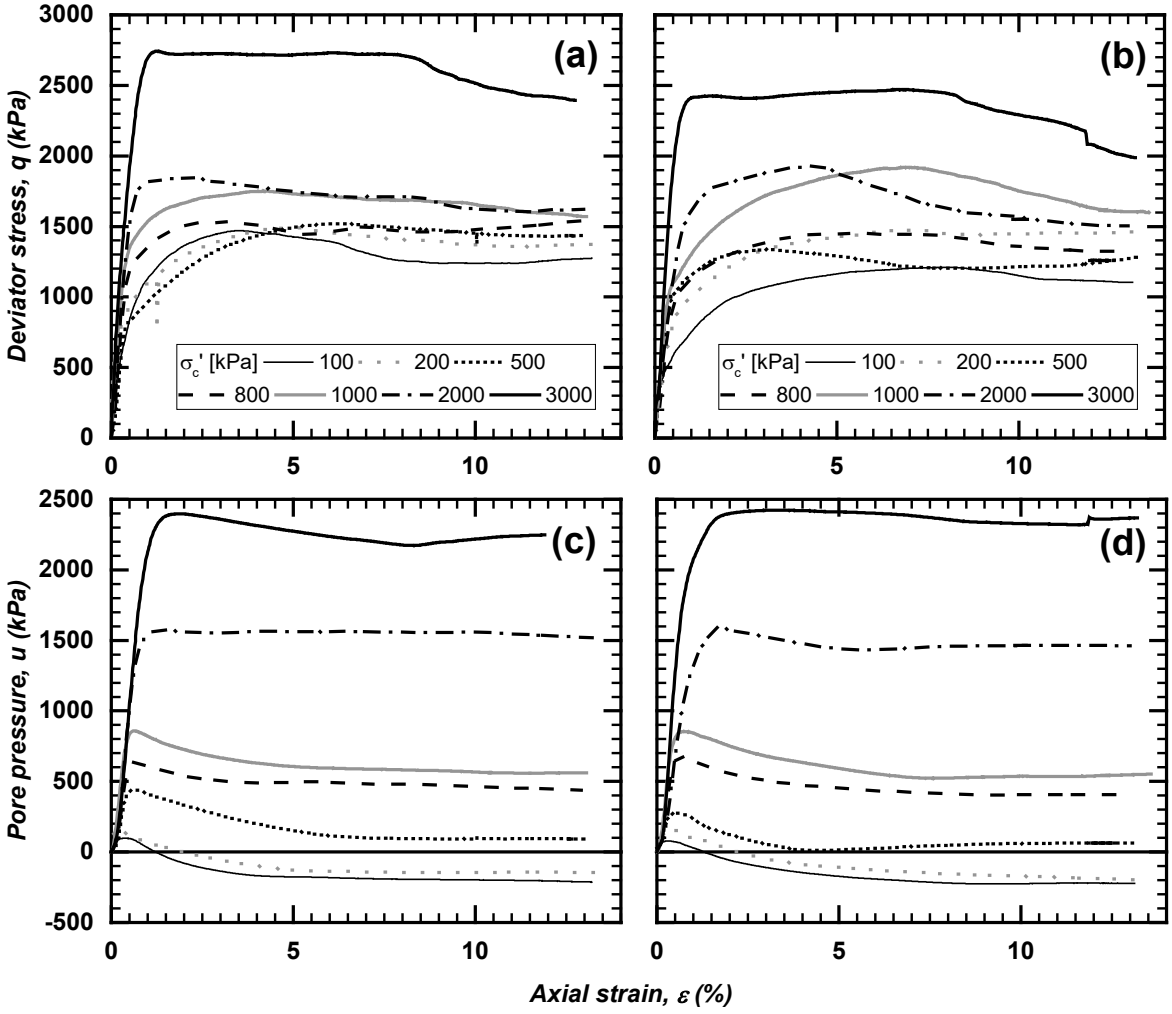

Figure 4- 5. Deviator stress versus strain and pore pressure versus strain relationships: (a) and (c) for C soilcrete, and (b) and (d) for CF soilcrete.

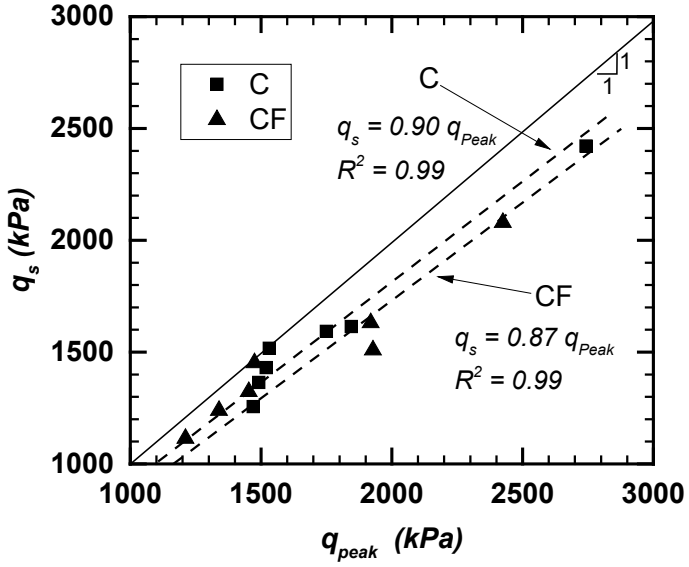

Figure 4- 6. Fully-softened deviator stress (q_s) versus the peak deviator stress (q_{peak}) for soilcrete specimens tested under undrained conditions with σc' between 100 and 3000 kPa.

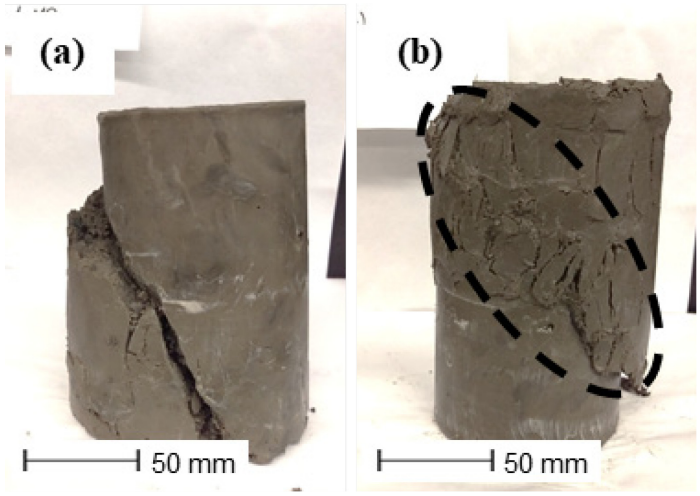

Figure 4- 7. Typical failure modes of soilcrete samples during ICU tests: (a) shear failure plane developed in the C soilcrete at σ_c' of 1 MPa, and (b) shear failure with crushing in the CF soilcrete at σ_c' of 200 kPa.

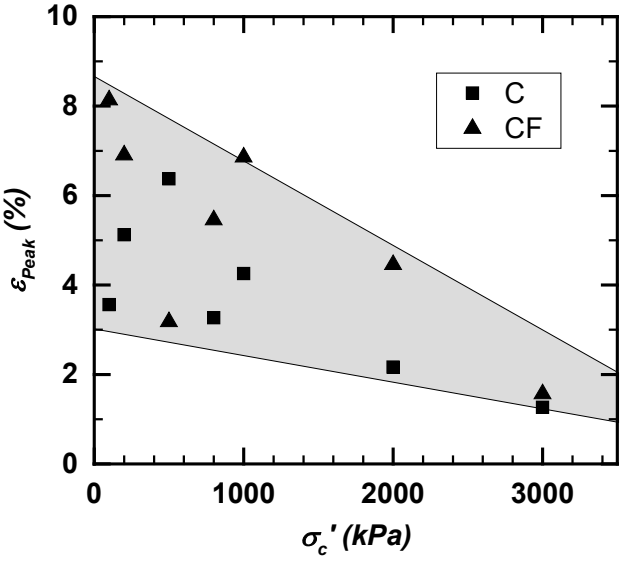

Figure 4- 8. Axial strain at peak strength versus confining stress for C and CF soilcrete.

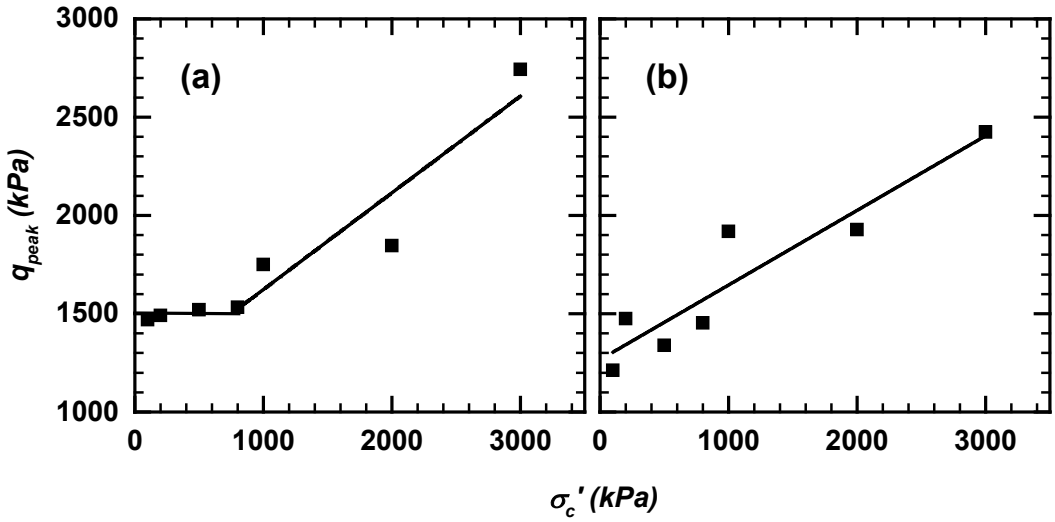

Figure 4- 9. Peak strength versus confining stress for: (a) C soilcrete and (b) CF soilcrete.

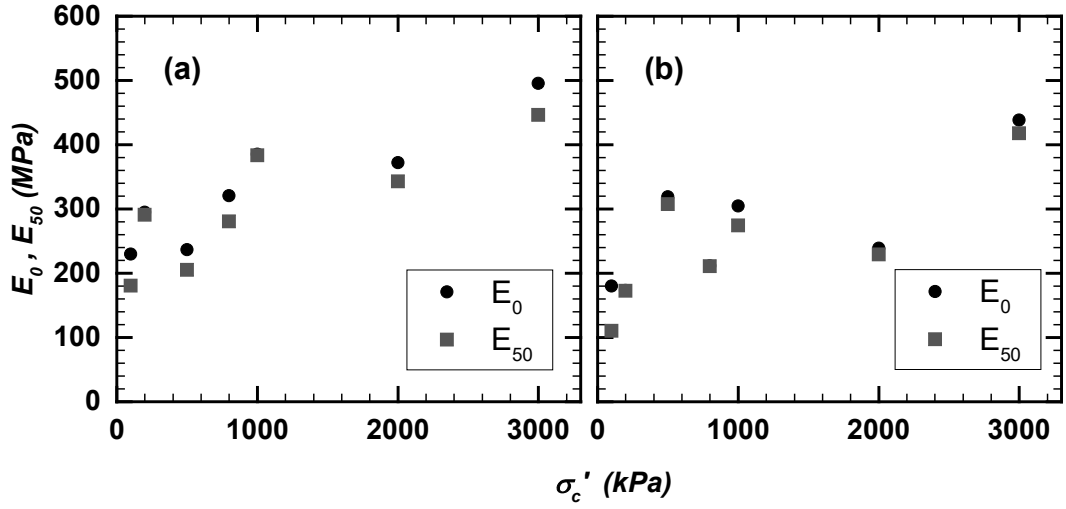

Figure 4- 10. Young's modulus E_0 and secant modulus E_{50} with respect to the confining stress for: (a) C soilcrete and (b) CF soilcrete.

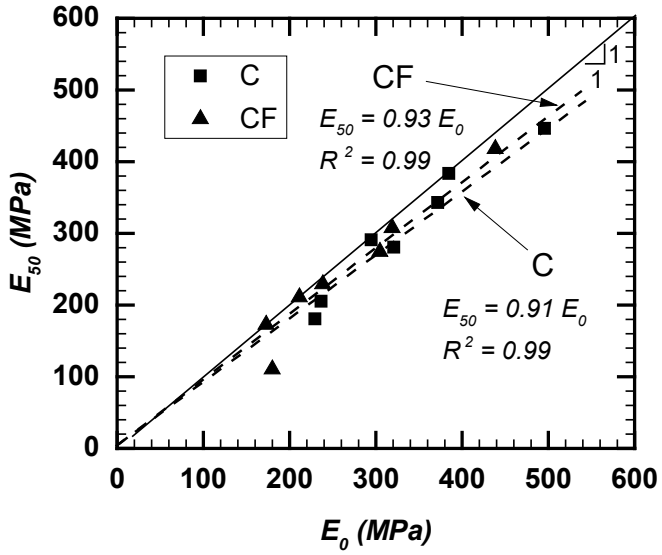

Figure 4- 11. Young's modulus E_0 versus secant modulus E_{50} for C and CF soilcrete.

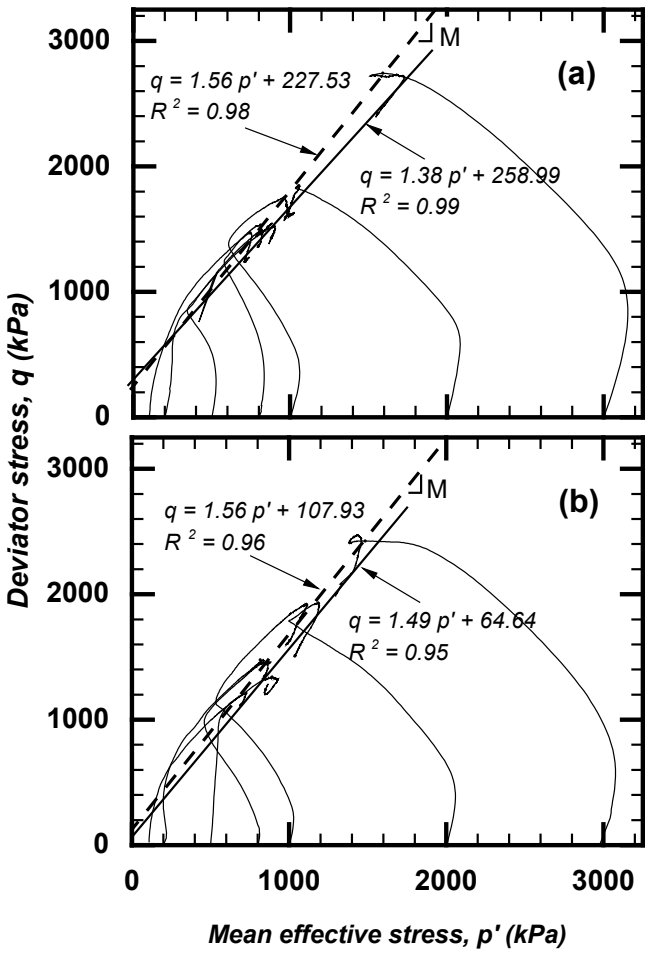

Figure 4- 12. Stress path during ICU tests: (a) C soilcrete, and (b) CF soilcrete. Dash line is the peak strength envelope and solid straight line is the fully-softened strength envelope.

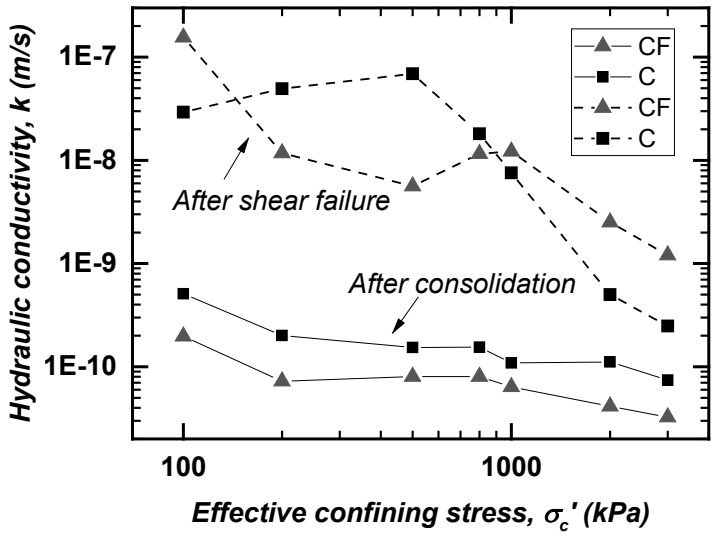

Figure 4- 13. Hydraulic conductivity (*k*) of soilcrete specimens after consolidation and after shear.

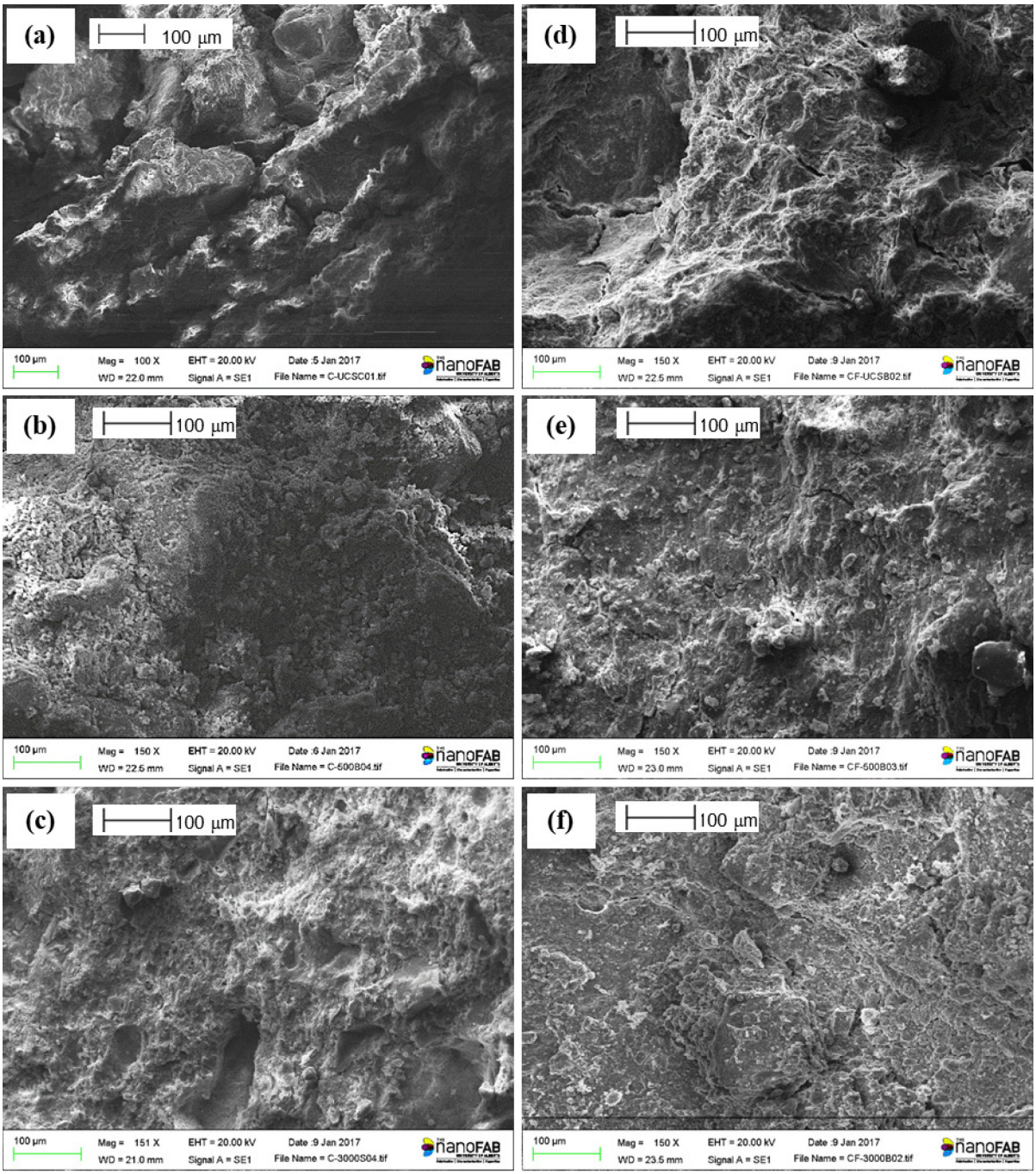

Figure 4- 14. SEM images on failure plane surface of soilcrete at σ_c' of 0, 500, and 3000 kPa. (a), (b), (c): C soilcrete failure plane with increasing σ_c', and (d), (e), (f): CF soilcrete failure plane with increasing σ_c'.

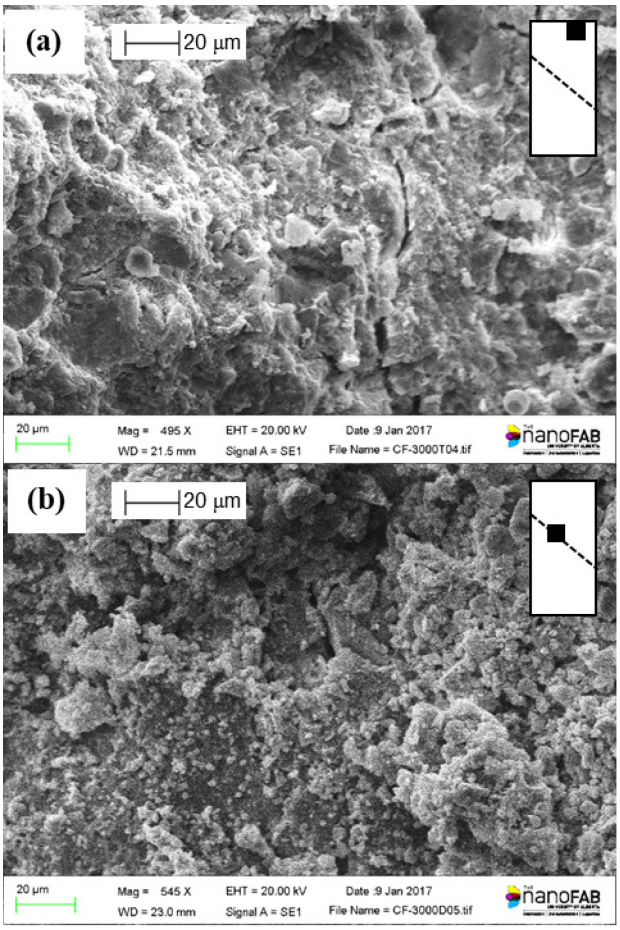

Figure 4- 15. Comparison between samples taken at different locations of a CF specimen at σ_c' of 3000 kPa after shear failure: (a) sample taken from end of specimen, and (b) sample taken from failure plane.

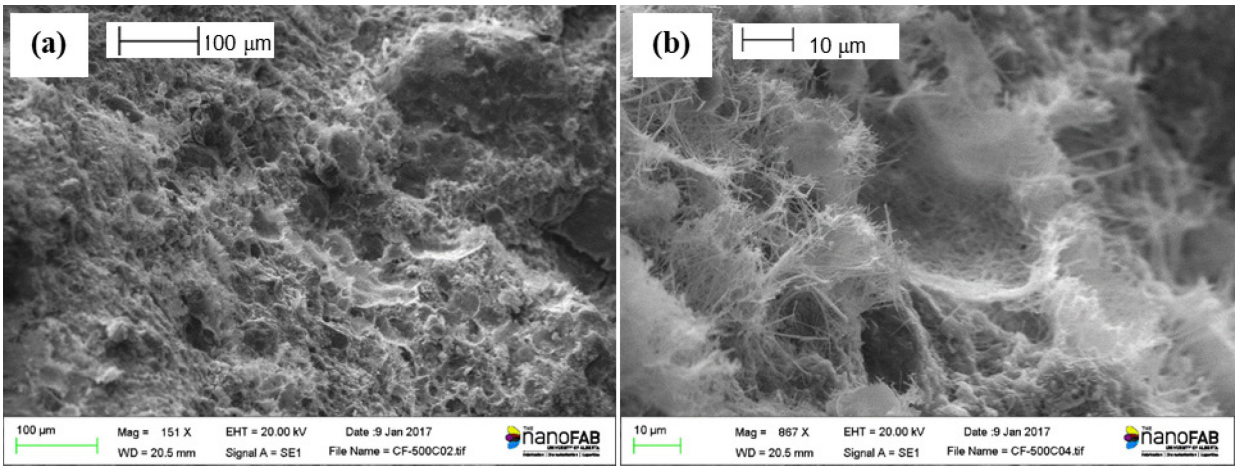

Figure 4- 16. SEM images of a sample taken from the failure plane of a CF specimen at σ_c' of 500 kPa: (a) image of failure surface with broken bonds and (b) closer image to show broken fibers.

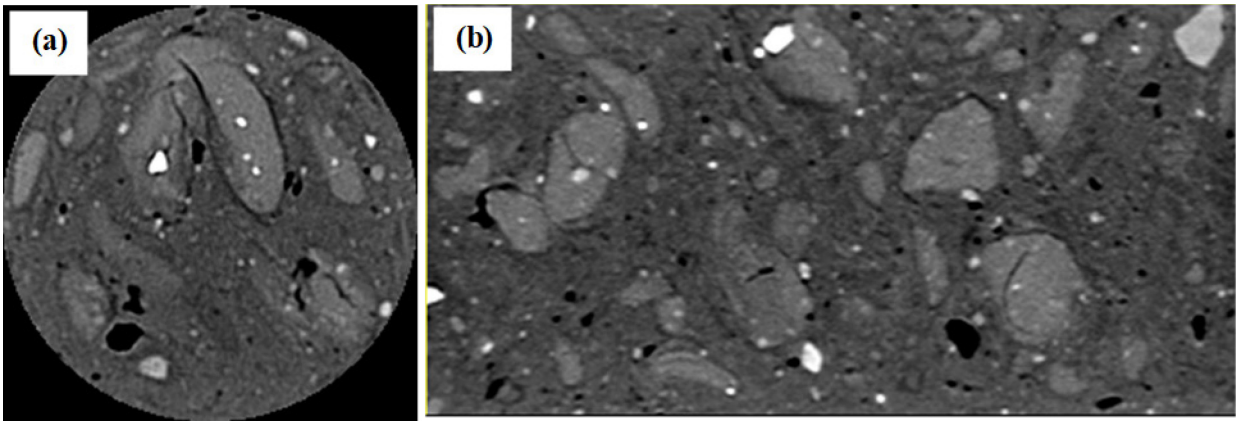

Figure 4- 17. CT scan images of a CF soilcrete specimen at σ_c' of 500 kPa: (a) transverse slice located near the bottom of the specimen, and (b) longitudinal slice along the central axis generated by the combination of 480 transverse slices.

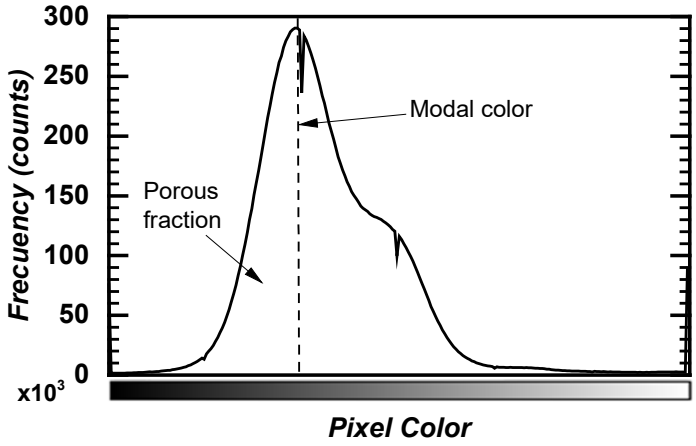

Figure 4- 18. A histogram of the total pixel number for each color in a stack of 480 images of the C soilcrete at σ_c' of 500 kPa.

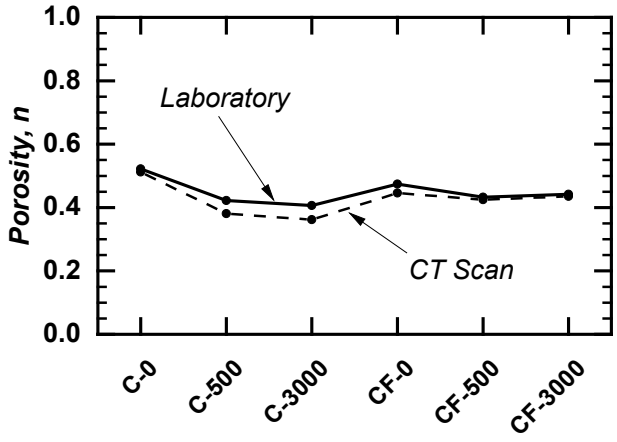

Figure 4- 19. Comparison between porosity estimated from CT scanned images and laboratory calculated porosity.

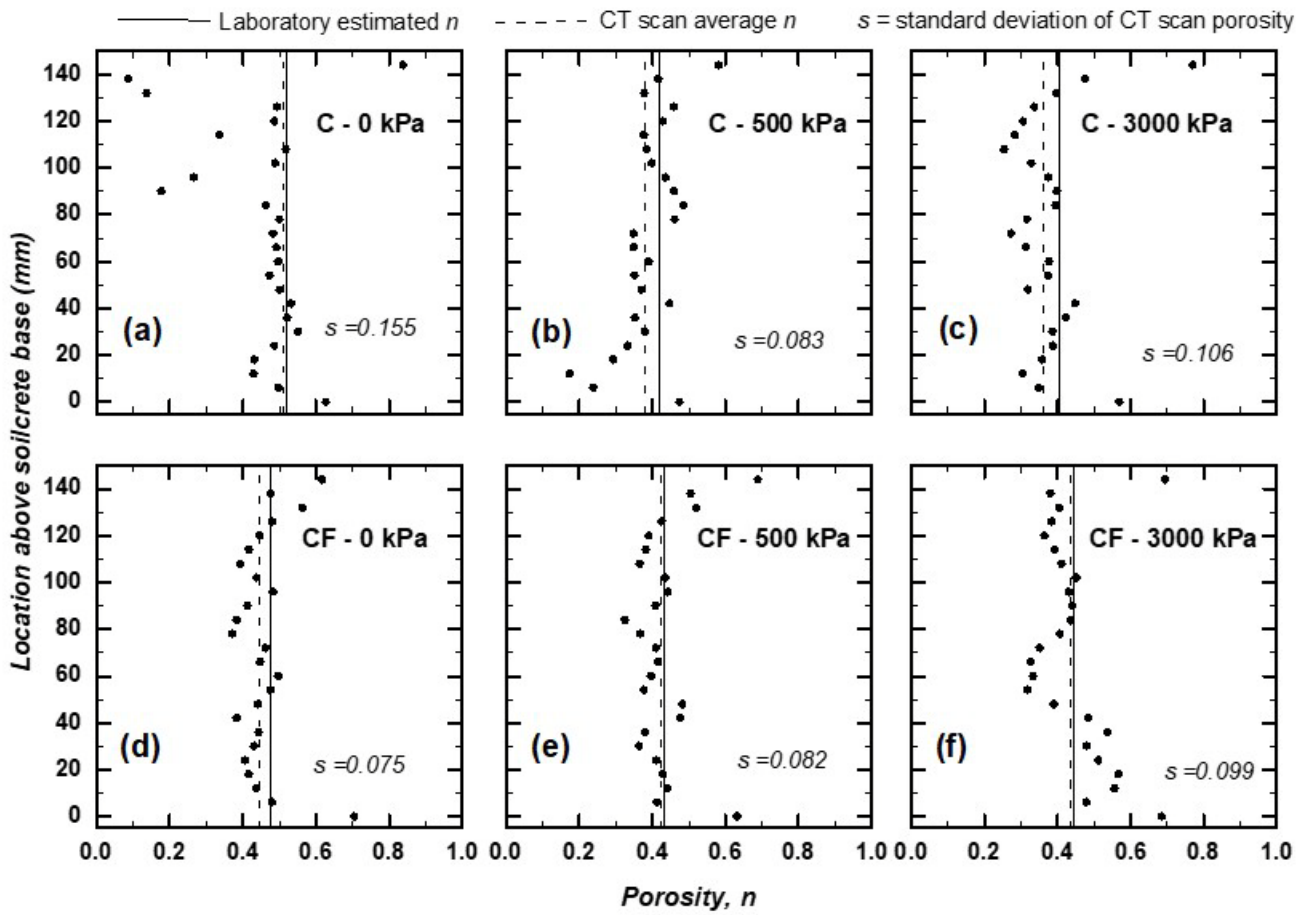

Figure 4- 20. Porosity profiles for soilcrete specimens consolidated at σ_c' of 0, 500, and 3000 kPa. (a), (b), and (c): C specimens, and (d), (e), and (f): CF specimens.

5. Conclusions and Recommendations

Edmonton stiff clays were mixed with cementitious binders containing OPC or a mix of 90% OPC and 10% fly ash. A mixing plan was designed to produce soilcrete specimens. The specimens were subject to destructive tests and image analysis in two phases of testing.

For the first testing phase, five types of soilcrete were produced in the laboratory with the two binders. The specimens were subject to UCS tests at different curing ages and images were taken on the specimens with SEM. The following conclusion may be drawn:

1. The q–ε behaviour of soilcrete specimens suggests that soilcrete behaved similar to a heavily overconsolidated clay with significant strain softening, while the natural stiff clay was normally-consolidated without any post-peak softening.
2. The results show that q_{peak} decreases with the increasing w_c/C_T ratio and increases with longer curing ages. After 28-day curing, the soilcrete with the lowest w_c/C_T ratio achieved the highest q_{peak}. However, the results show that soilcrete with w_c/C_T between 2.4 and 2.6 improved more strength than the soilcrete mixes with more cement during the second month of curing.
3. The q_{peak} versus ε_{peak} correlation shows that q_{peak} at different curing ages is reached at a very low axial strain from 0.42 to 1.25%. The ε_{peak} decreases with increasing q_{peak}, implying a stiffer stress-strain response as q_{peak} increases.
4. The measured moduli have a wide range from 30 to 270 MPa. E_{50} versus E_0 plot shows a good linear relation where E_{50} is 94% of E_0 on average; it suggests that in most cases 50% of q_{peak} develops within the linear region of the stress-strain curve under unconfined compression. Therefore, 50% of the maximum strength can be achieved without mobilizing significant damages to the cementation.
5. The development of the moduli on the first 28 days of curing is greater in specimens with lower w_c/C_T ratio; however, after 56 days of curing the increase of moduli in specimens with lower w_c/C_T is less significant, and the moduli values are similar for the different soilcrete mixes. A similar trend was shown for q_{peak} versus w_c/C_T.

6. For all specimens, the residual strength q_r ranges from 100 and 200 kPa. The relation of q_r versus q_{peak} exhibits nearly-linear trend lines; the specimens that have been curing for less than 28 days achieved a q_{peak} 3.7 times q_r. For mature samples q_{peak} is 7.3 times q_r.
7. SEM images taken from soilcrete samples show that soilcrete have a bonded and compact text, due to the action of hydration and pozzolanic reactions that develop cementation bonds. The dispersive action of fly ash on the soilcrete generates a more uniform appearance, with less concentrated cement clusters.
8. Samples taken from the failure surface have less cement clusters and cement bonding than samples from the outer surface of the soilcrete specimens, suggesting that the damage in a specimen of soilcrete subject to UCS occurs mainly along the failure plane, due to crushing of the cement clusters. The texture in the rest of the specimen presents less disturbance induced by crushing.

For the second phase of testing, 14 mature specimens produced with two binders were subject to ICU triaxial tests under confining stresses from 100 to 3000 kPa; hydraulic conductivity was measured during the triaxial test. The specimens were inspected with SEM and CT scanned images to estimate the physical properties, such as porosity and microstructure. The following conclusions may be drawn:

1. The $\Delta\varepsilon_v$ versus σ_c' curves shows that the slope increased significantly as σ_c' exceeded the yield strength P_y', similar to the consolidation curve of a clay. P_y' was 1400 kPa for C specimens and 1200 kPa for CF specimens, respectively.
2. Stress-strain relationships show slight strain-softening behaviour in all the specimens. When σ_c' was much less than P_y', the specimens were heavily overconsolidated; when σ_c' was greater than P_y', the specimens developed normally consolidated behaviour.
3. q_{peak} of CF specimens was less than that of C specimens due to the difference in the cement content. For C specimens, q_{peak} remained constant at σ_c' less than P_y'. For CF specimens, however, q_{peak} increased progressively with increasing σ_c'.
4. Soilcrete specimens exhibited the dilation potential at p' from 100 to 200 kPa. For C specimens, the transition from overconsolidated to normally consolidated behaviour occurred when the initial p' exceeded P_y'. For CF specimens, normally consolidated behaviour was exhibited when the initial p' exceeded 2 MPa. The two types of soilcrete

had the same peak friction angle (38.3°), but the C soilcrete had a stronger cohesion than CF soilcrete. At the fully-softened state, a significant c_s' was maintained and ϕ_s' ranged from 34.2 to 36.7°.

5. The post-consolidation k decreased with increasing σ_c'; k of CF specimens was less than k of C specimens due to a smaller porosity in CF specimens. After shear failure, k increased significantly from 3 to 700 times the post-consolidation k due to post-shear cracks; k amplification at high σ_c' was less pronounced because of crack closure.
6. SEM images showed rough failure surfaces when σ_c' was less than 1 MPa and smooth failure planes with greater σ_c'. CF specimens had rougher failure surfaces than C specimens at the same σ_c'.
7. For CT scanned images, the modal color was adopted to differentiate the voids from the solid volume and estimate the porosity. The porosity based on the developed method exhibited a good agreement with porosity estimated from laboratory data. Porosity was more homogenously distributed in CF specimens than in C specimens, and there were more voids near ends of specimens.

The results from this research may be valuable for the design of soilcrete mixes on stiff clays similar to the natural soils from Glacial Lake Edmonton. However, there is still lack of knowledge on the effective strength parameters of these cement-stabilized materials when reaching residual state. More research is recommended regarding the residual strength and effective strength parameters at residual state of laboratory-produced soilcrete, and also on the effects of other stresses that may affect the durability of the specimens, such as freeze-thaw cycles. Furthermore, the method proposed in this investigation for estimating the porosity variability along the soilcrete specimens may be valuable for inspecting the quality of the laboratory-mixing, and could be used on specimens taken from the in-situ mixed columns as well.

References

ASTM. (2010). Standard Test Methods for Measurement of Hydraulic Conductivity of Saturated Porous Materials Using a Flexible Wall Permeameter, D5084-10 American Society for Testing and Materials, West Conshohocken, PA.

ASTM. (2011). Standard Test Method for Consolidated Undrained Triaxial Compression Test for Cohesive Soils, D4767-11 American Society for Testing and Materials, West Conshohocken, PA.

ASTM (2015). Standard Practice for Capping Cylindrical Concrete Specimens, C617/C617M15 American Society for Testing and Materials ASTM International, West Conshohocken, PA.

Åhnberg, H., Johansson, S. E., Pihl, H., and Carlsson, T. (2003). Stabilizing effects of different binders in some Swedish soils. Proceedings of the Institution of Civil Engineers–Ground Improvement, 7(1), 9-23.

Åhnberg, H. (2007). On yield stresses and the influence of curing stresses on stress paths and strength measured in triaxial testing of stabilized soils. Canadian Geotechnical Journal, 44(1), 54-66.

Banks, S. (2001). Mechanical characteristics of kaolin-cement mixture, M.Sc. thesis, Civil and Environmental Engineering Department, University of Alberta, Edmonton, AB, Canada.

Bell, F. G. (1993). Engineering Treatment of Soils. London, England: E & FN Spon.

Bruce, M. E. C., Berg, R. R., Collin, J. G., Filz, G. M., Terashi, M., and Yang, D. S. (2013). Federal Highway Administration Design Manual: Deep Mixing for Embankment and Foundation Support. Report No. FHWA-HRT-13-046. US Department of Transportation. Federal Highway Administration. McLean, VA, USA.

Bushra, I., and Robinson, R. G. (2013). Effect of fly ash on cement admixture for a low plasticity marine soil. Advances in Civil Engineering Materials, 2(1), 608-621.

Chen, W. Y., Friesen, S. J., and Driller, M. W. (2015). Seismic remediation of Perris dam. Proceedings of the Deep Mixing 2015 Conference, San Francisco, CA. 21-34.

Chew, S., Kamruzzaman, A., and Lee, F. (2004). Physicochemical and engineering behavior of cement treated clays. Journal of Geotechnical and Geoenvironmental Engineering, 130:7(696), 696-706.

Das, B. M., and Sivakugan, N. (2016). Fundamentals of Geotechnical Engineering, Fifth Edition. Boston, MA: Cengage Learning.

Eskisar, T. (2015). Influence of cement treatment on unconfined compressive strength and compressibility of lean clay with medium plasticity. Arabian Journal for Science and Engineering, 40(3), 763-772.

Fell, R., MacGregor, P., Stapledon, D., Bell, G., and Foster, M. 2014. Chapter 6, Geotechnical Engineering of Dams, Boca Raton, FL.: CRC Press.

Filz, G. M., Hodges, D. K., Weatherby, D. E., and Marr, W. A. (2005). Standardized definitions and laboratory procedures for soil-cement specimens applicable to the wet method of deep mixing. Innovations in Grouting and Soil Improvement, ASCE, Reston, VA. 1-13.

Godfrey, J. D. (1993). Edmonton beneath Our Feet: A Guide to the Geology of the Edmonton Region. Edmonton, Alta: Edmonton Geological Survey.

Han, J. (2015). Principles and Practice of Ground Improvement. Hoboken, N.J.: John Wiley & Sons.

Holtz, R. D., Kovacs, W. D., and Sheahan, T. C. (2011). An Introduction to Geotechnical Engineering. Upper Saddle River, N.J.: Prentice-Hall.

Horpibulsuk, S., Miura, N., and Nagaraj, T. S. (2003). Assessment of strength development in cement-admixed high water content clays with Abrams' law as a basis. Geotechnique, 53(4), 439-444.

Horpibulsuk, S., Miura, N., and Bergado, D. T. (2004). Undrained shear behavior of cement admixed clay at high water content. Journal of Geotechnical and Geoenvironmental Engineering, 130(10), 1096-1105.

Horpibulsuk, S., Miura, N., and Nagaraj, T. (2005). Clay–water/cement ratio identity for cement admixed soft clays. Journal of Geotechnical and Geoenvironmental Engineering, 131(2), 187-192.

Horpibulsuk, S., Katkan, W., Sirilerdwattana, W., and Rachan, R. (2006). Strength development in cement stabilized low plasticity and coarse grained soils: laboratory and field study. Soils and Foundations, 46(3), 351-366.

Horpibulsuk, S., Rachan, R., and Raksachon, Y. (2009). Role of fly ash on strength and microstructure development in blended cement stabilized silty clay. Soils and Foundations, 49(1), 85-98.

Horpibulsuk, S., Rachan, R., Chinkulkijniwat, A., Raksachon, Y., and Suddeepong, A. (2010). Analysis of strength development in cement-stabilized silty clay from microstructural considerations. Construction and Building Materials, 24(10), 2011-2021.

Horpibulsuk, S., Rachan, R., and Suddeepong, A. (2011). Assessment of strength development in blended cement admixed Bangkok clay. Construction and Building Materials, 25(4), 1521-1531.

Jamshidi, R. J., and Lake, C. B. (2014). Hydraulic and strength properties of unexposed and freeze–thaw exposed cement-stabilized soils. Canadian Geotechnical Journal, 52(3), 283-294.

Kamruzzaman, A. H., Chew, S. H., and Lee, F. H. (2009). Structuration and destructuration behavior of cement-treated Singapore marine clay. Journal of Geotechnical and Geoenvironmental Engineering, 135(4), 573-589.

Kasama, K., Zen, K., and Iwataki, K. (2006). Undrained shear strength of cement-treated soils. Soils and Foundations, 46(2), 221-232.

Kirsch, K., and Bell, A. (2012). Ground Improvement. Boca Raton, FL: CRC Press.

Kitazume, M., and Terashi, M. (2013). The Deep Mixing Method. Leiden, The Netherlands: CRC Press.

Kosmatka, S. H., Panarese, W. C., and Kerkhoff, B. (2002). Design and control of concrete mixtures (Vol. 5420, pp. 60077-1083). Skokie, IL: Portland Cement Association.

Lee, F., Lee, Y., Chew, S., and Yong, K. (2005). Strength and modulus of marine clay-cement mixes. Journal of Geotechnical and Geoenvironmental Engineering, 131(2): 178-186.

Liu, C., and Starcher, R. D. (2012). Effects of curing conditions on unconfined compressive strength of cement-and cement-fiber-improved soft soils. Journal of Materials in Civil Engineering, 25(8), 1134-1141.

Lo, S. R., and Wardani, S. P. (2002). Strength and dilatancy of a silt stabilized by a cement and fly ash mixture. Canadian Geotechnical Journal, 39(1), 77-89.

Lorenzo, G., and Bergado, D. (2004). Fundamental parameters of cement-admixed clay—new approach. Journal of Geotechnical and Geoenvironmental Engineering, 130(10), 1042-1050.

Lorenzo, G. A., & Bergado, D. T. (2006). Fundamental characteristics of cement-admixed clay in deep mixing. Journal of Materials in Civil Engineering, 18(2), 161-174.

Luis, A., and Deng, L. (2017). Development of mechanical properties of Edmonton stiff clay treated with cement and fly ash. Construction and Building Materials, Elsevier (submitted).

Luis, A., Deng, L., Shao, L., and Li, H.A. (2017). Mechanical and physical properties of Edmonton stiff clay treated with cement and fly ash using triaxial tests and image analysis. Canadian Geotechnical Journal, NRC Research Press (submitted).

Ma, C., Chen, L., and Chen, B. (2014). Analysis of strength development in soft clay stabilized with cement-based stabilizer. Construction and Building Materials, 71, 354-362.

Mao, L., Shi, P., Tu, H., An, L., Ju, Y., and Hao, N. (2012). Porosity analysis based on CT images of coal under uniaxial loading. Advances in Computed Tomography, 1, 5-10.

Mitchell, J. K., and Soga, K. (2005). Fundamentals of Soil Behavior. 3rd Edition. Hoboken, NJ: John Wiley & Sons.

Miura, N., Horpibulsuk, S., and Nagaraj, T. S. (2001). Engineering behavior of cement stabilized clay at high water content. Soils and Foundations, 41(5), 33-45.

Pakbaz, M. S., and Alipour, R. (2012). Influence of cement addition on the geotechnical properties of an Iranian clay. Applied Clay Science, 67, 1-4.

Parry, R. H. G. (2004). Mohr Circles, Stress Paths and Geotechnics. London: Taylor and Francis.

Porbaha, A., Tanaka, H., and Kobayashi, M. (1998). State of the art in deep mixing technology: Part II. Applications. Proceedings of the Institution of Civil Engineers-Ground Improvement, 2(3), 125-139.

Porbaha, A., Shibuya, S., and Kishida, T. (2000). State of the art in deep mixing technology. Part III: geomaterial characterization. Proceedings of the Institution of Civil Engineers–Ground Improvement, 4(3), 91-110.

Peyton, R. L., Haeffner, B. A., Anderson, S. H., and Gantzer, C. J. (1992). Applying X-ray CT to measure macropore diameters in undisturbed soil cores. Geoderma, 53(3-4), 329-340.

Quiroga, A. J., Muraleetharan, K. K., Cerato, A. B., and Miller, G. A. (2015). Stress-strain behavior of cement-improved clays. In Proceedings of the International Foundations Congress and Equipment Expo, 2328-2338.

Rampello, S., and Callisto, L. (2003). Predicted and observed performance of an oil tank founded on soil-cement columns in clayey soils. Soils and Foundations, 43(4): 229-241.

Rasband, W. S. (1997). ImageJ [Computer software for image analysis]. US National Institutes of Health, Bethesda, MD.

Saadat, K., Rahimpour-Bonab, H., and Esfahani, M. R. (2011). Empirical correlation for porosity deduction from X-ray computed tomography (CT). Geopersia, 1(2), 47-54.

Sasanian, S., and Newson, T. A. (2014). Basic parameters governing the behaviour of cement-treated clays. Soils and Foundations, 54(2), 209-224.

Thomson, S. (1970). Riverbank stability study at the University of Alberta, Edmonton. Canadian Geotechnical Journal, 7(2), 157-168.

Timoney, M. J., McCabe, B. A., and Bell, A. L. (2012). Experiences of dry soil mixing in highly organic soils. Proceedings of the Institution of Civil Engineers–Ground Improvement, 165(GI1), 3-14.

Tomac, I., Van Impe, W., Verastegui Flores, R., and Mengé, P. (2005). Binder-soil interaction in Cement Deep Mixing through SEM analysis. In Proceedings of the 16th International Conference on Soil Mechanics and Geotechnical Engineering, Osaka, Japan, September 12-15, 2005. (pp. 1149-1936). Millpress.

Uddin, K., Balasubramaniam, A. S., and Bergado, D. T. (1997). Engineering behavior of cement-treated Bangkok soft clay. Geotechnical Engineering, 28, 89-119.

Waller, J. T. (2011). Influence of bio-cementation on shearing behavior in sand using x-ray computed tomography. MSc thesis, Department of Civil and Environmental Engineering, University of California, Davis, California.

Appendix A. Soilcrete mixing plan, soil characterization, and raw data of UCS tests.

Soilcrete mixing plan

Soilcrete Mix ID	CF-1	CF-2	CF-3	C-1	C-2
Binder content (kg/m^3 of grout + soil)	190	225	275	225	290
Weight of soil (kg)	11.369	12.655	12.376	12.662	11.394
Weight of fly ash (kg)	0.187	0.234	0.280	0.000	0.000
Weight of cement (kg)	1.681	2.109	2.523	2.339	2.802
Weight of water (kg)	3.576	3.327	3.094	3.331	3.095
Weight of grout (kg)	5.443	5.670	5.897	5.670	5.897

Binder ID	CF -1	CF-2	CF-3	C-1	C-2
Binder content (kg/m^3)	190	225	275	225	290
w_c (%)	59.7	53.4	51.9	54.1	55.1
C_c (%)	18.0	20.2	24.8	22.5	30.0
C_f (%)	2.0	2.2	2.8	0	0
C_T (%)	18.2	20.6	25.3	22.5	30.0
w_c/C_T	3.3	2.6	2.1	2.4	1.8

Natural soil characteristics

Results based on vane shear test on undisturbed clay

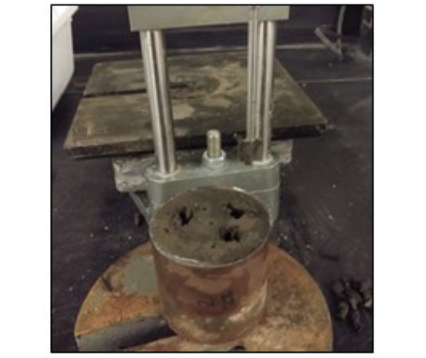

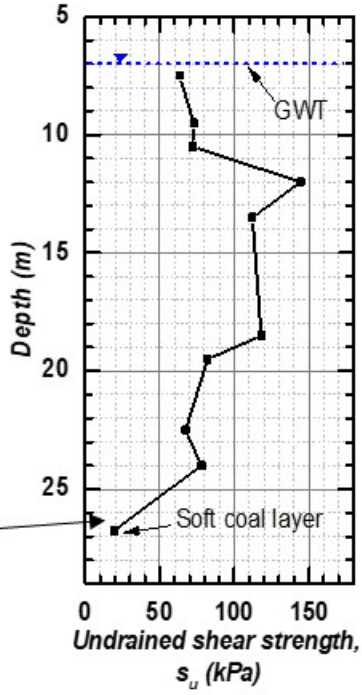

Results based on UCS test on undisturbed clay (9.5 m BGS)

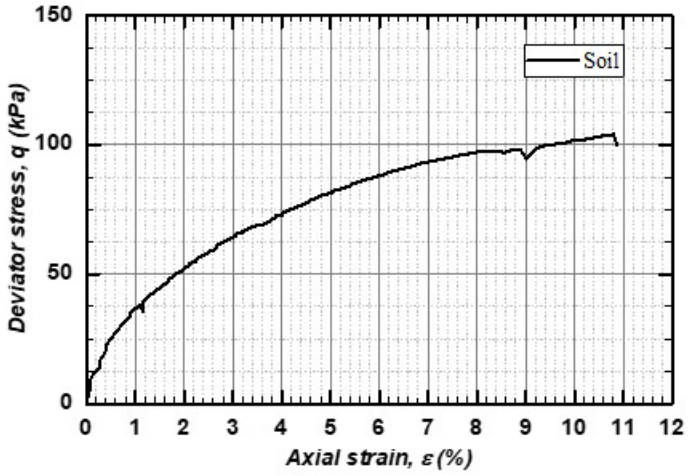

CF-1 UCS test results (8-days)

Age (days)	q_{peak} (kPa)	ε (%)	E_0 (MPa)	E_{50} (MPa)	q_r (kPa)
8	431.68	1.22	59.88	59.64	86.14
8	374.91	1.17	57.47	54.28	139.98

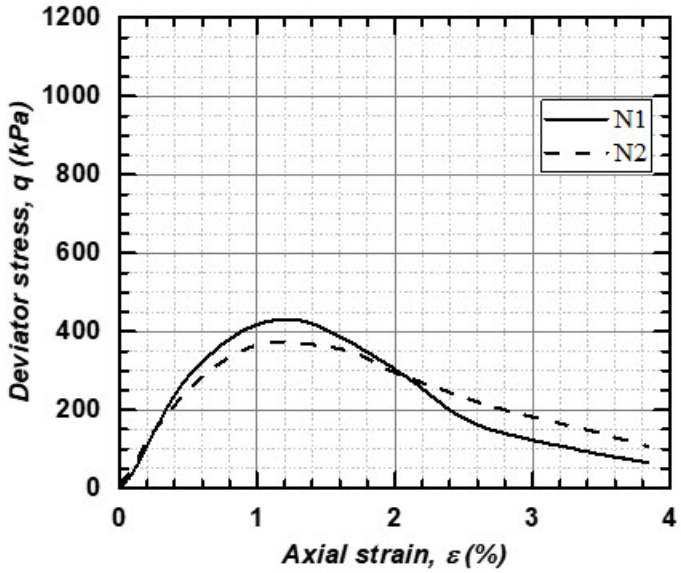

N1

N2

CF-1 UCS test results (15-days)

Age (days)	q_{peak} (kPa)	ε (%)	E_0 (MPa)	E_{50} (MPa)	q_r (kPa)
15	400.85	0.88	55.16	54.04	39.16
15	425.81	0.66	100.86	94.27	160.05

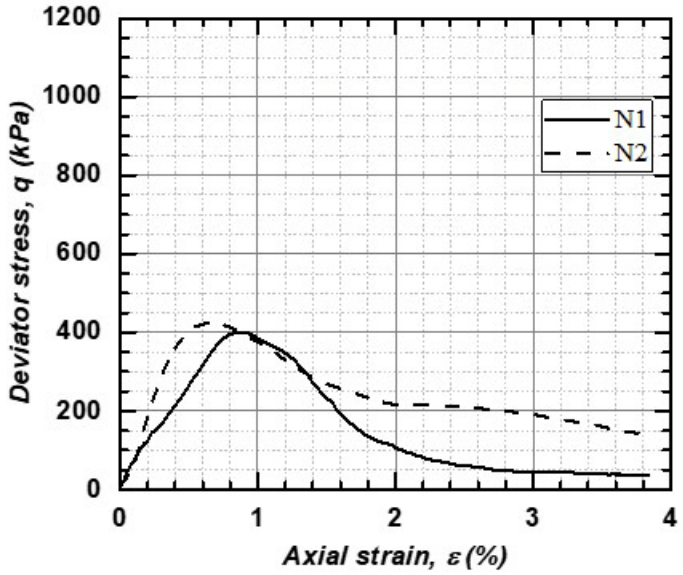

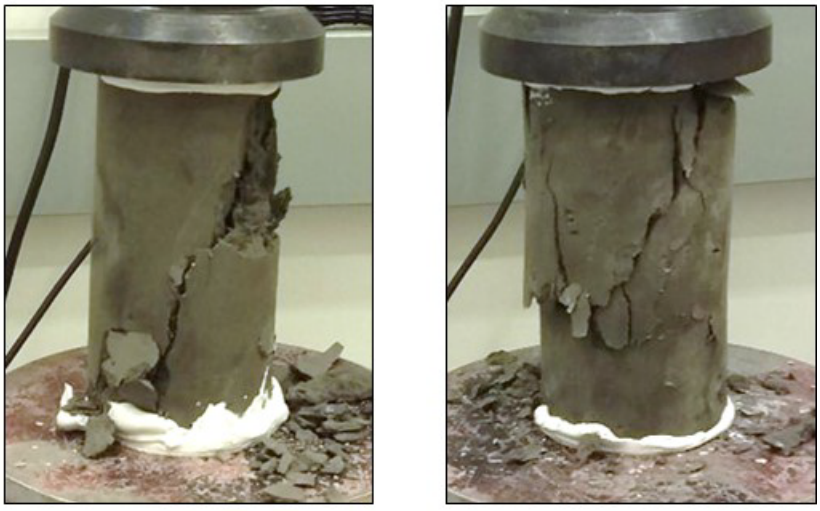

N1 N2

CF-1 UCS test results (28-days)

Age (days)	q_{peak} (kPa)	ε (%)	E_0 (MPa)	E_{50} (MPa)	q_r (kPa)
28	587.32	0.72	104.18	101.82	108.65
28	496.78	0.86	95.56	93.38	88.59

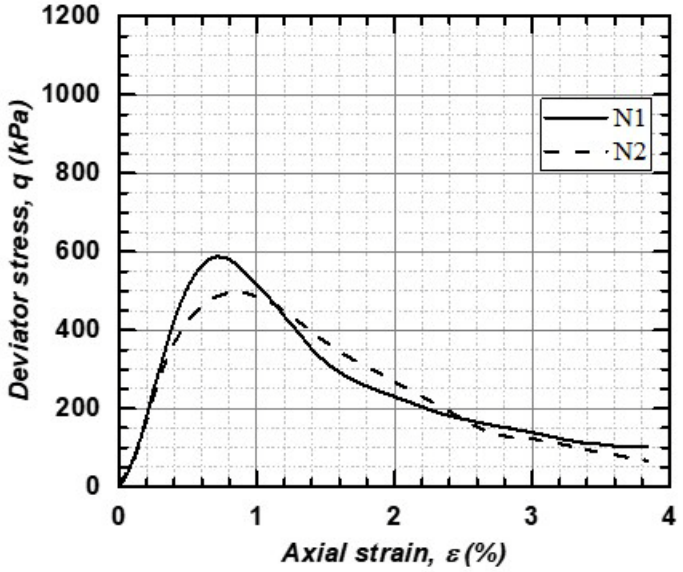

N1

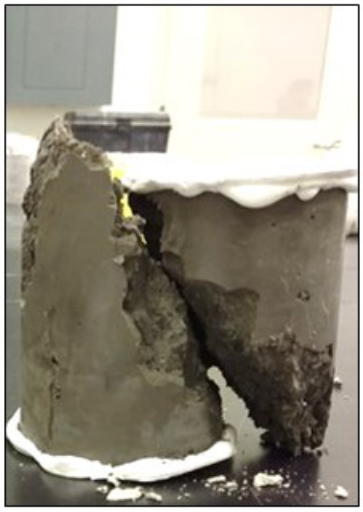

N2

CF-1 UCS test results (70-days)

Age (days)	q_{peak} (kPa)	ε (%)	E_0 (MPa)	E_{50} (MPa)	q_r (kPa)
70	776.73	0.52	190.63	168.46	134.11
70	726.32	0.54	179.95	162.98	45.52

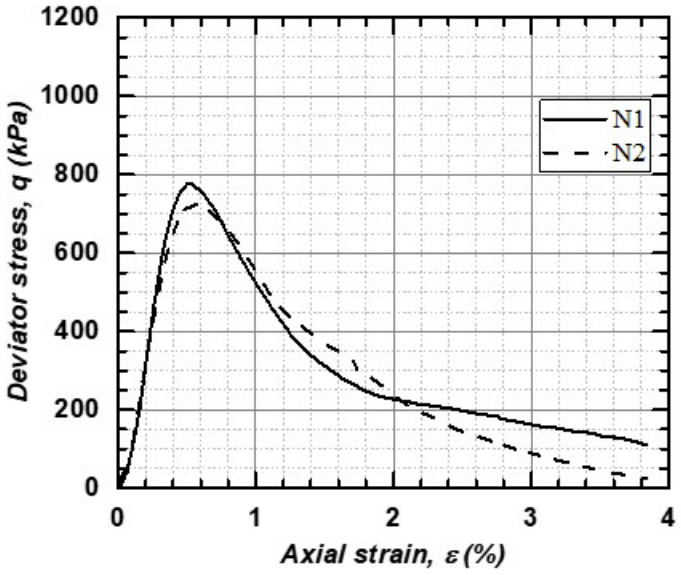

NO IMAGE

NO IMAGE

CF-2 UCS test results (3-days)

Age (days)	q_{peak} (kPa)	ε (%)	E_0 (MPa)	E_{50} (MPa)	q_r (kPa)
3	301.00	1.23	26.92	24.51	107.19
3	294.15	1.04	39.26	38.01	60.69

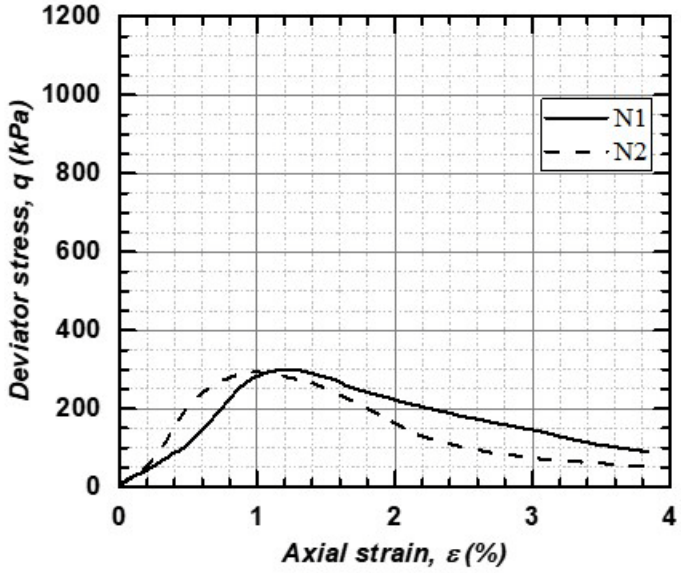

N1

N2

CF-2 UCS test results (7-days)

Age (days)	q_{peak} (kPa)	ε (%)	E_0 (MPa)	E_{50} (MPa)	q_r (kPa)
7	393.51	0.48	118.01	122.43	47.48
7	384.21	0.56	92.68	89.00	84.18

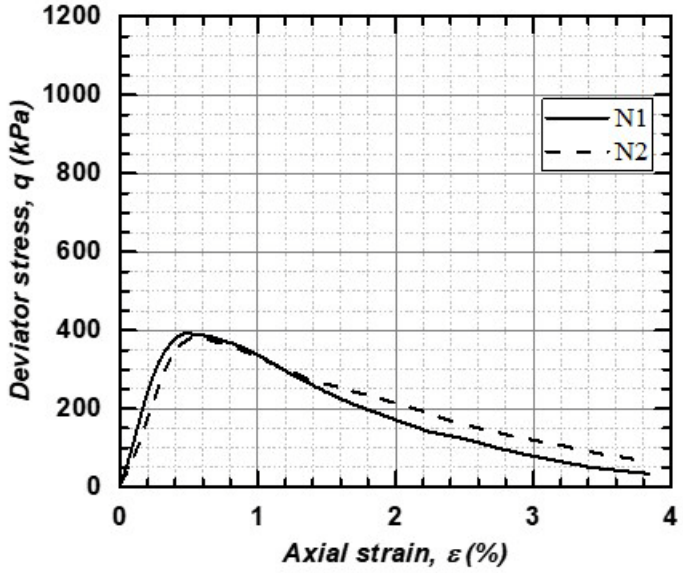

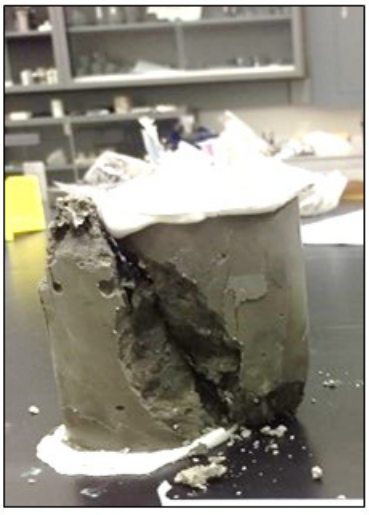

N1

N2

CF-2 UCS test results (14-days)

Age (days)	q_{peak} (kPa)	ε (%)	E_0 (MPa)	E_{50} (MPa)	q_r (kPa)
14	512.44	0.77	87.20	81.96	31.81
14	490.41	0.62	131.88	126.36	34.75

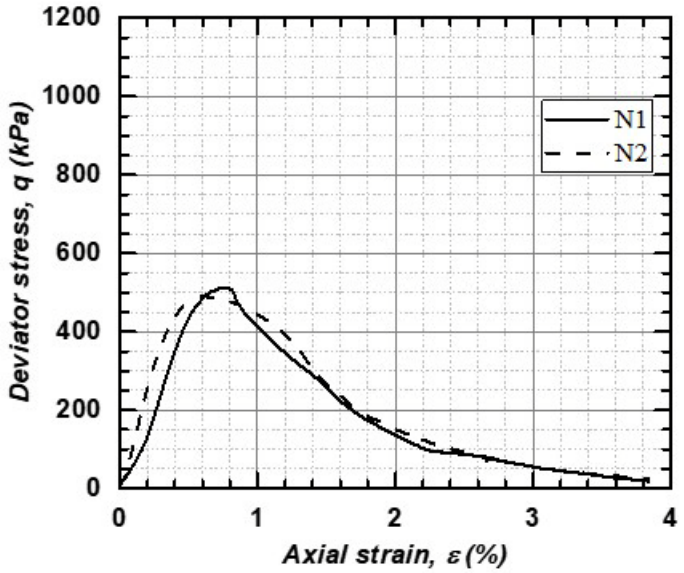

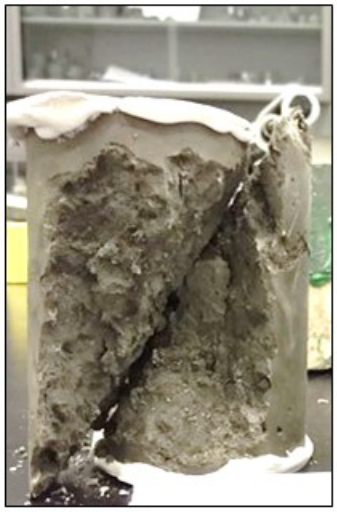

N1

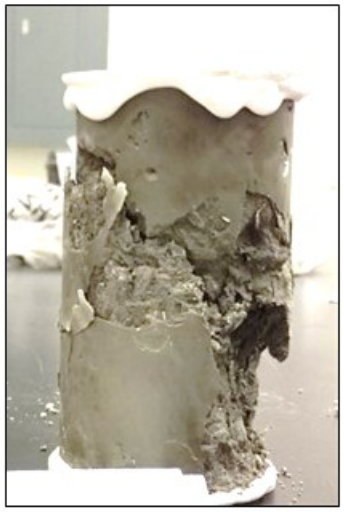

N2

CF-2 UCS test results (56-days)

Age (days)	q_{peak} (kPa)	ε (%)	E_0 (MPa)	E_{50} (MPa)	q_r (kPa)
56	949.01	0.54	221.19	201.16	116.00
56	880.00	0.71	147.94	144.16	142.92

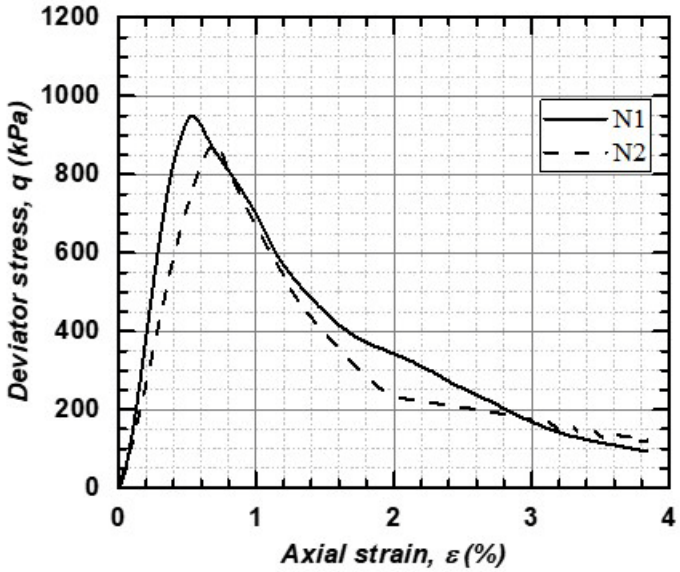

NO IMAGE

NO IMAGE

CF-3 UCS test results (3-days)

Age (days)	q_{peak} (kPa)	ε (%)	E_0 (MPa)	E_{50} (MPa)	q_r (kPa)
3	258.42	1.21	35.28	34.71	101.31
3	263.32	0.78	85.91	87.77	90.06

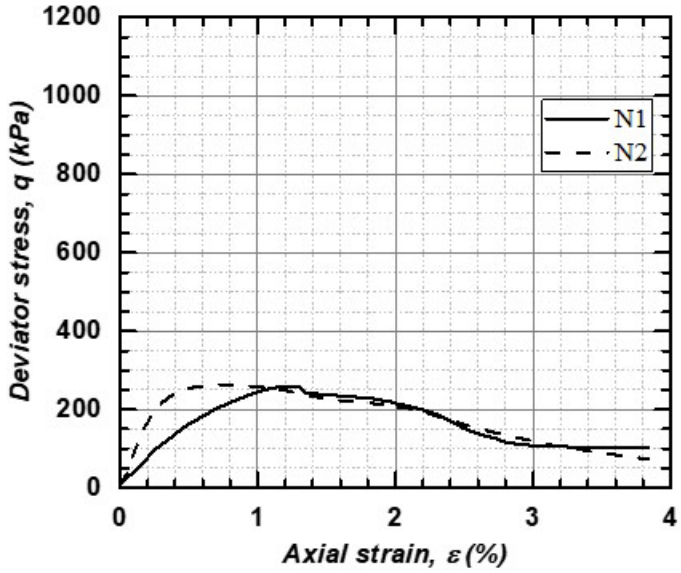

N1

N2

CF-3 UCS test results (7-days)

Age (days)	q_{peak} (kPa)	ε (%)	E_0 (MPa)	E_{50} (MPa)	q_r (kPa)
7	579.98	0.43	207.48	204.04	149.28
7	299.04	0.66	109.49	108.54	172.28

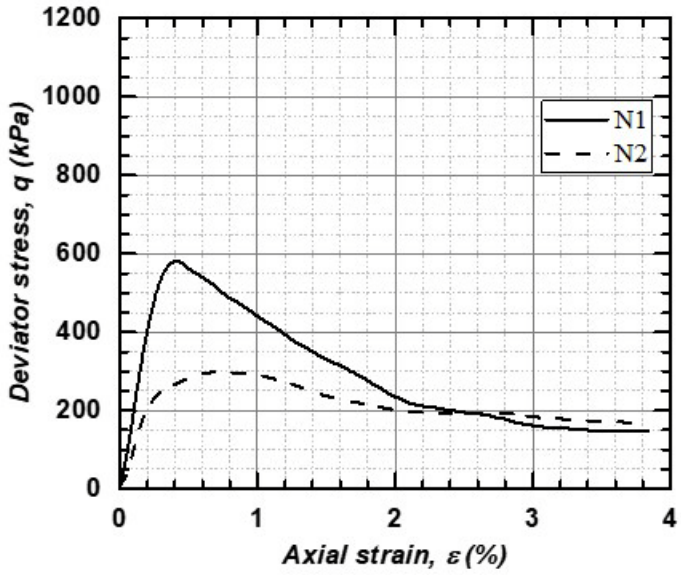

N1

N2

CF-3 UCS test results (14-days)

Age (days)	q_{peak} (kPa)	ε (%)	E_0 (MPa)	E_{50} (MPa)	q_r (kPa)
14	553.06	0.45	181.53	177.45	101.31
14	625.50	0.44	186.99	167.13	131.17

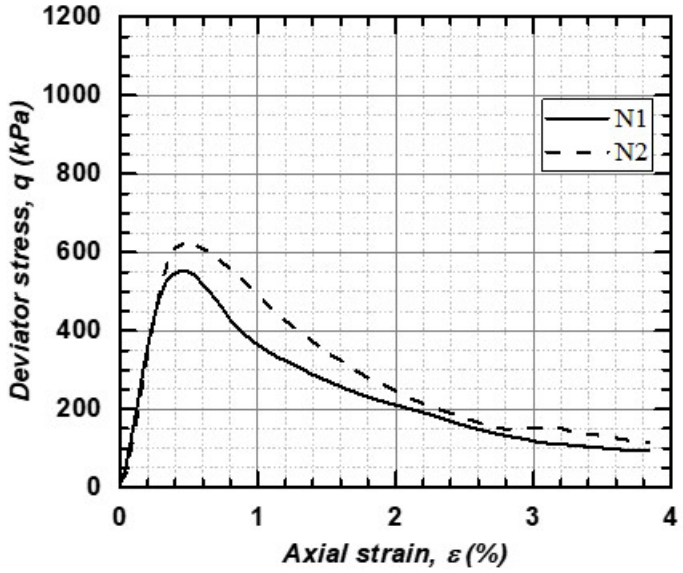

N1

N2

CF-3 UCS test results (56-days)

Age (days)	q_{peak} (kPa)	ε (%)	E_0 (MPa)	E_{50} (MPa)	q_r (kPa)
56	868.26	0.42	258.96	227.76	161.02
56	951.46	0.46	250.30	222.73	173.26

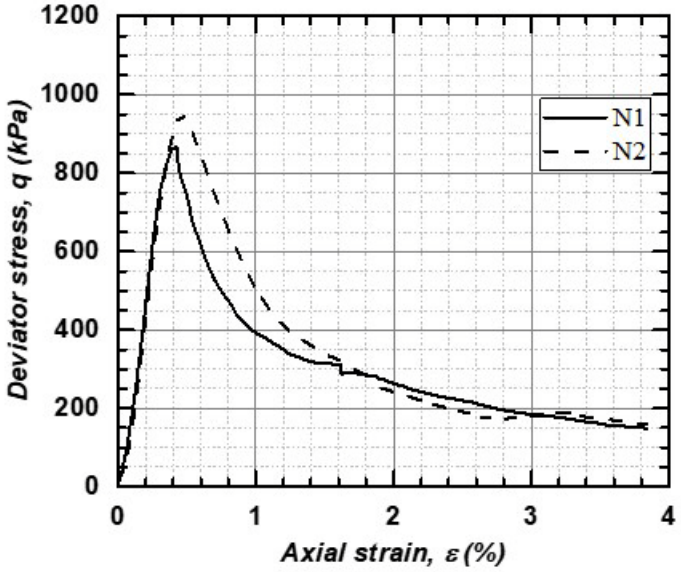

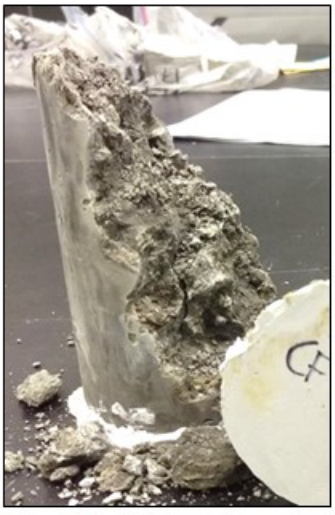

N1

N2

C-1 UCS test results (3-days)

Age (days)	q_{peak} (kPa)	ε (%)	E_0 (MPa)	E_{50} (MPa)	q_r (kPa)
3	293.66	0.53	77.56	72.44	71.95
3	330.86	0.67	71.02	67.68	109.63

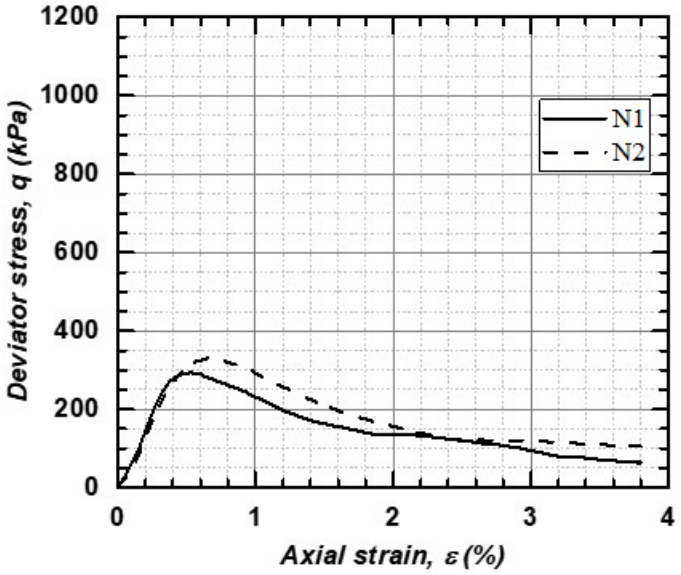

N1

N2

C-1 UCS test results (7-days)

Age (days)	q_{peak} (kPa)	ε (%)	E_0 (MPa)	E_{50} (MPa)	q_r (kPa)
7	397.42	0.79	91.37	96.43	127.25
7	339.18	0.78	86.98	92.37	238.35

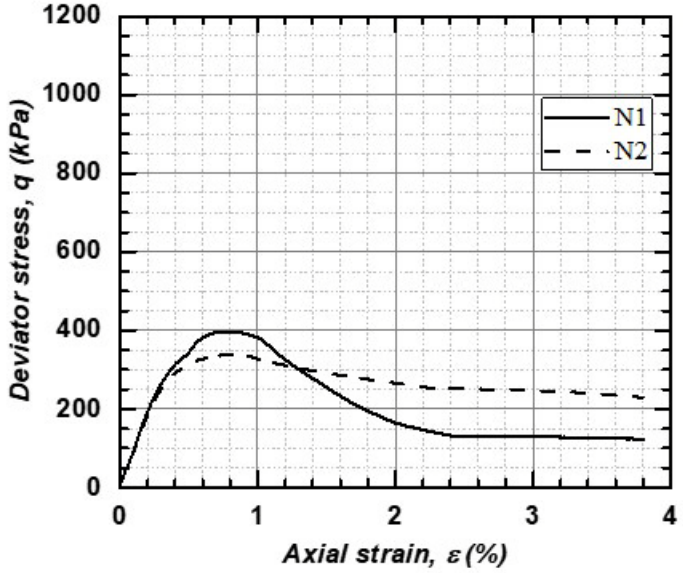

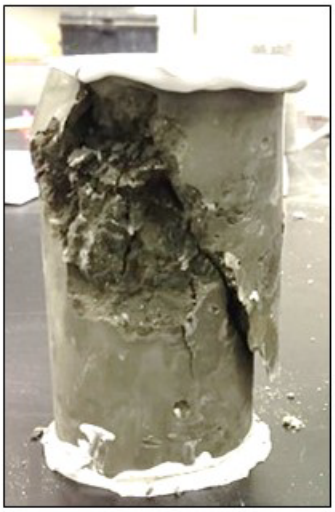

N1

N2

C-1 UCS test results (14-days)

Age (days)	q_{peak} (kPa)	ε (%)	E_0 (MPa)	E_{50} (MPa)	q_r (kPa)
14	594.66	0.54	165.78	163.65	148.79
14	509.50	0.71	119.41	110.12	210.46

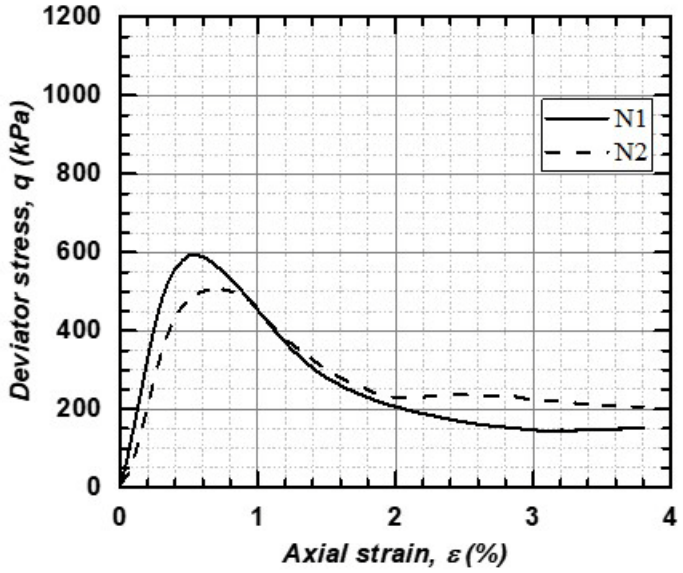

N1

N2

C-1 UCS test results (28-days)

Age (days)	q_{peak} (kPa)	ε (%)	E_0 (MPa)	E_{50} (MPa)	q_r (kPa)
28	744.43	0.63	197.48	181.91	164.94
28	794.35	0.46	217.24	186.63	198.22

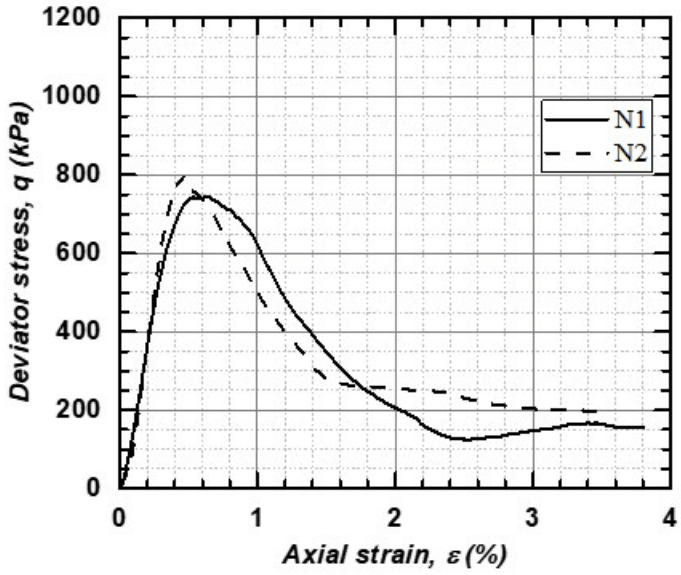

N1

N2

C-1 UCS test results (56-days)

Age (days)	q_{peak} (kPa)	ε (%)	E_0 (MPa)	E_{50} (MPa)	q_r (kPa)
56	1028.30	0.47	305.83	273.36	54.82

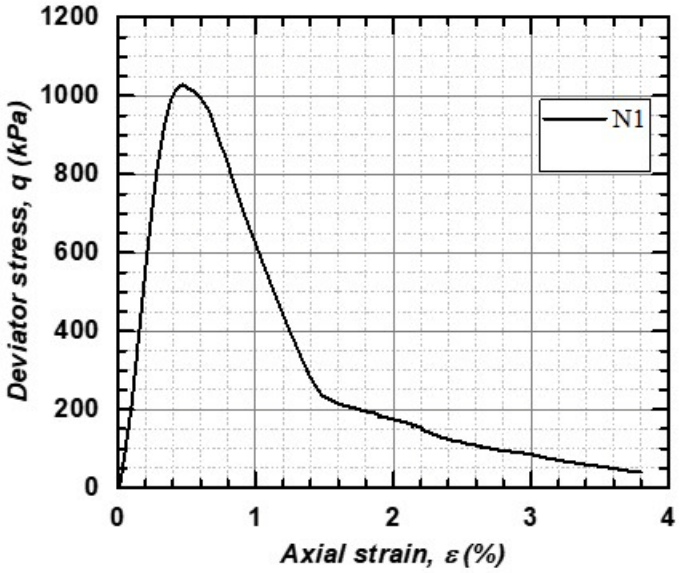

N1

N2

C-2 UCS test results (14-days)

Age (days)	q_{peak} (kPa)	ε (%)	E_0 (MPa)	E_{50} (MPa)	q_r (kPa)
14	718.98	0.51	171.00	155.35	166.90
14	719.96	0.55	173.98	159.90	208.50

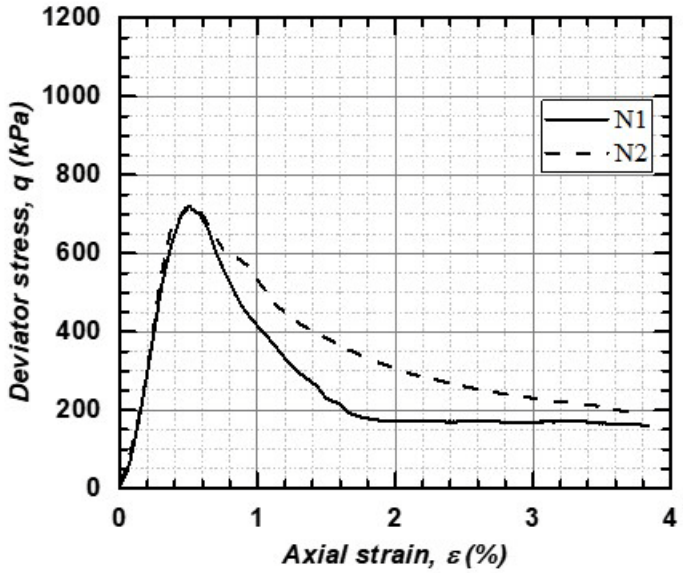

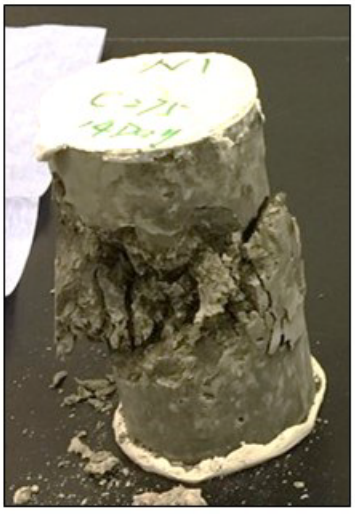

N1

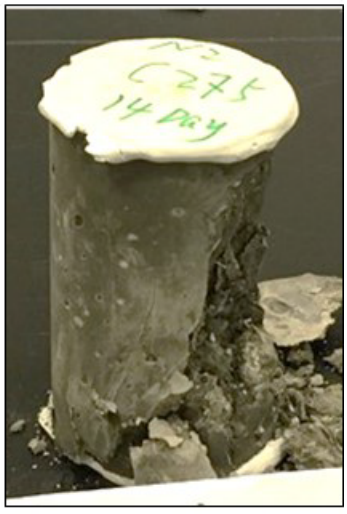

N2

C-2 UCS test results (28-days)

Age (days)	q_{peak} (kPa)	ε (%)	E_0 (MPa)	E_{50} (MPa)	q_r (kPa)
28	1135.98	0.51	270.86	246.05	109.63
28	986.21	0.67	203.66	190.75	82.23

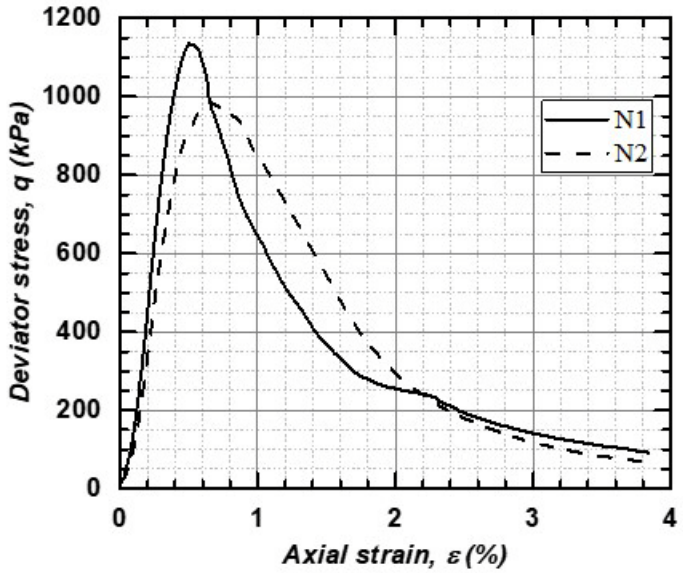

N1

N2

C-2 UCS test results (56-days)

Age (days)	q_{peak} (kPa)	ε (%)	E_0 (MPa)	E_{50} (MPa)	q_r (kPa)
56	1252.46	0.64	204.04	188.29	102.29
56	1168.77	0.59	228.16	207.03	119.91

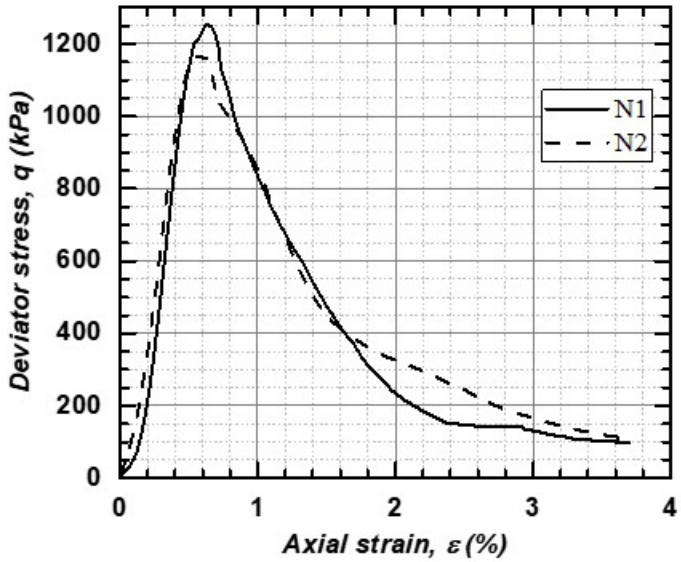

N1

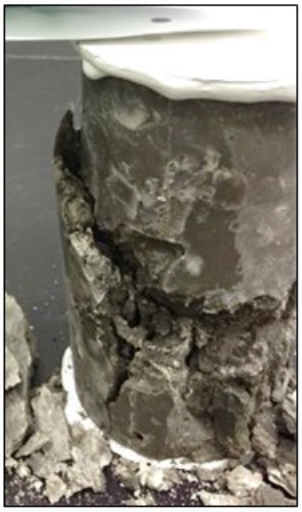

N2

Appendix B. Raw data of isotropically-consolidated undrained triaxial tests.

C-100 ICU test results (>56-days)

Sample ID	CU C-225-100
Confining stress	100 kPa

Height (mm)	Diameter (mm)
150.12	76.72
149.92	76.31
149.83	76.55
	76.83

Average Height	Average Diameter	
149.96	76.60	mm
15.00	7.66	cm

B-value	0.77
Volume change	0.569 cm^3

	Before shear	After shear	
Pressure head	9.32	9.04	kPa
Hydraulic gradient	6.34	6.15	m/m
k	5.10E-10	2.93E-08	m/s

	Before test	After test	
Water content	36.40	37.88	%
Volume	691.10	690.53	cm^3
Void ratio	1.022	1.020	
Porosity	0.505	0.505	
Saturation degree	0.944	0.984	

Notes:

There was dissolved air in the first consolidation stage. The final volumetric difference is very small. Rate for shear is 0.5%/hour or 0.0125 mm/min

Type of test	CU

Specific gravity Gs	2.65	
Density	1787.73	kg/m^3
Unit weight	17.54	kN/m^3

Initial mass BT	1235.5	g
Final mass AT	1248.9	g
Dry mass	905.8	g
Solids volume	341.81	cm^3

Peak strength	1470.06	kPa
Strain at peak	3.56	%
Peak pore pressure	-153.35	kPa
Young's Modulus	229.52	MPa
Secant Modulus	180.41	MPa
Residual strength	1256.54	kPa
Residual pore pressure	-204.78	kPa

Image of sample after test

C-100 ICU test results (>56-days)

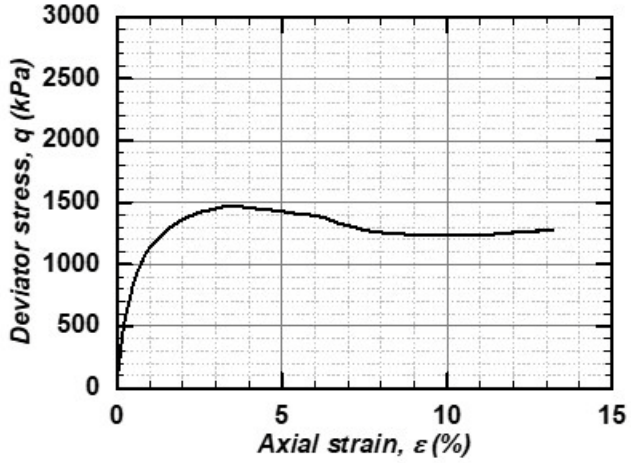

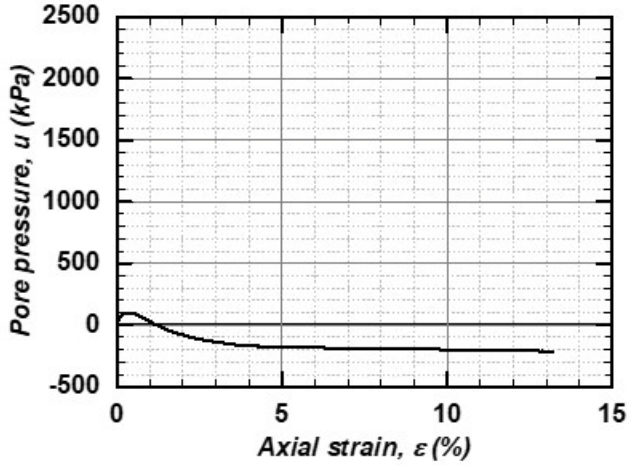

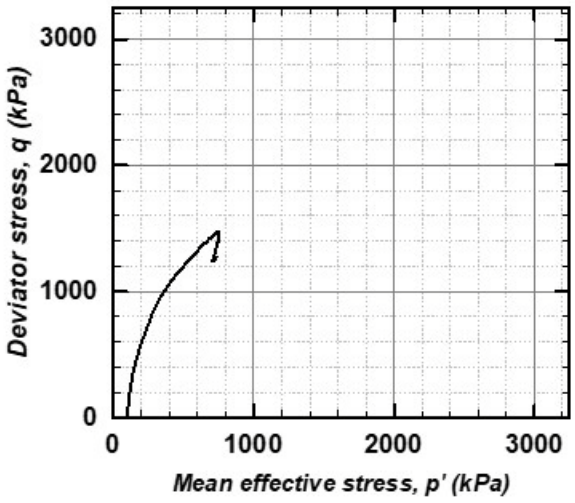

C-200 ICU test results (>56-days)

Sample ID	CU C-225-200
Confining stress	200 kPa

Height (mm)	Diameter (mm)
150.7	76.57
150.57	76.51
150.82	76.88
	76.73
Average Height	Average Diameter
150.70	76.67 mm
15.07	7.67 cm

Type of test	CU
Specific gravity Gs	2.65
Density	1823.56 kg/m^3
Unit weight	17.89 kN/m^3
Initial mass BT	1268.8 g
Final mass AT	1284.1 g
Dry mass	948 g
Solids volume	357.74 cm^3

B-value	0.70
Volume change	0.582 cm^3

	Before shear	After shear	
Pressure head	19.43	33.78	kPa
Hydraulic gradient	13.14	22.85	m/m
k	2.01E-10	4.94E-08	m/s

Peak strength	1491.20 kPa
Strain at peak	5.123 %
Peak pore pressure	-120.78 kPa
Young's Modulus	294.76 MPa
Secant Modulus	291.10 MPa
Residual strength	1363.84 kPa
Residual pore pressure	-142.56 kPa

	Before test	After test	
Water content	33.84	35.45	%
Volume	695.78	695.20	cm^3
Void ratio	0.945	0.943	
Porosity	0.486	0.485	
Saturation degree	0.949	0.996	

Notes:

B test for this samples was about 0.7. Shear rate was 0.5%/hour which is about 0.0125 mm/min

Image of sample after test

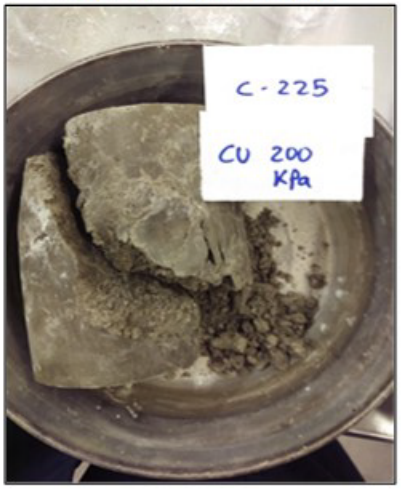

C-200 ICU test results (>56-days)

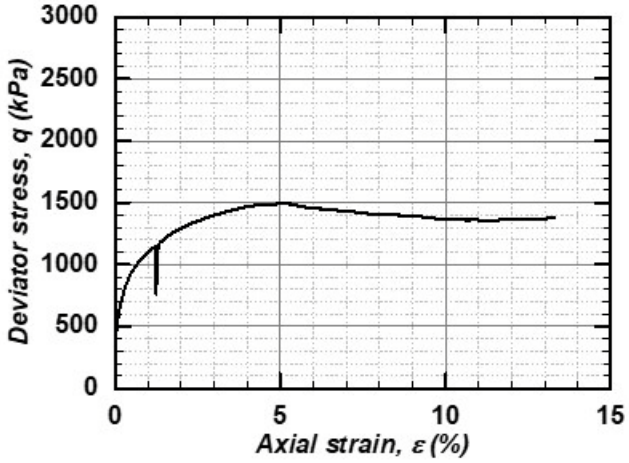

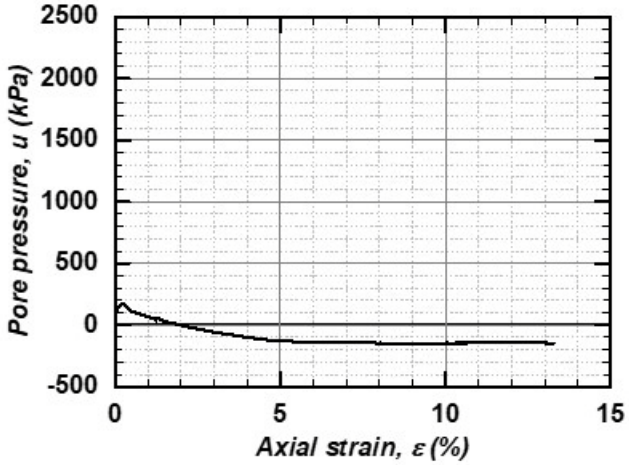

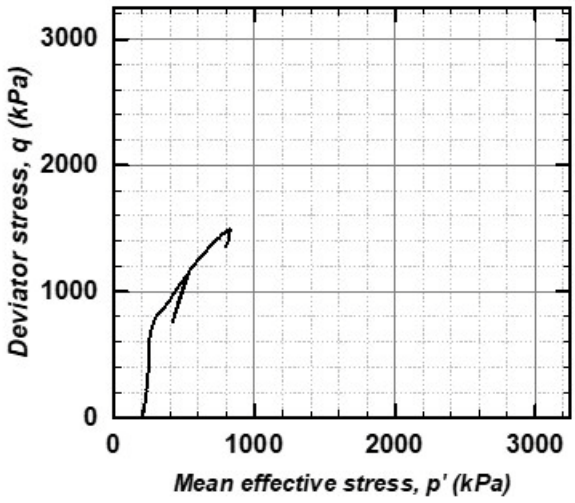

C-500 ICU test results (>56-days)

Sample ID	CU C-225-500
Confining stress	500 kPa

Height (mm)	Diameter (mm)
149.23	76.4
149.43	76.52
149.31	76.22
	76.53
Average Height	Average Diameter
149.32	76.42 mm
14.93	7.64 cm

B-value	0.88
Volume change	3.519 cm^3

	Before shear	After shear	
Pressure head	41.29	45.73	kPa
Hydraulic gradient	28.19	31.22	m/m
k	1.54E-10	6.90E-08	m/s

	Before test	After test	
Water content	33.07	33.93	%
Volume	684.86	681.34	cm^3
Void ratio	0.942	0.932	
Porosity	0.485	0.482	
Saturation degree	0.930	0.964	

Notes:

Shear rate was 0.5%/hour which is about 0.0125 mm/min.
Clear failure plane and some bulging

Type of test	CU

Specific gravity Gs	2.65
Density	1815.55 kg/m^3
Unit weight	17.81 kN/m^3
Initial mass BT	1243.4 g
Final mass AT	1251.4 g
Dry mass	934.4 g
Solids volume	352.60 cm^3

Peak strength	1519.70 kPa
Strain at peak	6.374 %
Peak pore pressure	106.68 kPa
Young's Modulus	236.52 MPa
Secant Modulus	205.37 MPa
Residual strength	1430.52 kPa
Residual pore pressure	95.71 kPa

Image of sample after test

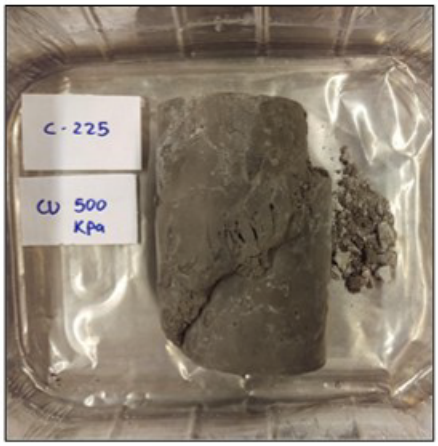

C-500 ICU test results (>56-days)

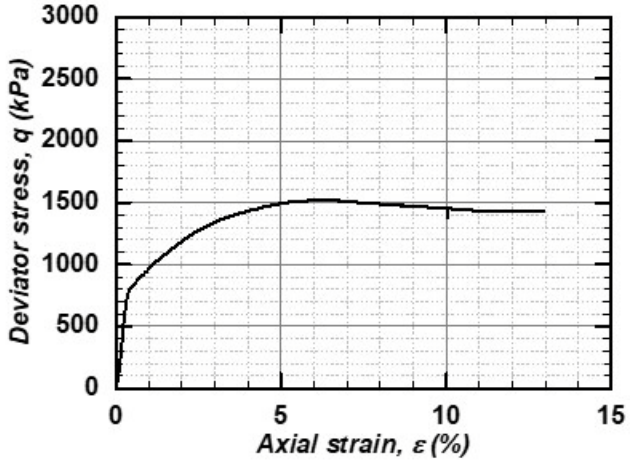

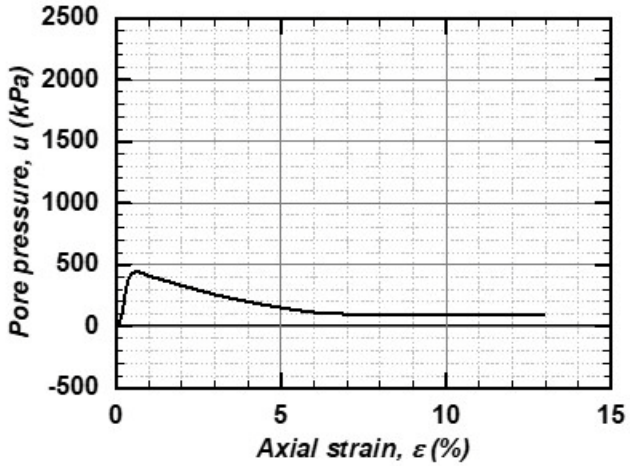

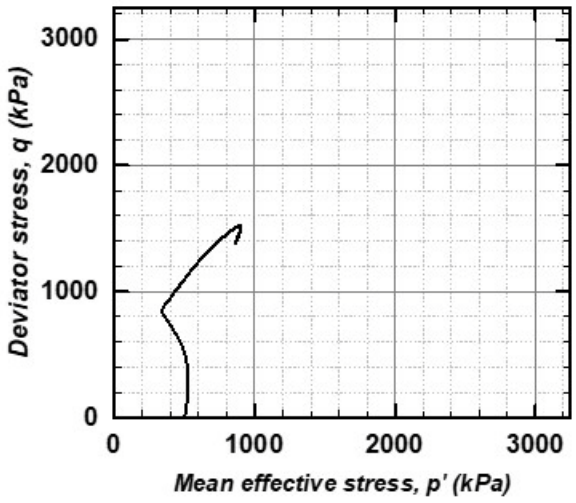

C-800 ICU test results (>56-days)

Sample ID	CU C-225-800
Confining stress	800 kPa

Height (mm)	Diameter (mm)
149.97	76.61
150.26	76.33
150.27	76.56
	76.97

Average Height	Average Diameter	
150.17	76.62	mm
15.02	7.66	cm

B-value	0.77	
Volume change	4.025	cm^3

	Before shear	After shear	
Pressure head	79.28	78.81	kPa
Hydraulic gradient	53.82	53.50	m/m
k	1.55E-10	1.81E-08	m/s

	Before test	After test	
Water content	33.77	34.50	%
Volume	692.34	688.31	cm^3
Void ratio	0.971	0.960	
Porosity	0.493	0.490	
Saturation degree	0.921	0.953	

Notes:

Shear rate was 0.5%/hour which is about 0.0125 mm/min.
Clear failure plane and some deformation around the failure plane due to crushing

Type of test	CU

Specific gravity Gs	2.65	
Density	1798.39	kg/m^3
Unit weight	17.64	kN/m^3
Initial mass BT	1245.1	g
Final mass AT	1251.9	g
Dry mass	930.8	g
Solids volume	351.25	cm^3
Peak strength	1531.95	kPa
Strain at peak	3.268	%
Peak pore pressure	497.58	kPa
Young's Modulus	320.84	MPa
Secant Modulus	280.34	MPa
Residual strength	1517.20	kPa
Residual pore pressure	446.89	kPa

Image of sample after test

C-800 ICU test results (>56-days)

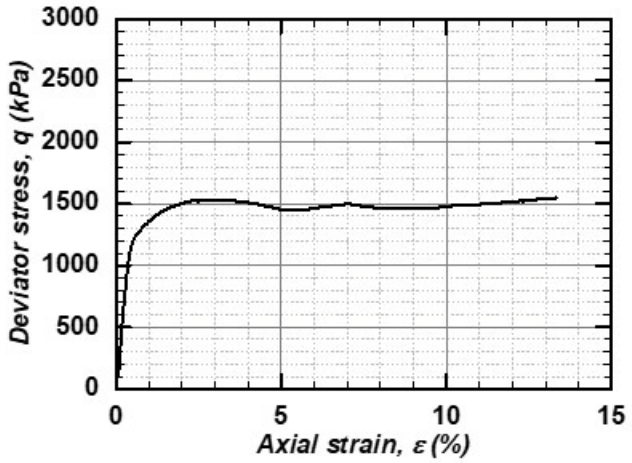

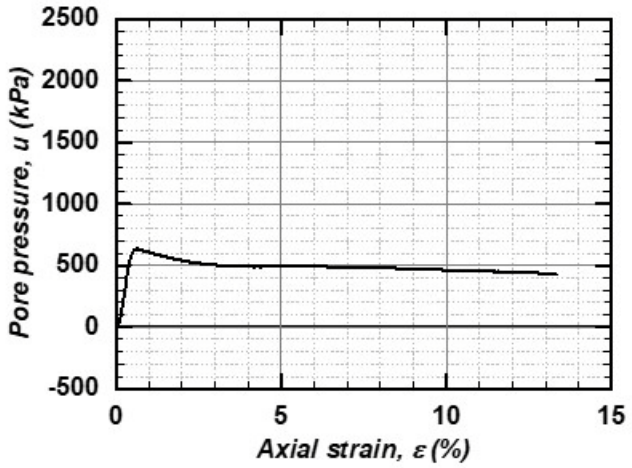

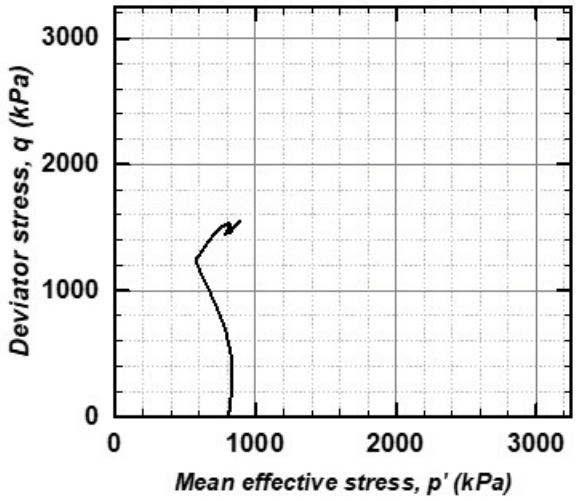

C-1000 ICU test results (>56-days)

Sample ID	CU C-225-1000
Confining stress	1000 kPa

Height (mm)	Diameter (mm)
149.13	77.01
149.67	76.45
149.93	76.46
	76.47
Average Height	Average Diameter
149.58	76.60 mm
14.96	7.66 cm

B-value	0.70
Volume change	6.092 cm^3

	Before shear	After shear	
Pressure head	99.22	99.06	kPa
Hydraulic gradient	67.62	67.51	m/m
k	1.09E-10	7.55E-09	m/s

	Before test	After test	
Water content	37.96	38.23	%
Volume	689.26	683.17	cm^3
Void ratio	1.024	1.006	
Porosity	0.506	0.501	
Saturation degree	0.983	1.007	

Notes:

Shear rate was 0.5%/hour which is about 0.0125 mm/min.
Clear failure plane and some deformation around the failure plane

Type of test	CU

Specific gravity Gs	2.65
Density	1806.58 kg/m^3
Unit weight	17.72 kN/m^3
Initial mass BT	1245.2 g
Final mass AT	1247.7 g
Dry mass	902.6 g
Solids volume	340.60 cm^3
Peak strength	1749.76 kPa
Strain at peak	4.257 %
Peak pore pressure	622.39 kPa
Young's Modulus	384.98 MPa
Secant Modulus	383.45 MPa
Residual strength	1592.42 kPa
Residual pore pressure	560.54 kPa

Image of sample after test

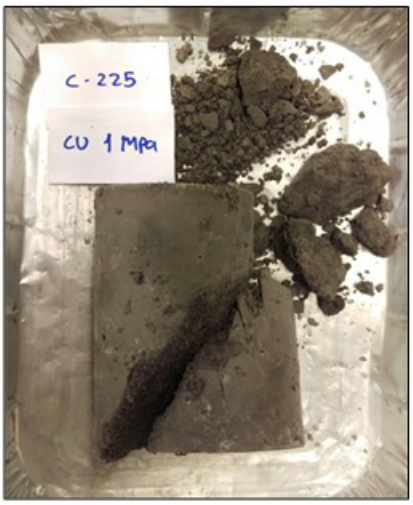

C-1000 ICU test results (>56-days)

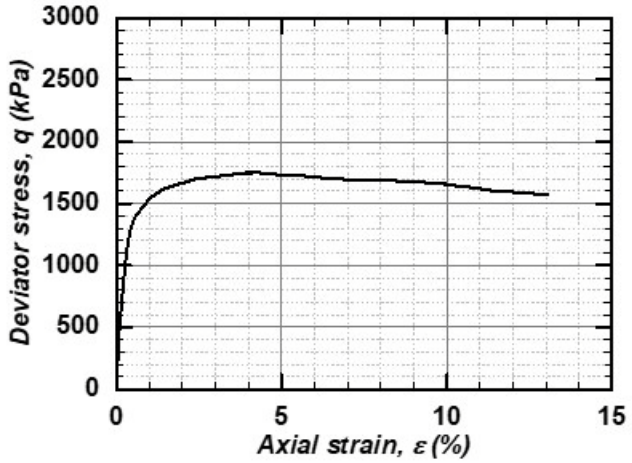

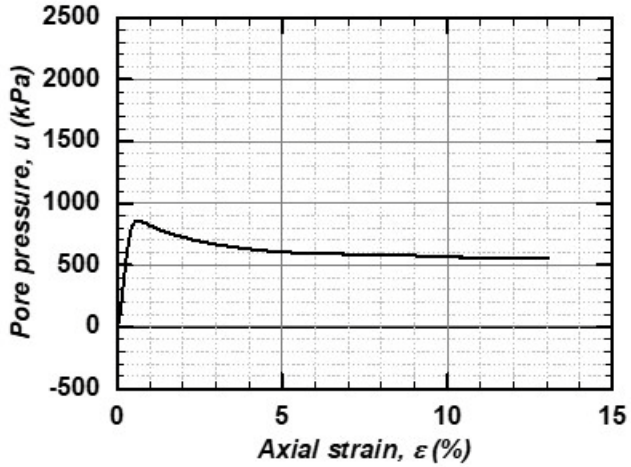

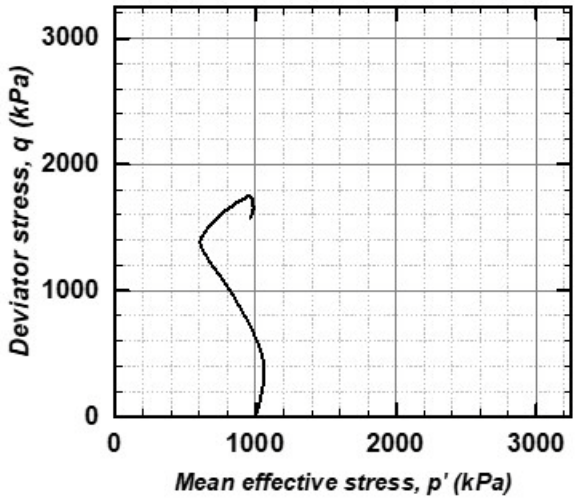

C-2000 ICU test results (>56-days)

Sample ID	CU C-225-2000
Confining stress	2000 kPa

Height (mm)	Diameter (mm)
149.23	76.63
149.75	76.57
150.07	76.86
	76.98

Average Height	Average Diameter	
149.68	76.76	mm
14.97	7.68	cm

B-value	0.87
Volume change	14.58 cm^3

	Before shear	After shear	
Pressure head	199.37	199.24	kPa
Hydraulic gradient	135.77	135.68	m/m
k	1.11E-10	5.00E-10	m/s

	Before test	After test	
Water content	38.34	37.88	%
Volume	692.68	678.10	cm^3
Void ratio	1.058	1.015	
Porosity	0.514	0.504	
Saturation degree	0.960	0.989	

Notes:

This test was innitially set for reaching a confining of 1 MPa. During consolidation one of the steps superated 1MPa of cofining so the final confinement was set to 2 Mpa in case the strucuture was damaged. Shear rate was 0.5%/hour which is about 0.0125 mm/min.

Type of test	CU

Specific gravity Gs	2.65	
Density	1781.48	kg/m^3
Unit weight	17.48	kN/m^3

Initial mass BT	1234	g
Final mass AT	1229.9	g
Dry mass	892	g
Solids volume	336.60	cm^3

Peak strength	1845.43	kPa
Strain at peak	2.166	%
Peak pore pressure	1559.25	kPa
Young's Modulus	371.88	MPa
Secant Modulus	342.94	MPa
Residual strength	1614.43	kPa
Residual pore pressure	1533.82	kPa

Image of sample after test

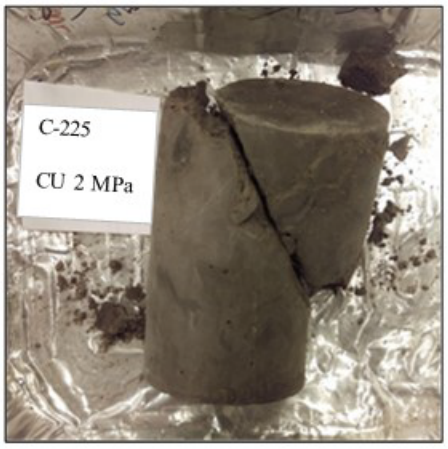

C-2000 ICU test results (>56-days)

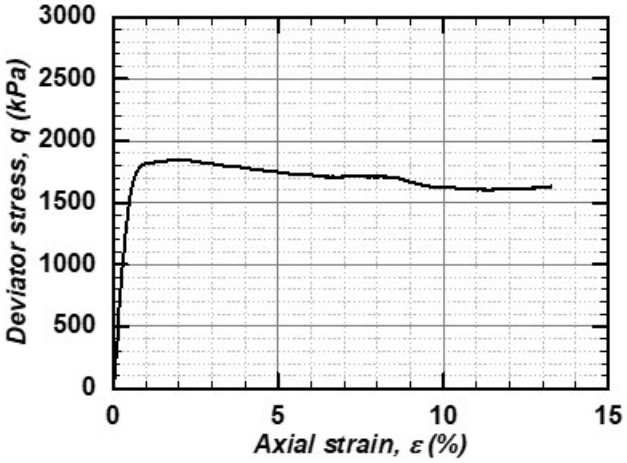

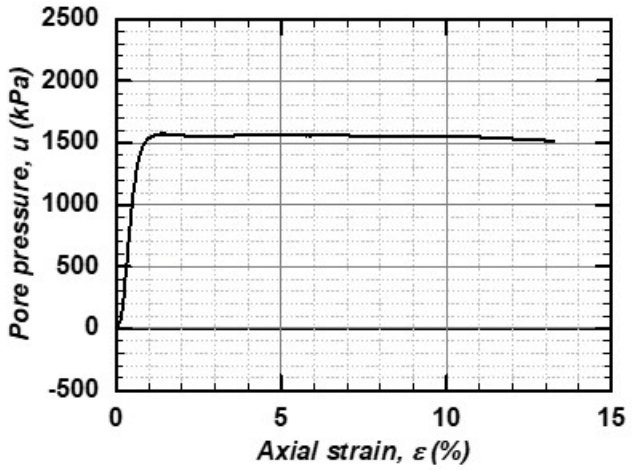

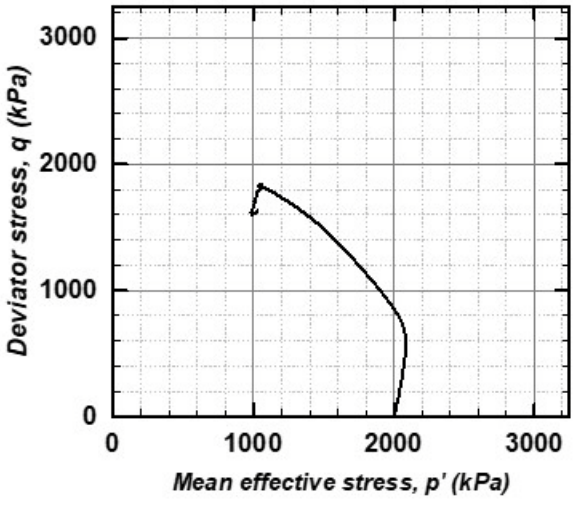

C-3000 ICU test results (>56-days)

Sample ID	CU C-225-3000
Confining stress	3000 kPa

Height (mm)	Diameter (mm)
150.3	76.23
150.67	76.05
150.73	76.4
	76.41

Average Height	Average Diameter	
150.57	76.27	mm
15.06	7.63	cm

B-value	0.86
Volume change	23.257 cm^3

	Before shear	After shear	
Pressure head	298.17	399.13	kPa
Hydraulic gradient	201.87	270.22	m/m
k	7.43E-11	2.48E-10	m/s

	Before test	After test	
Water content	31.97	30.26	%
Volume	687.95	664.69	cm^3
Void ratio	0.943	0.877	
Porosity	0.485	0.467	
Saturation degree	0.899	0.915	

Notes:

Shear rate was 0.5%/hour which is about 0.0125 mm/min

Type of test	CU

Specific gravity Gs	2.65	
Density	1800.29	kg/m^3
Unit weight	17.66	kN/m^3

Initial mass BT	1238.5	g
Final mass AT	1222.5	g
Dry mass	938.5	g
Solids volume	354.15	cm^3

Peak strength	2742.58	kPa
Strain at peak	1.264	%
Peak pore pressure	2321.74	kPa
Young's Modulus	495.68	MPa
Secant Modulus	446.52	MPa
Residual strength	2421.51	kPa
Residual pore pressure	2247.80	kPa

Image of sample after test

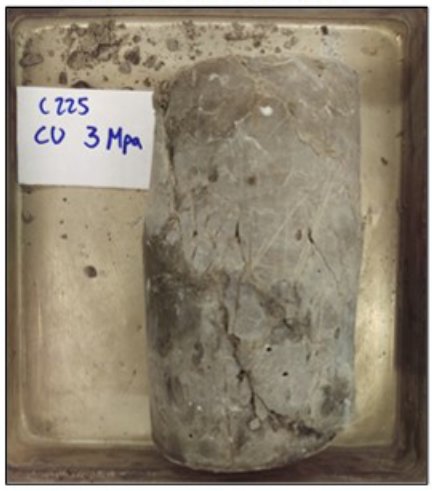

C-3000 ICU test results (>56-days)

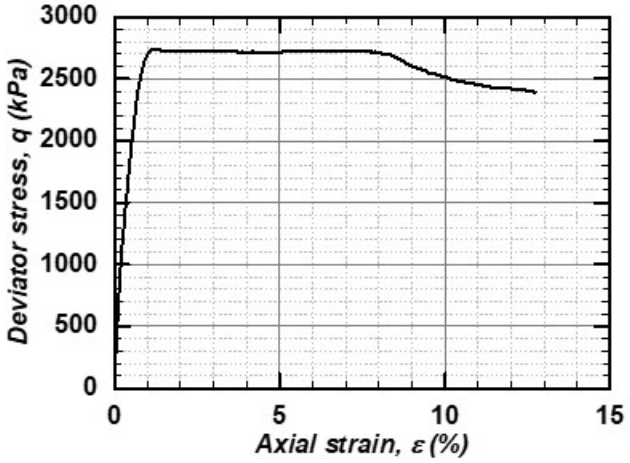

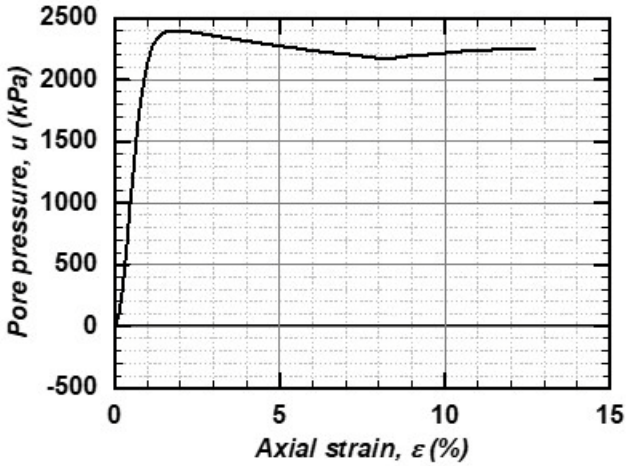

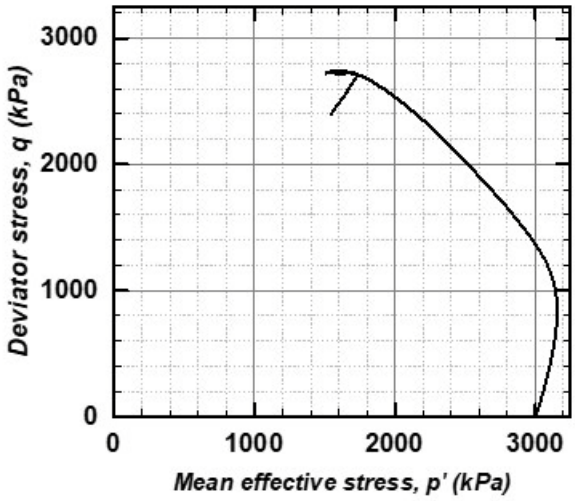

CF-100 ICU test results (>56-days)

Sample ID	CU CF-225-100
Confining stress	100 kPa

Height (mm)	Diameter (mm)
149.64	76.53
150.79	76.55
150.82	76.64
	76.48

Average Height	Average Diameter	
150.42	76.55	mm
15.04	7.66	cm

B-value	0.60
Volume change	0.448 cm^3

	Before shear	After shear	
Pressure head	19.49	11.32	kPa
Hydraulic gradient	13.21	7.67	m/m
k	1.97E-10	1.56E-07	m/s

	Before test	After test	
Water content	27.17	29.72	%
Volume	692.27	691.82	cm^3
Void ratio	0.849	0.848	
Porosity	0.459	0.459	
Saturation degree	0.845	0.925	

Notes:

B test is not so high after 24 hours, only reaches 0.6. Shear rate was 0.5%/hour which is about 0.0125 mm/min.

Type of test	CU

Specific gravity Gs	2.64	
Density	1815.47	kg/m^3
Unit weight	17.81	kN/m^3
Initial mass BT	1256.8	g
Final mass AT	1282	g
Dry mass	988.3	g
Solids volume	374.36	cm^3
Peak strength	1211.12	kPa
Strain at peak	8.135	%
Peak pore pressure	-221.62	kPa
Young's Modulus	179.81	MPa
Secant Modulus	110.27	MPa
Residual strength	1114.43	kPa
Residual pore pressure	-221.07	kPa

Image of sample after test

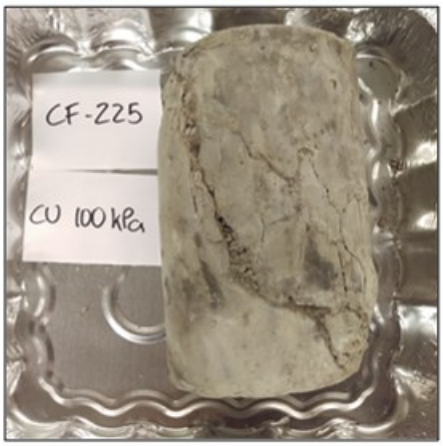

CF-100 ICU test results (>56-days)

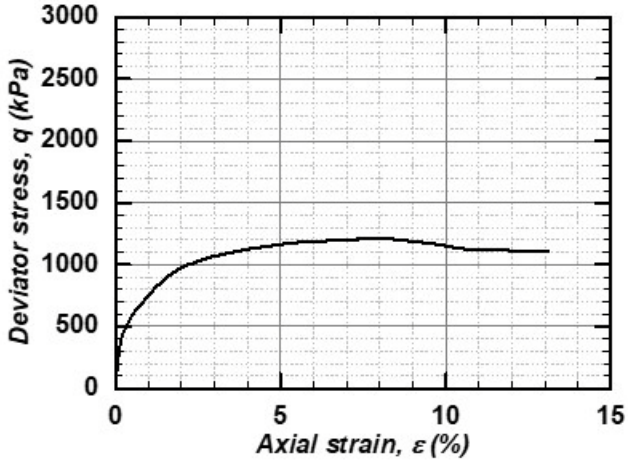

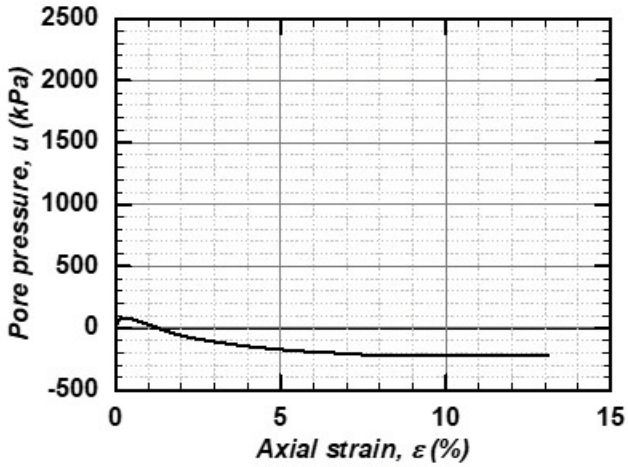

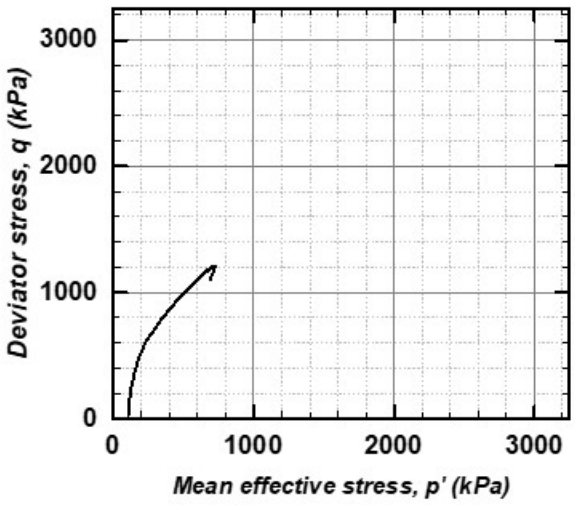

CF-200 ICU test results (>56-days)

Sample ID	CU CF-225-200
Confining stress	200 kPa

Height (mm)	Diameter (mm)
149.63	76.82
149.82	76.99
149.98	76.49
	76.39

Average Height	Average Diameter	
149.81	76.67	mm
14.98	7.67	cm

B-value	0.83
Volume change	1.145 cm^3

	Before shear	After shear	
Pressure head	19.35	19.06	kPa
Hydraulic gradient	13.17	12.97	m/m
k	7.24E-11	1.18E-08	m/s

	Before test	After test	
Water content	27.74	29.72	%
Volume	691.69	690.54	cm^3
Void ratio	0.884	0.881	
Porosity	0.469	0.468	
Saturation degree	0.829	0.891	

Notes:

B test around 0.8 after a day of saturation. Shear rate was 0.5%/hour which is about 0.0125 mm/min.

Type of test	CU

Specific gravity Gs	2.64
Density	1790.26 kg/m^3
Unit weight	17.56 kN/m^3

Initial mass BT	1238.3 g
Final mass AT	1257.5 g
Dry mass	969.39 g
Solids volume	367.19 cm^3

Peak strength	1475.17 kPa
Strain at peak	6.907 %
Peak pore pressure	-124.81 kPa
Young's Modulus	172.86 MPa
Secant Modulus	172.50 MPa
Residual strength	1452.43 kPa
Residual pore pressure	-188.13 kPa

Image of sample after test

CF-200 ICU test results (>56-days)

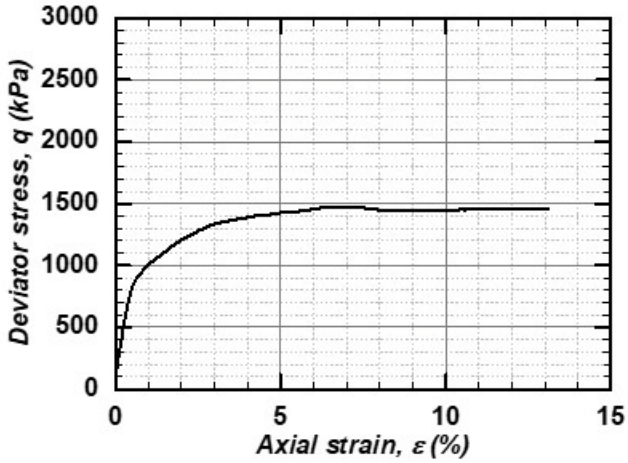

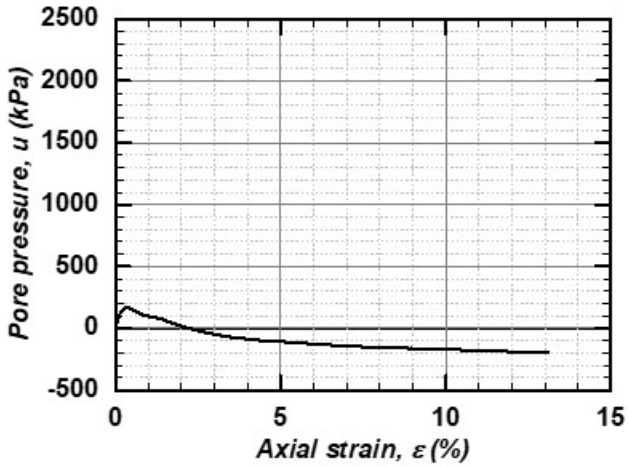

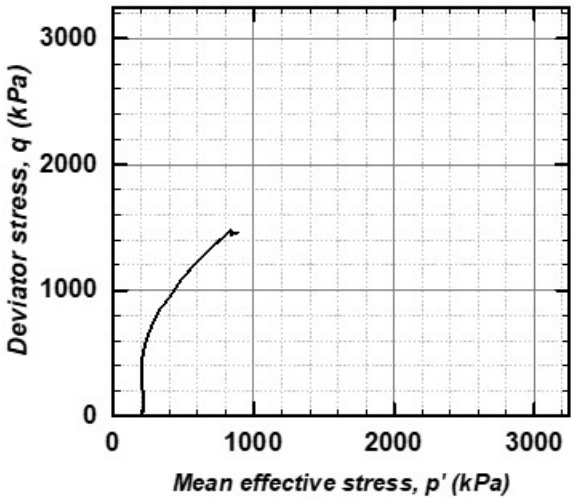

CF-500 ICU test results (>56-days)

Sample ID	CU CF-225-500
Confining stress	500 kPa

Height (mm)	Diameter (mm)
150.2	76.59
150.43	76.61
150.26	76.62
	76.44

Average Height	Average Diameter	
150.30	76.57	mm
15.03	7.66	cm

B-value	0.67
Volume change	2.752 cm^3

	Before shear	After shear	
Pressure head	49.39	49.07	kPa
Hydraulic gradient	33.50	33.28	m/m
k	8.04E-11	5.62E-09	m/s

	Before test	After test	
Water content	30.45	32.90	%
Volume	691.99	689.24	cm^3
Void ratio	0.947	0.939	
Porosity	0.486	0.484	
Saturation degree	0.849	0.925	

Notes:

Shear rate was 0.5%/hour which is about 0.0125 mm/min.

Type of test	CU

Specific gravity Gs	2.64	
Density	1768.81	kg/m^3
Unit weight	17.35	kN/m^3

Initial mass BT	1224	g
Final mass AT	1247	g
Dry mass	938.29	g
Solids volume	355.41	cm^3

Peak strength	1339.44	kPa
Strain at peak	3.18	%
Peak pore pressure	55.26	kPa
Young's Modulus	319.09	MPa
Secant Modulus	307.40	MPa
Residual strength	1239.10	kPa
Residual pore pressure	62.95	kPa

Image of sample after test

CF-500 ICU test results (>56-days)

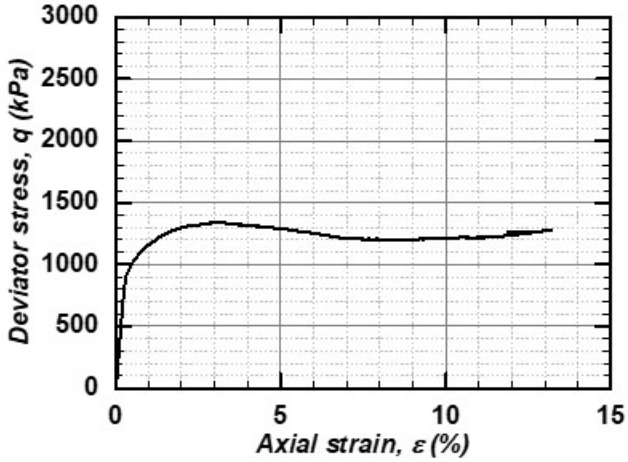

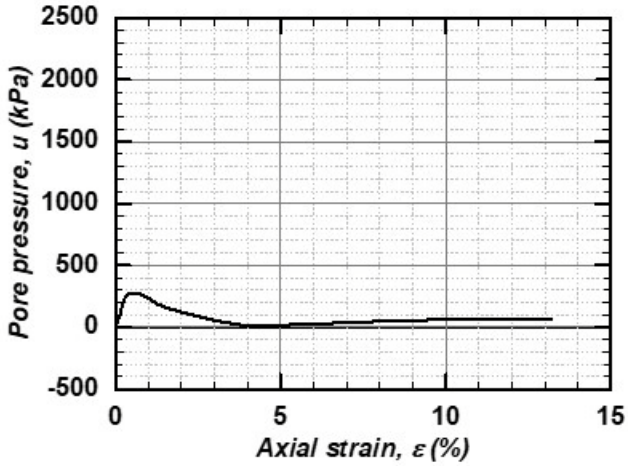

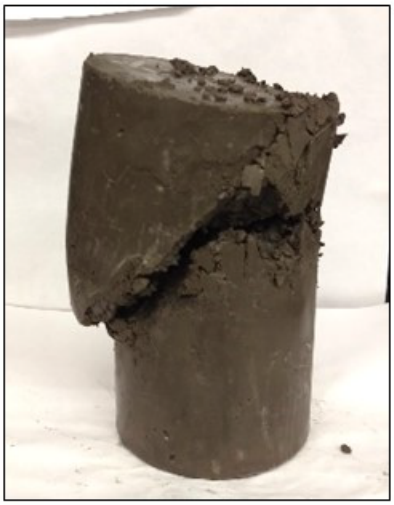

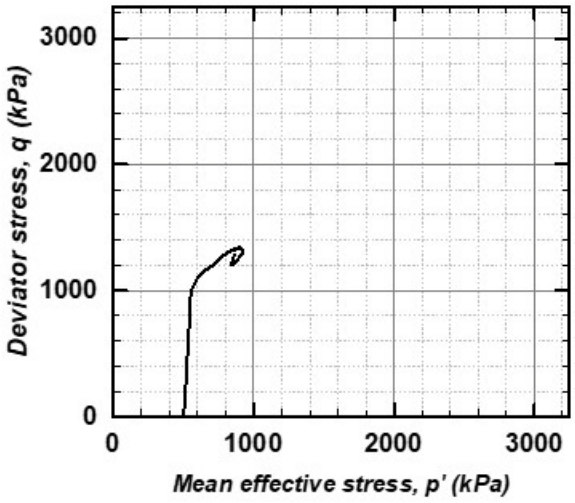

CF-800 ICU test results (>56-days)

Sample ID	CU CF-225-800
Confining stress	800 kPa

Height (mm)	Diameter (mm)
150.04	76.15
150.22	76.19
150.59	76.6
	76.53

Average Height	Average Diameter	
150.28	76.37	mm
15.03	7.64	cm

Type of test	CU

Specific gravity Gs	2.64	
Density	1796.73	kg/m^3
Unit weight	17.63	kN/m^3
Initial mass BT	1236.8	g
Final mass AT	1249.5	g
Dry mass	974.6	g
Solids volume	369.17	cm^3

B-value	0.86	
Volume change	4.838	cm^3

	Before shear	After shear	
Pressure head	79.18	79.02	kPa
Hydraulic gradient	53.71	53.60	m/m
k	8.05E-11	1.16E-05	m/s

Peak strength	1453.35	kPa
Strain at peak	5.457	%
Peak pore pressure	460.8	kPa
Young's Modulus	211.47	MPa
Secant Modulus	210.79	MPa
Residual strength	1323.67	kPa
Residual pore pressure	405.72	kPa

	Before test	After test	
Water content	26.90	28.21	%
Volume	688.36	683.53	cm^3
Void ratio	0.865	0.852	
Porosity	0.464	0.460	
Saturation degree	0.821	0.874	

Notes:

B test 0.86. Shear rate was 0.5%/hour which is about 0.0125 mm/min.

Image of sample after test

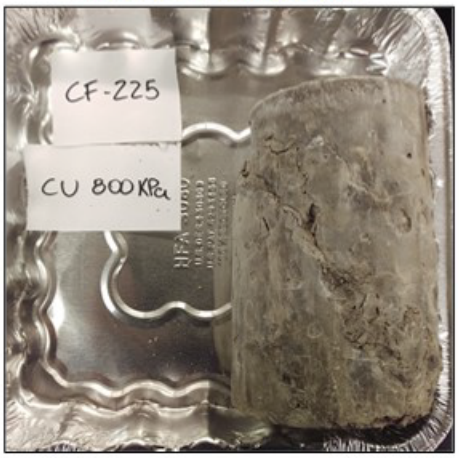

CF-800 ICU test results (>56-days)

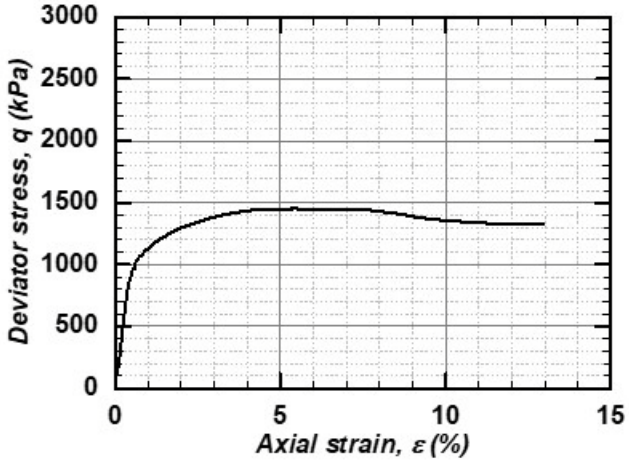

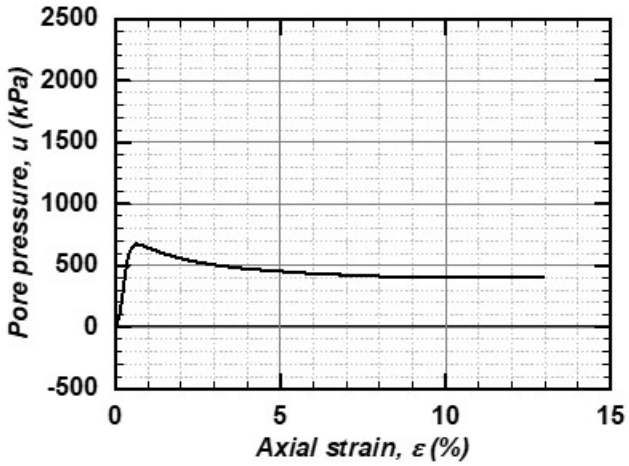

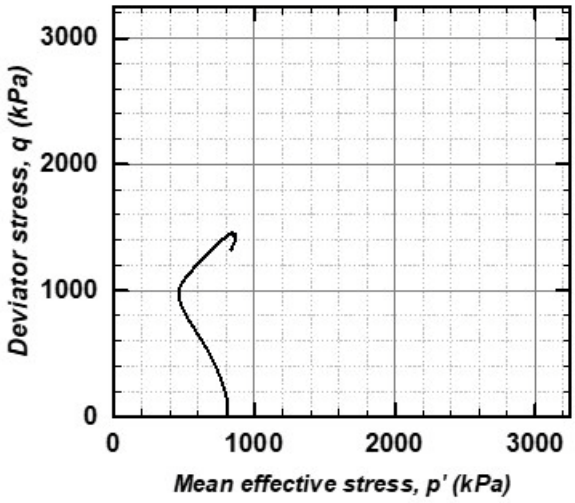

CF-1000 ICU test results (>56-days)

Sample ID	CU CF-225-1000
Confining stress	1000 kPa

Height (mm)	Diameter (mm)
150.47	76.46
150.38	76.84
150.86	76.36
	76.5

Average Height	Average Diameter	
150.57	76.54	mm
15.06	7.65	cm

B-value	0.82	
Volume change	4.542	cm^3

	Before shear	After shear	
Pressure head	99.36	98.91	kPa
Hydraulic gradient	67.27	66.96	m/m
k	6.40E-11	1.22E-08	m/s

	Before test	After test	
Water content	30.19	30.81	%
Volume	692.80	688.25	cm^3
Void ratio	0.941	0.928	
Porosity	0.485	0.481	
Saturation degree	0.847	0.876	

Notes:

B test is hihger than 0.8. Shear rate was 0.5%/hour which is about 0.0125 mm/min.

Type of test	CU	
Specific gravity Gs	2.64	
Density	1770.80	kg/m^3
Unit weight	17.37	kN/m^3
Initial mass BT	1226.8	g
Final mass AT	1232.6	g
Dry mass	942.3	g
Solids volume	356.93	cm^3
Peak strength	1919.30	kPa
Strain at peak	6.858	%
Peak pore pressure	529.94	kPa
Young's Modulus	304.74	MPa
Secant Modulus	274.29	MPa
Residual strength	1631.55	kPa
Residual pore pressure	538.91	kPa

Image of sample after test

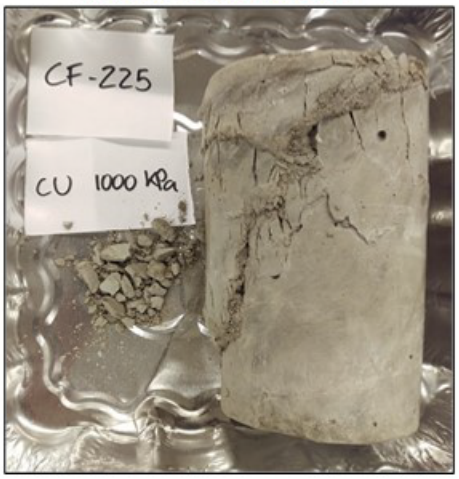

CF-1000 ICU test results (>56-days)

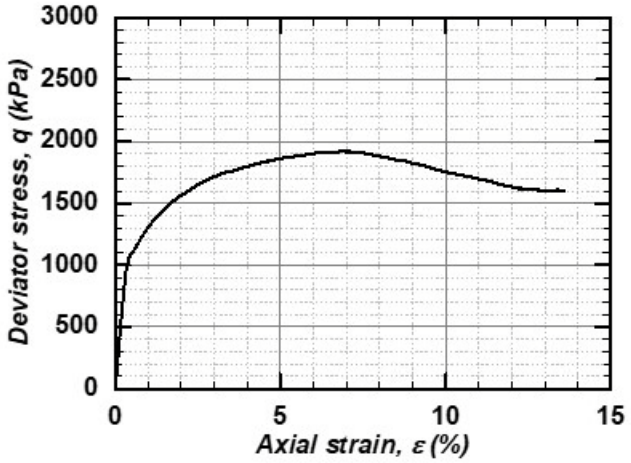

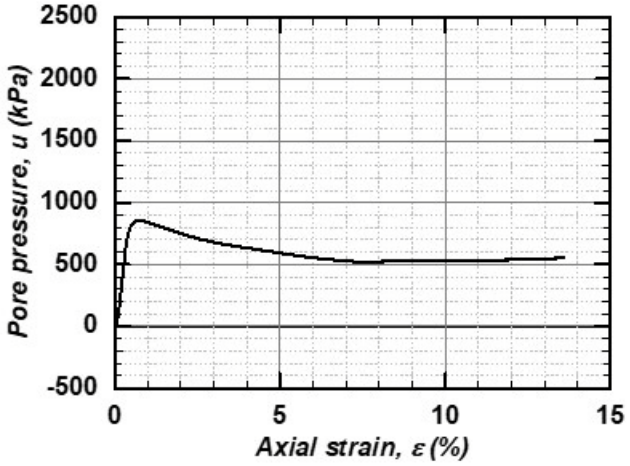

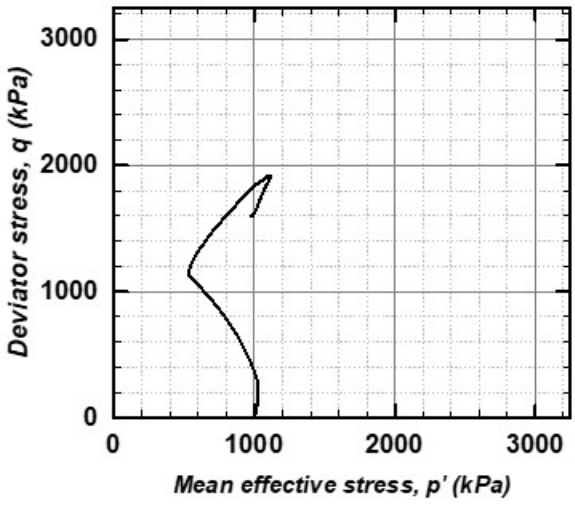

CF-2000 ICU test results (>56-days)

Sample ID	CU CF-225-2000
Confining stress	2000 kPa

Height (mm)	Diameter (mm)
150.6	76.16
151.07	76.58
150.77	76.57
	76.35

Average Height	Average Diameter	
150.81	76.42	mm
15.08	7.64	cm

B-value	0.90	
Volume change	15.043	cm^3

	Before shear	After shear	
Pressure head	199.35	199.06	kPa
Hydraulic gradient	134.74	134.55	m/m
k	4.14E-11	2.52E-09	m/s

	Before test	After test	
Water content	26.52	26.59	%
Volume	691.65	676.61	cm^3
Void ratio	0.858	0.817	
Porosity	0.462	0.450	
Saturation degree	0.816	0.859	

Notes:

B test is hihger than 0.8. Shear rate was 0.5%/hour which is about 0.0125 mm/min.

Type of test	CU

Specific gravity Gs	2.64	
Density	1798.02	kg/m^3
Unit weight	17.64	kN/m^3
Initial mass BT	1243.6	g
Final mass AT	1244.3	g
Dry mass	982.9	g
Solids volume	372.31	cm^3
Peak strength	1928.20	kPa
Strain at peak	4.456	%
Peak pore pressure	1458.24	kPa
Young's Modulus	238.76	MPa
Secant Modulus	229.42	MPa
Residual strength	1509.33	kPa
Residual pore pressure	1465.56	kPa

Image of sample after test

CF-2000 ICU test results (>56-days)

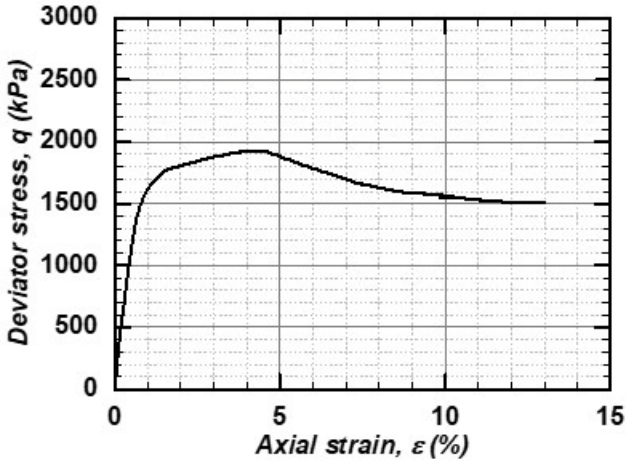

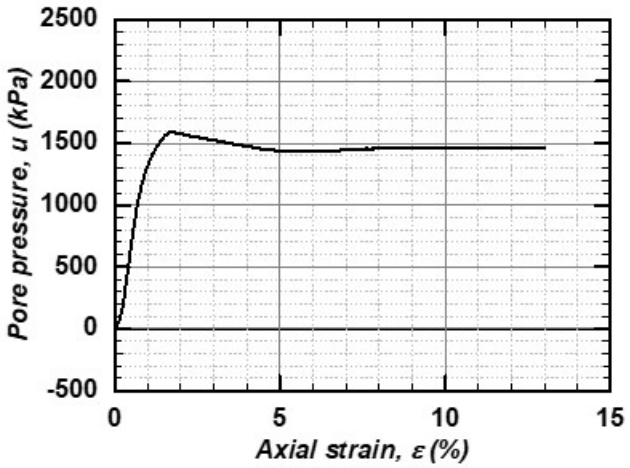

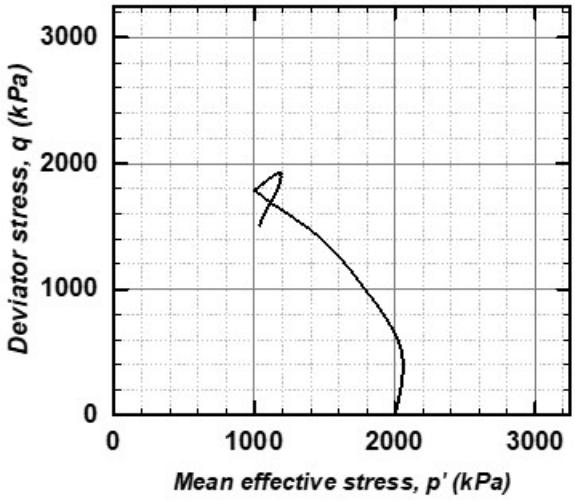

CF-3000 ICU test results (>56-days)

Sample ID	CU CF-225-3000
Confining stress	3000 kPa

Height (mm)	Diameter (mm)
150.45	76.58
150.47	76.62
150.5	77.14
	76.56

Average Height	Average Diameter	
150.47	76.73	mm
15.05	7.67	cm

B-value	0.76	
Volume change	20.578	cm^3

	Before shear	After shear	
Pressure head	298.23	298.23	kPa
Hydraulic gradient	202.03	201.86	m/m
k	3.25E-11	1.21E-09	m/s

	Before test	After test	
Water content	25.43	25.05	%
Volume	695.70	675.12	cm^3
Void ratio	0.881	0.825	
Porosity	0.468	0.452	
Saturation degree	0.762	0.801	

Notes:

B test is higher than 0.7. Shear rate was 0.5%/hour which is about 0.0125 mm/min.

Type of test	CU

Specific gravity Gs	2.64	
Density	1760.52	kg/m^3
Unit weight	17.27	kN/m^3
Initial mass BT	1224.8	g
Final mass AT	1221.1	g
Dry mass	976.5	g
Solids volume	369.89	cm^3
Peak strength	2424.39	kPa
Strain at peak	1.567	%
Peak pore pressure	2323.75	kPa
Young's Modulus	438.57	MPa
Secant Modulus	417.48	MPa
Residual strength	2079.84	kPa
Residual pore pressure	2357.61	kPa

Image of sample after test

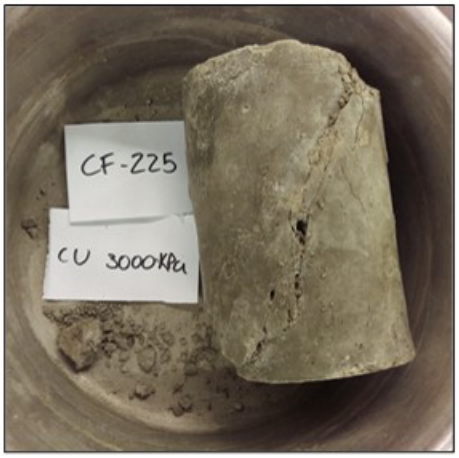

CF-3000 ICU test results (>56-days)

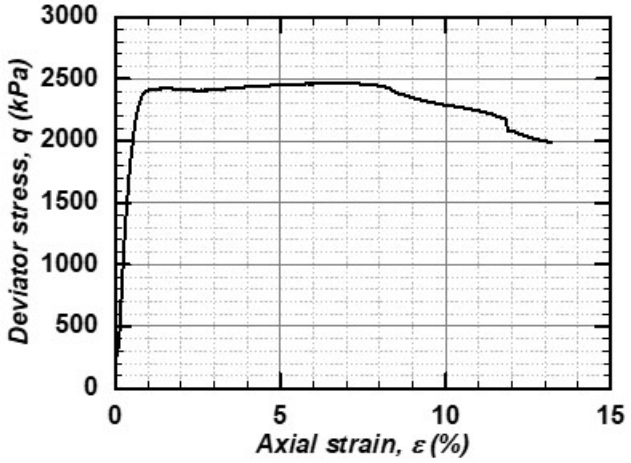

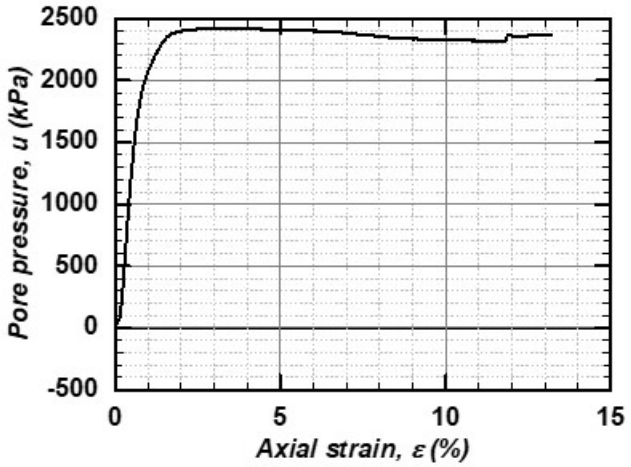

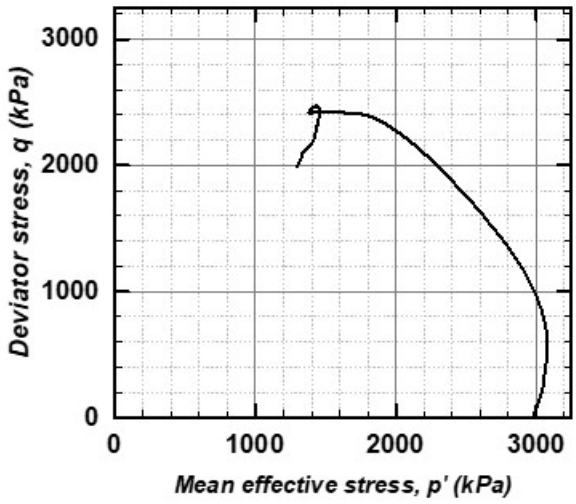

Appendix C. SEM images of failure surface and outer surface of soilcrete specimens.

C-0 SEM failure surface (sample a)

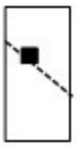

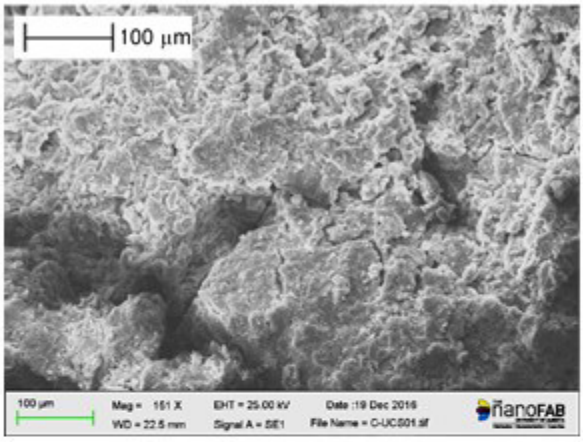

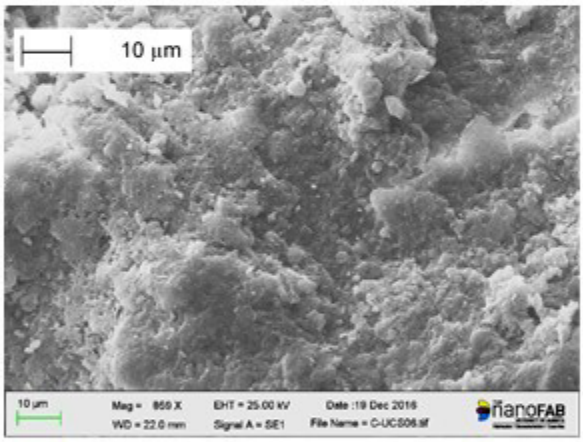

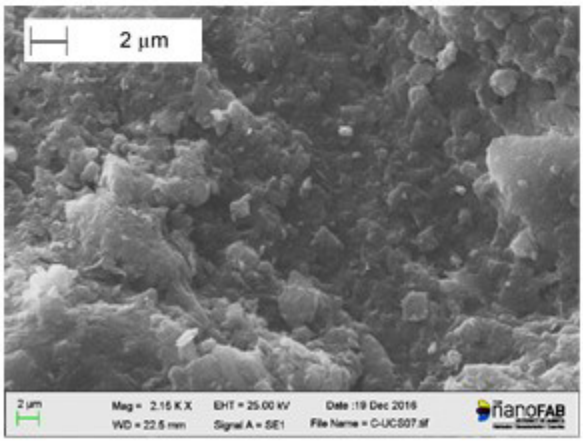

C-0 SEM failure surface (sample b)

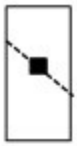

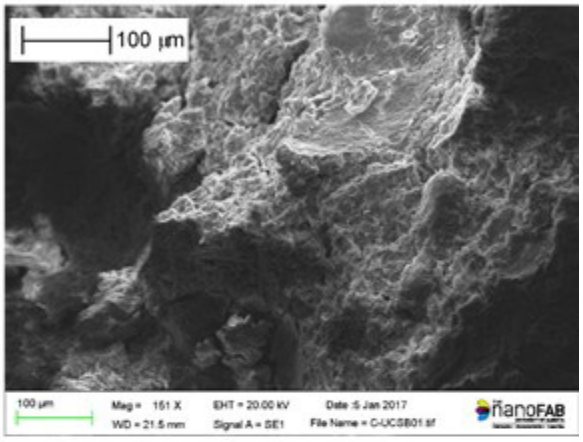

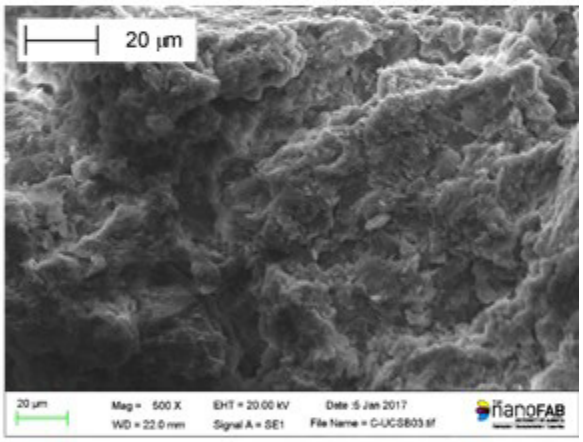

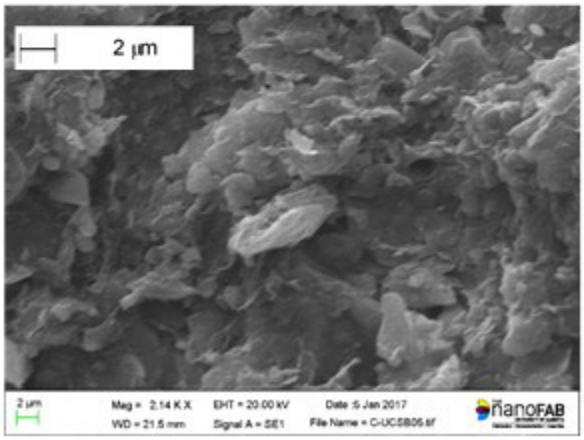

C-0 SEM failure surface (sample c)

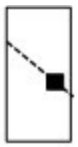

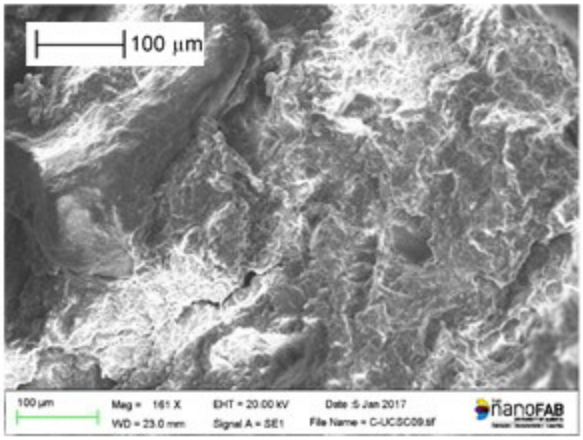

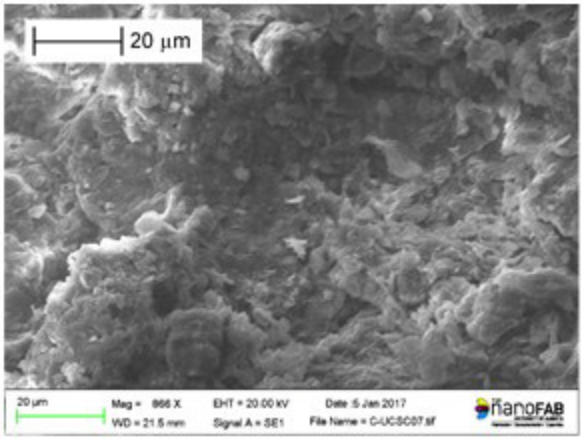

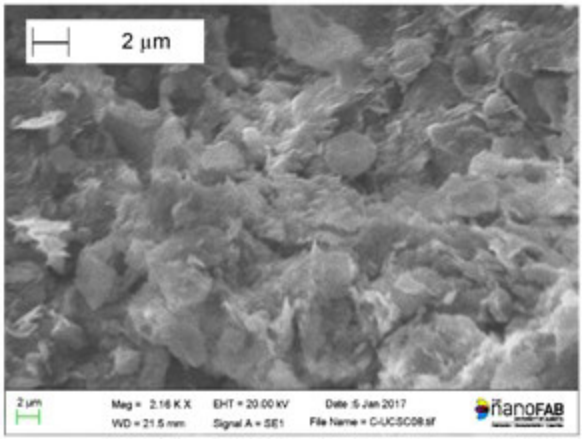

C-0 SEM outer surface (sample a)

C-0 SEM outer surface (sample b)

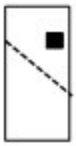

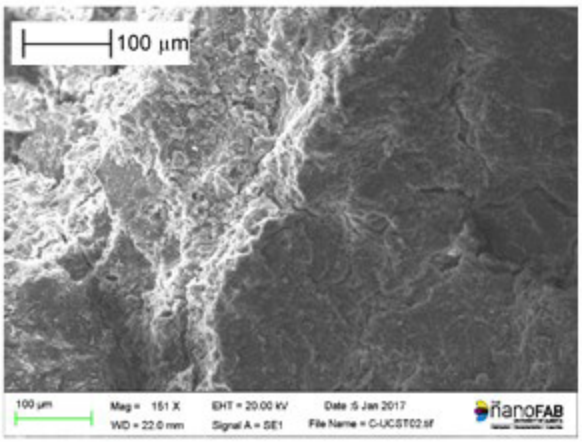

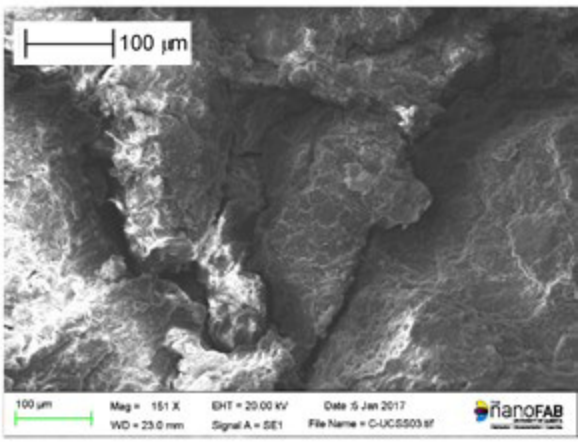

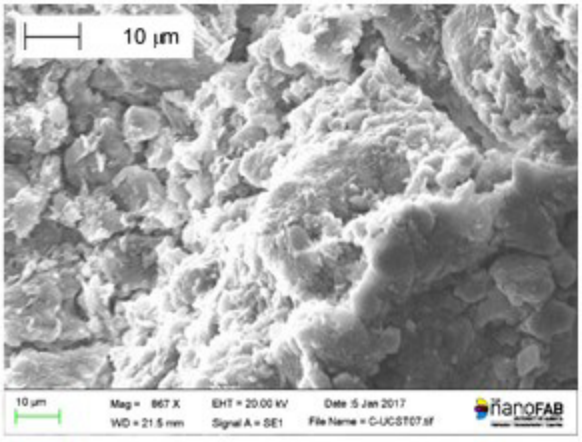

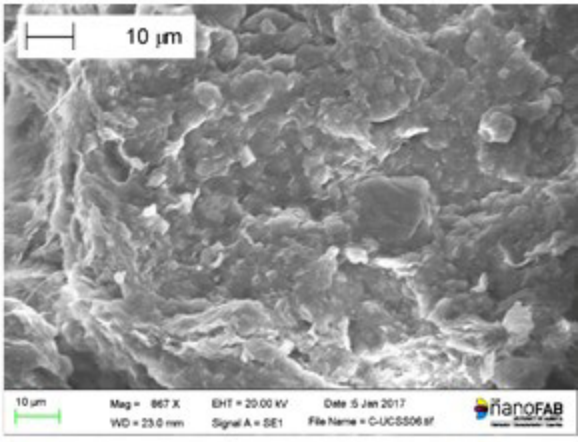

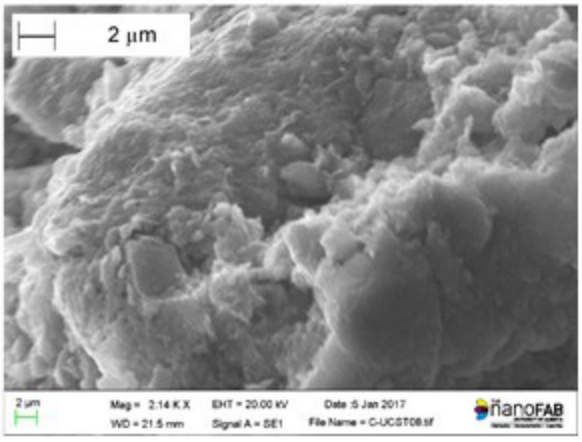

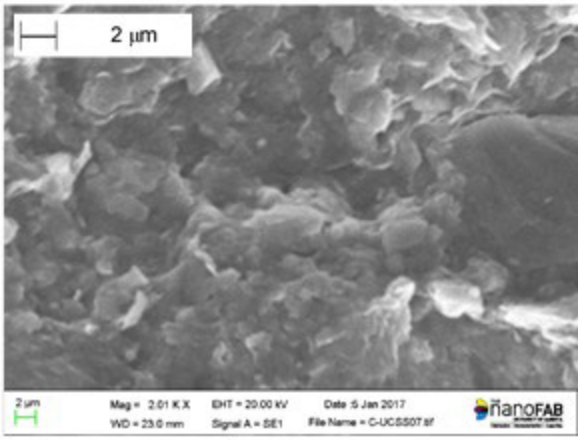

C-500 SEM failure surface (sample a)

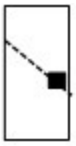

C-500 SEM failure surface (sample b)

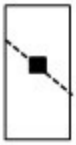

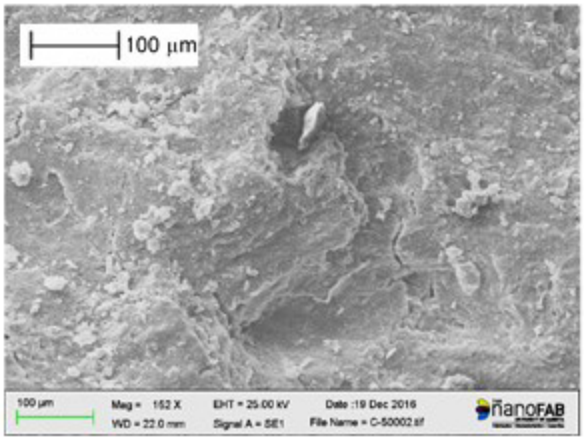

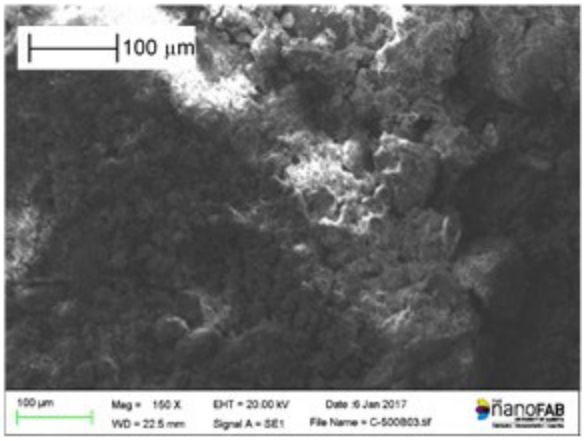

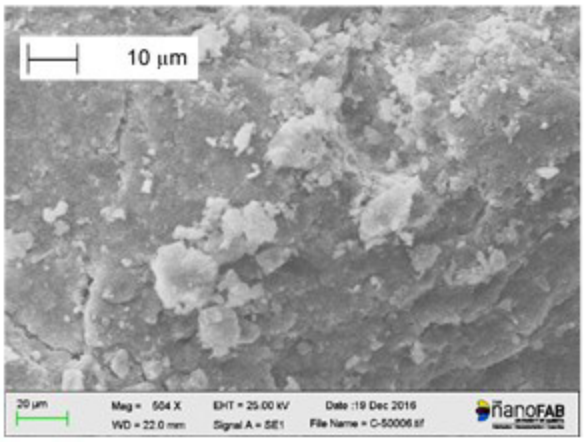

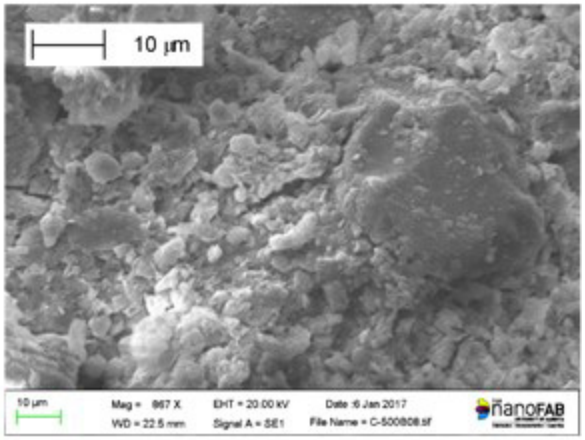

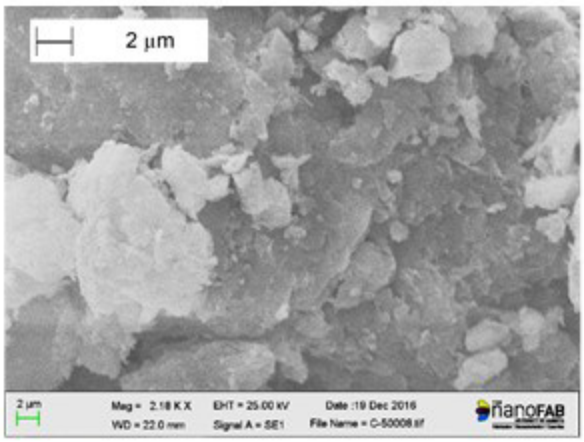

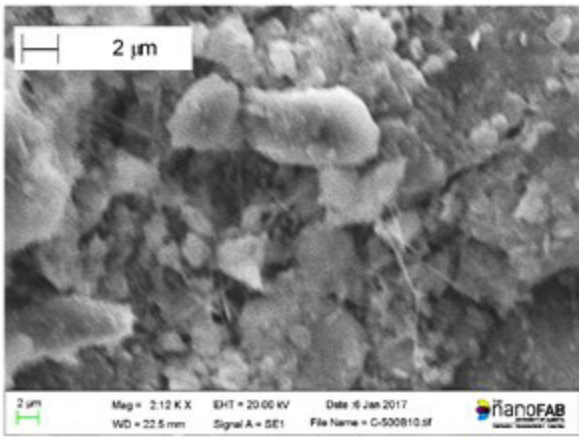

C-500 SEM failure surface (sample c)

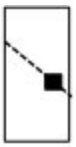

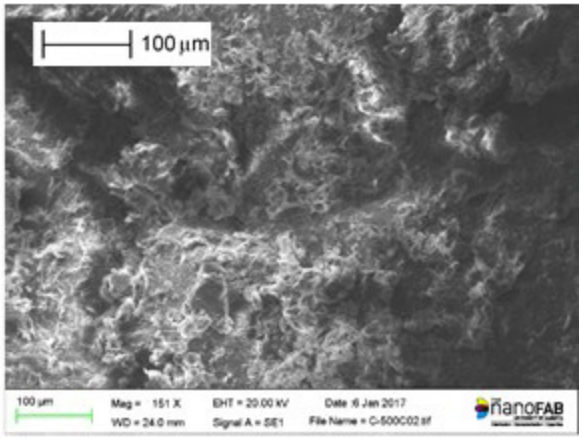

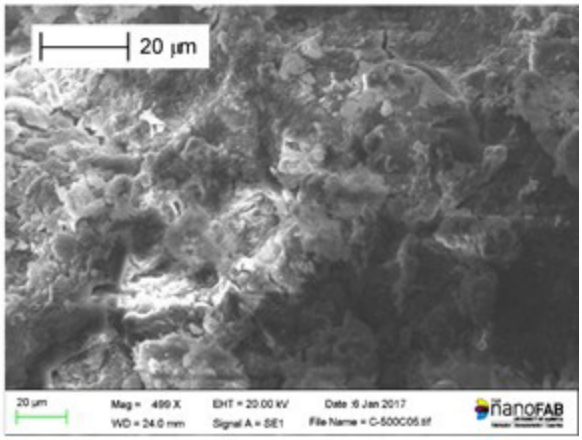

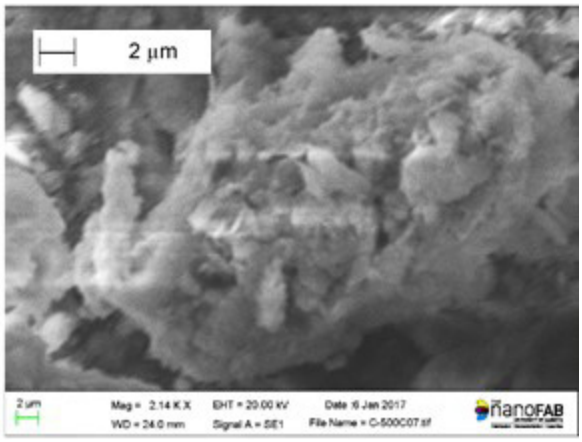

C-500 SEM outer surface (sample a)

C-500 SEM outer surface (sample b)

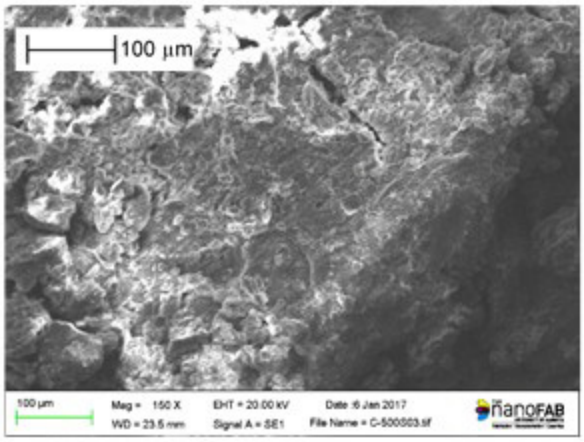

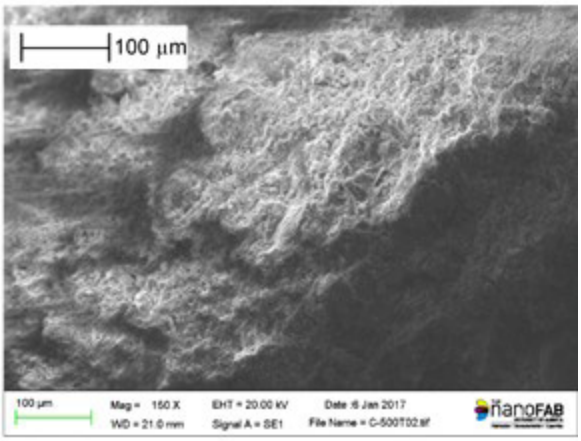

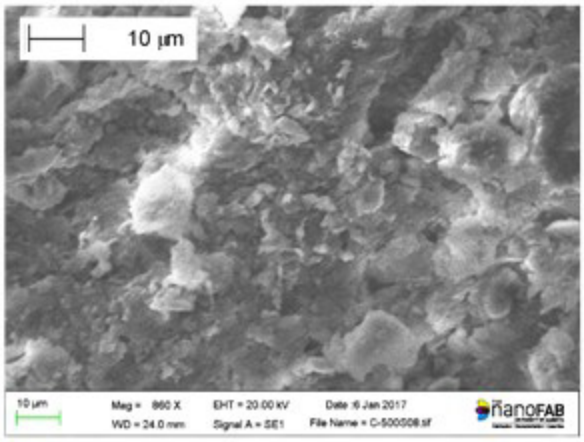

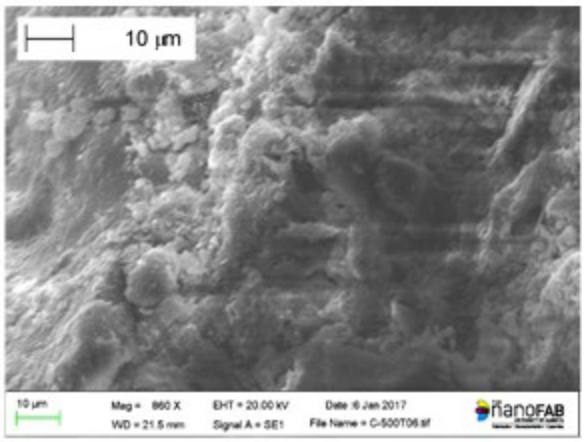

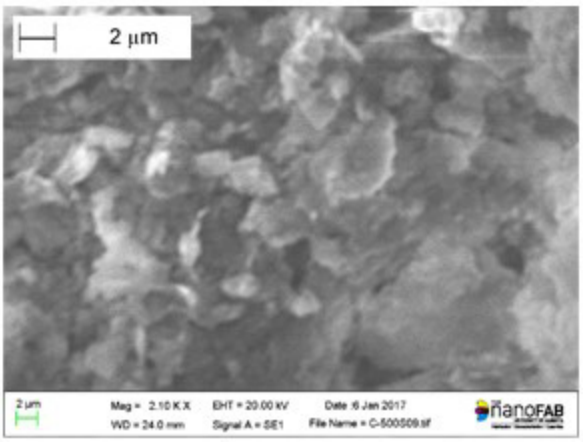

C-3000 SEM failure surface (sample a)

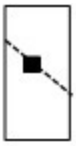

C-3000 SEM failure surface (sample b)

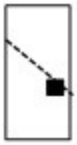

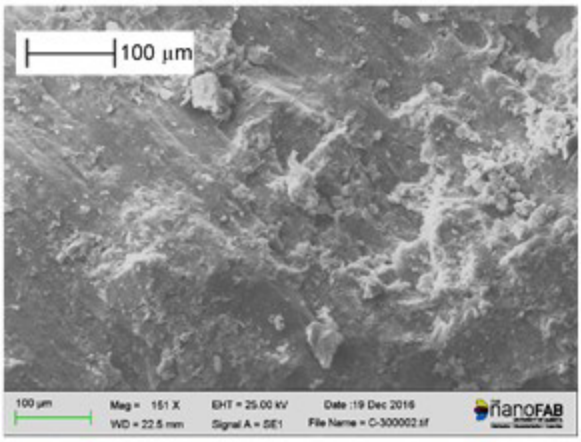

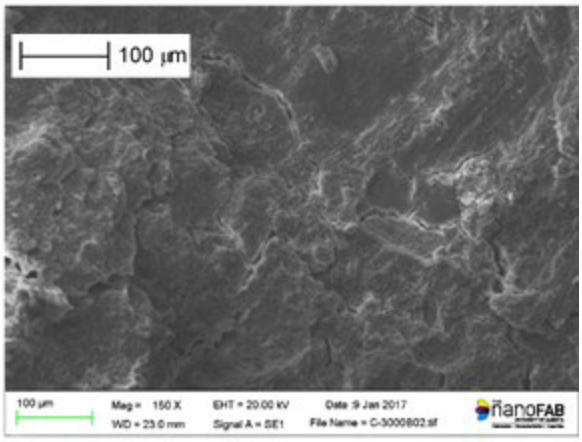

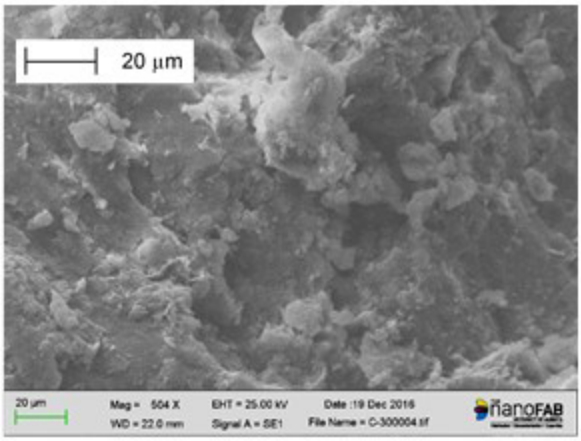

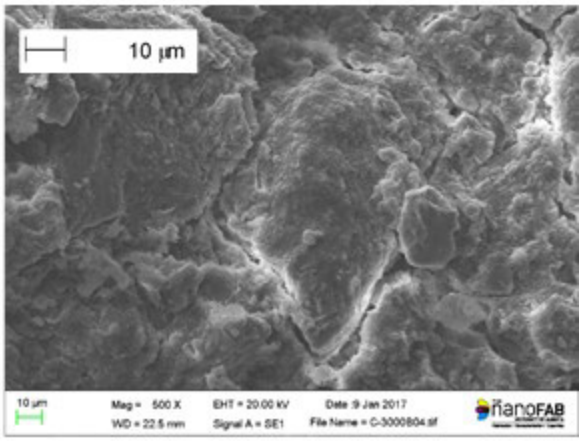

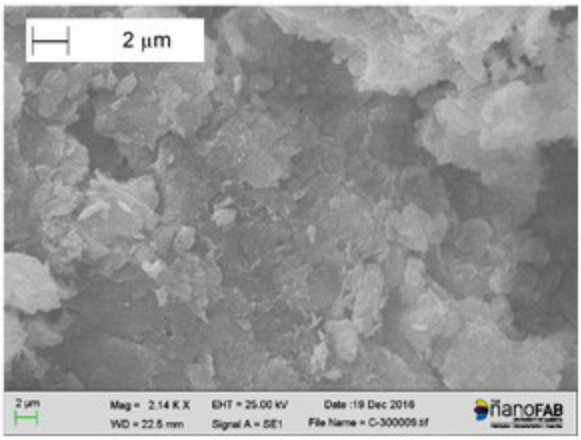

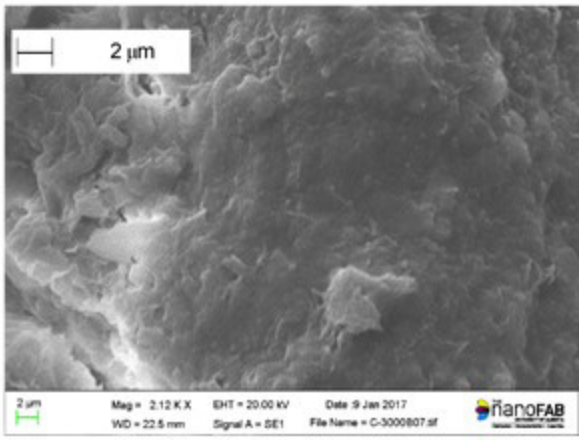

C-3000 SEM failure surface (sample c)

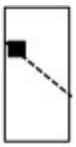

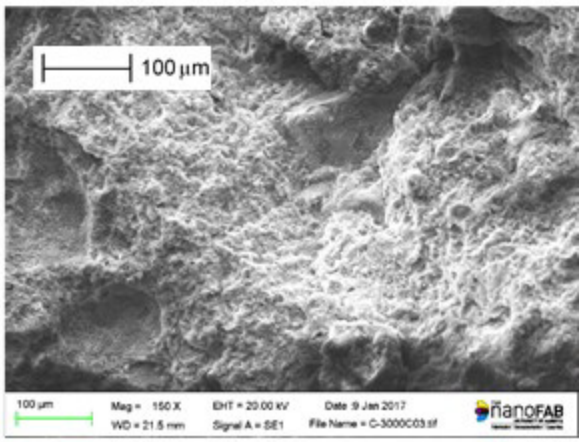

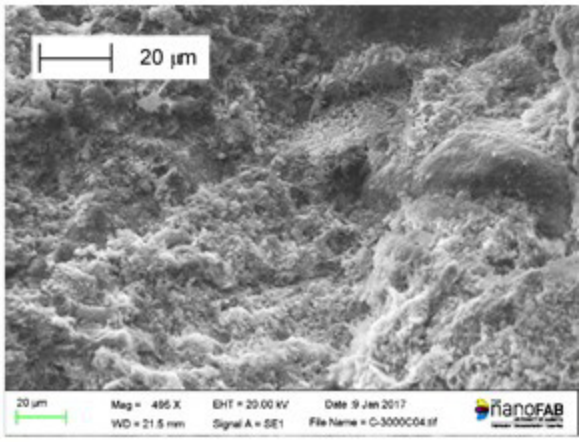

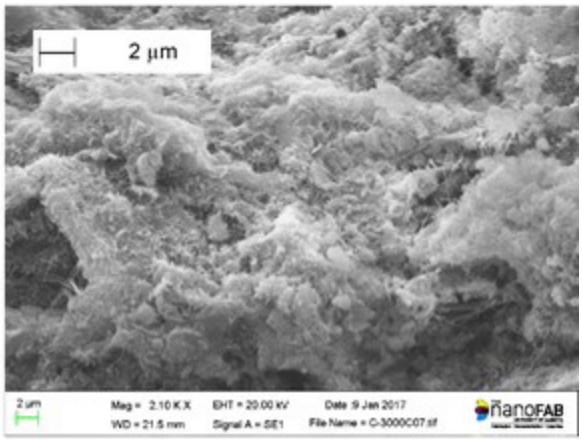

C-3000 SEM outer surface (sample a)

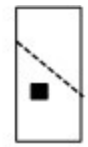

C-3000 SEM outer surface (sample b)

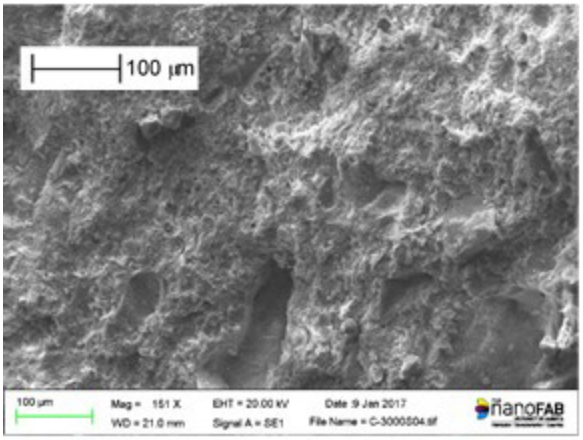

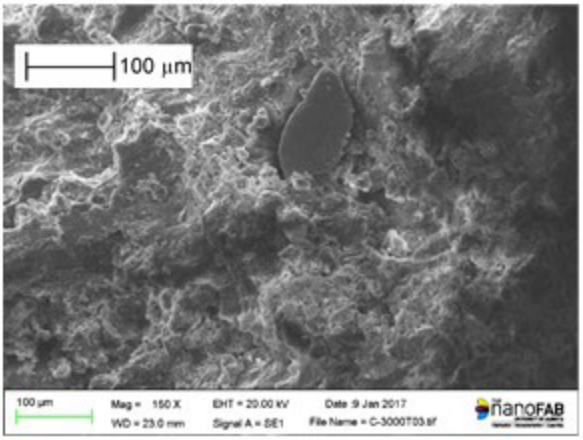

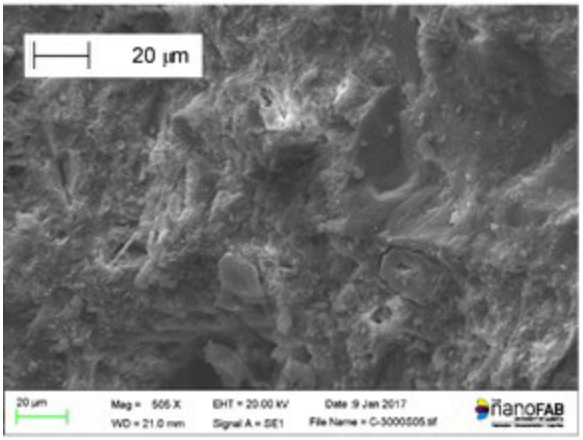

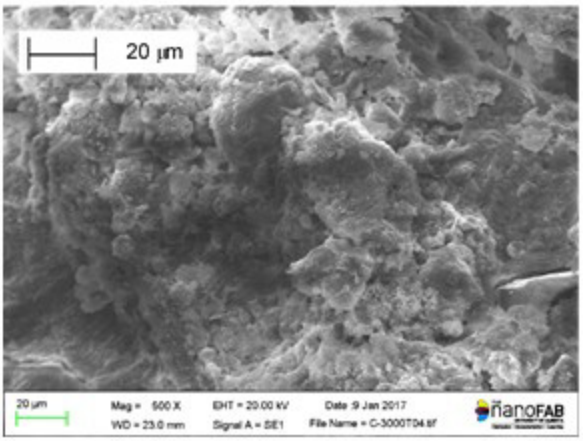

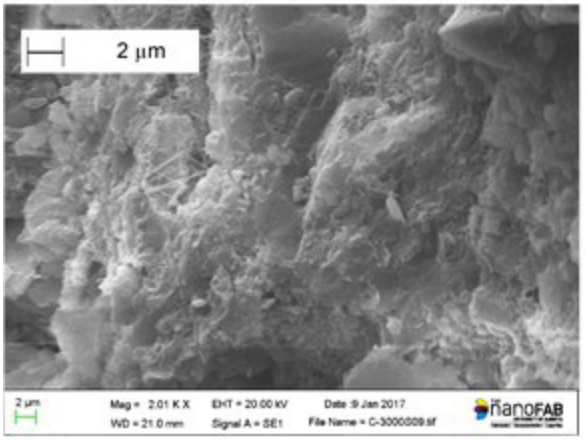

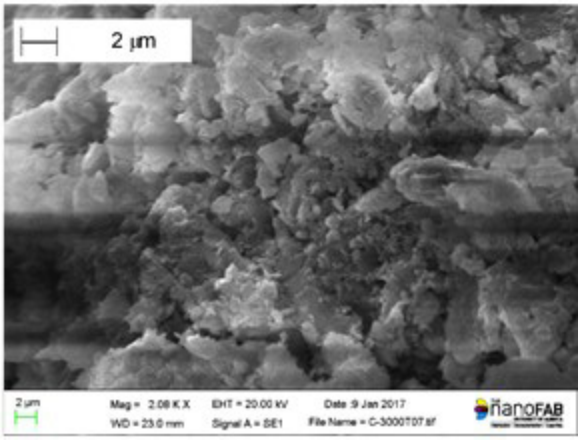

CF-0 SEM failure surface (sample a)

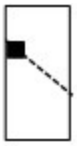

CF-0 SEM failure surface (sample b)

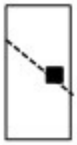

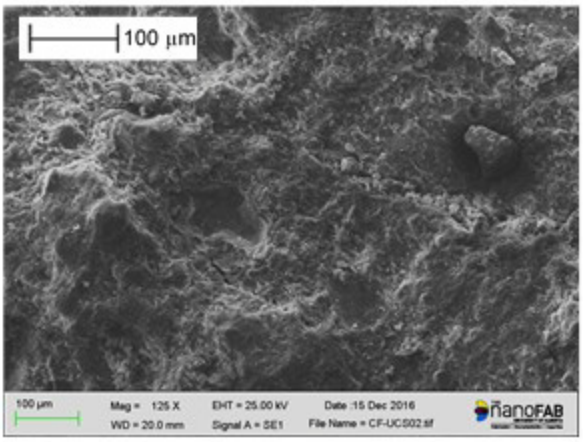

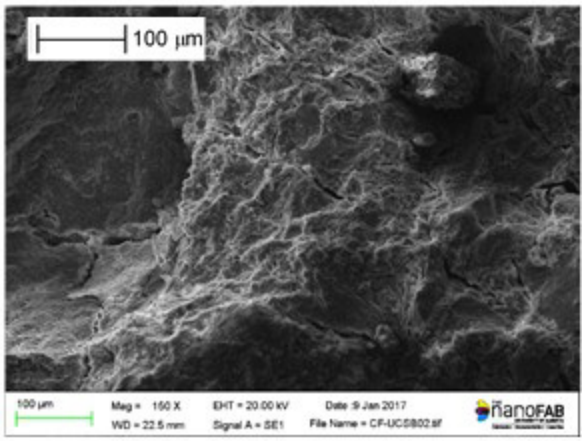

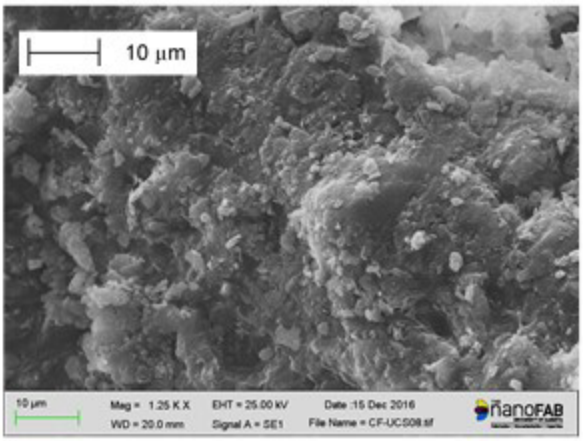

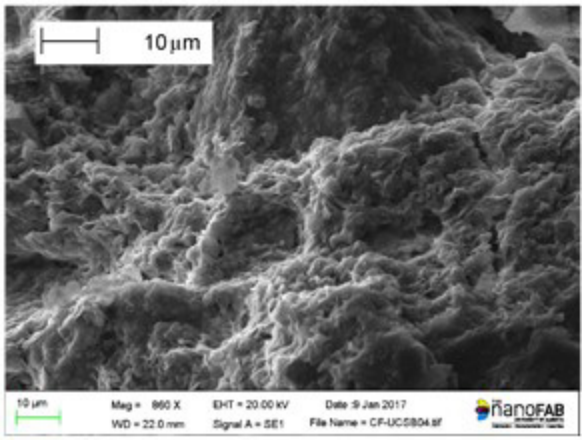

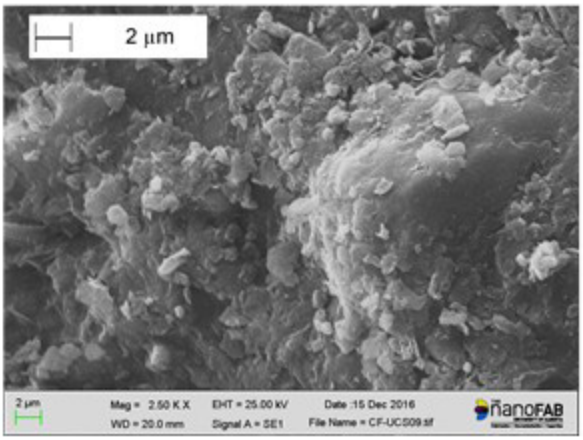

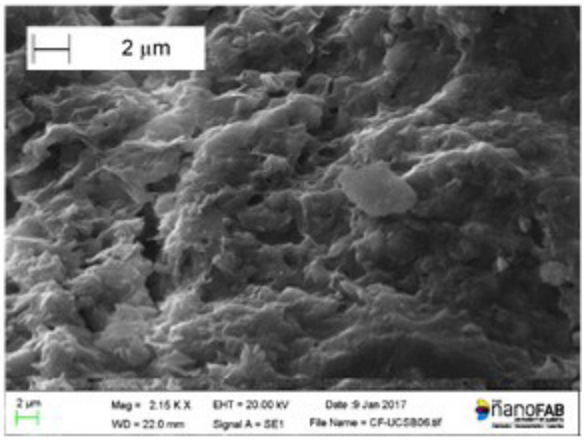

CF-0 SEM failure surface (sample c)

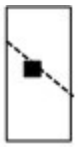

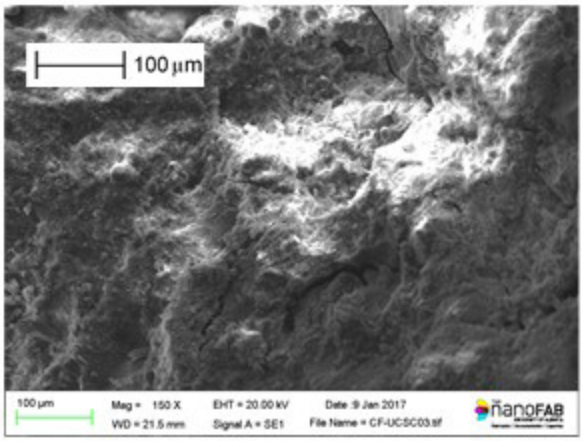

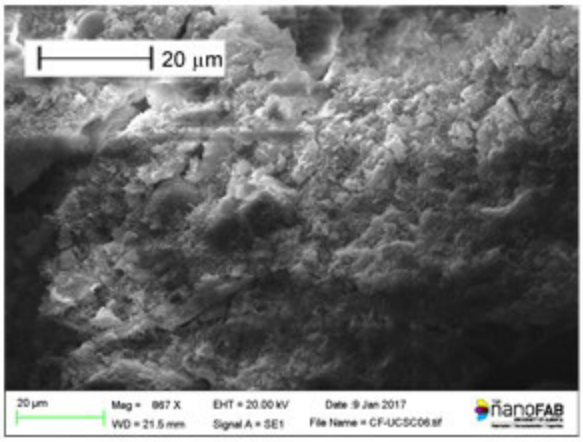

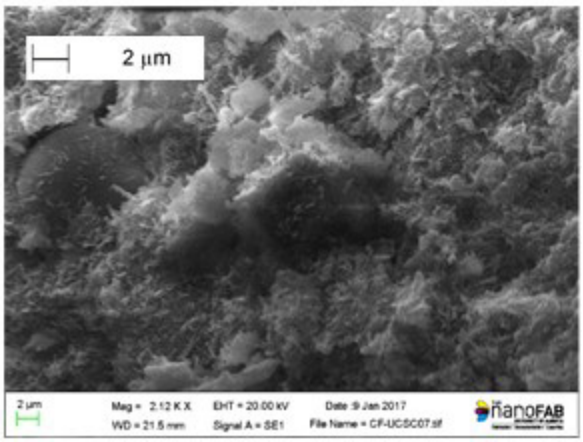

CF-0 SEM outer surface (sample a)

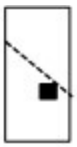

CF-0 SEM outer surface (sample b)

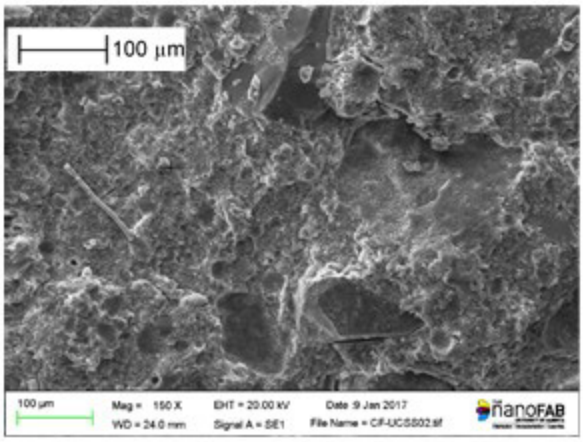

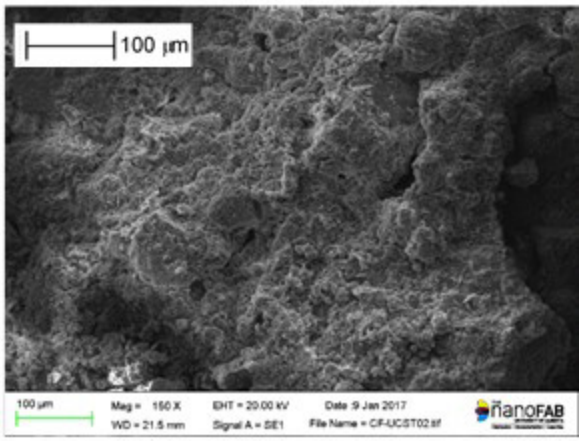

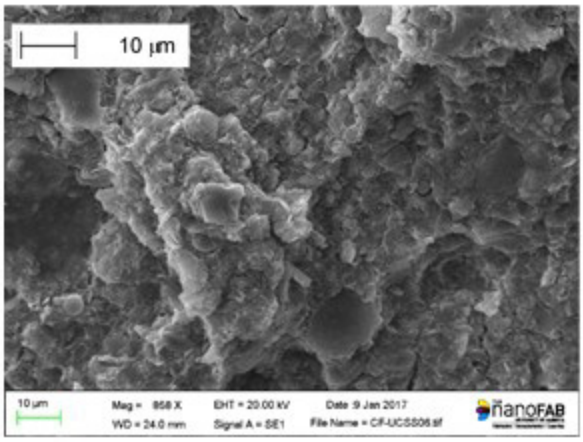

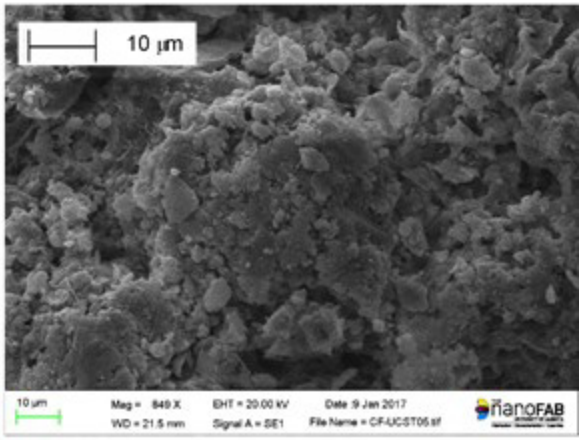

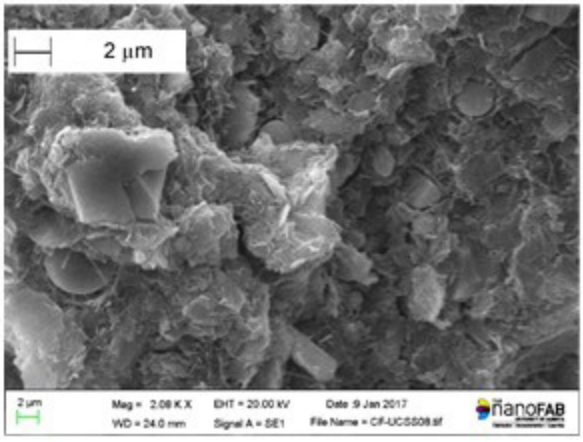

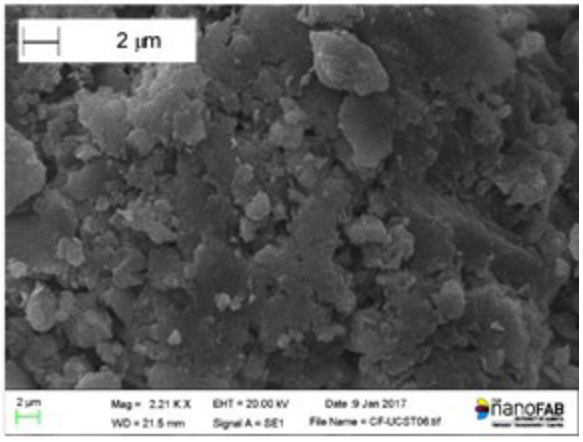

CF-500 SEM failure surface (sample a)

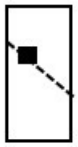

CF-500 SEM failure surface (sample b)

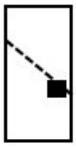

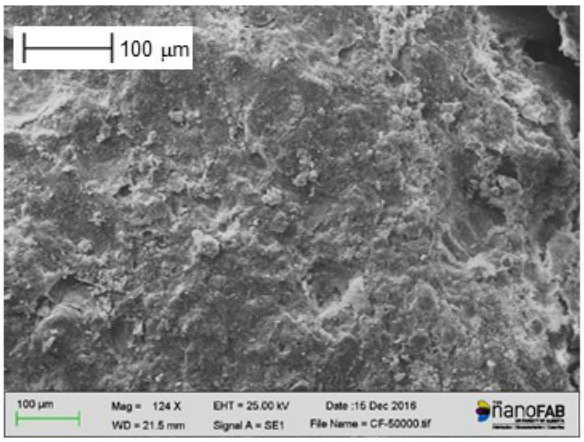

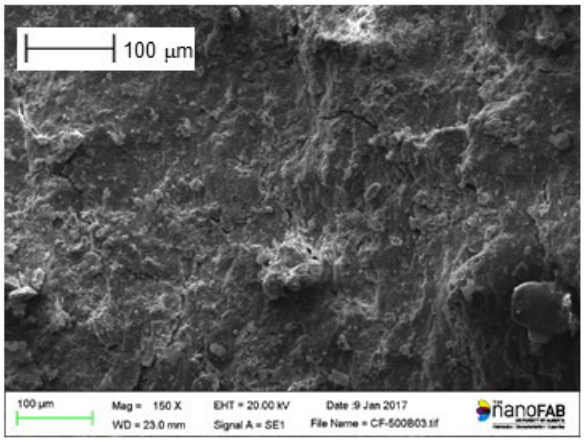

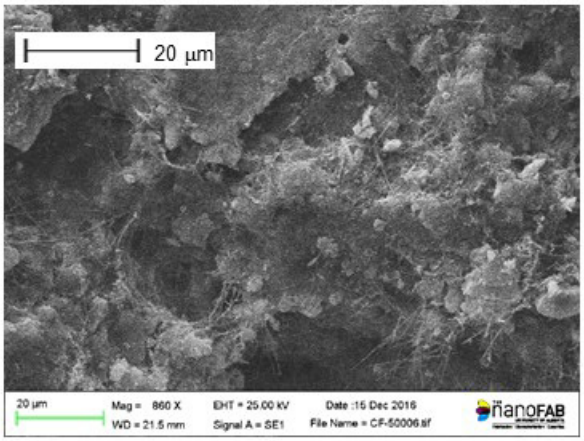

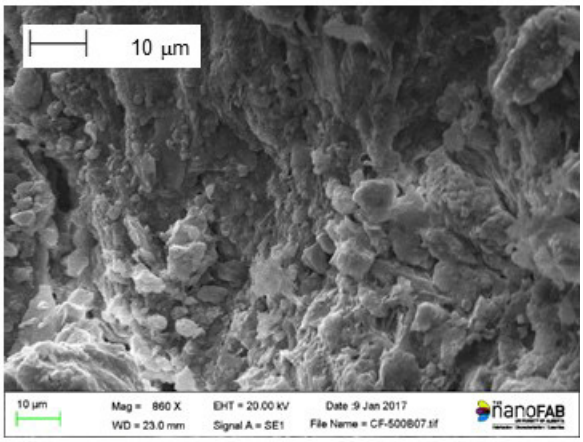

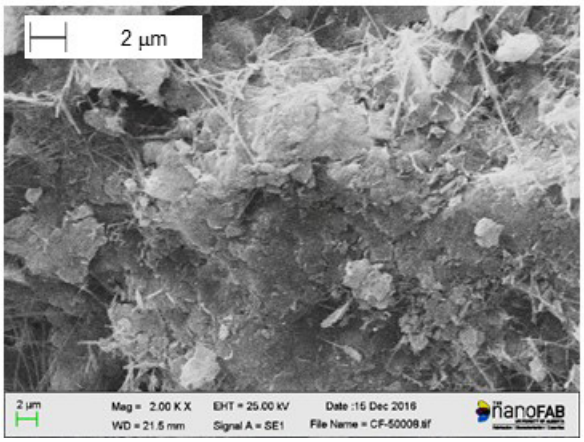

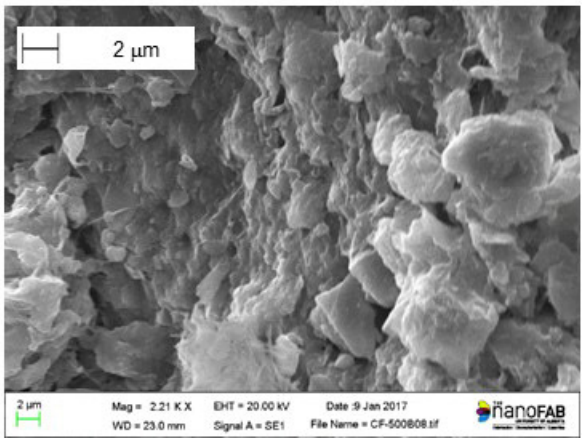

CF-500 SEM failure surface (sample c)

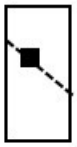

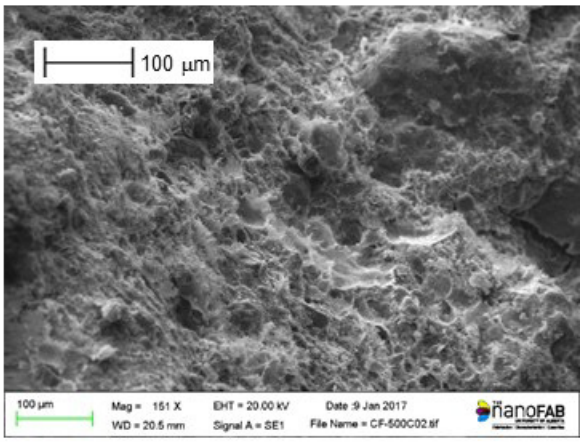

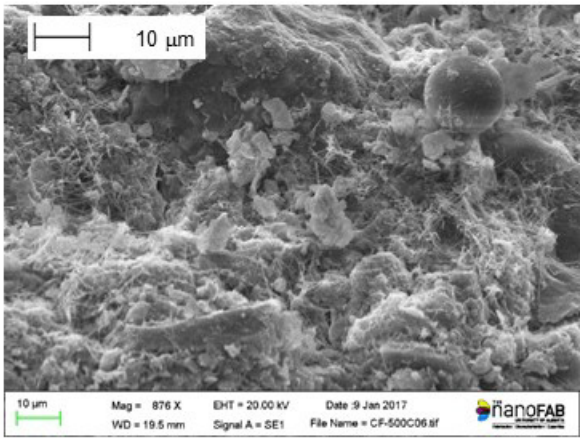

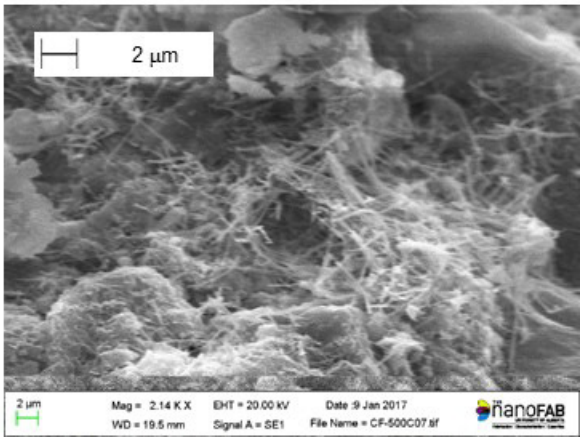

CF-500 SEM outer surface (sample a)

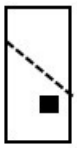

CF-500 SEM outer surface (sample b)

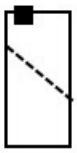

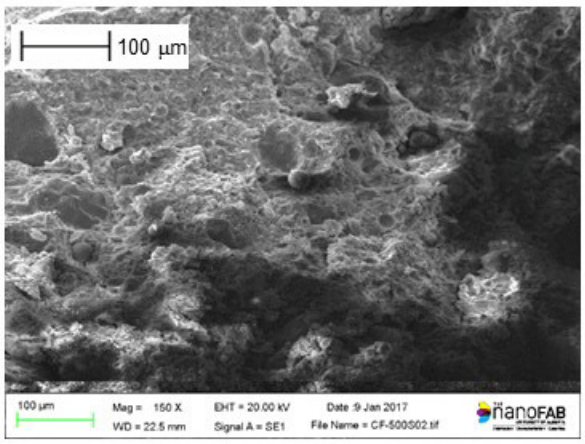

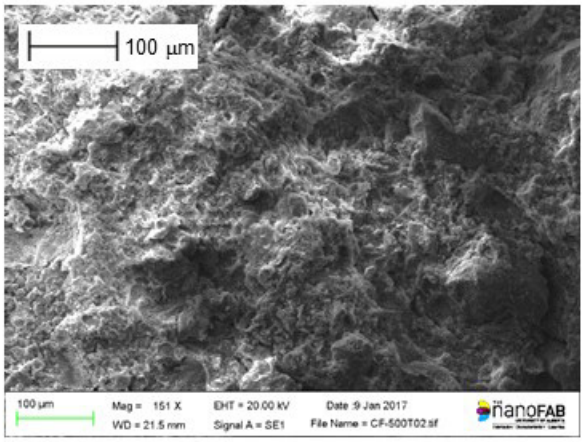

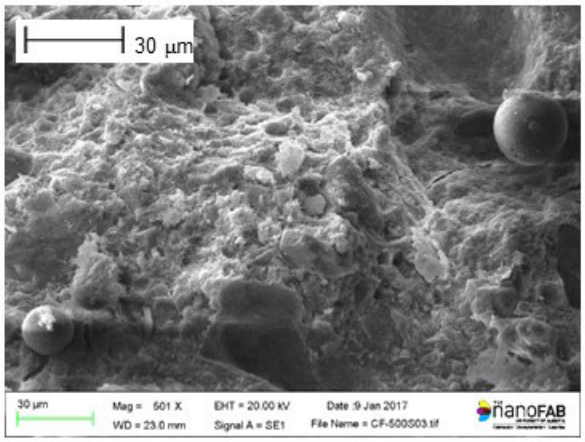

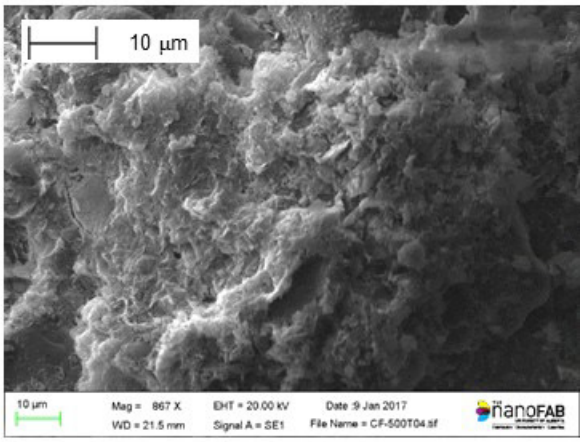

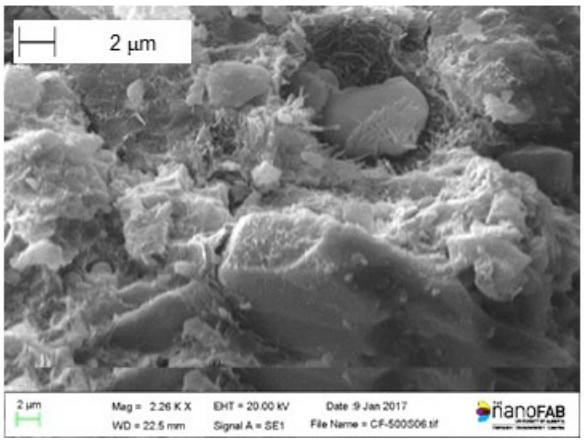

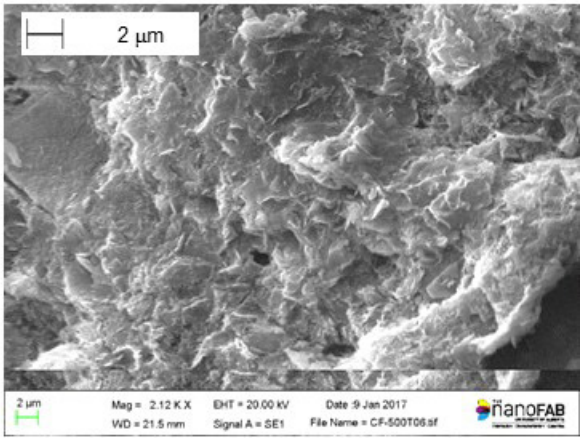

CF-3000 SEM failure surface (sample a)

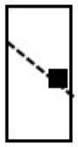

CF-3000 SEM failure surface (sample b)

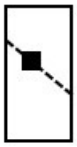

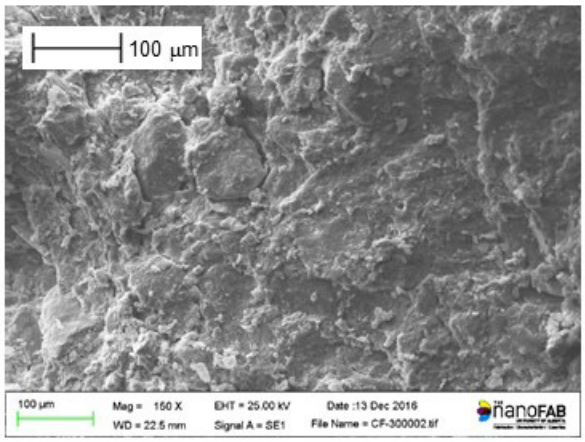

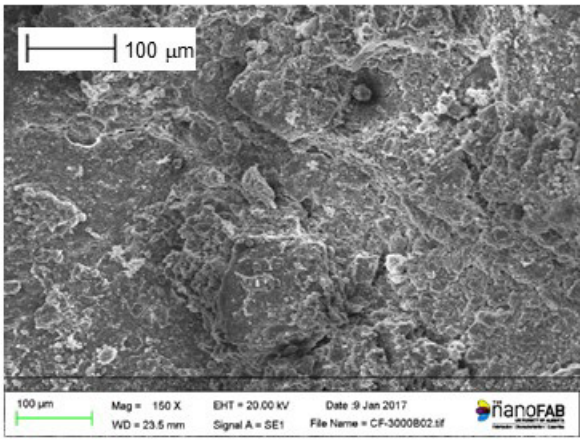

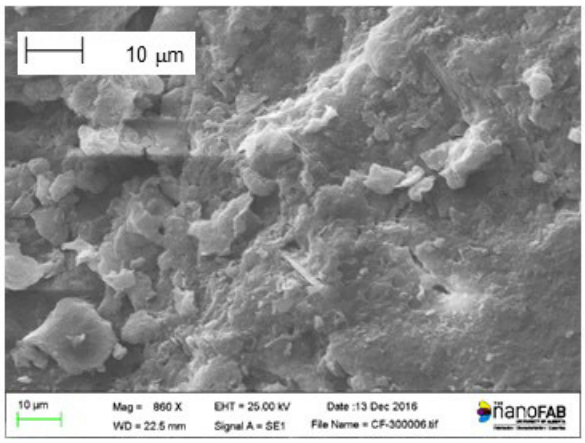

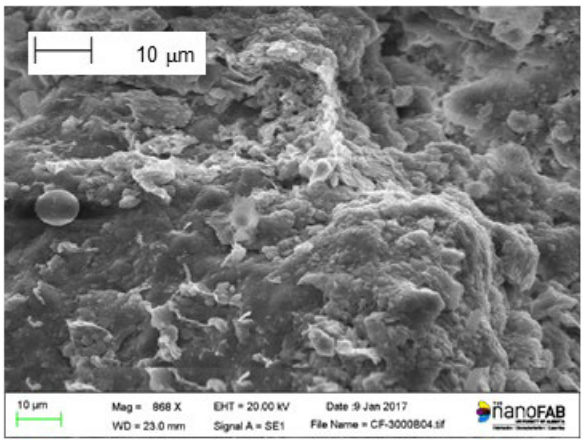

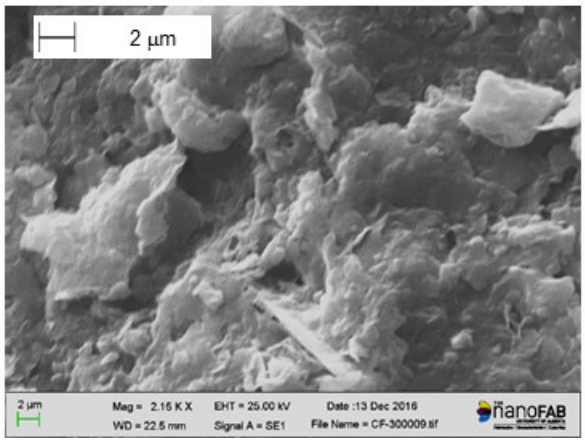

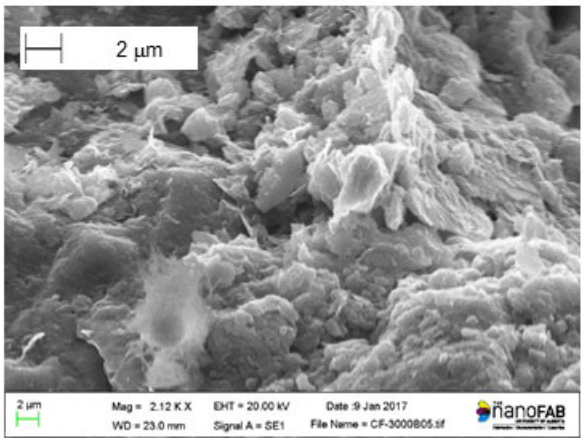

CF-3000 SEM failure surface (sample c)

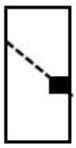

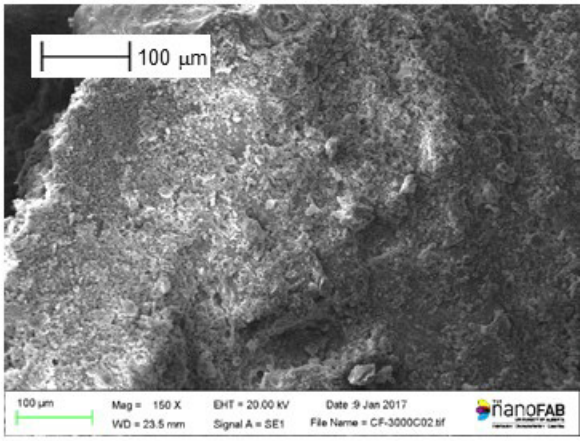

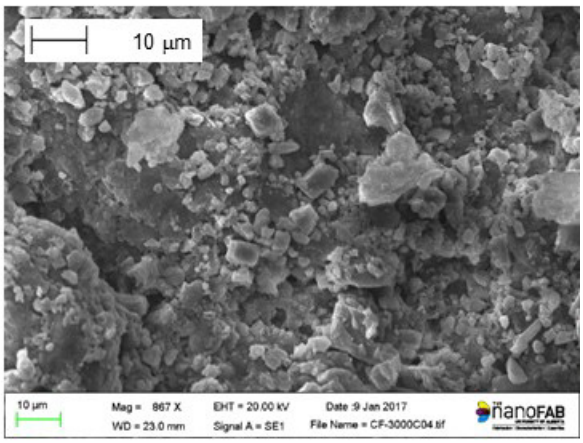

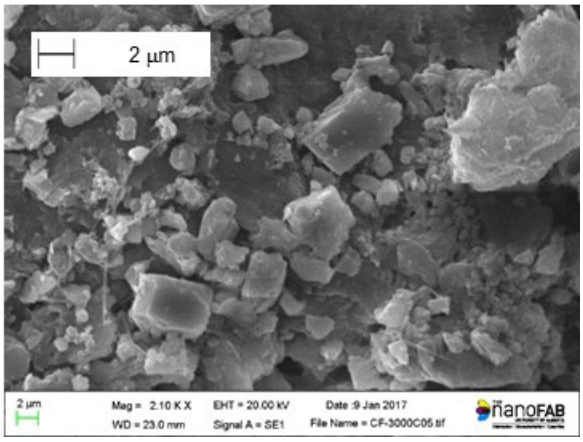

CF-3000 SEM outer surface (sample a)

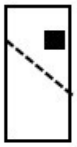

CF-3000 SEM outer surface (sample b)

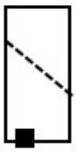

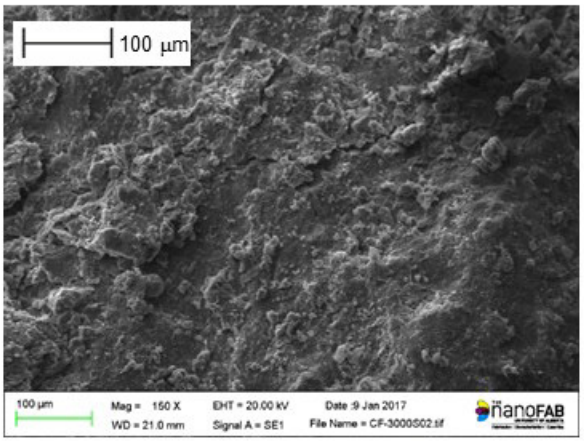

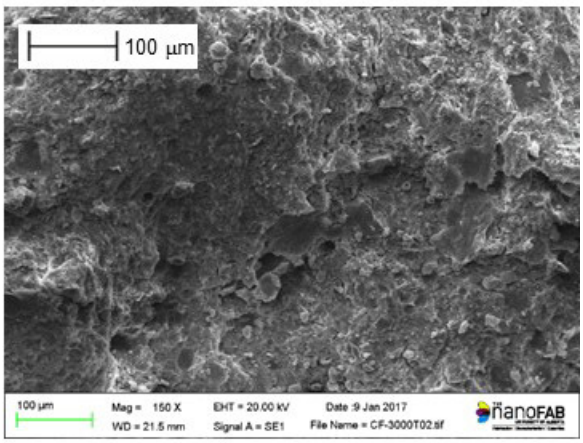

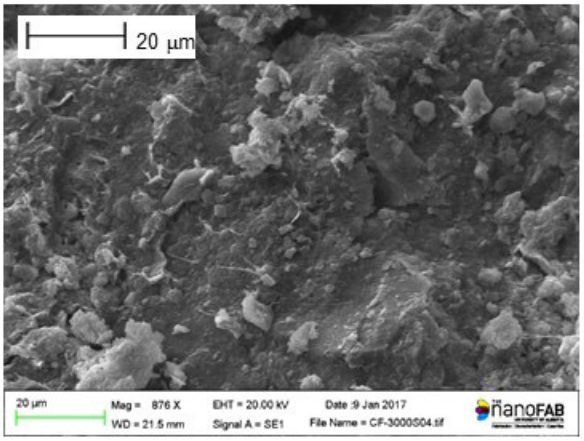

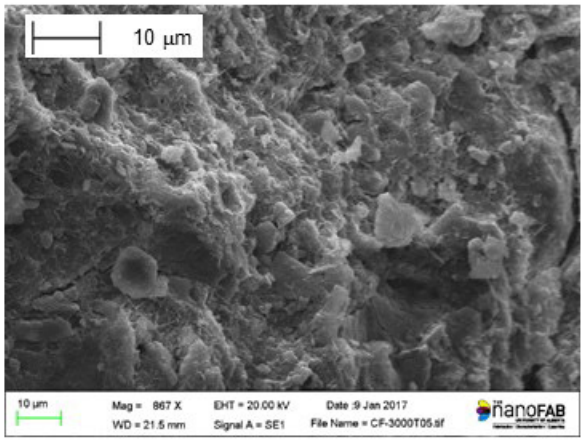

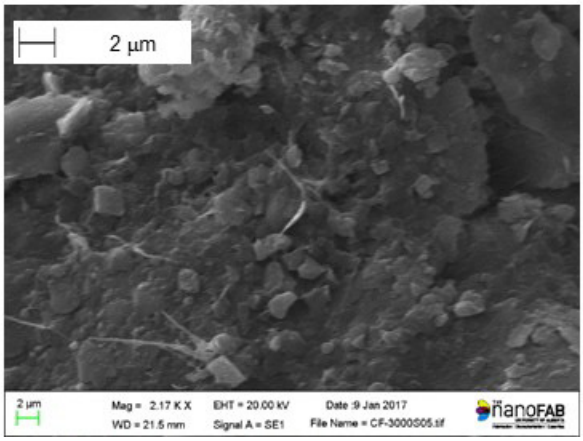

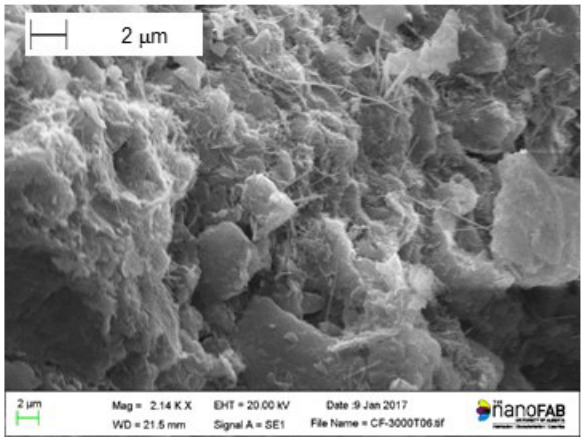

Appendix D. Results of CT scan and report of mercury intrusion porosimetry (MIP) tests.

C-0 CT scan specimen consolidation

Sample ID	CT C-225-0
Confining stress	0 kPa

Height (mm)	Diameter (mm)
149.99	76.03
149.69	77.02
149.87	76.62
	76.65
Average Height	Average Diameter
149.85	76.58 mm
14.99	7.66 cm

Type of test	Iso Consolidation
Specific gravity Gs	2.65
Density	1737.89 kg/m^3
Unit weight	17.05 kN/m^3
Initial mass BT	1199.5 g
Final mass AT	- g
Dry mass	874.62 g
Solids volume	330.05 cm^3

Water content	37.15 %
Volume	690.20 cm^3
Void ratio	1.091
Porosity	0.522
Saturation degree	0.902

Notes:

Intact specimen used for CT scan

Image of sample after test

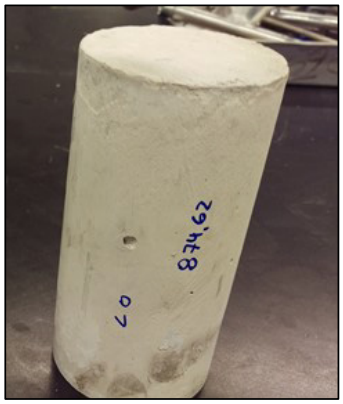

C-0 CT scan image analysis

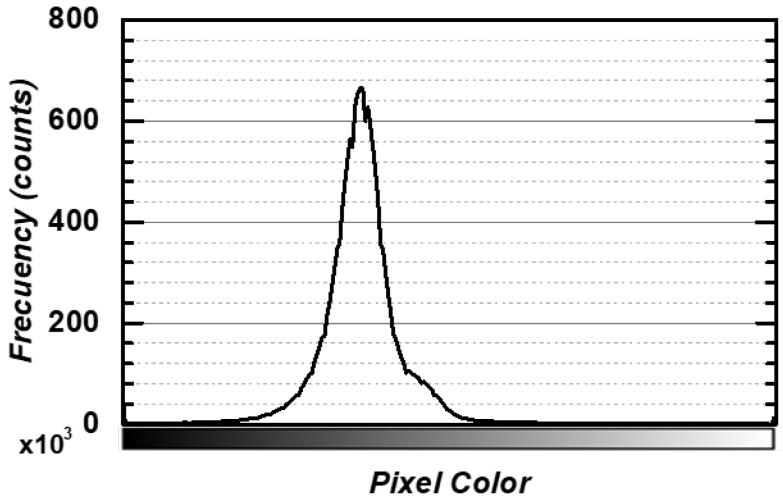

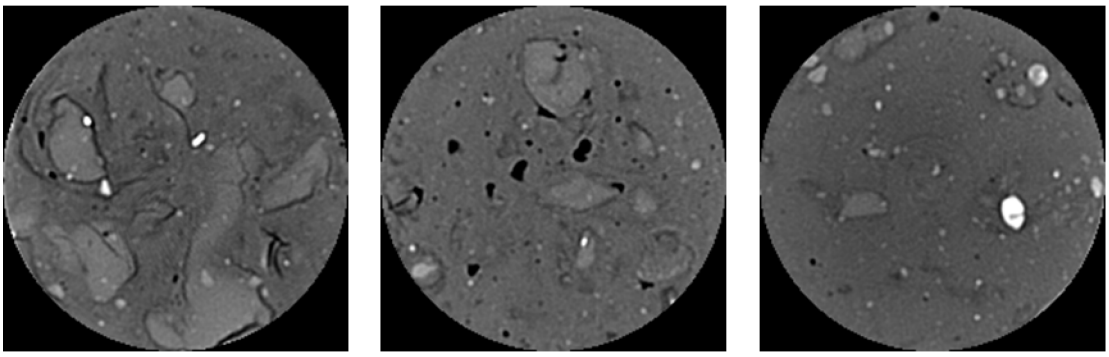

Top slice

Middle slice

Bottom slice

C-500 CT scan specimen consolidation

Sample ID	CT C-225-500
Confining stress	500 kPa

Height (mm)	Diameter (mm)
149.83	76.4
149.8	76.43
149.79	77.06
	77.06

Average Height	Average Diameter	
149.81	76.74	mm
14.98	7.67	cm

Type of test	Iso Consolidation
Specific gravity Gs	2.65
Density	1862.32 kg/m^3
Unit weight	18.27 kN/m^3
Initial mass BT	1290.3 g
Final mass AT	1298.8 g
Dry mass	1057.9 g
Solids volume	399.21 cm^3

B-value	0.70
Volume change	1.896 cm^3

	Trial 1	Trial 2	
Pressure head	20.22	49.11	kPa
Hydraulic gradient	13.76	33.42	m/m
k	2.12E-10	4.31E-10	m/s

	Before test	After test	
Water content	21.97	22.77	%
Volume	692.85	690.95	cm^3
Void ratio	0.736	0.731	
Porosity	0.424	0.422	
Saturation degree	0.791	0.826	

Notes:

Specimen used for CT scan. It was only consolidated to the required pressure. Not sheared with axial displacement. Permeability test was done after saturation and prior to consolidation with different pressure head

Image of sample after test

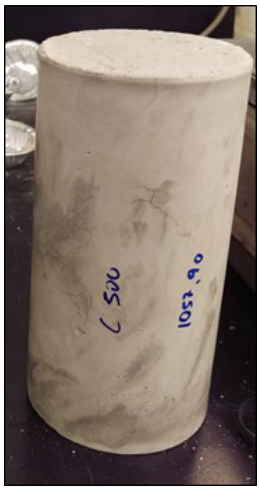

C-500 CT scan image analysis

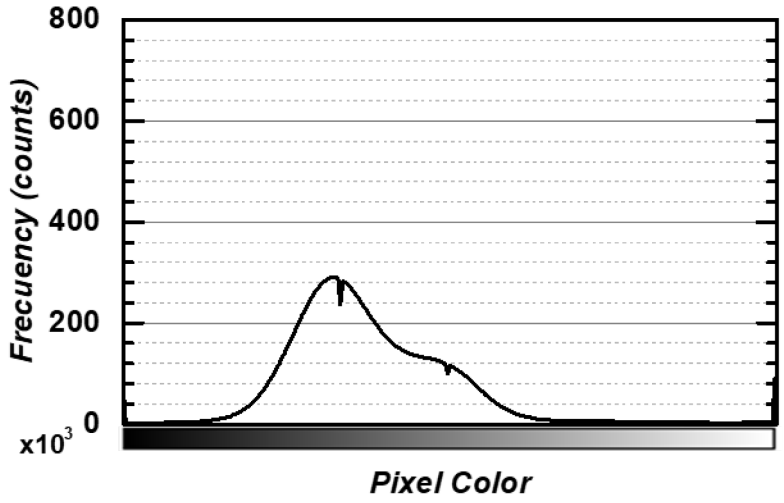

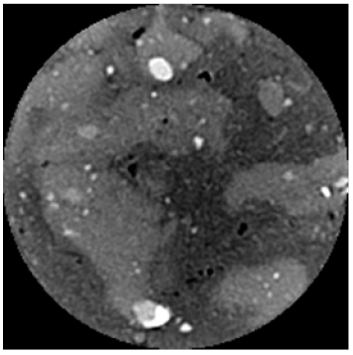

Top slice

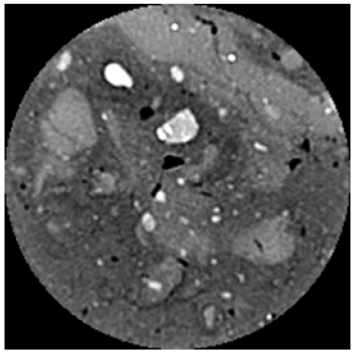

Middle slice

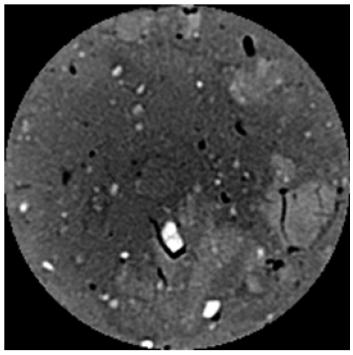

Bottom slice

C-3000 CT scan specimen consolidation

Sample ID	CT C-225-3000
Confining stress	3000 kPa

Height (mm)	Diameter (mm)
150.14	76.49
150.31	76.63
150.31	76.49
	76.42

Average Height	Average Diameter	
150.25	76.51	mm
15.03	7.65	cm

Type of test	Iso Consolidation	
Specific gravity Gs	2.65	
Density	1886.64	kg/m^3
Unit weight	18.51	kN/m^3
Initial mass BT	1303.2	g
Final mass AT	1304.4	g
Dry mass	1065.56	g
Solids volume	402.10	cm^3

B-value	0.78	
Volume change	13.168	cm^3

	Trial 1	Trial 2	
Pressure head	19.60	49.13	kPa
Hydraulic gradient	13.30	33.33	m/m
k	2.47E-10	1.61E-09	m/s

	Before test	After test	
Water content	22.30	22.41	%
Volume	690.75	677.58	cm^3
Void ratio	0.718	0.685	
Porosity	0.418	0.407	
Saturation degree	0.823	0.867	

Notes:

Specimen used for CT scan. It was only consolidated to the required pressure. Not sheared with axial displacement. Permeability test was done after saturation and prior to consolidation with different pressure head

Image of sample after test

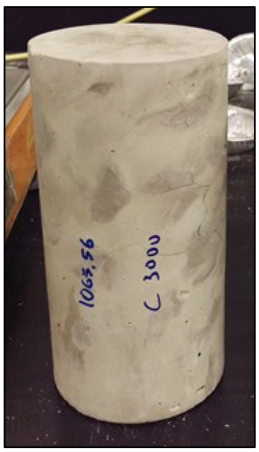

C-3000 CT scan image analysis

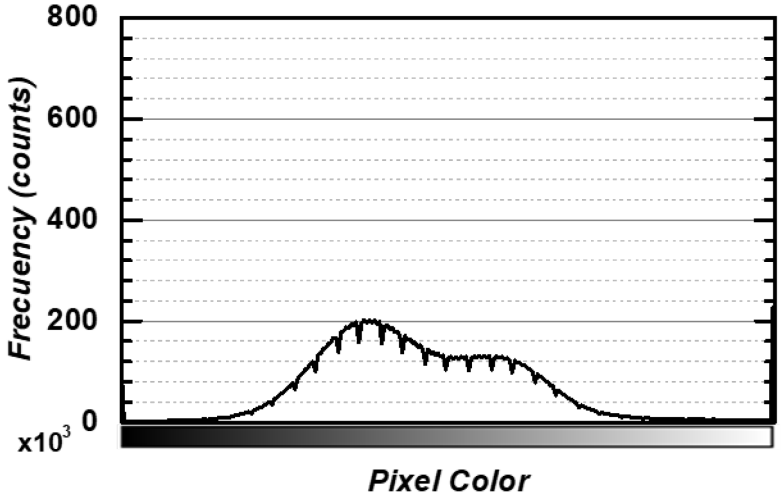

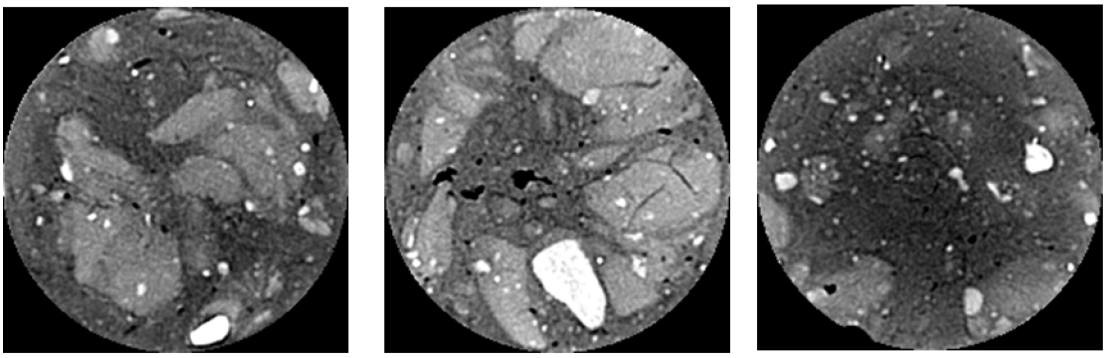

Top slice

Middle slice

Bottom slice

CF-0 CT scan specimen consolidation

Sample ID	CT CF-225-0
Confining stress	0 kPa

Height (mm)	Diameter (mm)
150.48	76.68
150.69	76.78
150.3	76.61
	76.58

Average Height	Average Diameter	
150.49	76.66	mm
15.05	7.67	cm

Type of test	Iso Consolidation	
Specific gravity Gs	2.64	
Density	1809.70	kg/m^3
Unit weight	17.75	kN/m^3
Initial mass BT	1257.1	g
Final mass AT	-	g
Dry mass	964.6	g
Solids volume	365.38	cm^3

Water content	30.32 %
Volume	694.65 cm^3
Void ratio	0.901
Porosity	0.474
Saturation degree	0.888

Notes:

Intact specimen used for CT scan

Image of sample after test

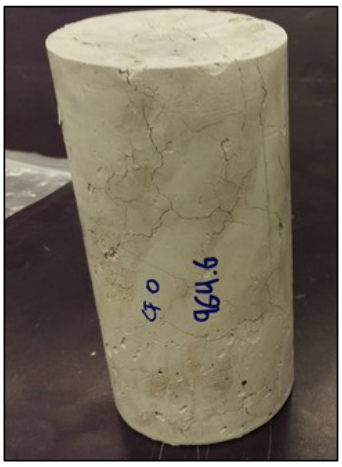

CF-0 CT scan image analysis

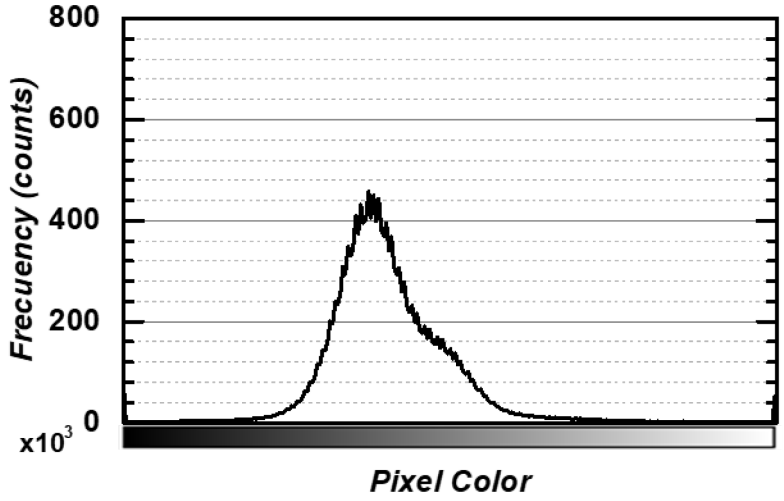

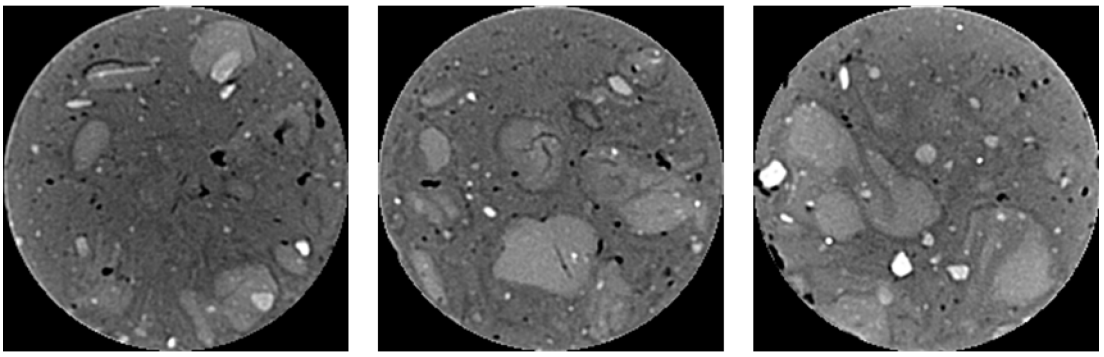

Top slice

Middle slice

Bottom slice

CF-500 CT scan specimen consolidation

Sample ID	CT CF-225-500
Confining stress	500 kPa

Height (mm)	Diameter (mm)
150.63	75.92
150.59	75.01
150.41	76.31
	76.38

Average Height	Average Diameter	
150.54	75.91	mm
15.05	7.59	cm

Type of test	Iso Consolidation
Specific gravity Gs	2.64
Density	1825.23 kg/m^3
Unit weight	17.91 kN/m^3
Initial mass BT	1243.4 g
Final mass AT	1254.8 g
Dry mass	1017.14 g
Solids volume	385.28 cm^3

B-value	0.70
Volume change	2.46 cm^3

	Trial 1	Trial 2	
Pressure head	19.88	48.37	kPa
Hydraulic gradient	13.48	32.79	m/m
k	1.80E-10	3.50E-08	m/s

	Before test	After test	
Water content	22.24	23.37	%
Volume	681.23	678.77	cm^3
Void ratio	0.768	0.762	
Porosity	0.434	0.432	
Saturation degree	0.765	0.810	

Notes:

Specimen used for CT scan. It was only consolidated to the required pressure. Not sheared with axial displacement. Permeability test was done after saturation and prior to consolidation with different pressure head

Image of sample after test

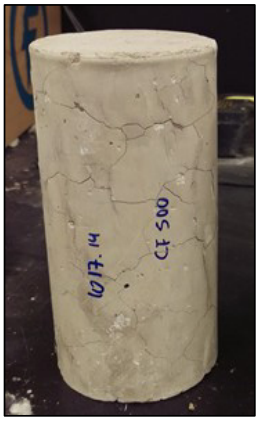

CF-500 CT scan image analysis

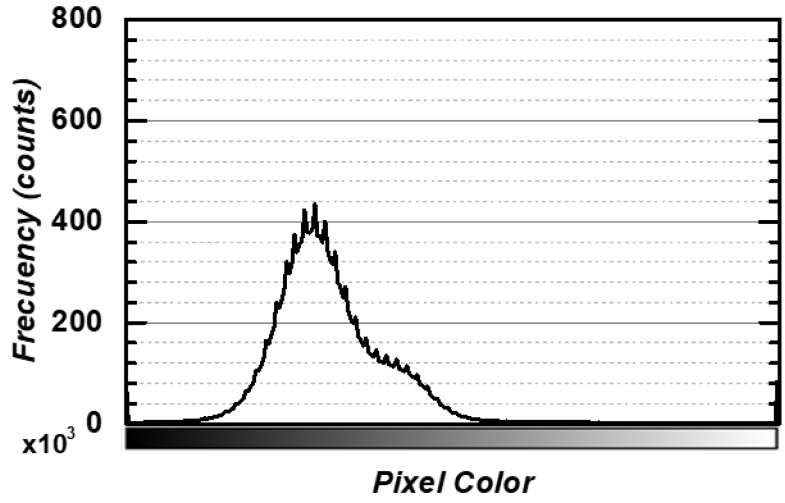

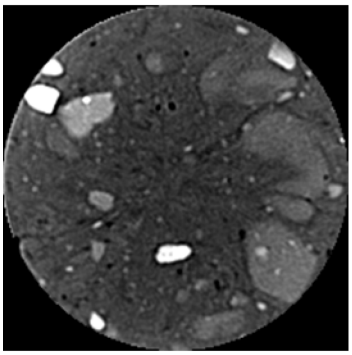

Top slice

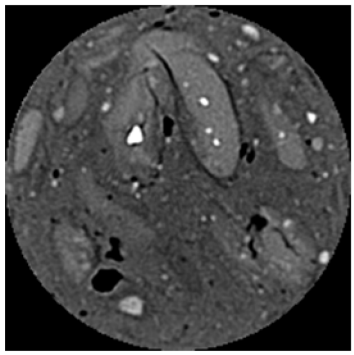

Middle slice

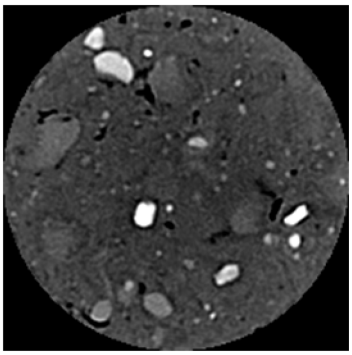

Bottom slice

CF-3000 CT scan specimen consolidation

Sample ID	CT CF-225-3000
Confining stress	3000 kPa

Height (mm)	Diameter (mm)
149.99	76.19
150.31	76.87
150.13	76.48
	76.54

Average Height	Average Diameter	
150.14	76.52	mm
15.01	7.65	cm

Type of test	Iso Consolidation
Specific gravity Gs	2.64
Density	1776.18 kg/m^3
Unit weight	17.42 kN/m^3
Initial mass BT	1226.4 g
Final mass AT	1224 g
Dry mass	985.6 g
Solids volume	373.33 cm^3

B-value	0.70
Volume change	21.252 cm^3

	Trial 1	Trial 2	
Pressure head	19.23	49.23	kPa
Hydraulic gradient	13.05	33.42	m/m
k	9.76E-10	8.31E-10	m/s

	Before test	After test	
Water content	24.43	24.19	%
Volume	690.47	669.22	cm^3
Void ratio	0.849	0.793	
Porosity	0.459	0.442	
Saturation degree	0.759	0.806	

Notes:

Specimen used for CT scan. It was only consolidated to the required pressure. Not sheared with axial displacement. Permeability test was done after saturation and prior to consolidation with different pressure head

Image of sample after test

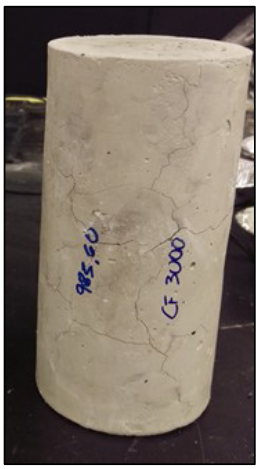

CF-3000 CT scan image analysis

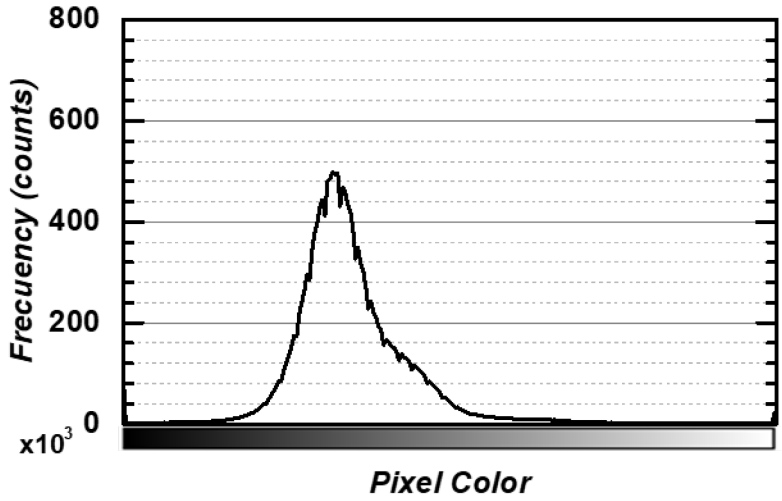

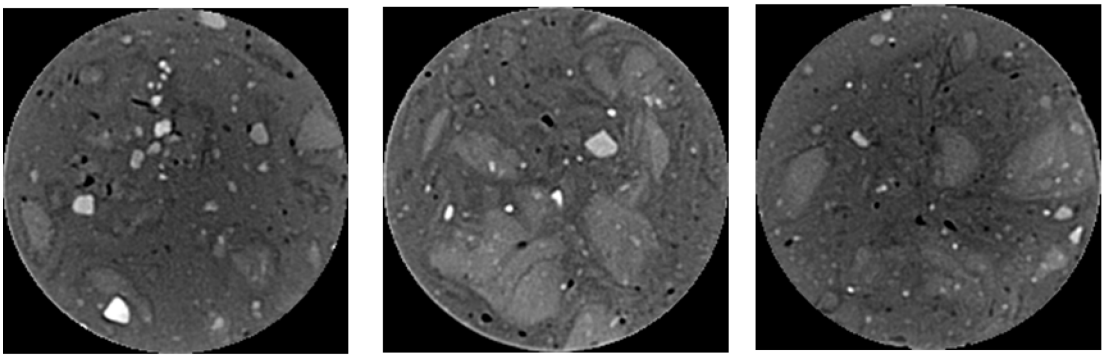

Top slice

Middle slice

Bottom slice

Mercury intrusion porosimetry summary report for soilcrete specimen samples

1. Objective

The following document summarizes the procedure and results for MIP tests conducted at the Energy Systems Design Laboratory at the University of Alberta. The soilcrete specimen C-0 was used for the CT scan analysis and samples from the top and bottom sections of the specimens were selected to conduct the MIP test.

2. Parameters

The following constants are needed for calculations:

• ρ_{Hg}, the density of mercury at room temperature and pressure: 13:5 g/cm^3

•γ, the surface tension of mercury on the sample material at room temperature and pressure: 480 dyne/cm^{-1}

• θ, the contact angle of mercury on the sample material at room temperature and pressure: 140°

3. Procedure and Theory

Porosimetry tests were performed using a PoreMaster 33 Mercury Porosimeter manufactured by Quantachrome Instruments.

The soilcrete specimen was dried in an oven overnight after performing the CT scan. Two samples were carved directly from the top and bottom section of the soilcrete specimen. The samples were carved with a square section, at least 1 cm long on each side, and approximately 0.5 to 1 cm thickness.

To perform the mercury intrusion tests, the sample was placed inside the bulb of a glass penetrometer cell with 0.5 cc stem volume. The penetrometer cell was evacuated to an absolute pressure of 0.004 psi and then further evacuated for 30 min. The cell was filed with mercury and the mercury was then pressurized, up to a maximum pressure of 33000 psi. The change in volume of mercury was measured as the pressure was raised. A plot of the cumulative amount of volume intruded at each step, plotted against the pressure at each step, given the cumulative

intruded volume curve. The volume is normalized with respect to the total intruded volume to allow comparison between multiple samples of differing volume.

3.1 Pore Size Distribution

The pressure at which intrusion occurs can be related to the presence of pores within the sample using the Washburn equation:

$$Pr = -2\gamma cos(\theta) \quad [1]$$

where P is the applied pressure, r is the pore radius,γ is the surface tension of mercury and θ is the contact angle between the mercury and the sample material.

The logarithmic pore size distribution, for a given pressure P_i normalized with respect to total sample volume, is calculated using the following equation:

$$\frac{DX}{D(ln(P))} = \frac{(V_i - V_{i-1})/V_{pore}}{ln(P_i) - ln(P_{i-1})} \quad [2]$$

where V_i is the absolute intruded volume measured up to pressure P_i, and V_{pore} is the total measured intruded volume.

DX is the volume of the pores ΔV intruded at radius r divided by the total pore volume of the entire sample V_{pore}. In this way, X represents the pore volume of each pore size normalized with respect to the total pore volume. The value X is used rather than ΔV so that when multiple tests are done with different sample volumes, the tests can be directly compared.

Note that, because smaller pores contain significantly less volume than larger ones, we need to adjust the pore size distribution graph to make the smaller pores in the sample more visible. To do this, we use ln(r) instead of r for the above graph, and we use a log scale for the x axis. This allows us to see more clearly the areas we are most interested in (i.e. those pores of 10 um or smaller).

3.2 Density and Porosity Calculations

There are three distinct values for density and porosity that can be found for a given sample: bulk, particle and true. The following section will explain the difference between each type and the calculations used to find it. Before discussion of the calculations of density and porosity, some terms must be defined:

• Interparticle Void Space: Void space formed between individual particles of a bulk material. This value may vary signi_cantly depending on the handling of the material. For instance, interparticle void space can be reduced by manually compressing the material.

• Intraparticle Void Space or Intraparticle Pores: The volume of the pores existing within each individual particle. This value will not vary significantly between samples of the same material, assuming the measured material is homogeneous.

For these calculations, the cumulative intruded volume curve as described above is needed. Also needed is the value V_{atm}, which is defined as the volume of mercury displaced by the sample when the mercury is pressurized to atmospheric pressure. To measure this value, another test procedure known as pycnometry is performed. The procedure for a pycnometry test is as follows:

1. The porosimeter cell is evacuated and filled with mercury while no sample is in the cell.

2. The mass of the cell filled with mercury, m_{cell}+Hg, is recorded with the mercury under atmospheric pressure.

3. The same cell is emptied, the sample is added, and the cell is again evacuated and filled with mercury.

4. The mass of the cell with both mercury and sample, m_{cell}+Hg+sample, is recorded, again at atmospheric pressure.

The difference in mass between these two measurements plus the mass of the sample itself, m_{sample}, corresponds to the mass of mercury displaced by the sample at atmospheric conditions. The equation used to find V_{atm} is:

$$V_{atm} = \frac{m_{cell+Hg} - m_{cell+Hg+sample} + m_{sample}}{\rho_{Hg}} \quad [3]$$

Note that since the pycnometry and porosimetry tests are done with two separate samples of the same material, they will likely have different masses. For calculation purposes, we must normalize our volumes with respect to the sample mass. Thus our normalized volume, V^*_{atm} is found using the equation:

$$V^\star_{atm} = \frac{V_{atm}}{m_{pycno}} \quad [4]$$

where m_{pycno} is the mass of sample used for the pycnometry experiment. V^*_{atm} has units of cm^3/g.

Once the value of V^*_{atm} is found, it can be used to find more significant volume values. The first of these is bulk volume, V_{bulk}, which is defined as the volume taken up by the solid sample material, as well as the volume of both interparticle void space and intraparticle void space. This volume cannot be directly measured by the porosimeter, but we can estimate this volume to be the volume of mercury displaced by the sample when the mercury is under extremely low pressure (0.004 psi of absolute pressure). The normalized bulk volume, V^*_{bulk}, is calculated as follows:

$$V^\star_{bulk} = V^\star_{atm} + V^\star_{int,atm} \quad [5]$$

where V^*_{atm} is defined as above and $V^*_{int,atm}$ is defined as the normalized volume intruded from 0.004 psi to 14.7 psi (atmospheric pressure). $V^*_{int,atm}$ can be obtained from the porosimetry test, specifically the normalized cumulative intruded volume curve.

The second useful is true volume, V_{true}, which is defined as the volume taken up by only the solid material of the sample. The normalized true volume, V_{true}, is calculated as follows:

$$V^{\star}_{true} = V^{\star}_{bulk} + V^{\star}_{int,33000psi} \quad [6]$$

V_{bulk} is defined as above and $V^*_{int,33000psi}$ is defined as the normalized volume intruded from 0.004 psi to 33000 psi (the maximum pressure attainable by the porosimeter). $V^*_{int,33000psi}$ can be obtained from the porosimetry test, specifically the normalized cumulative intruded volume curve.

The third volume needed is the particle volume, $V_{particle}$, which is defined as the volume taken up by the solid material of the sample plus the volume taken up by intraparticle void space. The normalized particle volume, $V^*_{particle}$, is calculated as follows:

$$V^{\star}_{particle} = V^{\star}_{bulk} + V^{\star}_{int,particle} \quad [7]$$

where $V_{int;particle}$ is defined as the normalized volume intruded from 0.004 psi up to a certain pressure, $P_{particle}$. $V^*_{int,particle}$ is harder to define compared to $V^*_{int,atm}$ and $V^*_{int,33000psi}$, as it depends on the size of the intraparticle pores present in the sample. $P_{particle}$ should be determined based on the appearance of the pore size distribution (PSD) curve. Commonly, the PSD curve will have a bimodal distribution with two distinct peaks. The peak in the region of larger pore sizes will correspond to interparticle void, while the other peak will correspond to intraparticle void. A $P_{particle}$ is picked by taking a pore size in the region of little or no intrusion between these two peaks and applying equation [1]. To ensure that a proper threshold radius is found, the pore radii of the peaks should be compared to the average particle size (if known). The size of pores in the smaller peak should be well below the average particle size (as the pores must fit within the particles). The size of the pores in the larger peak should be larger than the average particle size (otherwise intraparticle pores may be mistaken for intraparticle void).

Now, with these volumes determined, we can calculate porosity and density.

3.2.1 Density Calculations

True density, ρtrue, is defined as the ratio of sample mass to true volume. True density represents the density of the material disregarding all void space, both interparticle and

intraparticle. Given that the normalized true volume was just found above, the true density is simply found using the equation:

$$\rho_{true} = \frac{1}{V^{\star}_{true}} \quad [8]$$

Particle density, ρparticle, is defined as the ratio of sample mass to particle volume. Particle density represents the density of the material when including intraparticle void space, but excluding interparticle void space. The equation for particle density is:

$$\rho_{particle} = \frac{1}{V^{\star}_{particle}} \quad [9]$$

Bulk density, ρbulk, is defined as the ratio of sample mass to particle volume. Bulk density represents the density of the material when including both intraparticle void space and interparticle void space. Again, as stated above, the bulk properties of the material will change based on handling of the bulk material. The equation for bulk density is:

$$\rho_{bulk} = \frac{1}{V^{\star}_{bulk}} \quad [10]$$

Note that true density will always be greater than particle density, which will always be greater than bulk density.

3.2.2 Porosity Calculations

Porosity, in general, is given as a ratio of void volume to the total volume, Vtotal, of a material. In general, porosity, ϵ is calculated as:

$$\epsilon = \frac{V^{\star}_{total} - V^{\star}_{true}}{V^{\star}_{total}} \quad [11]$$

True, particle and bulk porosities are distinguished by where the control volume of the material is drawn. For bulk porosity the total volume of the material includes both interparticle and intraparticle void. For particle porosity only intraparticle void is included. Neither types of void are included for true porosity. By definition, true porosity is always 0%, as no void space is included in the total volume. Bulk porosity, ϵ_{bulk}, is calculated as follows:

$$\epsilon_{bulk} = \frac{V^{\star}_{bulk} - V^{\star}_{true}}{V^{\star}_{bulk}} \quad [12]$$

Particle porosity, $\epsilon_{particle}$ is calculated similarly:

$$\epsilon_{particle} = \frac{V^{\star}_{particle} - V^{\star}_{true}}{V^{\star}_{particle}} \quad [13]$$

Note that bulk porosity will always be greater than particle porosity.

4. Results

4.1 Porosity and density of the samples

The particle porosity and density are calculated using a $P_{particle}$ value of 209 PSI, i.e., the pore size is smaller than 1μm.

Table D-1. Summary of porosity and density values for tested samples.

Sample	Bulk porosity (%)	Particle porosity (%)
Top sample	38.56	36.94
Bottom sample	31.23	29.41

Sample	Bulk density (g/cc)	Particle density (g/cc)
Top sample	1.14	1.17
Bottom sample	1.19	1.22

The resulting porosity was compared to the porosity obtained from the CT scan analysis for the same specimen (C-0) and the results show a good agreement. The sample labeled as “top” showed a porosity of 38.59, which is similar to the one obtained for the section at 20 mm in the porosity distribution for the specimen C-0 (Figure 4-20a). The sample labeled as “bottom” showed a porosity of 31.23, which is similar to the one obtained on the other end of the soilcrete specimen C-0, specifically in a section tested at approximately 115 mm from the bottom end of the specimen (refer to Figure 4-20a).

4.2 Pore size distribution

Figure D-1 shows pore size distribution of the measured two samples. It can be seen from the Figure D-1 that the pore size distribution between the two samples are pretty similar.

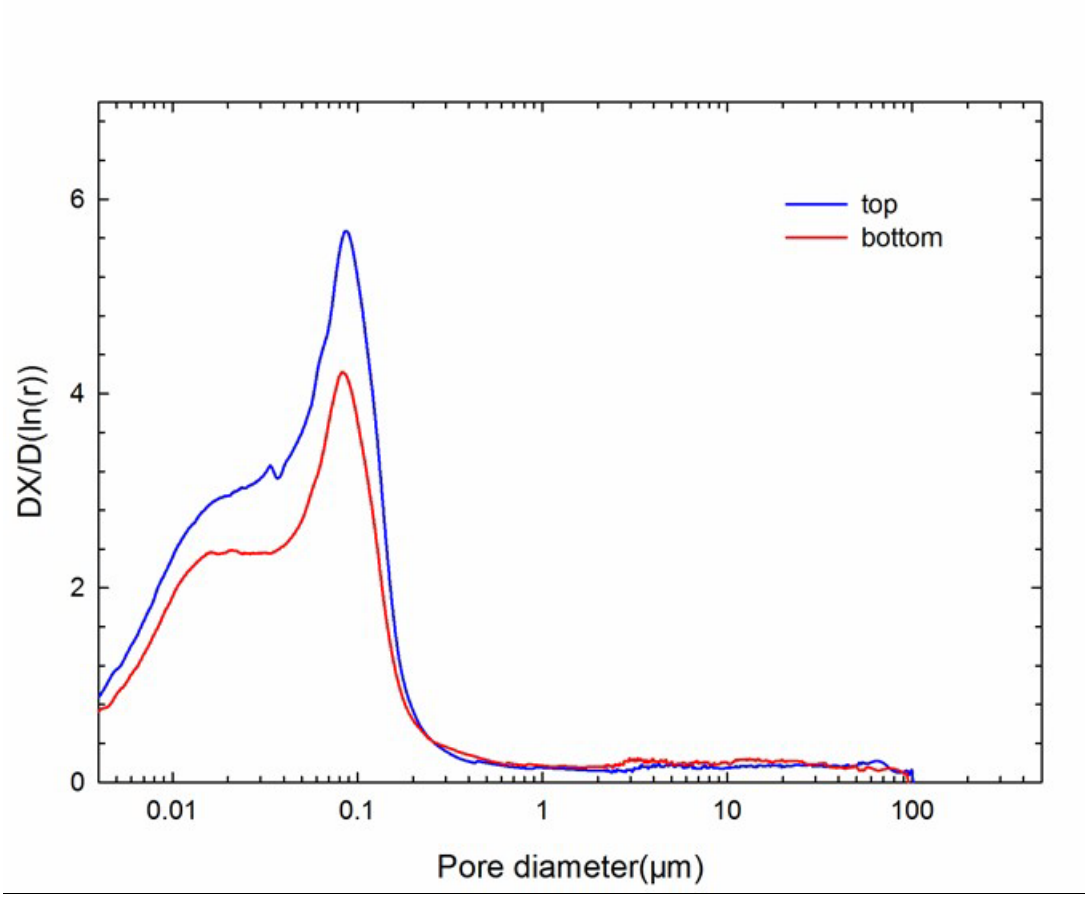

Figure D-1. Pore size distribution for samples at top and bottom of C-0 soilcrete specimen

Appendix E. Soilcrete mixing procedure.

Mixing methodology for laboratory production of soilcrete specimens

1. General

This document describes the mixing procedure used in the laboratory to produce cement-clay specimens (termed as *soilcrete*) in the context of a research project on ground improvement techniques applied to stiff Edmonton clay.

2. General Safety Precautions During Laboratory Procedure

2.1. There are inherent risks when working with electrical equipment and heavy objects, such as the mixing tools. The main concerns when working with the mixing equipment is the risk of malfunction or improper handling of the equipment.

2.2. Do NOT attempt to undertake these tests unless you have been trained in the safe use of the equipment, and have familiarized yourself in the correct use.

2.3. Proper PPE is required to be used during the mixing procedure according to the Laboratory safety rules. This includes but is not limited to: long pants, closed shoes, laboratory coat, safety glasses and nitrile gloves.

3. Apparatus

3.1. Electric blender (Warring Commercial model WSB60)

The electric blender is employed to mix the cement and water slurry. Prior to using the blender, it should be tested with clean water in a bucket to ensure proper functioning.

3.2. Automatic dough mixer (Hobart model Legacy HL200 18.9 Litre)

3.2.1. Hobart mixer base. Should be placed over a stable and flat surface for the mixing procedure. A plastic sheet can be placed underneath to facilitate cleaning after mixing.

3.2.2. Mixing cup. Has a capacity of 18.9 Litre, which is suitable for mixing around 10 kg of dry soil mass and the slurry volume. The cup must be placed correctly on the based and secured on the sides to avoid sliding during the mixing procedure.

3.2.3. Dough mixer hook (Figure E-1a). The shape of this hook provides adequate mixing considering that the soil used for this investigation is a stiff clay. When softer soils are used a palette-shaped hook may be more appropriate (Figure E-1b).

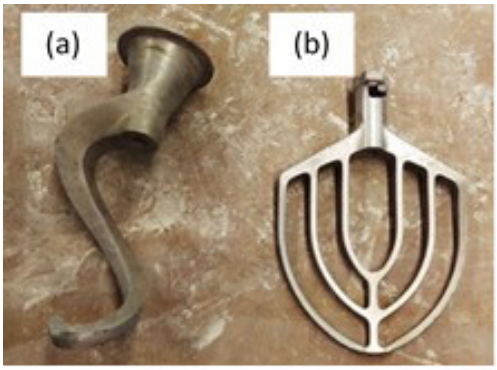

Figure E-1. Dough mixer tools: (a) dough mixer hook used for stiff soil in the present research, and (b) dough mixer palette for soft soil (not used in the present research)

4. Sampling
   - 4.1. The soil used in the mixing for this research project is representative of a location in Eastern Edmonton where the soil is more likely a stiff low plastic clay with some sands. A total of six buckets of soil were collected at the site and stored in a moisture room to avoid the loss of natural water content.
   - 4.2. To ensure a uniform water content among the sampling buckets the whole sample of soil was mixed thoroughly, and then stored in the same buckets until the time of the mixing.

5. Pre-Test Calculations
   - 5.1. Prior to the mixing the soil natural water content needs to be measured, since the natural water content is taken into account to select the water content for the mixing slurry.
   - 5.2. Atterberg limits test should be performed on the soil sample to identify the liquid and plastic limits.
   - 5.3. Determine the water content in the mix. The water content in the natural soil in addition to the water used in the slurry should range from 1.2 to 1.3 of the liquid limit of the soil, to ensure proper mixing.

6. Procedure
   - 6.1. Preparation
     - 6.1.1. All the devices must be placed in an appropriate and safe location for performing the mixing and tested to ensure proper functioning.
   - 6.2. Setup
     - 6.2.1. Soil content, binder content (additive) and water content need to be selected and properly measured in this stage.

6.2.2. Soil is weighted in humid state with the natural water content, and is broken to small pieces for the mixing. The soil is placed directly in the cup of the mixer. The cup is later set correctly on the mixer base and the dough mixer hook must be placed.

Figure E-2. (a) soil being weighted in dough mixer cup, and (b) cup with soil placed on dough mixer.

6.2.3. Cement and water are placed in independent containers for weighting. Cement content depends on the binder content selected by mass of dry soil for the mix. The water mass weighted is the water required for the slurry, as stated in 5.3.

6.2.4. The molds used for the production of the specimens are cylindrical plastic molds 75 mm diameter by 150 mm height. The molds must be greased inside before the mixing takes place

6.3. Slurry preparation

6.3.1. The water for the slurry is placed in a clean bucket and the blender is introduced in the bucket and turned-on to medium speed.

6.3.2. The cement or the binder weighted on 6.2.3. is introduced by parts into the bucket, and mixed in a rotary motion to avoid sticking of the cement to the walls of the bucket.

6.3.3. The mixing motion should be kept for at least 1 to 2 minutes.

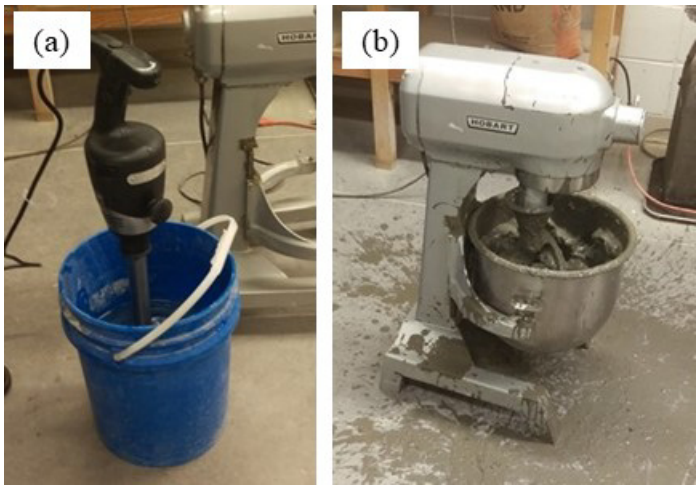

Figure E-3. (a) blender with bucket containing water-cement slurry, and (b) dough mixer with soil and slurry.

6.4. Mixing of the soilcrete

6.4.1. The slurry mixed in 6.3 is incorporated immediately to the soil in the blender cup.

6.4.2. The component will be mixed at medium speed in stages of 30 seconds each. After each stage the mix will be inspected and the portions of soil sticking to the sides of the cup will be separated with a spatula.

6.4.3. The total mixing time should not exceed 2 min, to avoid over-mixing.

6.5. Casting of the mix into the molds

6.5.1. The cup of the blender is removed and the mix is inspected. Hand mixing may be required for the portions of the mix sticked to the sides to fully blend with the rest of the paste.

6.5.2. The mix is cast into the molds by holding a ball size of the paste and pressing it against the inside wall of the mold. The mold is later tapped on a hard surface to make the paste fall by gravity to the bottom and release air. Once the surface of the paste is even and no air is released the procedure is repeated with a new portion of paste.

6.5.3. Once the mold is filled to the top, the surface is leveled with a spatula and plastic film or a plastic lid is placed to cover the open end of the cylinder.

6.5.4. The specimens are stored in a closed container at room temperature, ensuring to have a 2-inch level of water into the container to provide the humid conditions for curing of the specimens.

6.5.5. The specimens remain in the closed container until completing the curing time for the following tests.

Figure E-4. Soilcrete specimens in plastic molds.

Appendix F. Laboratory standard operation procedure for triaxial testing of soilcrete specimens.

Standard Operation Procedure for Consolidated-Undrained Triaxial Test with permeability measurement Using GDS System

1. General

This SOP details the requirements for conducting consolidated-undrained triaxial tests on cement-stabilized clay specimens using GDS triaxial test system measuring the mechanical properties of specimens, including Young's Modulus, friction angle, and cohesion. The SOP includes the measurement of permeability at different stages of the test and could further be adapted for other testing materials and consolidated-drained triaxial tests. This test method specifies the apparatus, instrumentation and procedures.

2. Referenced Documents

2.1. GeoREF Equipment Manuals

2.1.1. ISCO D-Series Pump, Installation and Operation Guide

2.1.2. GDS Pumps

2.1.3. ELE Tritest 50 Load Frame Operation Manual

3. General Safety Precautions and Corresponding SWP

3.1. There are inherent risks in working with high pressures, such as those required for consolidation. Programmable controllers are used for the pressure pumps, which require that the operator be familiar with the operation of the complete system.

3.2. Do NOT attempt to undertake these tests unless you have been trained in the safe use of the equipment, have familiarized yourself with the software and equipment manuals, as identified in Clause 2.1 above, and have read and understood the corresponding Safe Work Practices.

3.3. The corresponding Safe Work Practices include:

3.3.1. SWP – Pressure Safety

3.3.2. SWP – Mobile Crane

3.3.3. SWP – Hand Tools

4. Pre-test Safety Procedures
    4.1. Adjust the ELE Load frame to ensure that it is levelled and firmly sitting on the work station.
    4.2. Run the ISCO and GDS pressure pumps at 3MPa to check if there is any leakage in the pump and the pressure lines before assembling the setup.

5. Summary of Test Method
    5.1. A cement-stabilized clay specimen, shape of a cylinder is placed inside the triaxial cell. Tap water surrounding the specimen exerts confining pressure while ELE Tritest 50 load frame to apply axial load on the specimen.
    5.2. Two GDS pressure pumps and one ISCO D-Series pump are used in the GDS system. One of the GDS pressure pumps is used to apply top back pressure, and another is used to apply cell pressure. The ISCO pump is used to apply bottom back pressure.
    5.3. After a 25kPa back saturation overnight (back pressure at 500kPa and cell pressure at 525kPa), B-test is conducted on the specimen to ensure that the specimen has been fully saturated. Then the specimen could be consolidated to the targeted effective stress level.
    5.4. Permeability test is conducted after finalizing the consolidation stage by closing the by-pass valve for GDS and ISCO back pressure pumps and running a higher pressure at the bottom of the specimen using ISCO back pressure pump.
    5.5. When the targeted effective stress level is reached, shearing could be started using the ELE load frame at a certain shearing rate. The top crossbar of the load frame is fixed while the triaxial cell is moved up driven by a motor. The specimen volume change is directly measured by the GDS back pressure pump readings.

6. Mid-test Safety Procedures
    6.1. It is essential to make sure that the LVDT has enough travel during the whole process especially during shearing stage.
    6.2. It is of great importance to make sure that all three pumps have enough volume to accommodate the volume change during consolidation, permeability test and shearing.
    6.3. Before shearing, it has to be ensured that the top crossbar of the ELE load frame is fixed and the loading rod is in center with the load frame.
    6.4. When entering the shearing rate, it has to be ensured that the rate is correctively entered and really enforced by the system. Stay and monitor the LVDT and load cell readings in the initial stage of shearing.
    6.5. When operating the GDS and ISCO pressure pumps, it is important to distinguish between volume/flow rate control and pressure control. It is safer to operate in the

pressure control mode. Great caution has to be paid when operating these pressure pumps.

7. Significance and Use

7.1. The consolidated-undrained triaxial tests are commonly used to get the mechanical properties of soil/rock specimens like Young's Modulus, Poisson's ratio, friction angle, and cohesion. Also consolidation and permeability tests could be conducted to get the compressibility parameters and permeability of the specimen.

8. Apparatus

8.1. Compression Apparatus

The ELE Tritest 50 load frame is employed to apply axial load on the specimen. The axial load is exerted on the specimen by moving the triaxial cell up using a motor at the base of the load frame while the top crossbar of the load frame is fixed.

8.2. Confining System

8.2.1. Triaxial Cell. Prior to using, ensure that the selected cell has the required capacity to meet the confining pressure and axial load requirements for the diameter and depth (confining pressure) of the specimen to be tested.

8.2.2. Latex Rubber Membranes. Tap water is used as confining fluid in the GDS system and thus latex rubber membranes are suitable.

8.2.3. GDS Pressure Pump. A GDS pressure pump is used to apply cell pressure. The GDS pressure pump measures pressure and volume.

8.2.4. Confining pressure fluid. Tap water is used for applying confining pressure in this system.

8.2.5. Air pressure system. An air pressure system is connected to the three-way valve for confining pressure control. When the valve is opened to the air pressure system, this system could pressurize the triaxial cell to the target pressure first and then the GDS cell pressure pump could take over the control of confining pressure.

8.3. Flow Lines

8.3.1. GDS Pressure Pump. The GDS back pressure pump is connected to the top of the specimen to apply top back pressure.

8.3.2. ISCO Pressure Pump. The ISCO back pressure pump is connected to the bottom of the specimen to apply bottom back pressure. The ISCO pressure pump measures pressure, flow rate and volume.

8.3.3. Pore pressure transducer. The pore pressure transducer is connected to the bottom of the specimen to measure the pore pressure within the specimen.

8.4. Deformation

8.4.1. Axial deformation, if required, is determined through the use of a LVDT.

9. Calibrations

9.1. Pore pressure transducer, LVDT, and load cell should be re-calibrated annually.

9.2. GDS and ISCO pressure pumps should be re-calibrated regularly.

10. Sampling

10.1. The samples are all representative of a same mixing batch, where a natural low plasticity clay was mixed with a binder of 22.5% of cement and mixing water content of 55 to 60%. At the time the test is conducted the samples would have at least 28 days of curing age and would be demolded and inspected for any visible imperfections on the surface.

10.2. Specimen should have a diameter of 3”. The average-height-to-average-diameter ratio shall be between 2 and 2.5 (ASTM D4767-11).

11. Test Specimens

11.1. Test specimens will be circular cylinders with a diameter of 3’’.

12. Pre-Test Calculations

12.1. Determine the required confining pressure for the consolidation phase of the test based on the depth of the specimen. This is equal to the overburden unit weight/m^2 multiplied by depth.

12.2. Determine the average pore pressure according to the desired effective stress and the in-situ hydrostatic pressure.

13. Procedure

13.1. Preparation

13.1.1. Check if the right pump fluid is used. If not, both the ISCO pressure pump and GDS pressure pumps should be emptied and then refilled with the right fluid for a couple of times to make sure all the lines are both clean and saturated. Generally, brine and deionized water will be used in the testing system. The bottles for different fluid should be marked as it is hard to tell between brine and deionized water.

13.1.2. Saturate the base where the specimen will be seated. Inject deionized water from one side of the bottom back pressure channel and make sure the fluid comes out from another side. Then inject high-speed air into the channel for a while and finally refill the channel with the test fluid and close the valve. Repeat this procedure for cell pressure channel, and top back pressure channel.

13.1.3. Get two 3" porous stones ready by using ultrasonic cleaner and boiling in deionized water. Also cut two pieces of filter paper for the porous stones.

13.1.4. Check if the GDSLAB software is communicating well with the GDS system and getting reasonable readings from each instrument (LVDT, Load Cell, pore pressure transducer, GDS pumps and ISCO pump). Connect the ISCO and GDS pumps to atmosphere to check if the pressure reading is zero. If not, the pressure reading has to be zeroed.

13.2. Setup

13.2.1. Put a porous stone and then a filter paper on top of the specimen pedestal, and saturate them with test fluid. Carefully place the specimen on top of the pedestal.

13.2.2. Use the membrane holder to place two layers of Latex rubber membranes over the specimen.

13.2.3. Put a filter paper and then a porous stone on top of the specimen. Flood the top of the specimen test fluid, and then carefully put on the loading cap. Place the port of the loading cap at the comfortable position for connecting to the top back pressure line.

13.2.4. Use the membrane holder to place three O-rings in the pedestal area to fix the bottom part of latex rubber membrane. Then flip over the membranes to cover the O-rings. In a similar way, put another three O-rings in the loading cap area to fix the top part of the membrane and flip the membranes over to cover the O-rings.

13.2.5. Attach the top back pressure line and saturate the line.

13.2.6. Connect the top back pressure line to the loading cap. Hand tight first and then use wrenches to turn 1/8 circle to make sure the connection is tight.

13.2.7. The end of the loading rod is screwed into the main shaft and may be loose. Before putting on the triaxial cell, make sure that the end of loading rod is firmly fixed to the main shaft. Otherwise during shearing, the loading rod will be wobbling.

13.2.8. Put on the triaxial cell and transfer it to the ELE load frame using a mobile crane.

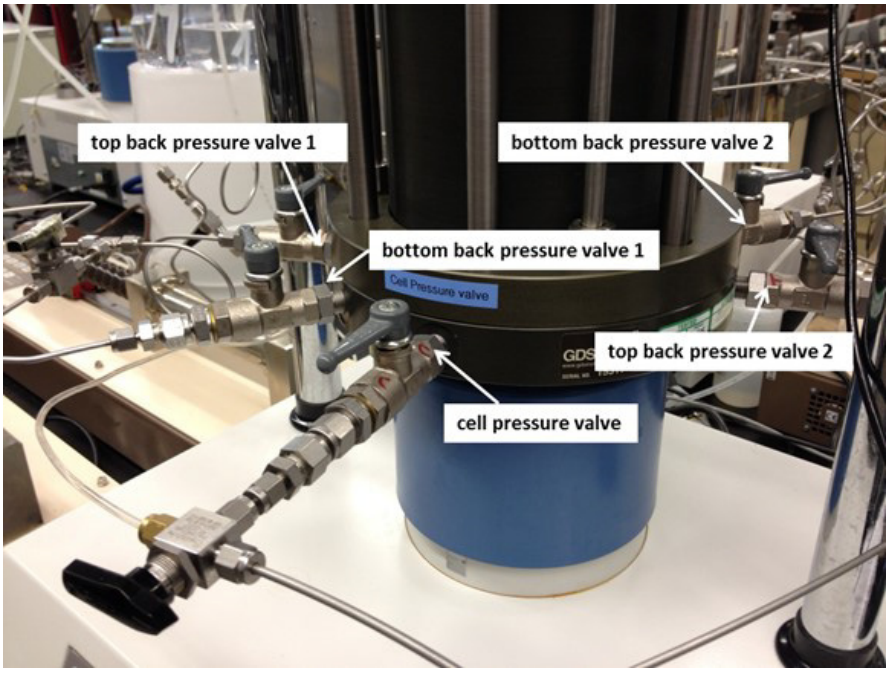

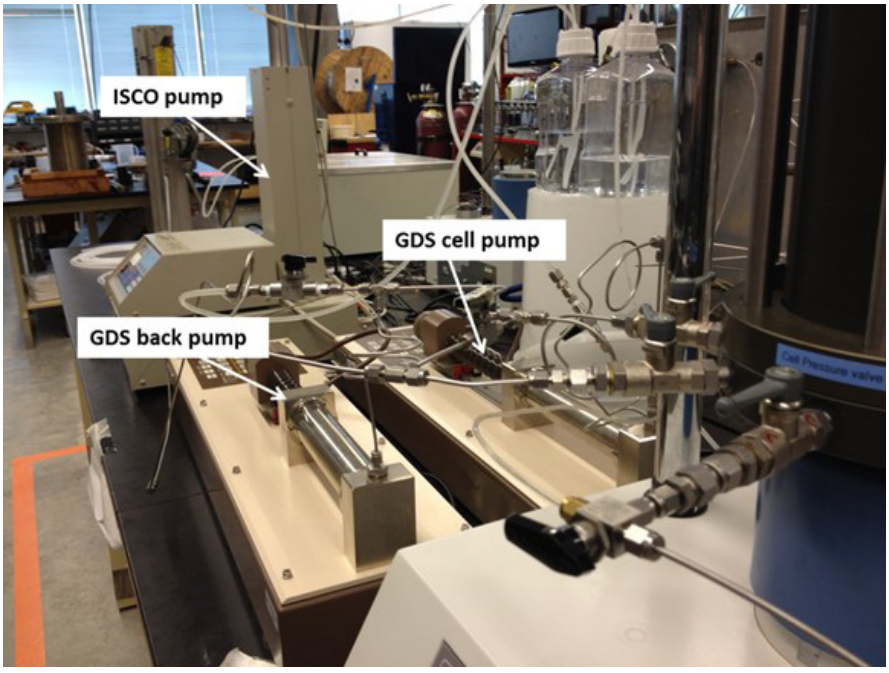

13.2.9. Connect the cell pressure port at the base of the triaxial cell to tap water and fill it up. The outlet at the top of the triaxial cell should be connected to atmosphere using a tube. When water comes out from the tube, the tap water should be stopped and let some time for the air inside the triaxial cell to escape. Then close the outlet.

13.2.10. Close the cell pressure valve, detach the tap water line, saturate the port and then connect the GDS cell pressure pump line to the cell pressure port.

13.2.11. Turn the three-way valve to the air pressure system. Open the cell pressure valve and use the air pressure to pressurize the triaxial cell to 525kPa. Watch out the water level indicator in the water tank of the air pressure system and make sure no air is injected into the triaxial cell. Make sure at this time, the GDS cell pressure pump is stopped.

13.2.12. Turn the three-way valve to the GDS cell pressure pump, and the readings on the pump control panel should indicate a pressure close to 525kPa. Then start running GDS cell pressure pump at 525kPa.

13.2.13. Saturate the ports for top (GDS) and bottom (ISCO) back pressure pump lines. Then connect the ISCO pump to bottom back pressure port 1. Connect the GDS back pressure pump to top back pressure port 1 and connect the pore pressure transducer to bottom back pressure port 2. At this time, make sure all ports are closed.

13.2.14. Open the valve for the pore pressure transducer.

13.2.15. Keep the by-pass valve for ISCO and GDS back pressure pumps open. Open the valves for back pressure pumps. Run the GDS back pressure pump and gradually increase the pressure to 500kPa. Make sure the pressure does not exceed the cell pressure.

13.2.16. Setup the GDS data logging system. At this time, the computer will take over the control of GDS system. Remember to reset the targeted pressure values each time the data logging is reset and also note that the volume reading for GDS back pressure pump will be automatically zeroed.

13.3. B-Test

13.3.1. Keep the back pressure at 500kPa and cell pressure at 525kPa overnight for back saturation.

13.3.2. Set the GDS back pressure pump in ‘HOLD’ mode using GDSLAB software. Increase the cell pressure by 50kPa each step and wait until the GDS back pressure pump readings stabilize. Repeat this step for at least 5 times.

13.3.3. If the B-value is more than 90% ~ 95% (depends on the material), then it means the specimen has been saturated.

13.4. Consolidation

13.4.1. Decrease the cell pressure gradually to 525 kPa and then run the GDS back pressure pump to restore the 500kPa back pressure. Let the system stabilize for a while.

13.4.2. For consolidation, effective consolidation pressure for each step should not exceed 2 times of that for the previous step. So consolidation pressure could be increased in such a way as 50kPa, 100kPa, 200kPa, 400kPa, 800kPa and etc. until the targeted effective stress level is reached.

13.4.3. To capture the full process of consolidation, for each consolidation step, the GDS back pressure pump should be set to 'HOLD' mode and then increase the cell pressure. When the GDS back pressure pump readings become stable, then restore the back pressure to 500kPa, which will start the consolidation.

13.4.4. During consolidation, the by-pass valve is kept open and ISCO back pressure pump is stopped.

13.5. Permeability test

13.5.1. Run the ISCO back pressure pump at 500kPa.

13.5.2. Close the by-pass valve for GDS and ISCO back pressure pumps.

13.5.3. The ISCO bottom back pressure pump will be used to exert higher pressure. And the pressure head for the permeability test should not exceed 10% of the effective consolidation pressure.

13.5.4. To make sure the overall back pressure within the specimen is maintained at 500kPa, the ISCO bottom back pressure pump should be running at (500+ permeability test pressure head/2) kPa and the GDS top back pressure pump should be running at (500- permeability test pressure head/2) kPa.

13.5.5. Monitor the ISCO and GDS back pressure pumps volume change for the initial one hour to ensure that the ISCO back pressure pump has enough volume remaining to pump out fluid and the GDS back pressure pump has enough capacity to receive fluid.

13.5.6. After the perm test, run both the GDS and ISCO back pressure pumps at 500kPa for a while. Then open the by-pass valve and stop the ISCO back pressure pump. Let the system stabilize.

13.5.7. Do the same for the permeability test after shearing.

13.6. Shearing

13.6.1. Setup the LVDT and ensure that there would be enough travel of LVDT for the shearing.

13.6.2. Set the shearing rate based on the consolidation data and the equation recommended at ASTM D4767-11.

13.6.3. For some specimens, it would take long time for the loading rod to touch the specimen. Thus, in the beginning, a higher velocity could be used to shorten the waiting time for the rod to touch the specimen. However, during this period, someone has to be monitoring the load cell readings. Once significant increase of load cell reading (~50N) is observed, the movement of loading rod should be stopped. Then use the shearing rate to move the loading rod.

13.7. Disassemble the triaxial cell

13.7.1. Decrease cell pressure to 600kPa.

13.7.2. Decrease back pressure to 100 ~ 200kPa and then stop the GDS back pressure pump.

13.7.3. Disconnect both ISCO and GDS back pressure pump lines and open both the top and bottom back pressure valves to atmosphere for a while. Then close the valves.

13.7.4. Decrease the cell pressure to 200kPa, during which suction will be developing in the specimen. The suction will help maintain the shape of specimen.

13.7.5. Disconnect GDS cell pressure pump line and then connect the cell pressure port to a tube for chamber fluid drainage. Open the outlet on top of the triaxial cell and let the fluid drainage by gravity for a while.

13.7.6. Connect the outlet on the top of triaxial cell to air pressure which will fasten cell fluid drainage.